

MGII QUASAR ABSORPTION LINE SYSTEMS AS A PROBE
OF GALAXY HALO KINEMATIC EVOLUTION

BY

JESSICA L. EVANS, M.S.

A dissertation submitted to the Graduate School

in partial fulfillment of the requirements

for the degree

Doctor of Philosophy

Major Subject: Astronomy

New Mexico State University

Las Cruces New Mexico

May 2011

“MgII Quasar Absorption Line Systems as a Probe of Galaxy Halo Kinematic Evolution,” a dissertation prepared by Jessica L. Evans in partial fulfillment of the requirements for the degree, Doctor of Philosophy, has been approved and accepted by the following:

Linda Lacey
Dean of the Graduate School

Christopher W. Churchill
Chair of the Examining Committee

Date

Committee in charge:

Dr. Christopher W. Churchill, Chair

Dr. Michael Engelhardt

Dr. Anatoly Klypin

Dr. Rene Walterbos

DEDICATION

To Mom, Dad and David.

ACKNOWLEDGMENTS

I would like to thank my advisor, Dr. Chris Churchill, for all his guidance and support during my graduate studies at NMSU. I would also like to thank Nikki Nielsen for all her help coadding the duplicate spectra in the survey, as well as Elizabeth Klimek for providing CLOUDY models. In addition, thanks to Dr. Michael Engelhardt, Dr. Anatoly Klypin, and Dr. Rene Walterbos for serving on my committee. Finally, thanks to Michael T. Murphy, Jason X. Prochaska, Michael Rauch, Wall Sargent, and Chuck Steidel for their contribution of data.

VITA

- 1998-2003 **B.S.** Physics Cum Laude, GPA 3.7, The College of New Jersey,
Ewing, NJ, USA
- 2005-2008 **M.S.** Astronomy, GPA 3.8, New Mexico State University,
Las Cruces, New Mexico, USA

AWARDS AND GRANTS

- 2000 Department of Energy Research Undergraduate Laboratory
Fellowship (\$5,000)
- 2007 National Optical Astronomy Observatory Graduate Student
Travel Grants (\$1,700 total)
- 2007 American Astronomical Society International Travel
Grant (\$1,028)
- 2007 Associated Students of New Mexico State University
Conference Funding (\$879 total)
- 2007 New Mexico State University Graduate School Conference
Travel Award (\$250)
- 2005–2008 New Mexico State University 21st Century Aerospace
Cluster Fellowship (\$18,000 per year)
- 2007–2008 New Mexico Space Grant Graduate Research Scholarship
(\$5,000 per year)
- 2009 Zia Award for Outstanding Research

REFEREED PUBLICATIONS

- do Couto e Silva, E. et al. 2001, NIM A, 474, 19; *Results from the beam test
of the engineering model of the GLAST large area telescope*
- Churchill, C. W., Kacprzak, G. G, Steidel, C. C., & **Evans, J. L.** 2007, ApJ,
661, 714; *On the Heterogeneity of Metal-Line and
Lyman-Alpha Absorption in Galaxy Halos at $z \sim 0.7$*
- Kacprzak, G. G, Churchill, C. W., Steidel, C. C., Murphy, M. T., & **Evans,
J. L.** 2007 ApJ, 662, 909; *A Correlation Between Galaxy Morphology
and MgII Halo Absorption Strength*

CONFERENCE PRESENTATIONS

- 2006 209th Meeting of the American Astronomical Society: *Evidence for Evolution in Weak MgII Absorbers at $z < 1.5$* , **Evans, J. L.**, Churchill, C. W., Murphy, M. T., & Widhalm, A. M.
- 2007 National Radio Astronomy Observatory New Mexico Symposium: *Statistical Properties of 215 MgII Absorbers at $z < 1.5$* , **Evans, J. L.**, Churchill, C. W., Widhalm, A. M., & Murphy, M. T.
- 2007 Max Planck Institute for Astrophysics, Gas Accretion and Star Formation in Galaxies: *Statistical Properties of 215 MgII Absorbers at $z < 1.5$* , **Evans, J. L.**, Churchill, C. W., Widhalm, A. M., & Murphy, M. T.
- 2007 New Mexico State University Graduate Student Research and Arts Symposium: *Evidence for Evolution in Weak MgII Absorbers at $z < 1.5$* , **Evans, J. L.**, Churchill, C. W., Murphy, M. T., & Widhalm, A. M.
- 2008 UC Irvine Center for Cosmology Workshop, Galaxy Formation and Evolution as Revealed by Cosmic Gas: *MgII Quasar Absorption Lines as a Probe of Galaxy Structural and Kinematic Evolution*, **Evans, J. L.**, Churchill, C. W., Murphy, M. T., & Widhalm, A. M.

ABSTRACT

MGII QUASAR ABSORPTION LINE SYSTEMS AS A PROBE
OF GALAXY HALO KINEMATIC EVOLUTION

BY

JESSICA L. EVANS, M.S.

Doctor of Philosophy

New Mexico State University

Las Cruces, New Mexico, 2011

Dr. Christopher W. Churchill, Chair

Quasar lines of sight can be employed to place constraints on scenarios of galaxy formation. Armed with the largest database of high resolution, high signal-to-noise quasar absorption line spectra ever compiled, we have identified 469 and analyzed 422 MgII $\lambda\lambda 2796, 2803$ doublet systems over the redshift range $0.1 < z < 2.6$ in order to shed much needed light on our current picture of galaxy halo and intergalactic medium gas kinematics and structure, and to chart how these have changed throughout cosmic time. The cumulative redshift path of the survey is ~ 230.8 and is $\sim 100\%$ complete to a 5σ equivalent width sensitivity of $W_r(2796) =$

0.05 Å. We have divided our sample into “weak” systems ($W_r(2796) < 0.3$ Å) and “strong” systems ($W_r(2796) \geq 0.3$ Å) for comparison with previous studies.

We fit a power law of slope 0.92 ± 0.02 to the weak MgII equivalent width distribution and find no evidence of a turnover down to the smallest observable equivalent widths. We find significant differences in the population of isolated weak MgII systems and the superficially similar high velocity weak subsystems of strong MgII systems.

By performing Voigt profile modeling of each system, we fit a power law of slope 1.451 ± 0.0002 to the resulting VP component distribution. Assuming thermal Doppler b parameters results in mean cloud temperatures of 18,000 - 26,000 K. Our two-point correlation function of VP velocity separations reveals that the majority of component clustering occurs on scales of $\lesssim 200$ km s⁻¹.

We construct the flux decrement distributions of MgII absorption in a grid of equivalent width, velocity, and redshift bins in order to identify and quantify kinematic evolution through cosmic time in the strongest systems. We also calculate the number of absorbers per unit redshift of weak MgII systems and find clear evidence for evolution.

We thus construct a statistical framework for understanding the physical processes selected by the presence of MgII.

CONTENTS

LIST OF TABLES	xlili
LIST OF FIGURES.....	xlvi
LIST OF COMPACT DISC DATA	xlvi
1 INTRODUCTION	1
1.1 Motivation	1
1.2 Background	2
1.2.1 Low Resolution MgII Surveys.....	4
1.2.2 High Resolution Strong MgII Surveys	9
1.2.3 High Resolution Weak MgII Surveys	14
1.2.4 Goals of the Project	18
2 DATA	22
2.1 The Spectra.....	22
2.2 Reduction	36
2.2.1 HIRES Spectra.....	36
2.2.2 UVES Spectra	36
2.2.3 HIRES and UVES Duplicate Coverage	36
2.3 Characteristics of the Spectra	37
2.3.1 Redshift Coverage.....	37
2.3.2 Redshift Path Sensitivity	37

2.4	Identifying MgII Doublets	41
2.5	Problems at High Redshift	44
2.6	Global Absorption Line System Characteristics	45
2.6.1	System Redshifts.....	45
2.6.2	Required System Equivalent Width Limit	45
2.7	Possible Sample Bias	47
2.8	Selected Atomic Transitions and Example MgII Systems	53
3	ANALYSIS OF MGII SYSTEMS	61
3.1	Equivalent Width Regions.....	65
3.2	Equivalent Widths.....	67
3.3	System Redshifts and Velocities	68
3.4	Total Velocity Widths, Mean Velocities, and Velocity Spreads.....	69
3.5	Results.....	72
3.5.1	Equivalent Width Distribution of MgII Systems	72
3.5.2	Kinematic Properties of MgII Systems	74
3.5.3	Kinematic Subsystem Properties of Strong MgII Systems.....	75
3.5.4	Weak MgII Systems versus High Velocity Kinematic Subsystems of Strong MgII Systems	78
4	VOIGT PROFILE ANALYSIS	81
4.1	Introduction to Voigt Profile Fitting	81
4.2	Fitting Philosophy	85
4.3	Fitting Procedure.....	86

4.3.1	Saturated Regions	88
4.3.2	Masking Spectral Regions	88
4.3.3	χ^2 Minimization and Model Convergence	88
4.3.4	Column Density Limits	90
4.4	Results	90
4.4.1	Number of VP Components	90
4.4.2	Column Density Distribution	92
4.4.3	Doppler Parameter Distribution	94
4.4.4	Cloud-Cloud Velocity Clustering	97
5	REDSHIFT EVOLUTION	101
5.1	Evolution of Strong MgII Systems.....	101
5.2	Evolution of Weak MgII Systems.....	111
5.2.1	Calculation of the Redshift Path Sensitivity.....	111
5.2.2	Cumulative Redshift Path and Survey Completeness.....	112
5.2.3	Number of Absorbers per Unit Redshift	115
6	CONCLUSION	122
6.1	Strong MgII Systems	125
6.2	Weak MgII Systems	131
6.2.1	Evolution of Absorber Sizes Using Cosmological Structure Growth.....	133
6.2.2	Evolution of Absorber Sizes Using CLOUDY	137
6.2.3	Two Scenarios of MgII-Selected Gas Structure	141
Appendix A	DISCUSSION OF MGII SYSTEMS.....	144

A.1	J000323-260318	144
A.1.1	$z_{abs} = 1.434037$	144
A.2	J000149-015939	145
A.2.1	$z_{abs} = 0.870821$	145
A.3	J000520+052411	145
A.3.1	$z_{abs} = 0.298058$	145
A.3.2	$z_{abs} = 0.591364$	145
A.3.3	$z_{abs} = 0.851393$	145
A.3.4	$z_{abs} = 0.866529$	146
A.3.5	$z_{abs} = 0.956028$	146
A.4	J000344-232355	146
A.4.1	$z_{abs} = 0.452397$	146
A.4.2	$z_{abs} = 0.949116$	146
A.4.3	$z_{abs} = 1.586132$	147
A.4.4	$z_{abs} = 1.651460$	147
A.4.5	$z_{abs} = 2.184448$	147
A.5	J000448-415728	148
A.5.1	$z_{abs} = 0.836627$	148
A.5.2	$z_{abs} = 1.541851$	148
A.5.3	$z_{abs} = 1.988657$	149
A.5.4	$z_{abs} = 2.167883$	149
A.5.5	$z_{abs} = 2.301941$	149

A.5.6	$z_{abs} = 2.464126$	150
A.6	J001130+005550	150
A.6.1	$z_{abs} = 1.395604$	150
A.6.2	$z_{abs} = 1.777928$	150
A.7	J001210-012207	150
A.7.1	$z_{abs} = 1.202983$	150
A.7.2	$z_{abs} = 1.385936$	151
A.8	J001306+000431	151
A.8.1	$z_{abs} = 1.212007$	151
A.9	J001602-001225	151
A.9.1	$z_{abs} = 0.635095$	151
A.9.2	$z_{abs} = 0.857465$	152
A.9.3	$z_{abs} = 1.146778$	152
A.9.4	$z_{abs} = 1.971326$	152
A.9.5	$z_{abs} = 2.029186$	153
A.10	J002133+004301	154
A.10.1	$z_{abs} = 0.520353$	154
A.10.2	$z_{abs} = 0.942041$	154
A.11	J002151-012833	154
A.11.1	$z_{abs} = 0.695180$	154
A.11.2	$z_{abs} = 1.241235$	154
A.11.3	$z_{abs} = 1.308740$	155

A.12	J002208-150539	155
A.12.1	$z_{abs} = 1.700022$	155
A.13	J004428-243417	155
A.14	J004508-291432	156
A.15	J004812-255003	156
A.15.1	$z_{abs} = 0.690864$	156
A.16	J004816-254745	156
A.17	J004848-260020	156
A.18	J005024-252234	156
A.18.1	$z_{abs} = 0.699887$	156
A.19	J005109-255216	157
A.20	J005127-280433	157
A.21	J005211-251857	157
A.21.1	$z_{abs} = 0.887325$	157
A.21.2	$z_{abs} = 1.067163$	157
A.22	J005419-254900	158
A.23	J005758-264314	158
A.23.1	$z_{abs} = 1.267863$	158
A.23.2	$z_{abs} = 1.533672$	158
A.24	J005925-411043	158
A.25	J010054+021136	159
A.25.1	$z_{abs} = 0.346669$	159

A.25.2	$z_{abs} = 0.612586$	159
A.25.3	$z_{abs} = 0.725100$	159
A.25.4	$z_{abs} = 0.734779$	159
A.26	J010311+131617	160
A.26.1	$z_{abs} = 1.758901$	160
A.26.2	$z_{abs} = 1.797435$	160
A.26.3	$z_{abs} = 2.298687$	160
A.26.4	$z_{abs} = 2.309309$	161
A.27	J011143-350300	161
A.27.1	$z_{abs} = 0.769642$	161
A.27.2	$z_{abs} = 1.182696$	161
A.27.3	$z_{abs} = 1.349591$	161
A.28	J012156+144824	162
A.29	J012227-042127	162
A.29.1	$z_{abs} = 0.338567$	162
A.29.2	$z_{abs} = 0.657432$	162
A.29.3	$z_{abs} = 0.719595$	162
A.30	J012017+213347	163
A.30.1	$z_{abs} = 0.576397$	163
A.30.2	$z_{abs} = 0.729076$	163
A.30.3	$z_{abs} = 1.047970$	163
A.30.4	$z_{abs} = 1.325293$	164

A.31	J012417-374423	164
A.31.1	$z_{abs} = 0.443384$	164
A.31.2	$z_{abs} = 0.822095$	164
A.31.3	$z_{abs} = 0.859261$	164
A.31.4	$z_{abs} = 0.909587$	165
A.31.5	$z_{abs} = 1.173634$	165
A.31.6	$z_{abs} = 1.243344$	165
A.31.7	$z_{abs} = 1.909192$	165
A.31.8	$z_{abs} = 1.973356$	165
A.32	J012642+255901	166
A.33	J012944-403346	166
A.34	J013105-213446	166
A.35	J013405+005109	166
A.35.1	$z_{abs} = 0.684746$	166
A.35.2	$z_{abs} = 0.821387$	167
A.35.3	$z_{abs} = 0.842235$	167
A.35.4	$z_{abs} = 1.272233$	167
A.36	J013442-413611	167
A.37	J013857-225447	168
A.37.1	$z_{abs} = 0.802369$	168
A.37.2	$z_{abs} = 0.884865$	168
A.37.3	$z_{abs} = 1.184190$	168

A.37.4	$z_{abs} = 1.261748$	168
A.37.5	$z_{abs} = 1.294135$	169
A.37.6	$z_{abs} = 1.353669$	169
A.38	J015234+335032	169
A.38.1	$z_{abs} = 0.520292$	169
A.39	J015327-431137	170
A.39.1	$z_{abs} = 0.663065$	170
A.39.2	$z_{abs} = 1.708494$	170
A.39.3	$z_{abs} = 2.451566$	170
A.40	J015734+744244	171
A.40.1	$z_{abs} = 0.745002$	171
A.41	J015733-004824	171
A.41.1	$z_{abs} = 0.768336$	171
A.41.2	$z_{abs} = 1.415684$	171
A.42	J020346+113445	172
A.42.1	$z_{abs} = 1.574187$	172
A.43	J020455+364918	172
A.43.1	$z_{abs} = 0.731671$	172
A.44	J020930+051730	173
A.44.1	$z_{abs} = 1.280753$	173
A.44.2	$z_{abs} = 1.532246$	173
A.45	J021857+081728	173

A.45.1	$z_{abs} = 1.459030$	173
A.46	J023145+132254	174
A.47	J024008-230915	174
A.47.1	$z_{abs} = 1.184618$	174
A.47.2	$z_{abs} = 1.365057$	174
A.47.3	$z_{abs} = 1.637107$	174
A.47.4	$z_{abs} = 1.657430$	175
A.47.5	$z_{abs} = 1.672358$	175
A.48	J024401-013402	175
A.49	J024854+180250	175
A.50	J025134+431516	176
A.50.1	$z_{abs} = 0.655111$	176
A.50.2	$z_{abs} = 0.736163$	176
A.51	J025240-553832	176
A.51.1	$z_{abs} = 1.568340$	176
A.51.2	$z_{abs} = 2.143195$	176
A.52	J025518+004847	177
A.53	J025607+011038	177
A.53.1	$z_{abs} = 0.725487$	177
A.54	J025634-401300	177
A.54.1	$z_{abs} = 0.549057$	177
A.54.2	$z_{abs} = 0.888692$	178

A.54.3	$z_{abs} = 1.283867$	178
A.55	J030211-314030	178
A.56	J030449-000813	178
A.57	J030449-221152	179
A.57.1	$z_{abs} = 1.009382$	179
A.58	J031009-192207	179
A.58.1	$z_{abs} = 0.889888$	179
A.58.2	$z_{abs} = 1.433701$	179
A.58.3	$z_{abs} = 1.636001$	179
A.58.4	$z_{abs} = 1.788440$	180
A.58.5	$z_{abs} = 2.032104$	180
A.59	J033032-270438	180
A.59.1	$z_{abs} = 0.787945$	180
A.59.2	$z_{abs} = 1.122903$	181
A.59.3	$z_{abs} = 1.298884$	181
A.59.4	$z_{abs} = 1.306925$	181
A.60	J033106-382404	181
A.60.1	$z_{abs} = 0.762781$	181
A.60.2	$z_{abs} = 0.929587$	182
A.60.3	$z_{abs} = 0.970951$	182
A.60.4	$z_{abs} = 1.438023$	182
A.61	J033900-013318	182

A.62	J034943-381030	183
A.62.1	$z_{abs} = 1.457112$	183
A.62.2	$z_{abs} = 1.526344$	183
A.63	J035405-272421	183
A.63.1	$z_{abs} = 1.405187$	183
A.64	J040356-170324	184
A.65	J040718-441013	184
A.65.1	$z_{abs} = 0.818400$	184
A.65.2	$z_{abs} = 1.017638$	184
A.65.3	$z_{abs} = 1.912359$	184
A.65.4	$z_{abs} = 2.412425$	185
A.65.5	$z_{abs} = 2.550400$	185
A.66	J042214-384452	186
A.66.1	$z_{abs} = 1.880422$	186
A.67	J042315-012033	186
A.67.1	$z_{abs} = 0.633002$	186
A.68	J042353-261801	186
A.68.1	$z_{abs} = 1.210044$	186
A.69	J042408+020425	187
A.69.1	$z_{abs} = 0.738949$	187
A.70	J042707-130253	187
A.70.1	$z_{abs} = 1.034519$	187

A.70.2	$z_{abs} = 1.407984$	187
A.71	J043037-485523	188
A.71.1	$z_{abs} = 0.554375$	188
A.71.2	$z_{abs} = 1.119028$	188
A.71.3	$z_{abs} = 1.355354$	188
A.72	J043038-133546	189
A.73	J044017-433308	189
A.73.1	$z_{abs} = 1.433457$	189
A.73.2	$z_{abs} = 1.880918$	189
A.73.3	$z_{abs} = 2.347761$	189
A.74	J044026-163234	190
A.75	J044117-431343	190
A.75.1	$z_{abs} = 0.440751$	190
A.76	J045142-132033	191
A.76.1	$z_{abs} = 1.266634$	191
A.77	J045218-130503	191
A.77.1	$z_{abs} = 0.548068$	191
A.77.2	$z_{abs} = 1.174630$	192
A.77.3	$z_{abs} = 1.229493$	192
A.77.4	$z_{abs} = 1.310674$	192
A.78	J045523-421617	192
A.78.1	$z_{abs} = 0.726105$	192

A.78.2	$z_{abs} = 0.759820$	193
A.78.3	$z_{abs} = 0.908508$	193
A.78.4	$z_{abs} = 1.039518$	193
A.78.5	$z_{abs} = 1.149873$	193
A.78.6	$z_{abs} = 1.629987$	194
A.78.7	$z_{abs} = 1.858376$	194
A.78.8	$z_{abs} = 2.304567$	195
A.79	J045608-215909	195
A.79.1	$z_{abs} = 0.474417$	195
A.79.2	$z_{abs} = 0.483337$	195
A.80	J045647+040053	196
A.80.1	$z_{abs} = 0.642827$	196
A.80.2	$z_{abs} = 0.859569$	196
A.80.3	$z_{abs} = 0.931502$	196
A.80.4	$z_{abs} = 1.153249$	197
A.81	J050112-015914	197
A.81.1	$z_{abs} = 0.890257$	197
A.81.2	$z_{abs} = 2.039284$	197
A.82	J051707-441055	198
A.82.1	$z_{abs} = 0.222241$	198
A.82.2	$z_{abs} = 0.429123$	198
A.82.3	$z_{abs} = 0.940626$	198

A.82.4	$z_{abs} = 1.150872$	198
A.83	J053007-250329	199
A.83.1	$z_{abs} = 0.944063$	199
A.83.2	$z_{abs} = 1.672122$	199
A.83.3	$z_{abs} = 2.141121$	199
A.84	J053008-250330	200
A.85	J053056+133154	200
A.85.1	$z_{abs} = 1.576187$	200
A.85.2	$z_{abs} = 1.963172$	200
A.86	J055158-211949	200
A.86.1	$z_{abs} = 0.439830$	200
A.87	J055246-363727	201
A.87.1	$z_{abs} = 0.505570$	201
A.87.2	$z_{abs} = 1.225244$	201
A.87.3	$z_{abs} = 1.492188$	201
A.87.4	$z_{abs} = 1.961208$	201
A.88	J064204+675836	202
A.88.1	$z_{abs} = 1.293828$	202
A.89	J064326-504112	202
A.90	J064632+445117	203
A.91	J074521+473436	203
A.91.1	$z_{abs} = 0.857331$	203

A.91.2	$z_{abs} = 0.891322$	203
A.91.3	$z_{abs} = 1.611153$	203
A.92	J075054+425219	204
A.93	J075112+291938	204
A.94	J080117+521034	204
A.95	J081240+320808	204
A.95.1	$z_{abs} = 1.223076$	204
A.96	J081331+254503	205
A.96.1	$z_{abs} = 0.821724$	205
A.96.2	$z_{abs} = 0.831524$	205
A.97	J083141+524518	205
A.97.1	$z_{abs} = 1.180673$	205
A.97.2	$z_{abs} = 1.290840$	206
A.97.3	$z_{abs} = 1.549929$	206
A.97.4	$z_{abs} = 1.812894$	206
A.97.5	$z_{abs} = 2.041735$	207
A.98	J083052+241100	207
A.98.1	$z_{abs} = 0.524966$	207
A.99	J083933+111207	208
A.100	J084424+124546	208
A.100.1	$z_{abs} = 0.709230$	208
A.100.2	$z_{abs} = 1.098401$	208

A.100.3	$z_{abs} = 1.131402$	208
A.100.4	$z_{abs} = 1.219175$	209
A.100.5	$z_{abs} = 1.863904$	209
A.100.6	$z_{abs} = 2.374482$	209
A.101	J090033+421546	210
A.101.1	$z_{abs} = 1.355719$	210
A.102	J091127+055054	210
A.102.1	$z_{abs} = 0.774684$	210
A.102.2	$z_{abs} = 0.994627$	210
A.102.3	$z_{abs} = 1.210128$	210
A.103	J091613+070224	211
A.103.1	$z_{abs} = 1.187206$	211
A.103.2	$z_{abs} = 1.332451$	211
A.104	J092913-021446	211
A.104.1	$z_{abs} = 1.096330$	211
A.104.2	$z_{abs} = 1.106422$	211
A.104.3	$z_{abs} = 1.232216$	212
A.105	J093337+284532	212
A.106	J093748+730158	212
A.107	J094253-110426	212
A.107.1	$z_{abs} = 1.059675$	212
A.107.2	$z_{abs} = 1.789114$	213

A.107.3	$z_{abs} = 1.918429$	213
A.107.4	$z_{abs} = 2.174545$	213
A.108	J094835+432302	214
A.108.1	$z_{abs} = 1.232747$	214
A.109	J095122+263514	214
A.110	J095355-050418	214
A.111	J095500-013006	214
A.111.1	$z_{abs} = 1.625062$	214
A.112	J095744+330820	215
A.113	J095852+120245	215
A.114	J100120.8+555354	215
A.114.1	$z_{abs} = 0.903934$	215
A.114.2	$z_{abs} = 1.024809$	215
A.114.3	$z_{abs} = 1.124273$	215
A.115	J100120.9+555349	216
A.115.1	$z_{abs} = 1.124587$	216
A.116	J100129+545438	216
A.116.1	$z_{abs} = 1.211316$	216
A.116.2	$z_{abs} = 1.272383$	216
A.117	J101155+294141	216
A.117.1	$z_{abs} = 1.111735$	216
A.118	J100930-002619	217

A.118.1	$z_{abs} = 0.842755$	217
A.118.2	$z_{abs} = 0.886487$	217
A.119	J101447+430031	217
A.119.1	$z_{abs} = 1.416350$	217
A.119.2	$z_{abs} = 2.042606$	218
A.120	J101549+002019	218
A.121	J102156+300141	218
A.121.1	$z_{abs} = 1.274372$	218
A.122	J102837-010027	219
A.122.1	$z_{abs} = 0.708803$	219
A.123	J103623-034320	219
A.124	J104117+061016	219
A.124.1	$z_{abs} = 0.441452$	219
A.124.2	$z_{abs} = 0.655331$	219
A.125	J104733+052454	220
A.125.1	$z_{abs} = 0.198417$	220
A.125.2	$z_{abs} = 0.318212$	220
A.125.3	$z_{abs} = 0.801159$	220
A.126	J104800+052209	220
A.127	J105440-002048	221
A.127.1	$z_{abs} = 0.830173$	221
A.127.2	$z_{abs} = 0.941984$	221

A.127.3	$z_{abs} = 0.951693$	221
A.128	J105756+455552	222
A.128.1	$z_{abs} = 1.386417$	222
A.128.2	$z_{abs} = 1.522192$	222
A.128.3	$z_{abs} = 1.567824$	222
A.129	J110325-264515	223
A.129.1	$z_{abs} = 1.186892$	223
A.129.2	$z_{abs} = 1.202831$	223
A.129.3	$z_{abs} = 1.211354$	223
A.129.4	$z_{abs} = 1.267694$	223
A.129.5	$z_{abs} = 1.551516$	224
A.129.6	$z_{abs} = 1.838688$	224
A.130	J111038+483116	224
A.130.1	$z_{abs} = 0.807537$	224
A.130.2	$z_{abs} = 0.861875$	224
A.130.3	$z_{abs} = 1.015805$	225
A.131	J111113-080402	225
A.131.1	$z_{abs} = 1.901669$	225
A.131.2	$z_{abs} = 1.975442$	225
A.132	J111350-153333	226
A.132.1	$z_{abs} = 1.038732$	226
A.132.2	$z_{abs} = 1.256076$	226

A.133	J222006-280323	226
A.133.1	$z_{abs} = 0.599508$	226
A.133.2	$z_{abs} = 0.786511$	226
A.133.3	$z_{abs} = 0.942415$	227
A.133.4	$z_{abs} = 1.082795$	227
A.133.5	$z_{abs} = 1.555851$	227
A.133.6	$z_{abs} = 1.627859$	227
A.133.7	$z_{abs} = 1.692150$	228
A.134	J111654-221652	228
A.135	J112442-170517	228
A.135.1	$z_{abs} = 0.682269$	228
A.135.2	$z_{abs} = 0.806213$	229
A.135.3	$z_{abs} = 1.234142$	229
A.136	J113007-144927	229
A.136.1	$z_{abs} = 0.190569$	229
A.136.2	$z_{abs} = 0.312709$	229
A.137	J113508+222716	230
A.137.1	$z_{abs} = 0.718958$	230
A.138	J114254+265457	230
A.138.1	$z_{abs} = 1.711805$	230
A.138.2	$z_{abs} = 2.196632$	231
A.139	J114308+345220	231

A.140	J115129+382552	231
A.140.1	$z_{abs} = 0.553363$	231
A.141	J115944+011206	232
A.141.1	$z_{abs} = 0.790815$	232
A.141.2	$z_{abs} = 1.098251$	232
A.141.3	$z_{abs} = 1.330499$	232
A.141.4	$z_{abs} = 1.943649$	232
A.142	J120523-074232	233
A.142.1	$z_{abs} = 1.754690$	233
A.143	J120550+020131	234
A.143.1	$z_{abs} = 1.252126$	234
A.144	J120858+454036	234
A.144.1	$z_{abs} = 0.927592$	234
A.144.2	$z_{abs} = 0.934277$	234
A.145	J121135+090223	234
A.146	J121140+103002	235
A.146.1	$z_{abs} = 0.392923$	235
A.146.2	$z_{abs} = 1.049608$	235
A.147	J121303+171423	235
A.147.1	$z_{abs} = 0.841454$	235
A.147.2	$z_{abs} = 1.891680$	235
A.147.3	$z_{abs} = 1.931468$	236

A.148	J121509+330955	236
A.149	J121549-003434	236
A.149.1	$z_{abs} = 1.127698$	236
A.149.2	$z_{abs} = 1.320047$	236
A.149.3	$z_{abs} = 1.554148$	237
A.150	J121732+330539	237
A.151	J121930+494051	237
A.152	J122310-181642	237
A.153	J122527+223513	238
A.153.1	$z_{abs} = 0.668056$	238
A.154	J122607+173648	238
A.155	J122824+312838	238
A.155.1	$z_{abs} = 0.530457$	238
A.155.2	$z_{abs} = 1.794827$	238
A.156	J122607+173650	239
A.156.1	$z_{abs} = 1.421516$	239
A.156.2	$z_{abs} = 1.492086$	239
A.156.3	$z_{abs} = 2.465802$	239
A.157	J123200-022404	240
A.157.1	$z_{abs} = 0.395139$	240
A.157.2	$z_{abs} = 0.700375$	240
A.157.3	$z_{abs} = 0.756903$	240

A.157.4	$z_{abs} = 0.768850$	241
A.157.5	$z_{abs} = 0.830851$	241
A.158	J123437+075843	241
A.158.1	$z_{abs} = 0.765120$	241
A.158.2	$z_{abs} = 0.861292$	241
A.159	J124410+172104	242
A.159.1	$z_{abs} = 0.550481$	242
A.160	J124604-073046	242
A.161	J124714+312640	242
A.161.1	$z_{abs} = 0.850493$	242
A.162	J124524-000938	243
A.162.1	$z_{abs} = 1.275301$	243
A.163	J124913-055918	243
A.163.1	$z_{abs} = 0.639908$	243
A.163.2	$z_{abs} = 0.902603$	243
A.163.3	$z_{abs} = 1.201507$	243
A.164	J124924-023339	244
A.164.1	$z_{abs} = 0.436843$	244
A.164.2	$z_{abs} = 0.725983$	244
A.164.3	$z_{abs} = 1.341271$	244
A.164.4	$z_{abs} = 1.775414$	244
A.164.5	$z_{abs} = 1.780539$	245

A.164.6	$z_{abs} = 1.892961$	245
A.165	J125048+395140	245
A.165.1	$z_{abs} = 0.772956$	245
A.165.2	$z_{abs} = 0.854562$	246
A.166	J125659+042734	246
A.166.1	$z_{abs} = 0.934231$	246
A.167	J131011+460124	246
A.168	J131956+272808	247
A.168.1	$z_{abs} = 0.660049$	247
A.169	J132323-002155	247
A.169.1	$z_{abs} = 0.564142$	247
A.169.2	$z_{abs} = 0.716096$	247
A.170	J133141+410158	248
A.170.1	$z_{abs} = 0.998359$	248
A.171	J133335+164903	248
A.171.1	$z_{abs} = 0.744641$	248
A.171.2	$z_{abs} = 1.328180$	248
A.171.3	$z_{abs} = 1.776598$	249
A.171.4	$z_{abs} = 1.786300$	249
A.172	J134002+110630	250
A.172.1	$z_{abs} = 1.636630$	250
A.172.2	$z_{abs} = 2.138662$	250

A.172.3	$z_{abs} = 2.149819$	250
A.173	J134427-103541	251
A.173.1	$z_{abs} = 0.752226$	251
A.173.2	$z_{abs} = 0.786156$	251
A.173.3	$z_{abs} = 0.872827$	251
A.173.4	$z_{abs} = 1.276747$	251
A.173.5	$z_{abs} = 1.915412$	252
A.174	J134916-033715	252
A.175	J135038-251216	252
A.175.1	$z_{abs} = 0.575543$	252
A.175.2	$z_{abs} = 1.439264$	252
A.175.3	$z_{abs} = 1.508140$	253
A.175.4	$z_{abs} = 1.752902$	253
A.176	J135646-110128	253
A.176.1	$z_{abs} = 0.764777$	253
A.176.2	$z_{abs} = 2.212410$	253
A.177	J135704+191906	254
A.178	J140039+112022	254
A.178.1	$z_{abs} = 1.077748$	254
A.179	B1422+231A	254
A.180	B1422+231B	254
A.181	B1422+231C	255

A.182	J142326+325220	255
A.182.1	$z_{abs} = 0.843247$	255
A.182.2	$z_{abs} = 0.902870$	255
A.182.3	$z_{abs} = 1.172607$	255
A.183	J142656+602551	256
A.183.1	$z_{abs} = 1.586326$	256
A.184	J142756-420619	256
A.185	J142906+011705	256
A.186	J143229-010614B.....	256
A.187	J143229-010616A.....	256
A.187.1	$z_{abs} = 0.400768$	256
A.187.2	$z_{abs} = 1.512464$	257
A.187.3	$z_{abs} = 1.662854$	257
A.188	J143649-161341	257
A.189	J143912+295447	257
A.189.1	$z_{abs} = 1.225850$	257
A.190	J144453+291905	258
A.191	J144331+272436	258
A.192	J144653+011356	258
A.192.1	$z_{abs} = 0.444005$	258
A.192.2	$z_{abs} = 0.509678$	258
A.192.3	$z_{abs} = 0.660216$	258

A.192.4	$z_{abs} = 1.102006$	259
A.192.5	$z_{abs} = 1.129140$	259
A.192.6	$z_{abs} = 1.159458$	259
A.193	J145102-232930	259
A.193.1	$z_{abs} = 1.473211$	259
A.193.2	$z_{abs} = 1.585465$	260
A.194	J145418+121053	260
A.195	J151352+085555	260
A.195.1	$z_{abs} = 1.179037$	260
A.196	J154420+591227	260
A.197	J155152+191104	260
A.198	J155103+090850	261
A.199	J160455+381214	261
A.200	J162439+234512	261
A.200.1	$z_{abs} = 0.317597$	261
A.200.2	$z_{abs} = 0.368111$	261
A.200.3	$z_{abs} = 0.471930$	262
A.200.4	$z_{abs} = 0.656105$	262
A.200.5	$z_{abs} = 0.702901$	262
A.200.6	$z_{abs} = 0.797078$	263
A.200.7	$z_{abs} = 0.891275$	263
A.201	J162645+642654	263

A.201.1	$z_{abs} = 0.585946$	263
A.202	J163145+115602	264
A.202.1	$z_{abs} = 0.900256$	264
A.203	J163429+703133	264
A.203.1	$z_{abs} = 0.653417$	264
A.203.2	$z_{abs} = 0.818166$	264
A.203.3	$z_{abs} = 0.905563$	264
A.203.4	$z_{abs} = 0.990248$	265
A.203.5	$z_{abs} = 1.041435$	265
A.204	J164656+551446	265
A.205	J170100+641209	265
A.205.1	$z_{abs} = 0.722179$	265
A.205.2	$z_{abs} = 0.864598$	265
A.205.3	$z_{abs} = 1.157277$	266
A.206	J173302-130449	266
A.207	J174358-035004	266
A.208	J175746+753916	266
A.208.1	$z_{abs} = 1.348499$	266
A.209	J182402+104424	267
A.209.1	$z_{abs} = 0.570319$	267
A.209.2	$z_{abs} = 1.250752$	267
A.210	J185230+401907	267

A.211	J194025-690756	267
A.212	J194454+770552	268
A.212.1	$z_{abs} = 1.119022$	268
A.213	J200324-325144	268
A.213.1	$z_{abs} = 1.176407$	268
A.213.2	$z_{abs} = 1.249861$	268
A.213.3	$z_{abs} = 2.032931$	268
A.213.4	$z_{abs} = 2.292483$	269
A.214	J204719-163905	269
A.214.1	$z_{abs} = 1.328615$	269
A.214.2	$z_{abs} = 1.342527$	269
A.215	J213135-120704	269
A.215.1	$z_{abs} = 0.429811$	269
A.216	J212912-153841	270
A.216.1	$z_{abs} = 2.022555$	270
A.217	J213302-464026	270
A.218	J213314-464030	270
A.218.1	$z_{abs} = 0.858062$	270
A.218.2	$z_{abs} = 0.866594$	270
A.218.3	$z_{abs} = 0.976707$	271
A.218.4	$z_{abs} = 1.239735$	271
A.219	J214225-442018	271

A.219.1	$z_{abs} = 0.882526$	271
A.219.2	$z_{abs} = 0.986668$	271
A.219.3	$z_{abs} = 1.054139$	272
A.219.4	$z_{abs} = 1.153996$	272
A.219.5	$z_{abs} = 1.571067$	272
A.219.6	$z_{abs} = 1.756896$	273
A.219.7	$z_{abs} = 2.112678$	273
A.219.8	$z_{abs} = 2.253089$	273
A.220	J214805+065738	274
A.220.1	$z_{abs} = 0.790866$	274
A.221	J215501-092224	274
A.222	J220734-403655	274
A.222.1	$z_{abs} = 1.335290$	274
A.223	J220852-194359	275
A.223.1	$z_{abs} = 0.751922$	275
A.223.2	$z_{abs} = 0.948362$	275
A.223.3	$z_{abs} = 1.017049$	275
A.223.4	$z_{abs} = 1.297040$	276
A.223.5	$z_{abs} = 1.532744$	276
A.223.6	$z_{abs} = 1.920499$	276
A.224	J221653-445156	276
A.225	J222826-400957	277

A.225.1	$z_{abs} = 1.278561$	277
A.226	J223409+000002	277
A.226.1	$z_{abs} = 0.855069$	277
A.226.2	$z_{abs} = 1.086635$	277
A.226.3	$z_{abs} = 1.212785$	277
A.227	J223235+024755	278
A.227.1	$z_{abs} = 1.059191$	278
A.227.2	$z_{abs} = 1.358435$	278
A.227.3	$z_{abs} = 1.779723$	278
A.227.4	$z_{abs} = 1.858585$	278
A.227.5	$z_{abs} = 1.863297$	279
A.228	J223619+132620	280
A.229	J223953-055219	280
A.230	J224708-601545	281
A.230.1	$z_{abs} = 0.828079$	281
A.230.2	$z_{abs} = 1.389900$	281
A.230.3	$z_{abs} = 1.755705$	281
A.230.4	$z_{abs} = 2.329761$	281
A.231	J230001-341319	282
A.231.1	$z_{abs} = 0.882589$	282
A.231.2	$z_{abs} = 1.283661$	282
A.232	J230445+031146	283

A.233	J231646-404120	283
A.233.1	$z_{abs} = 1.044634$	283
A.234	J232059-295521	283
A.235	J232121-294350	283
A.236	J232820+002238	283
A.236.1	$z_{abs} = 0.401901$	283
A.236.2	$z_{abs} = 0.412753$	284
A.236.3	$z_{abs} = 0.651926$	284
A.237	J234023-005326	284
A.238	2343+125.....	285
A.238.1	$z_{abs} = 0.731219$	285
A.238.2	$z_{abs} = 2.171346$	285
A.239	2344+125.....	285
A.239.1	$z_{abs} = 1.046488$	285
A.239.2	$z_{abs} = 1.116097$	286
A.240	J234451+343349	286
A.241	J234625+124743	286
A.242	J234819+005721A	287
A.242.1	$z_{abs} = 1.130321$	287
A.243	J234825+002040	287
A.244	2348-147.....	287
A.245	J235034-432559	287

A.245.1	$z_{abs} = 1.109631$	287
A.245.2	$z_{abs} = 1.405362$	288
A.245.3	$z_{abs} = 1.796237$	288
A.246	J235057-005209	288
A.246.1	$z_{abs} = 0.773680$	288
A.246.2	$z_{abs} = 0.814061$	288
A.246.3	$z_{abs} = 0.862944$	289
A.246.4	$z_{abs} = 1.444764$	289
REFERENCES		290

LIST OF TABLES

1.1	Summary of Low Resolution MgII Surveys.....	8
1.2	Summary of High Resolution Strong MgII Surveys ($W_r(2796) \geq 0.3 \text{ \AA}$) ..	13
1.3	Summary of High Resolution Weak MgII Surveys ($W_r(2796) < 0.3 \text{ \AA}$) ...	17
2.1	Journal of Observations	25
2.1	Journal of Observations	26
2.1	Journal of Observations	27
2.1	Journal of Observations	28
2.1	Journal of Observations	29
2.1	Journal of Observations	30
2.1	Journal of Observations	31
2.1	Journal of Observations	32
2.1	Journal of Observations	33
2.1	Journal of Observations	34
2.1	Journal of Observations	35
2.2	Exponential Function Maximum Likelihood Fit Results	52
2.3	Analyzed Transitions	54
3.1	Example System Properties	63
3.2	Example Kinematic Subsystem Properties	64
4.1	Example Voigt Profile Fitting Results.....	84

LIST OF FIGURES

2.1	Example Spectrum	24
2.2	Redshift Coverage	38
2.3	Redshift Coverage	39
2.4	Redshift Coverage	40
2.5	Redshift Path Sensitivity	42
2.6	Example MgII $\lambda\lambda 2796, 2803$ Doublet	43
2.7	Absorption System Redshifts	46
2.8	Equivalent Width Limit versus Absorption Redshift	48
2.9	Equivalent Width Limit Cumulative Distribution	49
2.10	Equivalent Width Distribution	51
2.11	Cumulative Equivalent Width Distribution and K-S Tests	52
2.12	J000323–260318, $z_{abs} = 1.434037$ and J000149–015939, $z_{abs} = 0.870821$	56
2.13	J000520+052411, $z_{abs} = 0.298058$ and J000520+052411, $z_{abs} = 0.591364$	57
2.14	J000520+052411, $z_{abs} = 0.851393$ and J000520+052411, $z_{abs} = 0.866529$	58
2.15	J000520+052411, $z_{abs} = 0.956028$ and J000344–232355, $z_{abs} = 0.452397$	59
2.16	J000344–232355, $z_{abs} = 0.949116$ and J000344–232355, $z_{abs} = 1.586132$	60
3.1	Equivalent Width Regions	66
3.2	Equivalent Width Distribution	73
3.3	MgII System Total Velocity Widths and Velocity Spreads	75

3.4	Kinematic Subsystem Properties of Strong MgII Systems	76
3.5	Weak MgII Systems versus High Velocity Kinematic Subsystems.....	79
4.1	Voigt Profile Modeling Process	87
4.2	Number of VP Components	91
4.3	Column Density Distribution	93
4.4	Doppler Parameter Distribution.....	95
4.5	VP Component Velocity Two-Point Correlation Function	98
5.1	Flux Decrement Distribution Evolution	103
5.2	Flux Decrement Distribution Evolution	104
5.3	Flux Decrement Distribution Evolution	105
5.4	Flux Decrement Distribution Evolution	106
5.5	Survey Completeness	114
5.6	Weak MgII Absorbers per Unit Redshift	117
5.7	Weak MgII Absorbers per Unit Redshift and dN/dz to NEE ratio	120
6.1	Composite Strong MgII Absorption Profiles	128
6.2	Fraction of Absorbing Pixels and Number of Subsystems in Strong MgII Profiles.....	130
6.3	Evolution of Absorber Sizes Using Cosmological Structure Growth	135
6.4	Evolution of Absorber Sizes Using CLOUDY	140

LIST OF COMPACT DISC DATA

System Properties	systemproperties.pdf
Kinematic Subsystem Properties	kinematicssubsystemproperties.pdf
System Profiles and Fits	systemprofilesandfits.pdf
Voigt Profile Fitting Results	voigtprofilefittingresults.pdf

1 INTRODUCTION

1.1 Motivation

Our current understanding of galaxy formation and evolution is still far from complete. We would like a more comprehensive picture of the structure and kinematics of galaxy gas and the intergalactic medium (IGM). Quasar absorption line spectra are an extremely useful means of statistically constraining the various scenarios of metal enrichment, inflow and outflow, ionization conditions, gas kinematics, and gas structure.

Quasars are one of the intrinsically brightest classes of objects in the universe. Their spectra contain absorption lines which sample gas cosmologically distributed in the line of sight. The resonant MgII $\lambda\lambda 2796, 2803$ doublet is a particularly important feature in quasar absorption line spectra. It is convenient to identify because its members have relatively strong oscillator strengths compared to other metal lines that exist under comparable ionization conditions, and because they have a relatively narrow separation of $\sim 7 \text{ \AA}$ in the rest frame. In addition, information can be gleaned about a plethora of galactic environments by studying MgII absorption because it samples more than five decades of HI column density, from $15.5 \lesssim \log N(\text{HI}) \lesssim 20.5 \text{ atoms cm}^{-2}$ (e.g. Bergeron & Stasińska (1986); Steidel & Sargent (1992); Churchill et al. (2000)). It therefore probes a wide range of HI environments associated with star formation, i.e. galaxies. In addition, weak MgII absorption, having rest equivalent width $< 0.3 \text{ \AA}$, is thought to sample dwarf galaxies as well as the IGM (Rigby et al., 2002). Analysis of

quasar absorption line spectra allows more tenuous gas to be studied over a large span of cosmic time than would imaging alone.

In their analysis of MgII systems with rest equivalent width $> 1.8 \text{ \AA}$, Bond et al. (2001a,b) favored expanding superbubbles as the process accounting for a substantial fraction of this equivalent width regime. Steidel et al. (1994) concluded that “strong” MgII absorption systems (defined as having rest equivalent widths $\geq 0.3 \text{ \AA}$) typically originated in normal luminous galaxies, while Churchill et al. (1999) suggested that some fraction of “weak” MgII absorption (defined as having rest equivalent width $W_r(2796) < 0.3 \text{ \AA}$) might also arise in dwarf or low surface brightness galaxies. Milutinović et al. (2006) used an ionization model to study weak MgII absorption and concluded that filamentary and sheetlike geometries were likely, and that most of these absorbers were arising within the cosmic web in the vicinities of luminous galaxies. Photoionization modeling of weak MgII systems with associated CIV led Lynch & Charlton (2007) to argue for a scenario of a shell geometry as might be expected for supernova remnants or high velocity clouds moving in a hot corona. MgII absorption systems can be used to study all of these structures in and around galaxies.

1.2 Background

MgII surveys began in the late 1980s using long slit spectra taken with 4-meter telescopes. The goal was to obtain a uniform sensitivity survey; these early studies culminated in the work of Steidel & Sargent (1992), in which 103 lines of sight were

surveyed. By 2005, the situation had radically changed due to the availability of thousands of Sloan Digital Sky Survey spectra of comparable quality (e.g. Nestor et al. (2005)).

In addition, the advent of the much more powerful 8-10 meter class telescopes made large scale high resolution quasar spectroscopy possible; today several hundred such spectra are available from the Keck HIRES and VLT UVES instruments. This spectral quality has enabled researchers to investigate in detail the kinematics of MgII absorption line systems, as well as to identify and study extremely weak equivalent width systems.

A cosmological model is needed when studying MgII systems in order to compare the distribution of the number of absorbers per unit redshift, dN/dz , with the no-evolution expectation (NEE). In the beginning of the study of MgII absorption, a Friedmann cosmology was commonly assumed with $\Lambda = 0$. In that case, the no evolution function for dN/dz is then

$$\left(\frac{dN}{dz}\right)_{NEE} = N_0 \frac{(1+z)}{\sqrt{1+2q_0z}}, \quad (1.1)$$

where N_0 is the number of absorbers per unit redshift in the current epoch and q_0 is the cosmological deceleration parameter, which had a highly uncertain value ranging from ~ 0 to ~ 0.5 at the time of these earlier works. This allows the observed dN/dz distribution to be parameterized by a power law:

$$\frac{dN}{dz} = N_0(1+z)^\gamma, \quad (1.2)$$

where γ is the evolution parameter and is equal to 1 when $q_0 = 0$ and 0.5 when $q_0 = 0.5$. The value of the Hubble constant H_0 was uncertain, and generally taken to be $50 \text{ km s}^{-1} \text{ Mpc}^{-1}$ when $q_0 = 0$ was assumed and $100 \text{ km s}^{-1} \text{ Mpc}^{-1}$ when $q_0 = 0.5$ was assumed.

The era of the Wilkinson Microwave Anisotropy Probe (WMAP) (Bennett et al., 2003) placed powerful new constraints on what has become the standard cosmological model. In this currently favored model, $\Omega_m = 0.3$, $\Omega_\Lambda = 0.7$, and $H_0 = 70.5 \text{ km s}^{-1} \text{ Mpc}^{-1}$. The evolution of dN/dz under this model is parameterized as

$$\frac{dN}{dz} = N_0 \frac{(1+z)^{2+\epsilon}}{\sqrt{\Omega_m(1+z)^3 + \Omega_\Lambda}}, \quad (1.3)$$

where $\epsilon = 0$ represents the case of a nonevolving population of absorbers (the NEE). Changes in the number of absorbers per unit redshift as a function of redshift when $\epsilon = 0$ would be due solely to the cosmological expansion of the universe.

As a caveat, the change in the cosmological model over the span of MgII absorption studies can make it difficult to directly compare model fits among various researchers' results for dN/dz .

1.2.1 Low Resolution MgII Surveys

The earliest studies of MgII absorption (Lanzetta et al., 1987; Sargent et al., 1988; Steidel & Sargent, 1992) were conducted using low resolution spectra of $0.7 - 4.5 \text{ \AA}$. Lanzetta et al. (1987) analyzed the redshift distribution of the 22 MgII systems in their survey relative to the quasar emission redshifts and were the first to show that

the systems were consistent with being a cosmologically distributed (i.e. unrelated to the quasar itself), although they did not account for varying survey sensitivity with absorption redshift. The authors noted that their redshift coverage was not very good at low ejection velocities ($\beta \simeq 0$), which would be the likely portions of the spectra to show an excess of intrinsic quasar absorption that would skew the distribution. They also found that their MgII equivalent width distribution was well fit by either an exponential or power law function. Over the redshift range of their survey, $1.3 \leq z_{abs} \leq 2.0$, they obtained a mean number of absorbers per unit redshift (dN/dz) of 1.25 ± 0.27 for strong systems. Furthermore, they found only marginal evidence for redshift evolution in dN/dz in this equivalent width and redshift range. Their fit for the evolution parameter was $\gamma = 5.4 \pm 4.0$, far above the no-evolution expectation of $0.5 \leq \gamma \leq 1.0$, but with such a large uncertainty as to render the result insignificant.

In their lower redshift ($0.2 \leq z_{abs} \leq 1.5$) survey of 40 MgII systems, Sargent et al. (1988) also concluded that their sample was consistent with cosmologically distributed intervening absorption. They found that MgII absorption redshifts were significantly clustered on scales of $\Delta v \leq 200 \text{ km s}^{-1}$, and attributed this to the relative motions of clouds within galaxies. Their study also found no significant evidence that the number of MgII absorbers evolves with redshift; they found $dN/dz = 1.13 \pm 0.20$ for strong systems.

The largest of the three main early low resolution surveys was that of Steidel & Sargent (1992). It contained 107 systems in with redshifts $0.2 \leq z \leq 2.2$, which

encompassed the range of the Lanzetta et al. (1987) and Sargent et al. (1988) studies. The authors' dN/dz result for strong systems was 0.97 ± 0.10 , in agreement with the previous two works. The study also found that either an exponential or a power law fit adequately characterized the equivalent width distribution, and their fit parameters were in line with previous works. They also claimed that at least 80% of all MgII systems were strong (our results show that at least 42% of systems are weak). It is likely that their conclusion was inaccurate due to lower spectral quality compared to what is available today.

Steidel & Sargent (1992) also found absorption clustering on scales of $600 \leq \Delta v \leq 5,000 \text{ km s}^{-1}$; their resolution did not allow study of the two-point correlation function (TPCF) on velocity scales smaller than $\sim 250 \text{ km s}^{-1}$.

A major result of the study was that the evolution parameter γ , which characterized the slope of dN/dz , changed significantly when equivalent width cutoffs of higher than 0.3 \AA were applied. A power law fit of the form $(1+z)^\gamma$ to their dN/dz distribution resulted in $\gamma = 0.78 \pm 0.42$ for $W_r \geq 0.3 \text{ \AA}$; this was consistent with a nonevolving population of absorbers ($0.5 \leq \gamma \leq 1.0$) for a Friedmann cosmological model in which $0 \leq q_0 \leq 0.5$. However, they found that at a higher rest equivalent width cutoff of $W_r \geq 1.0 \text{ \AA}$, $\gamma = 2.24 \pm 0.76$, which means that dN/dz evolves such that these very high equivalent width absorbers diminish in number toward the present.

With the advent of the Sloan Digital Sky Survey, the number of quasar absorption line spectra and thus the number of MgII doublets available was vastly increased.

Nestor et al. (2005) surveyed 3,814 spectra and located 1,331 strong MgII systems in the redshift range $0.4 \leq z_{abs} \leq 2.3$. Using greatly improved statistics, they found that a power law fit to the equivalent width distribution was inadequate and that an exponential function best described their data. The study also analyzed enough systems to allow the binning of the equivalent widths by redshift to study evolution in their distribution. It was found that the characteristic equivalent width of the distribution, W^* , decreased with decreasing redshift. In line with the result of Steidel & Sargent (1992), the authors also found that dN/dz is inconsistent with a nonevolving population in the strongest absorption systems, though they found statistically significant evolution only in systems having equivalent widths $\simeq 2 \text{ \AA}$. Like the earlier study, they concluded that the strongest MgII systems are evolving away toward the present. It should be noted that Nestor et al. (2005) assumed a WMAP, Einstein-de Sitter Λ cosmology, in contrast to the earlier low resolution works.

The results of these low resolution MgII surveys are summarized in Table 1.1. Column (1) lists the study, (2) the number of quasar lines of sight, (3) the number of MgII systems identified, (4) the redshift range, (5) the spectral resolution, (6) the exponential fit parameters of the equivalent width distribution, (7) the power law fit slope of the equivalent width distribution, (8) the assumed cosmology, (9) the number of absorbers per unit redshift, and (10) the power law fit result for dN/dz .

Table 1.1. Summary of Low Resolution MgII Surveys

Study	N_{QSO}	N_{sys}	Redshift Range	Resolution	$n(W_r)$ Exponential Fit	$n(W_r)$ Power Law Fit	Cosmology	dN/dz	dN/dz Power Law Fit
LTW87 ^a	32	22	$1.3 \leq z_{abs} \leq 2.0$	4.5 Å	$N_{(W_r \geq 0.3)}^* = 1.76 \pm 0.40$ $W_{(W_r \geq 0.3)}^* = 0.88 \pm 0.19$	$\delta_{(W_r \geq 0.3)} = 1.99 \pm 0.81$	$q_0 = 0$ $\Lambda = 0$ $H_0 = 50$	$1.25 \pm 0.27, W_r \geq 0.3$ $0.85 \pm 0.21, W_r \geq 0.6$	$\gamma_{(W_r \geq 0.3)} = 5.4 \pm 4.0$ $\gamma_{(W_r \geq 0.6)} = 3.2 \pm 2.8$
SSB88 ^b	55	40	$0.2 \leq z_{abs} \leq 1.5$	0.7 – 1.5 Å	$N_{(W_r \geq 0.3)}^* = 2.34 \pm 0.46$ $W_{(W_r \geq 0.3)}^* = 0.55 \pm 0.10$ $N_{(W_r \geq 0.6)}^* = 1.23 \pm 0.28^c$ $W_{(W_r \geq 0.6)}^* = 0.84 \pm 0.20^c$...	$q_0 = 0$ $\Lambda = 0$ $H_0 = 50$	$1.13 \pm 0.20, W_r \geq 0.3$ $0.54 \pm 0.08, W_r \geq 0.6^c$	$\gamma_{(W_r \geq 0.3)} = -0.16 \pm 1.2$ $\gamma_{(W_r \geq 0.6)} = 1.45 \pm 0.63^c$
SS92 ^d	103	107	$0.2 \leq z_{abs} \leq 2.2$	2.1 – 6.2 Å	$N_{(W_r \geq 0.3)}^* = 1.55 \pm 0.20$ $W_{(W_r \geq 0.3)}^* = 0.66 \pm 0.11$	$\delta_{(W_r \geq 0.3)} = 1.65 \pm 0.09$	$q_0 = 0.05$ $\Lambda = 0$ $H_0 = 50$	$0.97 \pm 0.10, W_r \geq 0.3$ $0.52 \pm 0.07, W_r \geq 0.6$ $0.27 \pm 0.05, W_r \geq 1.0$	$\gamma_{(W_r \geq 0.3)} = 0.78 \pm 0.42$ $\gamma_{(W_r \geq 0.6)} = 1.02 \pm 0.53$ $\gamma_{(W_r \geq 1.0)} = 2.24 \pm 0.76$
NTR05 ^e	3,814	1,331	$0.4 \leq z_{abs} \leq 2.3$	$\sim 150 \text{ km s}^{-1}$	$N_{(lowz)}^*{}^f = 1.22 \pm 0.12$ $W_{(lowz)}^*{}^f = 0.59 \pm 0.02$ $N_{(medz)}^*{}^g = 1.17 \pm 0.08$ $W_{(medz)}^*{}^g = 0.74 \pm 0.03$ $N_{(hiz)}^*{}^h = 1.27 \pm 0.09$ $W_{(hiz)}^*{}^h = 0.80 \pm 0.03$...	$\Omega_m = 0.3$ $\Omega_\Lambda = 0.7$ $H_0 = 70$	$0.78 \pm 0.03, W_r \geq 0.3$ $0.49 \pm 0.02, W_r \geq 0.6$ $0.28 \pm 0.01, W_r \geq 1.0$...

^aLanzetta et al. (1987). ^bSargent et al. (1988). ^cThe $W_r \geq 0.6$ Å sample included MgII systems from the works of Lanzetta et al. (1987) and Tytler et al. (1987). ^dSteidel & Sargent (1992).

^eNestor et al. (2005). ^f"Low z " corresponds to $0.366 \leq z_{abs} < 0.871$. ^g"Med z " corresponds to $0.871 \leq z_{abs} < 1.311$. ^h"Hi z " corresponds to $1.311 \leq z_{abs} < 2.269$.

1.2.2 High Resolution Strong MgII Surveys

Petitjean & Bergeron (1990) had sufficient spectral resolution ($0.37 - 0.65 \text{ \AA}$) to begin to analyze the velocity clustering of MgII system components, concluding that both individual galaxy halos as well as galaxy pairs were needed to explain their results. They modeled the systems in their $0.4 \leq z_{abs} \leq 1.3$ sample using Voigt profiles (see § 4) and fit the resulting velocity TPCF using a two-component Gaussian with dispersions of $\sigma_1 = 80 \text{ km s}^{-1}$, which they attributed to clustering within galaxy halos, and $\sigma_2 = 390 \text{ km s}^{-1}$, which they attributed to galaxy-galaxy clustering (this latter interpretation is now thought to be incorrect due to subsequent narrower Gaussian fits with higher resolution data). The sample size of this study, however, was small, consisting of 14 MgII systems fit with a total of 33 Voigt profile (VP) components. The authors fit their VP column density distribution with a slope of 1.0 ± 0.1 . They also fit most of the VP components of the sample with Doppler parameters of $10 < b < 15 \text{ km s}^{-1}$. Since b quantifies the absorption line broadening due to thermal and/or turbulent gas motions, it was concluded that a large turbulent broadening component had to exist in most of their Doppler parameters because a purely thermal b translated to unphysically high gas temperatures at which the MgII ion could not survive. Petitjean & Bergeron (1990) also found that the absorption strengths (i.e. equivalent widths) of strong MgII systems correlate strongly with the number of components.

Still higher resolution data of $\sim 6.7 \text{ km s}^{-1}$ (Churchill & Vogt, 2001; Churchill et al., 2003; Mshar et al., 2007) has allowed detailed analysis of MgII system kinematic

structure. The survey of 18 lines of sight by Churchill & Vogt (2001) and Churchill et al. (2003) over the redshift range $0.4 \leq z_{abs} \leq 1.2$ yielded 23 strong MgII systems. The authors analyzed the properties of individual kinematic subsystems. They found that the equivalent width of a system is proportional to the velocity width of the dominant subsystem. They also performed an analysis of high velocity kinematic subsystems, which were defined as having velocities of $\langle v \rangle > 40 \text{ km s}^{-1}$ relative to the system's zero point. They found that these kinematic subsystems, though they are generally of equivalent width $< 0.3 \text{ \AA}$, exhibit a fundamentally different equivalent width distribution than isolated weak MgII systems (those defined as having total $W_r < 0.3 \text{ \AA}$).

The Churchill & Vogt (2001) and Churchill et al. (2003) study also investigated kinematics using VP fitting. A power law was found to fit the column density distribution of VP components with a slope of 1.59 ± 0.05 over the range $12.4 \leq \log N \leq 16.0 \text{ cm}^{-2}$. The increased resolution most likely caused this much steeper slope than the result of Petitjean & Bergeron (1990), since lower resolution would cause blending of weaker, lower column density components. Similarly, the later study also found a smaller mean VP component Doppler parameter of 5.4 ± 4.3 , which is almost certainly a more accurate result due to the finer velocity resolution. Unlike Petitjean & Bergeron (1990), the Churchill & Vogt (2001) and Churchill et al. (2003) study found the MgII Doppler parameters to be consistent with thermal broadening and to correspond to temperatures of 30,000 - 40,000 K. They also obtained significantly narrower Gaussian component fits to their TPCF of $\sigma_1 = 54 \text{ km s}^{-1}$ and $\sigma_2 = 166 \text{ km s}^{-1}$, which is also

thought to be a resolution effect and which is consistent with intrahalo clustering but not galaxy-galaxy clustering.

The study of Mshar et al. (2007), though it was of equal spectral resolution to that of Churchill & Vogt (2001) and Churchill et al. (2003), did not include VP fitting. The survey analyzed 33 systems drawn from 20 quasar lines of sight over the redshift range $0.3 \leq z_{abs} \leq 2.5$. The authors analyzed fractions of absorbing pixels to nonabsorbing pixels in MgII systems and found that this fraction tends to decrease with decreasing redshift. Kinematic subsystems, defined as regions of detected absorption separated by regions of no detected absorption within a single MgII system, also were studied. The authors claimed that high redshift (defined as $1.2 < z < 2.5$) systems contained smaller numbers of kinematic subsystems than their low redshift (defined as $0.3 < z < 1.2$) counterparts because at high redshift weak absorbing components more often connect stronger regions of absorption, whereas at low redshift these stronger regions are more likely to be separated by nonabsorbing pixels. This trend was thought to indicate that high redshift galactic structures tend to have a larger number of accreting or outflowing clouds than those at low redshift. (We refute both of these findings in § 6.1.) Their low redshift subsample, they argued, exhibited the disk-halo characteristics of the Churchill & Vogt (2001) sample, but their high redshift subsample did not because the systems that comprised it did not exhibit the same characteristic velocity asymmetry.

The results of these high resolution strong MgII surveys are summarized in Table 1.2. Column (1) lists the study, (2) the number of quasar lines of sight, (3) the number

of MgII systems identified, (4) the redshift range, (5) the spectral resolution, (6) the power law fit slope of the VP component column density distribution, (7) the Doppler parameter, (8) the results of the Gaussian fits to the velocity TPCF distribution, and (9) the mean number of VP components.

Table 1.2. Summary of High Resolution Strong MgII Surveys ($W_r(2796) \geq 0.3$
Å)

Study	N_{QSO}	N_{sys}	Redshift Range	Resolution	$n(\log N_{VP}(\text{MgII}))$ Power Law Fit	Doppler b_{VP}	TPCF Gaussian Fit	Mean N_c
PB90 ^a	10	14	$0.4 \leq z_{abs} \leq 1.3$	0.37 - 0.65 Å	$\delta = 1.0 \pm 0.1$ for $12.0 \leq \log N \leq 14.3 \text{ cm}^{-2}$	typically 10 - 15 km s ⁻¹	$\sigma_1 = 80 \text{ km s}^{-1}$ $\sigma_2 = 390 \text{ km s}^{-1}$	2.5
CVC03 ^b	18	23	$0.4 \leq z_{abs} \leq 1.2$	6.7 km s ⁻¹	$\delta = 1.59 \pm 0.05$ for $12.4 \leq \log N \leq 16.0 \text{ cm}^{-2}$	$\langle b \rangle = 5.4 \pm 4.3 \text{ km s}^{-1}$	$\sigma_1 = 54 \text{ km s}^{-1}$ $\sigma_2 = 166 \text{ km s}^{-1}$	7.7
MSHAR07 ^c	20	33	$0.3 \leq z_{abs} \leq 2.5$	6.7 km s ⁻¹

^aPetitjean & Bergeron (1990). ^bThe results of this study were presented in Churchill & Vogt (2001) and Churchill et al. (2003). ^cMshar et al. (2007); Voigt profile (VP) fitting was not performed.

1.2.3 High Resolution Weak MgII Surveys

The studies mentioned in § 1.2.1 and § 1.2.2 all focused on rest equivalent widths of $W_r(2796) \geq 0.3 \text{ \AA}$. However, with the high quality of spectra that have become possible with the largest ground-based telescopes, the sensitivity to smaller equivalent widths has been improved. The works of Churchill et al. (1999), Lynch et al. (2006), Milutinović et al. (2006), and Narayanan et al. (2007) have investigated at $\sim 6.7 \text{ km s}^{-1}$ resolution the weak MgII absorption regime, defined as $W_r < 0.3 \text{ \AA}$, down to $W_r \simeq 0.02 \text{ \AA}$.

The first high resolution weak MgII survey was conducted by Churchill et al. (1999) and analyzed 30 systems discovered in 26 quasar sight lines over the redshift range $0.4 \leq z_{abs} \leq 1.4$. The resulting equivalent width distribution was found to follow a power law with slope 1.04 ± 0.07 and to exhibit no turnover down to the smallest observable equivalent widths. dN/dz was also calculated in various redshift bins (all weak MgII dN/dz results are shown in Table 1.3). Using a Friedmann cosmology, the authors reported no evidence for evolution in this quantity with redshift. Although VP fitting was not performed, the average linewidths were found to imply temperatures of $\sim 25,000 \text{ K}$. Finally, by assuming a radius-luminosity relationship between galaxies and MgII gas following the work of Steidel (1995), a fiducial absorber size of $35h^{-1} - 63h^{-1} \text{ kpc}$ was inferred.

Lynch et al. (2006) conducted a survey which extended to higher redshift ($0.4 \leq z_{abs} \leq 2.4$) and included 38 systems. They found that the dN/dz of weak MgII systems

peaked at $z \sim 1$ and that the behavior of the quantity with redshift was inconsistent with a nonevolving population of absorbers. It was furthermore hypothesized that the peak in dN/dz might be related to the evolution in the star formation rate of dwarf galaxies because weak MgII might correlate with these galaxies.

The study by Milutinović et al. (2006) did not calculate the number of absorbers per unit redshift; instead, the authors analyzed six MgII systems over the range $0.6 \leq z_{abs} \leq 0.9$ and used ionization conditions to assess possible geometries and physical models for the absorbing gas. A search for metal-line systems in 35 quasar spectra was conducted; in order to constrain ionization conditions, systems were included in the sample only if spectral coverage of both low ionization (i.e. MgII, SiII, and CII) and high ionization (i.e. CIV and SiIV) transitions existed. Various scenarios of possible weak MgII absorbing structures were evaluated by considering this data with previous photoionization studies such as Rigby et al. (2002). It was concluded that filamentary and sheetlike geometries were most likely to give rise to this absorption due to the relatively small cloud sizes, but large statistical cross section, of systems exhibiting only high ionization transitions.

The most recent weak MgII study (Narayanan et al., 2007) surveyed 81 quasar spectra and found 112 systems within $0.4 \leq z_{abs} \leq 2.4$. Like Lynch et al. (2006), they concluded that the number of absorbers per unit redshift is inconsistent with the no-evolution expectation derived from cosmological expansion, and dN/dz was found to peak at $z = 1.2$. In addition, contrary to the result of Churchill et al. (1999), the

authors conclude that evidence for a turnover exists in the equivalent width distribution at $W_r < 0.1 \text{ \AA}$, although they did not perform their own fit. They speculated that the apparent paucity of weak MgII at $z \sim 2$ might be due to the high redshift analogs of low redshift weak MgII absorption being associated with strong MgII. In this scenario, weak MgII absorption at high redshift would be in the kinematic vicinity of strong MgII and thus would not be recognized as isolated weak absorption.

The results of these high resolution weak MgII surveys are summarized in Table 1.3. Column (1) lists the study, (2) the number of quasar lines of sight, (3) the number of MgII systems identified, (4) the redshift range, (5) the spectral resolution, (6) the cumulative redshift path, (7) the power law fit slope of the equivalent width distribution, and (8), (9), (10) and (11) the dN/dz results within the indicated redshift bins.

Table 1.3. Summary of High Resolution Weak MgII Surveys ($W_r(2796) < 0.3$
Å)

Study	N_{QSO}	N_{sys}	Redshift Range	Resolution	Z^a	$n(W_r)$ Power Law Fit	dN/dz $0.4 \leq z < 0.7$	dN/dz $0.7 \leq z < 1.0$	dN/dz $1.0 \leq z < 1.4$	dN/dz $1.4 \leq z < 2.4$
CRCV99 ^b	26	30	$0.4 \leq z_{abs} \leq 1.4$	6.7 km s^{-1}	17.2	$\delta = 1.04 \pm 0.07$	1.43 ± 0.21	1.84 ± 0.26	2.19 ± 0.80	...
LCK06 ^c	18	38	$0.4 \leq z_{abs} \leq 2.4$	6.7 km s^{-1}	23.0	...	1.44 ± 0.52	3.56 ± 0.74	1.44 ± 0.23	0.99 ± 0.11
MRMLPC06 ^d	35	6	$0.6 \leq z_{abs} \leq 0.9$	$6.5 - 10.0 \text{ km s}^{-1}$
NMCK07 ^e	81	112	$0.4 \leq z_{abs} \leq 2.4$	6.7 km s^{-1}	77.3	...	1.06 ± 0.10	1.51 ± 0.09	1.76 ± 0.08	1.06 ± 0.04

^aThe cumulative redshift path. ^bChurchill et al. (1999). ^cLynch et al. (2006). ^dMilutinović et al. (2006). ^eNarayanan et al. (2007).

1.2.4 Goals of the Project

One of the main results of previous MgII absorption line studies is that the strongest MgII absorbers ($W_r(2796) > 1.0 \text{ \AA}$) exhibit the most pronounced redshift evolution (Steidel & Sargent, 1992; Nestor et al., 2005) in the sense that their numbers per unit redshift are evolving away. The moderate equivalent width systems ($0.3 < W_r(2796) < 1.0 \text{ \AA}$) do not seem to exhibit this evolution, implying that there are two distinct phenomena giving rise to the absorption. The evolution in the strongest systems is one of the most intriguing topics of MgII absorption. To determine the physical cause of the decrease in the number of these systems having equivalent widths greater than $\sim 1.0 \text{ \AA}$, two possible scenarios must be explored. One factor that could cause the absorber strengths to decrease is a decrease in the column densities of system components; this would mean either a decrease in the gas masses of the clouds or a change in the ionization conditions to disfavor MgII. The other possible factor is a decrease in the average kinematic spreads of the systems - i.e., the MgII absorbing gas might still be present in comparable quantities, but has become kinematically less active or complex, and the system components have become more aligned in velocity space.

A large statistical database of high resolution spectra is needed to study the contribution of these two effects to the equivalent width evolution. With high resolution, Voigt profile (VP) modeling can also be used to decompose systems into their components and extract the number of components as well as their column densities, velocities, and Doppler parameters. In addition, the distributions of flux decrements per

pixel can be analyzed, yielding excellent statistics regarding the relative optical depths of absorption systems. The kinematic characteristics of MgII systems can be examined by using the VP component velocities to construct a two-point correlation function as well as by measuring the velocity widths of systems. All of these distributions should be compared for various redshift bins and at various equivalent widths cutoffs in order to create a dynamical picture of MgII selected structures.

Another area of intense interest in the study of MgII absorbers is in the weak systems. Many of the earlier surveys did not have the spectral resolution or quality to study this equivalent width regime. Again, what is needed is a large sample of high resolution, high signal-to-noise spectra, which can probe down to very small (< 0.02 Å) equivalent widths. If evolution is detected in the number of weak absorbers per unit redshift, this may be due to changes in gas structure, ionization conditions, or blending effects whereby the weak systems are obscured by the presence of strong systems at high redshift.

In order to address these and other questions related to MgII absorbing gas structures, we have compiled 252 HIRES and UVES quasar spectra (see § 2). This survey allows us to explore the evolution of the gas giving rise to this absorption and indirectly of the galaxies that are associated with this gas. The quantities to be studied fall into two groups. The first includes those that are extracted directly from the flux values in the spectra: the equivalent widths, the flux decrements in each pixel, the total velocity widths, and the velocity spreads. The second includes those that require VP modeling:

the column densities, the Doppler parameters, the number of VP components in a system, and the velocity two-point correlation function, which measures the separations between all of the VP component velocity pairs. By studying the equivalent width, column density, and other distributions down to the weakest observable systems, I hope to probe the interface of galaxies and the IGM. The goals of this project include:

1. Study the equivalent width and column density distributions of MgII absorbers to see whether there is a turnover at small equivalent widths and/or column densities and what the implications are for gas halos.
2. Study the Doppler b parameter distribution to learn about the temperature and turbulence conditions of MgII absorbing gas.
3. Use velocity information to explore the kinematics of MgII selected galaxies. For instance, we can calculate the two-point velocity correlation function of VP components within systems, the velocity spread and the total velocity width. These quantities yield clues about the nature of the kinematics; they indicate the kinematic extent and structure of the gas, and may offer information on whether the systems are consistent with disk-like rotation, inflow, or outflow, for instance.
4. Analyze the distributions of flux decrements per pixel for different redshift, velocity, equivalent width bins to gain insight about the evolution of the absorbing gas. The flux decrement is useful because it is a measure of the optical depths

of the systems and its evolution with redshift is easily studied. As an example, an observation of decreasing flux decrements within systems of similar equivalent width could be interpreted as clouds breaking up into smaller, optically thinner components in velocity.

5. Study the statistics of MgII absorbers over the redshift range $0.1 < z < 2.6$ in order to characterize changes that are taking place in MgII selected structures over a large span of cosmic time.

2 DATA

2.1 The Spectra

We have analyzed 252 high resolution, high signal-to-noise High Resolution Echelle Spectrometer (HIRES) and Ultraviolet and Visual Echelle Spectrograph (UVES) quasar spectra obtained from the Keck and Very Large Telescope (VLT) observatories, respectively. The wavelength coverage of the spectra is approximately 3,000 - 10,000 Å. An example spectrum is shown in Figure 2.1. The resolving power of both instruments is $R = \lambda/\Delta\lambda = 45,000$, or $\sim 6.6 \text{ km s}^{-1}$, and the spectra have three pixels per resolution element. The resolution is constant in velocity. The signal-to-noise ratios are typically 25 - 80. Such high quality spectra allow for an in-depth investigation into the distributions and kinematics of the galactic halos and intergalactic structures selected by the presence of the MgII $\lambda\lambda 2796, 2803$ doublet. The high resolution allows us to discern fine substructure within the absorption features; in § 4, we utilize this wealth of data to extract information about individual absorbing components or “clouds”.

The HIRES spectra were provided by Charles Steidel (Caltech), Jason Prochaska (UCSC), Christopher Churchill (NMSU), Wallace Sargent (Caltech), and Michael Rauch (Carnegie). The UVES spectra were provided by the UVES Squad, an international collaboration headed by Michael Murphy (Swinburne) that mines UVES archived quasar spectra. The spectra of Churchill and Steidel were explicitly observed for MgII absorption (Churchill & Vogt, 2001; Churchill et al., 2003; Steidel et al., 2002) and were

selected based upon previous studies which used low resolution spectra to detect MgII absorption of equivalent widths $W_r(2796) \geq 0.3 \text{ \AA}$ (Sargent et al., 1988; Steidel & Sargent, 1992). Those of Sargent and Rauch were selected for high resolution analysis of Ly α forest and CIV absorption, and those of Prochaska for damped Lyman alpha (DLA) absorption (Prochaska et al., 2007). The UVES Squad spectra were drawn from the UVES/VLT archive by Michael Murphy. These spectra were obtained by several researchers for various purposes, including Ly α forest, MgII, CIV, OIV, and DLA studies. The heterogeneous selection bias of our sample is addressed in § 2.7.

The spectra used for this study are listed in Table 2.1. For each quasar, column (1) lists the name we have adopted, (2) a common alias, (3) the emission redshift, (4) the lower wavelength limit observed, (5) the upper wavelength limit observed, and (6) the instrument with which the spectrum was obtained.

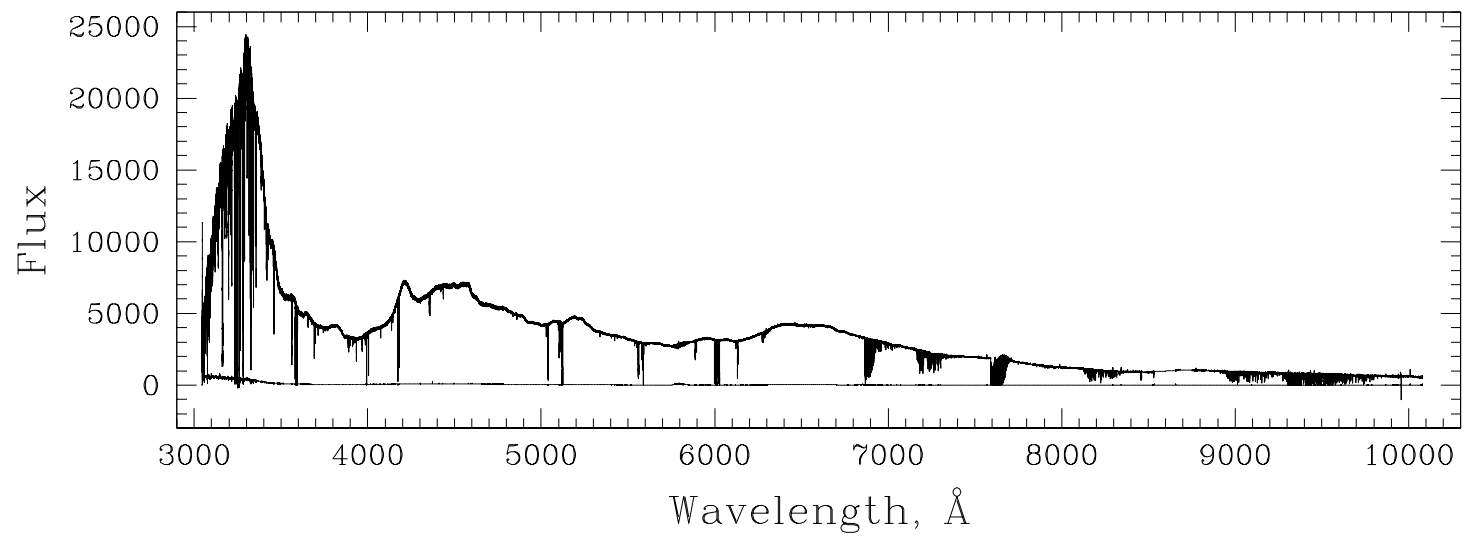


Figure 2.1 The UVES spectrum J051707-441055 and its uncertainty spectrum.

Table 2.1. Journal of Observations

Quasar ^a	Alias	z_{em}	λ_{blue} (Å)	λ_{red} (Å)	Facility
J000323–260318	Q0000–263	4.111	5122	8143	HIRES
J000149–015939	UM196	2.817	3045	10087	HIRES & UVES
J000520+052411	UM18	1.900	3188	6081	HIRES
J000344–232355	HE0001–2340	2.280	3044	10088	UVES
J000448–415728	Q0002–422	2.760	3044	10087	UVES
J001130+005550	SDSSJ00115+0055	2.309	3760	10431	UVES
J001210–012207	UM211	1.999	3284	6106	UVES
J001306+000431	Q0010–002B	2.165	3045	6653	UVES
J001602–001225	UM224	2.086	3041	9396	UVES
J002133+004301	PB5888	1.245	3284	6652	UVES
J002151–012833	PB5893	1.588	3936	9284	UVES
J002208–150539	BR0019–15	4.530	5316	8327	HIRES
J004428–243417	CT43	0.807	3284	6652	UVES
J004508–291432	Q0042–2930	2.388	3283	6809	UVES
J004812–255003	Q0045–2606	1.242	3285	6651	UVES
J004816–254745	PHL2981	0.486	3284	6651	UVES
J004848–260020	Q0046–2616	1.410	3284	6651	UVES
J005024–252234	Q0047–2538	1.969	3285	6652	UVES
J005109–255216	Q0048–261	2.249	3284	6651	UVES
J005127–280433	CS73	2.256	3283	6650	UVES
J005211–251857	Q0049–2535	1.528	3284	6652	UVES
J005419–254900	Q0051–2605	0.624	3284	6652	UVES
J005758–264314	H0055–2659	3.655	3044	9898	HIRES & UVES
J010054+021136	PHL938	1.961	3324	5791	HIRES

Table 2.1—Continued

Quasar ^a	Alias	z_{em}	λ_{blue} (Å)	λ_{red} (Å)	Facility
J005925–411043	Q0057–4126	2.050	3045	6810	UVES
J010311+131617	PHL957	2.681	3290	10087	HIRES & UVES
J010821+062327	UM86	1.960	3478	9913	UVES
J011143–350300	Q0109–3518	2.410	3045	10087	UVES
J012227–042127	Q0119–0437	1.969	3323	6023	HIRES
J012017+213347	Q0117+213	1.500	4317	6774	HIRES
J012156+144824	Q0119+1432	2.865	3642	6792	HIRES
J012642+255901	4c25.05	2.358	3679	6078	HIRES
J012417–374423	Q0122–380	2.189	3042	10087	UVES
J012944–403346	RXSJ01297–4033	0.513	3283	6809	UVES
J013105–213446	Q0128–2150	1.900	3042	6808	UVES
J013405+005109	SDSSJ01340+0051	1.520	3045	6653	UVES
J013442–413611	MS01325–4151	0.172	3285	6812	UVES
J013857–225447	PKS0136–231	1.893	3280	6650	UVES
J014333–391700	HE0141–3932	1.807	3044	10087	UVES
J015234+335032	Q0149+33	2.430	4069	6517	HIRES
J015327–431137	HE0151–4326	2.740	3043	10087	UVES
J015733–004824	SDSSJ01575–0048	1.545	3286	6811	UVES
J015734+744244	Q0153+744	2.338	3414	4952	HIRES
J020346+113445	PKS0201+113	3.639	3753	10086	UVES
J020455+364918	Q0201+36	2.912	4721	7181	HIRES
J020930+051730	Q0207+0503	4.174	5193	8093	HIRES
J021857+081728	Q0216+0803	2.996	4219	7639	HIRES
J023145+132254	Q0229+131	2.067	3188	4785	HIRES

Table 2.1—Continued

Quasar ^a	Alias	z_{em}	λ_{blue} (Å)	λ_{red} (Å)	Facility
J024008–230915	PKS0237–23	2.223	3044	10088	HIRES & UVES
J024401–013402	BRI0241–0146	4.053	4469	7608	HIRES
J024854+180250	Q0246+175	4.422	4572	8572	HIRES
J025134+431516	S40248+43	1.316	4051	6451	HIRES
J025240–553832	CTSH25.01	2.370	3758	9466	UVES
J025518+004847	J0255+00	3.970	5802	8156	HIRES
J025607+011038	Q0253+0058	1.348	3282	6655	UVES
J025634–401300	Q0254–404	2.290	3283	6651	UVES
J030000+004828	SDSSJ03000+0048	0.900	3283	6651	UVES
J030211–314030	CT635	2.370	3284	6650	UVES
J030449–221152	Q0302–2223	1.400	3505	5930	HIRES
J030449–000813	Q0302–003	3.290	4222	6221	HIRES
J031009–192207	UM681	2.122	3045	10431	UVES
J033032–270438	PKS0328–272	1.816	3224	6650	UVES
J033106–382404	Q0329–385	2.423	3045	10087	UVES
J033900–013318	Q0336–01	3.200	4318	6767	HIRES
J034943–381030	Q0347–383	3.205	3291	10086	HIRES & UVES
J035405–272421	UM684	2.819	3283	6811	UVES
J040356–170324	Q0401–1711	4.227	5130	7573	HIRES
J040718–441013	CTSC29.01	3.000	3290	10087	UVES
J042214–384452	Q0420–388	3.110	3291	10087	UVES
J042315–012033	PKS0420–014	0.915	3810	6277	HIRES
J042353–261801	HE0421–2624	2.277	3283	6652	UVES
J042408+020425	PKS0421+019	2.055	3323	4872	HIRES

Table 2.1—Continued

Quasar ^a	Alias	z_{em}	λ_{blue} (Å)	λ_{red} (Å)	Facility
J042707–130253	PKS0424–13	2.159	3284	6811	UVES
J043037–485523	CTSG30.01	1.940	3040	10086	UVES
J043038–133546	Q0428–1342	3.200	4382	6782	HIRES
J044017–433308	PKS0438–43	2.863	3047	10087	UVES
J044026–163234	1E0438–166	1.965	3064	6651	UVES
J044117–431343	PKS0439–433	0.593	3753	10087	UVES
J045142–132033	Q0449–1326	3.100	3679	6629	HIRES
J045218–130503	Q0450–132	2.253	3986	6756	HIRES
J045523–421617	Q0453–423	2.660	3044	10087	UVES
J045608–215909	PKS0454–220	0.534	3765	6189	HIRES
J045647+040053	PKS0454+039	1.350	3765	6189	HIRES
J050112–015914	PKS0458–02	2.286	3043	10087	HIRES & UVES
J051707–441055	HE0515–4414	1.710	3042	10087	UVES
J053008–250330	PKS0528–250	2.779	3505	8654	HIRES
J053007–250329	PKS0528–250	2.813	3040	10086	UVES
J053056+133154	PKS0528+134	2.060	3286	10432	UVES
J055158–211949	MC0549–213	2.245	3248	6651	UVES
J055246–363727	Q0551–366	2.317	3045	9397	UVES
J064204+675836	S40636+680	3.178	3643	6643	HIRES
J064326–504112	ALW11	3.090	3753	9466	UVES
J064632+445117	OH471	3.408	4327	6777	HIRES
J074521+473436	HS0741+4741	3.220	4420	8343	HIRES
J075054+425219	Q0747+4259	1.897	3327	4883	HIRES
J075112+291938	Q0748+2927	0.915	3735	6185	HIRES

Table 2.1—Continued

Quasar ^a	Alias	z_{em}	λ_{blue} (Å)	λ_{red} (Å)	Facility
J080117+521034	Q0757+5218	3.235	4048	6748	HIRES
J081240+320808	FJ0812+32	2.670	4332	8206	HIRES
J081331+254503	HS0810+2554	1.510	3044	6650	UVES
J081336+481303	3c196	0.870	3566	5978	HIRES
J082601−223027	PKS0823−223	0.911	3977	6411	HIRES
J083141+524518	Q0827+5255	3.911	5185	9254	HIRES
J083052+241100	Q0827+243	0.940	3646	5593	HIRES
J083933+111207	Q0836+11	2.700	4074	7181	HIRES
J084424+124546	H0841+1256	2.510	3293	10088	HIRES & UVES
J090033+421546	J0900+42	3.290	5203	7579	HIRES
J091127+055054	RXJ09114+0551	2.799	3293	6650	UVES
J091613+070224	Q0913+0715	2.774	3288	10087	UVES
J092913−021446	HE0926−0201	1.661	3043	10088	UVES
J093337+284532	Q0930+2858	3.421	3811	7161	HIRES
J093748+730158	Q0933+732	2.528	4071	6501	HIRES
J094253−110426	HE0940−1050	3.054	3041	10087	HIRES & UVES
J094835+432302	Q0948+43	1.891	4007	6417	HIRES
J095122+263514	FBQ0951+2635	1.240	3596	5091	HIRES
J095355−050418	BR0951−04	4.370	6031	8388	HIRES
J095500−013006	BRI0952−0115	4.430	3754	10087	HIRES & UVES
J095744+330820 ^b	PSS0957+33	4.250	6438	8759	HIRES
J095852+120245	Q0956+1217	3.306	4332	6781	HIRES
J100120.8+555354	Q0957+5608A	1.413	3506	6768	HIRES
J100120.9+555349	Q0957+5608B	1.415	3506	6768	HIRES

Table 2.1—Continued

Quasar ^a	Alias	z_{em}	λ_{blue} (Å)	λ_{red} (Å)	Facility
J100129+545438	MKN132	1.760	5389	7839	HIRES
J101155+294141	CSO38	2.620	3644	6043	HIRES
J100930−002619	SDSSJ10095−0026	1.242	3285	6651	UVES
J101447+430031	HS1011+4315	3.126	4445	8995	HIRES
J101549+002019	BRI1013+0035	4.405	6109	8556	HIRES
J102156+300141	Q1021+30	3.120	4739	7172	HIRES
J102837−010027	Q1026−0045B	1.532	3283	6552	UVES
J103623−034320	Q1033−0327	4.509	4589	8539	HIRES
J104117+061016	4c06.41	1.265	3975	6407	HIRES
J104733+052454	Q1044+056	1.334	3044	6814	UVES
J104800+052209	Q1045+056	1.231	3044	6810	UVES
J105440−002048	SDSSJ10546−0020	1.019	3283	6652	UVES
J105756+455552	Q1055+4611	4.137	4587	7986	HIRES
J110325−264515	Q1101−264	2.145	3043	10088	UVES
J111038+483116	Q1107+487	3.000	3644	6663	HIRES
J111113−080402	BRI1108−07	3.920	5928	8347	HIRES
J111350−153333	CTSR07.04	3.370	3285	9903	UVES
J111654−221652	PKS1114−220	2.282	3285	6651	UVES
J112442−170517	HE1122−1648	2.400	3043	10088	UVES
J113007−144927	PKS1127−14	1.184	3041	6809	UVES
J113508+222716	Q1132+2243	2.880	3636	6078	HIRES
J114308+345220	Q1140+3509	3.147	4224	6752	HIRES
J114254+265457	US2844	2.630	3751	10086	UVES
J115129+382552	4c38.31	1.304	3986	6424	HIRES

Table 2.1—Continued

Quasar ^a	Alias	z_{em}	λ_{blue} (Å)	λ_{red} (Å)	Facility
J115944+011206	PKS1157+014	2.000	3044	9392	HIRES & UVES
J120523−074232	Q1202−0725	4.695	4901	9001	HIRES
J120550+020131	SDSSJ12058+0201	2.133	3289	6810	UVES
J120858+454036	PG1206+459	1.158	3810	6635	HIRES
J121135+090223	Q1209+0919	3.297	4067	6488	HIRES
J121140+103002	Q1209+1046	2.192	3290	6651	UVES
J121303+171423	Q1210+1731	2.540	3045	10088	HIRES & UVES
J121509+330955	TON1480	0.614	3288	6653	UVES
J121549−003434	UM485	2.691	5008	7357	HIRES
J121732+330539	Q1215+33	2.610	3897	6308	HIRES
J121930+494051	B1217+4957	2.698	3112	4640	HIRES
J122310−181642	CTSJ09.04	2.160	3282	6654	UVES
J122607+173648	Q1223+178	2.918	3870	7180	HIRES
J122527+223513	TON1530	2.048	3810	6267	HIRES
J122824+312838	B1225+3145	2.219	3031	8181	HIRES
J122607+173650	Q1223+1753	2.936	3291	10087	UVES
J123200−022404	PKS1229−02	1.044	3291	6650	UVES
J123437+075843	Q1232+0815	2.567	3291	6651	UVES
J124410+172104	PG1241+176	1.273	3766	6190	HIRES
J124714+312640	Q1244+317	2.960	4018	6467	HIRES
J124524−000938	UM516	2.084	3281	6655	UVES
J124604−073046	PKS1243−072	1.286	3044	6809	UVES
J124913−055918	Q1246−057	2.236	3845	6296	HIRES
J124924−023339	Q1246−0217	2.117	3282	9466	UVES

Table 2.1—Continued

Quasar ^a	Alias	z_{em}	λ_{blue} (Å)	λ_{red} (Å)	Facility
J125048+395140	PG1248+401	1.030	3765	6190	HIRES
J125659+042734	PG1254+047	1.024	3766	6190	HIRES
J131011+460124	HS1307+4617	2.134	3026	5075	HIRES
J131956+272808 ^b	TON153	1.022	3810	6249	HIRES
J132323−002155	Q1320−0006	1.388	3282	6655	UVES
J133141+410158	PG1329+412	1.938	3765	5790	HIRES
J133335+164903	PB3977	2.084	3042	10086	HIRES & UVES
J134002+110630	Q1337+1121	2.919	3499	10200	HIRES & UVES
J134427−103541	HE1341−1020	2.134	3041	10087	UVES
J134916−033715	BRI1346−03	3.990	5896	8345	HIRES
J135038−251216	HE1347−2457	2.534	3041	10087	HIRES & UVES
J135256−441240	PKS1349−439	0.050	3282	10416	UVES
J135646−110128	PKS1354−107	3.000	3752	10087	UVES
J135704+191906	PKS1354+195	0.719	3766	6190	HIRES
J140039+112022	H1400+009	2.571	3517	5917	HIRES
B1422+231A ^c	Q1422+231A	3.620	3576	7323	HIRES
B1422+231B ^c	Q1422+231AB	3.620	3576	7306	HIRES
B1422+231C ^c	Q1422+231C	3.620	3576	7323	HIRES
J142326+325220	MKN679	1.904	3818	6290	HIRES
J142656+602551	Q1425+6039	3.170	3724	7975	HIRES
J142756−420619	PKS1424−41	1.522	3282	10489	UVES
J142906+011705	MARK1383	0.086	3285	6655	UVES
J143229−010614B	B142954−005302B	2.086	3284	10451	UVES
J143229−010616A	B142954−005304A	2.086	3285	10429	UVES

Table 2.1—Continued

Quasar ^a	Alias	z_{em}	λ_{blue} (Å)	λ_{red} (Å)	Facility
J143649–161341	HE1434–1600	0.144	3292	6650	UVES
J143912+295447	Q1437+3007	2.990	3578	6460	HIRES
J144453+291905	Q1442+295	2.670	3625	6151	HIRES
J144331+272436	PSSJ1443+2724	4.420	4779	9182	HIRES & UVES
J144653+011356	Q1444+0126	2.206	3235	6650	UVES
J145102–232930	PKS1448–232	2.215	3041	10086	UVES
J145418+121053	Q1451+1223	3.246	3635	9402	UVES
J151352+085555 ^b	Q1511+091	2.878	3643	6193	HIRES
J154420+591227	Q1543+5921	0.807	3693	6093	HIRES
J155152+191104 ^b	Q1549+1919	2.830	3640	6040	HIRES
J155103+090850	Q1548+092	2.739	4560	5791	HIRES
J160455+381214	Q1603+3820	2.510	3119	4640	HIRES
J162439+234512	3C336.0	0.927	3292	6550	UVES
J162645+642654	Q1626+6433	2.320	3001	6151	HIRES
J163145+115602	PKS1629+120	1.795	3045	6810	UVES
J163429+703133	PG1634+706	1.337	3001	6672	HIRES
J164656+551446	Q1645+5520	4.037	4526	8075	HIRES
J170100+641209	HS1700+642	2.722	3211	6111	HIRES
J173302–130449	NRAO530	0.902	3283	10428	UVES
J174358–035004	PKS1741–03	1.054	3283	10428	UVES
J175746+753916	Q1759+75	3.050	3504	7599	HIRES
J182402+104424	PKS1821+107	1.364	4032	6382	HIRES
J185230+401907	UT1850+402	2.120	3807	7756	HIRES
J194025–690756	PKS1935–692	3.154	4781	6811	UVES

Table 2.1—Continued

Quasar ^a	Alias	z_{em}	λ_{blue} (Å)	λ_{red} (Å)	Facility
J194454+770552	HS1946+769	3.020	3852	6451	HIRES
J200324−325144	PKS2000−330	3.773	3289	10088	UVES
J204719−163905	PKS2044−168	1.932	3282	9907	UVES
J213135−120704	PHL1598	0.501	3632	6031	HIRES
J212912−153841	PKS2126−15	3.268	3289	10088	UVES
J213302−464026	B212945−465345	2.230	3283	6653	UVES
J213314−464030	B212957−465349	2.204	3283	6653	UVES
J214225−442018	Q2139−4434	3.230	4132	9394	UVES
J214805+065738	PKS2145+06	0.999	3283	10430	HIRES & UVES
J215501−092224	PHL1811	0.190	3293	6653	UVES
J220734−403655	Q2204−408	3.155	3287	6807	UVES
J220852−194359	Q2206−1958	2.558	3043	10088	HIRES & UVES
J221653−445156	RXSJ22169−4451	0.136	3284	6650	UVES
J222006−280323	HE2217−2818	2.406	3044	10086	UVES
J222826−400957	Q2225−404	2.020	3284	6650	UVES
J223409+000002	Q2231−002	3.015	3975	6432	HIRES
J223235+024755	Q2230+0232	2.150	3044	10086	HIRES & UVES
J223619+132620	Q2233+131	3.298	4898	7303	HIRES
J223953−055219	Q2237−0608	4.558	4934	8784	HIRES
J224708−601545	B224357−603135	3.010	3047	10087	UVES
J230001−341319	CTSA12.03	2.200	3283	6652	UVES
J230445+031146	PG2302+029	1.052	3332	6002	HIRES
J231646−404120	PKS2314−409	2.448	3293	6648	UVES
J232059−295521	2QZJ232059−2955	2.317	3047	10428	UVES

Table 2.1—Continued

Quasar ^a	Alias	z_{em}	λ_{blue} (Å)	λ_{red} (Å)	Facility
J232121–294350	2QZJ232121–2943	2.184	3046	10429	UVES
J232820+002238	SDSSJ23283+0022	1.300	3283	6655	UVES
J234023–005326	J2340–00	2.090	3912	6304	HIRES
2343+125(HB89)	Q2343+125	2.515	3606	8906	HIRES
2344+125(HB89)	Q2344+125	2.763	3610	6010	HIRES
J234451+343349	Q2342+34	2.917	4000	10197	HIRES
J234625+124743	B234352+123103	2.578	3282	6651	UVES
J234819+005721A	Q2345+007A	2.160	3285	6651	UVES
J234825+002040	BGCFH46	2.650	3282	6650	UVES
J235034–432559	CTSC15.05	2.885	3045	10086	UVES
J235057–005209	UM184	3.024	3287	7493	HIRES & UVES
2348–147 ^d	Q2348–14	2.940	3845	6296	HIRES

^aQuasar names are as listed in Veron-Cetty & Veron (2001). Quasars not listed in that catalog are denoted with an alternate reference. ^bSee Schneider et al. (2007). ^cSee Patnaik et al. (1992). ^dSee Pettini et al. (1995).

2.2 Reduction

2.2.1 HIRES Spectra

The spectra of Churchill were reduced using the standard Image Reduction and Analysis Facility (IRAF¹) software, the process of which is detailed in Churchill (1997). Those of Sargent, Rauch, Prochaska, and Steidel were reduced using the Mauna Kea Echelle Extraction (MAKEE) data reduction package of Barlow (2005), which is optimized for the spectral extraction of single, unresolved point sources. All the spectra have been corrected to heliocentric vacuum velocities.

2.2.2 UVES Spectra

The UVES Squad spectra were reduced using the UVES pipeline (Dekker et al., 2000), which is provided by the European Southern Observatory (ESO). Some, but not all, of the exposures were then combined into one dimensional spectra using the UVES P_Ost-Pipeline Echelle Reduction (UVES POPLER) software (Murphy, 2008), which is an extra reduction step that facilitates cosmic ray removal.

2.2.3 HIRES and UVES Duplicate Coverage

In cases where multiple spectra of a quasar line of sight were available, the spectra were optimally combined in order to increase the wavelength coverage and signal-to-

¹IRAF is distributed by the National Optical Astronomy Observatories, which are operated by the Association of Universities for Research in Astronomy, Inc., under cooperative agreement with the National Science Foundation.

noise ratio.

2.3 Characteristics of the Spectra

2.3.1 Redshift Coverage

The MgII $\lambda 2796$ redshift coverage of the survey is $0.1 < z < 2.6$ (illustrated in Figures 2.2 - 2.4); our quasar spectra thus sample approximately 10 Gyr of the history of MgII-selected objects. The redshift corresponding to a given absorption feature is:

$$z_{abs} = \frac{\lambda_{obs}}{\lambda_r} - 1 \quad (2.1)$$

where λ_{obs} and λ_r are the observed and rest wavelengths of the feature. The thin lines in the figures indicate total coverage toward each quasar line of sight, while the thick lines indicate those regions of the spectra for which the 6σ rest limiting equivalent width limit $W_{r,lim}$ is no greater than 0.02 \AA . This quantity, discussed further in § 2.6.2, traces the sensitivity of spectra in each pixel, and in turn allows us to determine what range of equivalent widths are detectable in a given portion of a spectrum. Small gaps in the spectra are possible above $\sim 5000 \text{ \AA}$ due to incomplete coverage of the echelle orders by the CCDs.

2.3.2 Redshift Path Sensitivity

Another useful characterization of the survey is the redshift path sensitivity function $g(W_r, z)$ (Lanzetta et al., 1987). This function represents the number of absorbers of a given rest equivalent width at a given redshift that could have been detected in

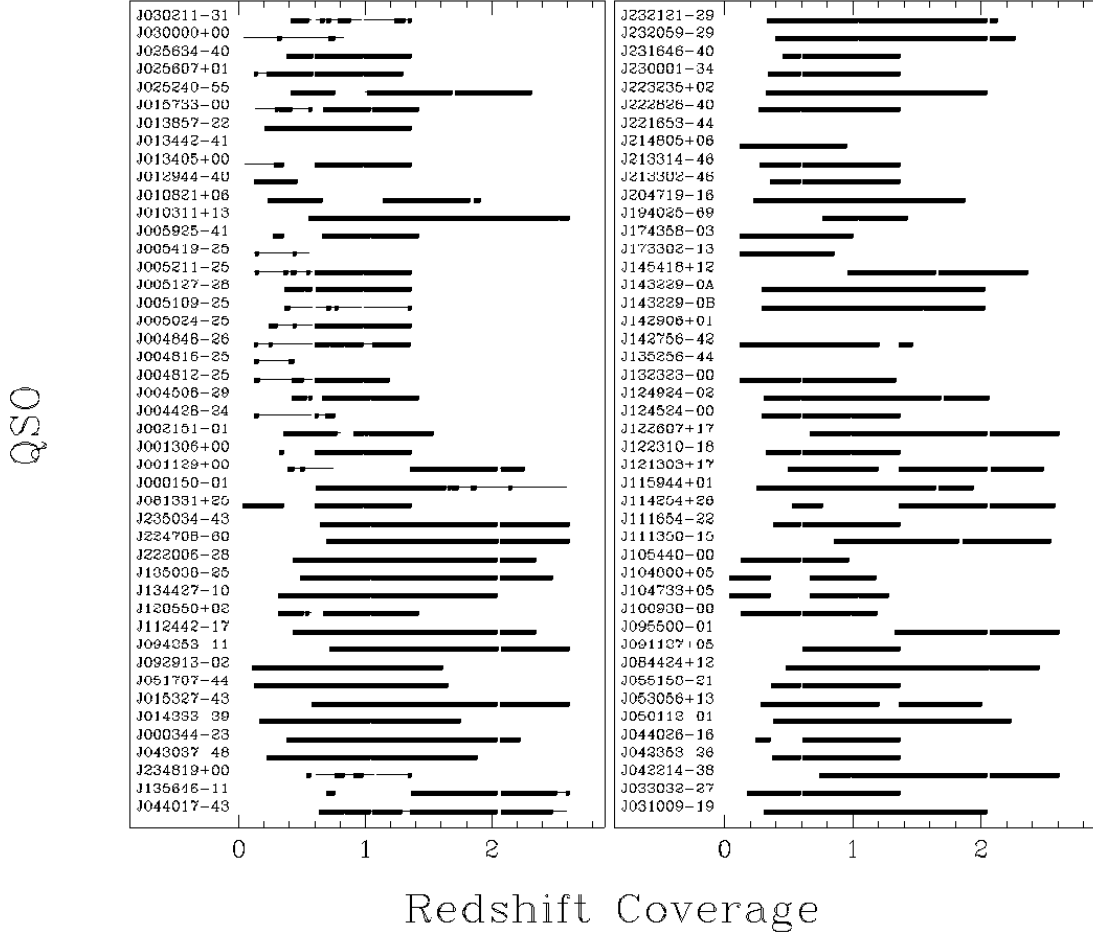


Figure 2.2 The redshift coverage of each quasar spectrum in the sample. The thin lines indicate all coverage, while the thick lines indicate those regions of the spectra for which the $6 \sigma W_{r,lim} \leq 0.02 \text{ \AA}$, a measure of spectral sensitivity.

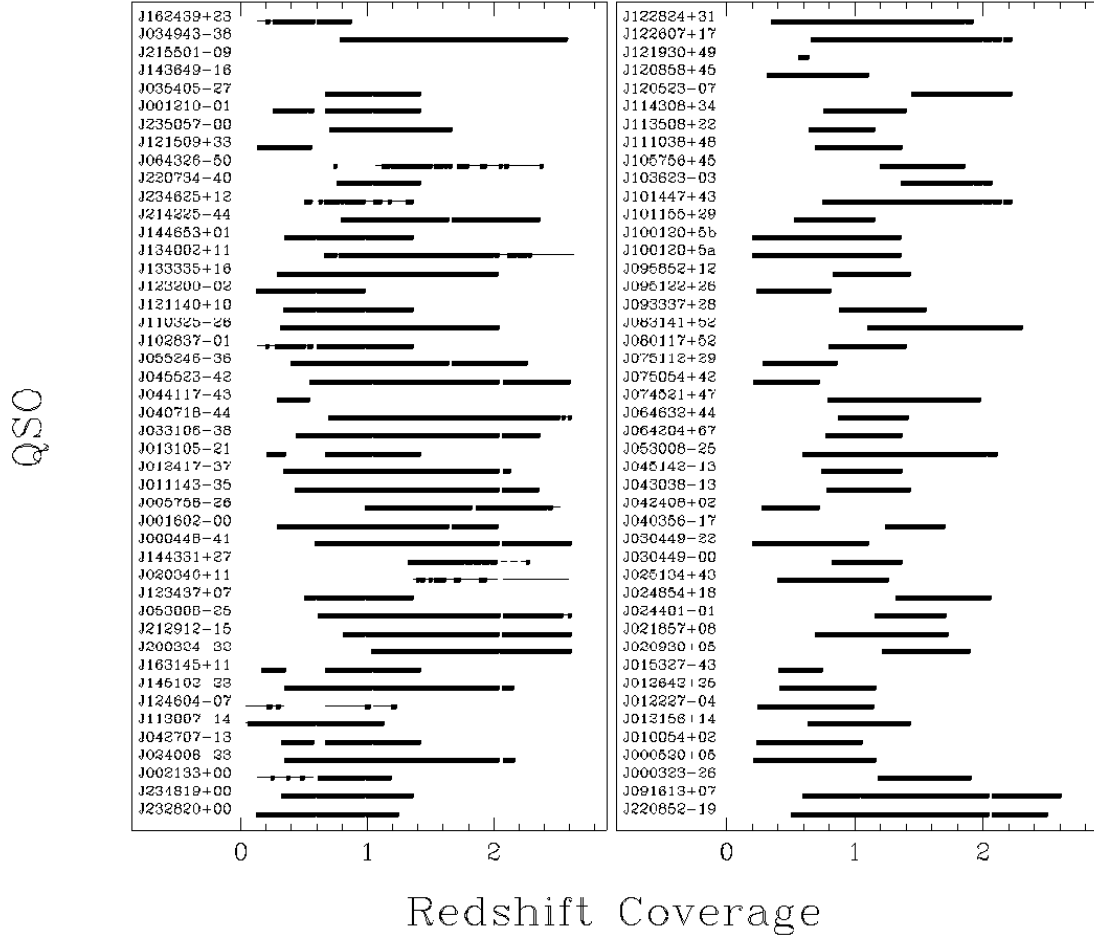


Figure 2.3 The redshift coverage continued.

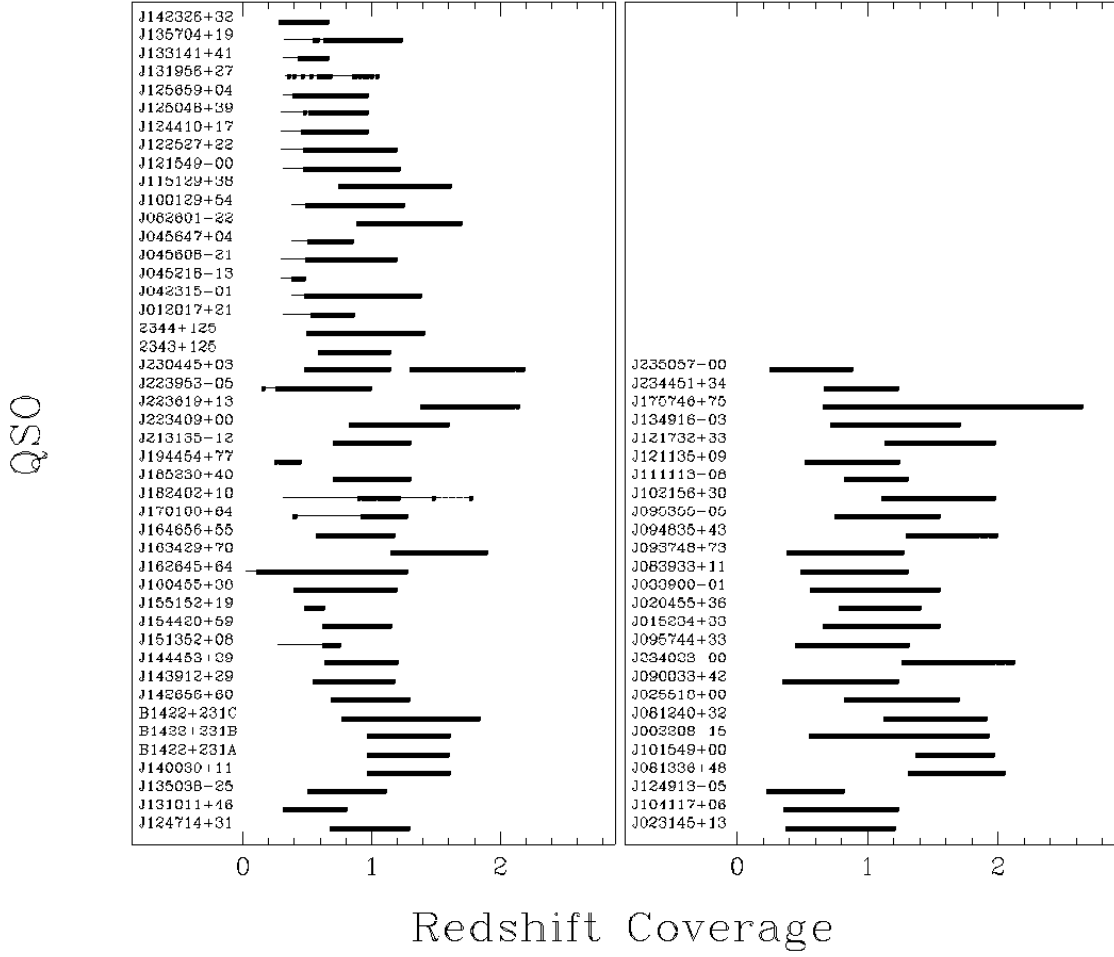


Figure 2.4 The redshift coverage continued.

the sample. The maximum possible value of $g(W_r, z)$ is equal to the total number of lines of sight. The redshift path sensitivity of our survey is shown in Figure 2.5 and the method of calculating it is discussed in § 5.2.1. Note that the $g(W_r, z)$ function rises quickly with increasing equivalent width and thereafter is limited chiefly by the number of lines of sight that cover a given redshift, with the sensitivity peaking at $z \sim 1$.

2.4 Identifying MgII Doublets

The quasar spectrum for each line of sight must be searched to locate every MgII $\lambda\lambda 2796, 2803$ doublet. Spectra are searched only in the region spanning the Ly α emission redshift up to 5,000 km s⁻¹ blueward of the MgII emission redshift. This conservative upper limit was placed on the wavelength range being searched in order to ensure that no detected MgII absorption features are intrinsic to the quasar and its immediate vicinity (Weymann et al., 1991). Using the program SEARCH (Churchill et al., 1999), the spectra are objectively searched for MgII doublet candidates. The initial criteria are the detection of a 5 σ feature, which is taken to be the $\lambda 2796$ line, along with a corresponding 3 σ detection at what would be the location of the $\lambda 2803$ feature in the spectrum. Detections and significance levels follow the formalism of Schneider et al. (1993). The candidates are then checked for doublet ratios consistent with $1.0 \leq DR \leq 2.0$, where

$$DR = \frac{W_r(2796)}{W_r(2803)}. \quad (2.2)$$

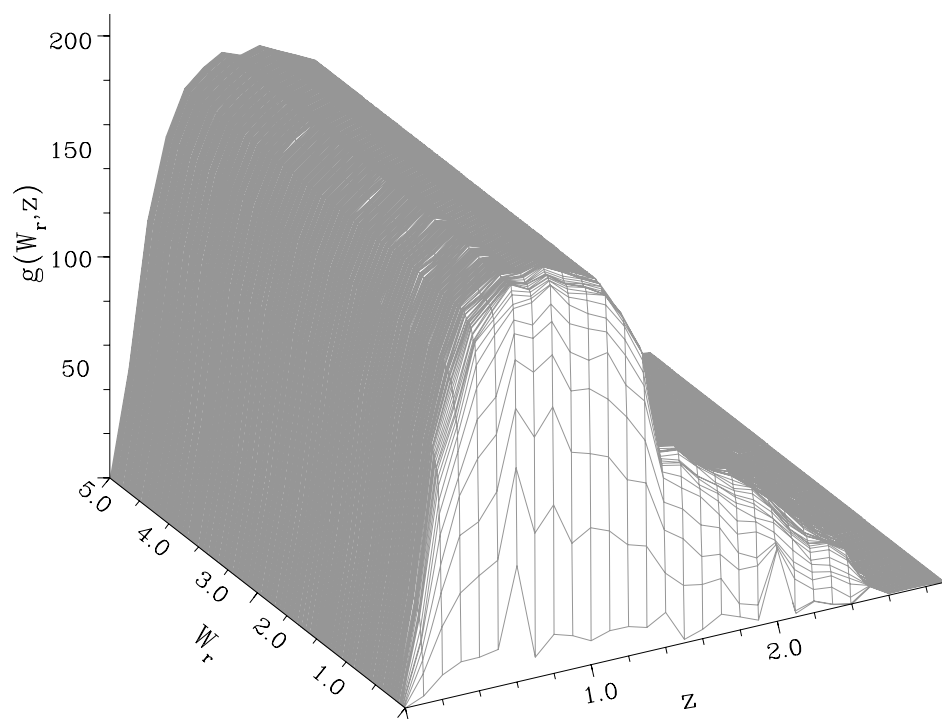


Figure 2.5 The redshift path sensitivity of the spectra as a function of rest equivalent width and redshift.

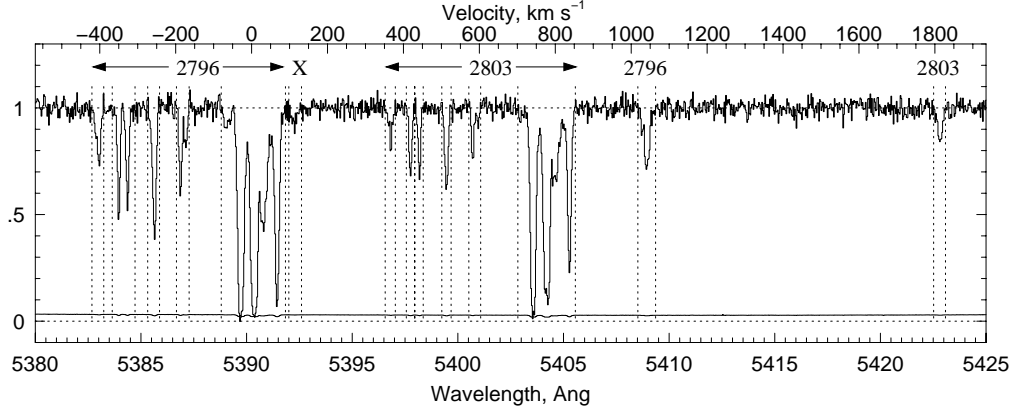


Figure 2.6 An example of a MgII $\lambda\lambda 2796, 2803$ doublet with several kinematic subsystems. The $\lambda 2796$ feature at $\sim 1000 \text{ km s}^{-1}$ and its corresponding $\lambda 2803$ feature at $\sim 1800 \text{ km s}^{-1}$ are considered a separate system since they lie $\geq 800 \text{ km s}^{-1}$ away from the other features. The feature marked with an "X" is not part of the MgII system. Figure provided by Churchill (2012) with permission.

The doublet ratio for weak MgII $\lambda\lambda 2796, 2803$ absorption is 2.0 and arises from the ratio of the transitions' oscillator strengths. As equivalent width increases, line saturation tends to increase and the doublet ratio approaches 1.0. Finally, line profiles are visually inspected to ensure that they are consistent with each other and to eliminate any spurious features. Two or more MgII features are considered to be two kinematic subsystems within a single system if they lie within 800 km s^{-1} of each other. The candidates are also checked automatically for corresponding absorption in numerous other atomic transitions, including MgI $\lambda 2853$; FeII $\lambda 2344$, $\lambda 2374$, $\lambda 2383$, $\lambda 2587$, and $\lambda 2600$; CaII $\lambda 3935$ and $\lambda 3970$; and MnII $\lambda 2577$, $\lambda 2594$, and $\lambda 2606$. An example MgII $\lambda\lambda 2796, 2803$ doublet is illustrated in Figure 2.6.

Using this algorithm, 469 MgII $\lambda\lambda 2796, 2803$ systems were identified. However, after

eliminating systems which were MgII doublets but which failed to meet a minimum standard of data quality (see § 2.6.2), 422 systems remained to comprise our sample.

2.5 Problems at High Redshift

Within the higher wavelength regimes of our sample (above ~ 5900 Å), corresponding to higher MgII $\lambda 2796$ absorption redshifts, feature detection becomes more difficult due to the presence of telluric absorption lines caused by the Earth’s atmosphere. The strongest lines occur in the A- and B-bands (7600 - 7630 and 6860 - 6890 Å, respectively) and also between 7170 and 7350 Å (Barlow, 2005). These lines are generally distinguishable from the MgII $\lambda\lambda 2796, 2803$ doublet. A chance alignment of two telluric lines at the precise separation needed, along with the required doublet ratio needed to be mistaken for the MgII $\lambda\lambda 2796, 2803$ doublet, is unlikely; furthermore, the A- and B-band features in particular occur in a distinctive pattern of closely spaced pairs (too close to be confused with the MgII $\lambda\lambda 2796, 2803$ doublet) that are readily recognizable. Nevertheless, these spurious features may obscure underlying weak MgII absorption or cause significant line blending. However, the search algorithm is such that the redshifted MgII $\lambda 2803$ wavelength corresponding to a candidate MgII $\lambda 2796$ feature is visually inspected to determine whether absorption is present. The locations of the MgI, FeII, CaII, and MnII features mentioned in § 2.4 are also visually inspected for possible corroboration of the presence of the MgII $\lambda\lambda 2796, 2803$ doublet. These procedures ensure that the maximum possible number of absorbing systems are recovered

from the spectra.

2.6 Global Absorption Line System Characteristics

2.6.1 System Redshifts

In Figure 2.7 we present the binned redshift distributions of our detected MgII $\lambda\lambda 2796, 2803$ absorbing systems for $W_r(2796) < 0.3 \text{ \AA}$ (“weak” systems), $W_r(2796) \geq 0.3 \text{ \AA}$ (“strong” systems), and the full equivalent width sample spanning $0.006 \leq W_r(2796) \leq 6.23 \text{ \AA}$. (The equivalent width distribution is discussed in § 2.7 and measurement of the equivalent widths in § 3.) The absorbing redshifts span the range $0.19 \leq z_{abs} \leq 2.55$, with a mean of 1.18. The more sharply declining tail at the high end of the weak population versus the strong is due in general to a decline in the sensitivity of the spectra in the higher redshift regime, as can be seen in the illustration of the redshift path sensitivity in Figure 2.5. This phenomenon inhibits detection of MgII $\lambda\lambda 2796, 2803$ absorbing systems, with the smallest W_r systems suffering the most loss of completeness.

2.6.2 Required System Equivalent Width Limit

An equivalent width limit of the MgII $\lambda 2796$ feature consistent with $W_{r,lim} \leq 0.02 \text{ \AA}$ was a prerequisite for inclusion in our final sample. This quantity is defined as the minimum rest equivalent width detectable in a given portion of a spectrum, and is a measure of the signal-to-noise ratio. In this case, the mean $6 \sigma W_{r,lim}$ was calculated over $\pm 600 \text{ km s}^{-1}$ about the $\lambda 2796$ feature. The rest frame equivalent width limits

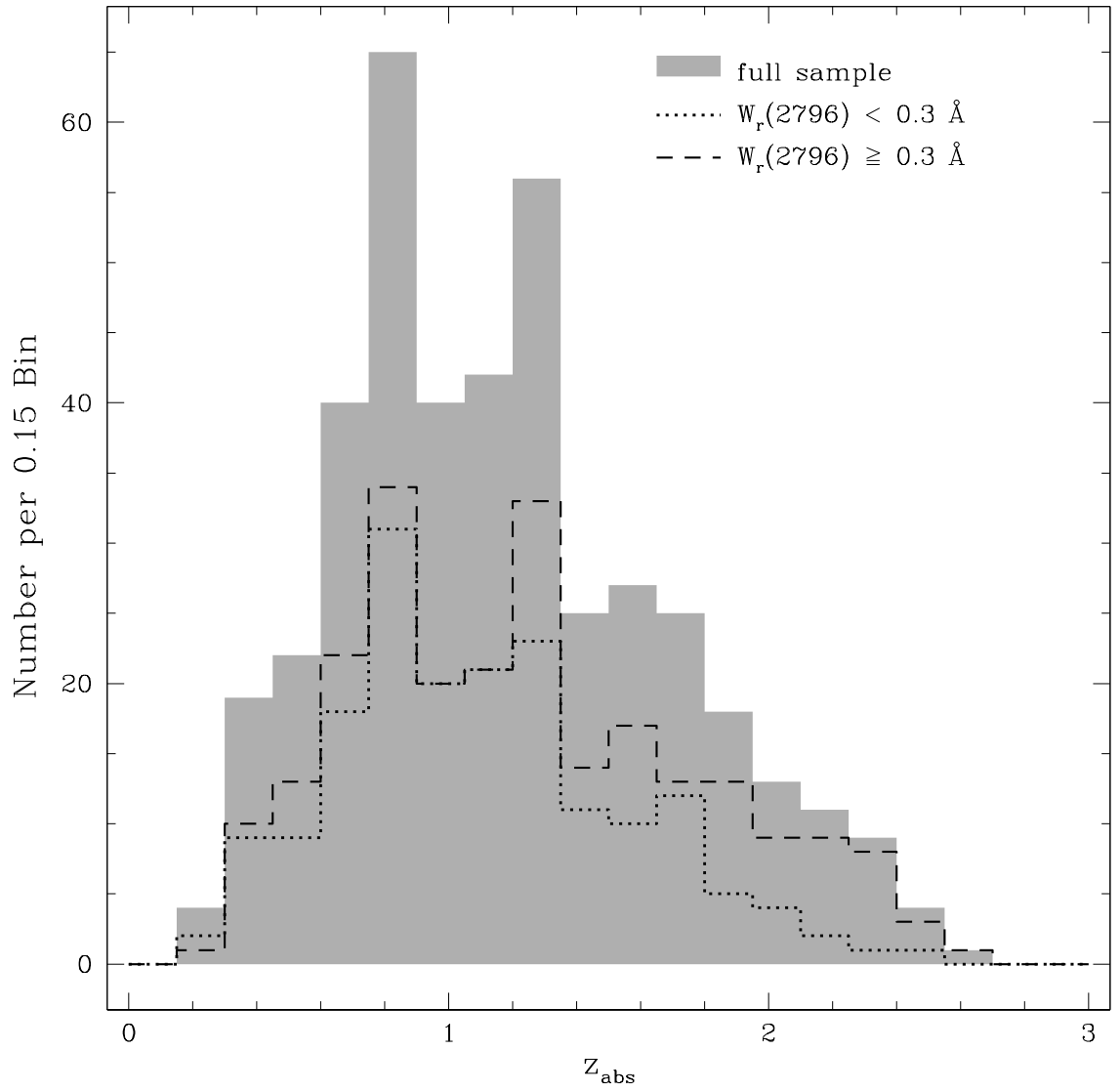


Figure 2.7 The absorption redshifts for $W_r(2796) < 0.3 \text{ \AA}$, $W_r(2796) \geq 0.3 \text{ \AA}$, and the full sample.

are plotted versus the absorption redshifts for all the systems included in our sample in Figure 2.8. Systems were included for which (1) $W_{r,lim} \leq 0.02 \text{ \AA}$; *or* (2) for which $W_{r,lim}$ was greater than 0.02 \AA but for which the standard deviation of that quantity over the $\pm 600 \text{ km s}^{-1}$ window was such that $W_{r,lim}$ minus the standard deviation was less than or equal to 0.02 \AA . This provision allows systems having a high variation in spectral quality across the absorption region to be included in the sample. Using these criteria for system quality, our sample was reduced from 469 to 422 MgII $\lambda\lambda 2796, 2803$ doublets.

Figure 2.9 illustrates the cumulative distribution of 6σ rest equivalent width limits for all systems included in the sample. 94% of the systems average $W_{r,lim}(2796) \leq 0.02 \text{ \AA}$ over the $\pm 600 \text{ km s}^{-1}$ window. The remaining 6% of included systems do have higher equivalent width limits, but were included because they were considered consistent with $W_{r,lim}(2796) \leq 0.02 \text{ \AA}$ based on criteria (2).

2.7 Possible Sample Bias

The early studies that discovered the existence of strong MgII absorbers, i.e. $W_r(2796) \geq 0.3 \text{ \AA}$, did not have the sensitivity to detect weak absorbers, which have $W_r(2796) < 0.3 \text{ \AA}$; therefore, quasar spectra were never selected based upon the presence of weak absorption. Furthermore, no correlation exists between strong and weak absorbers along a given line of sight (Churchill et al., 1999). The sample is therefore unbiased for weak systems; however, some of the spectra were selected because the

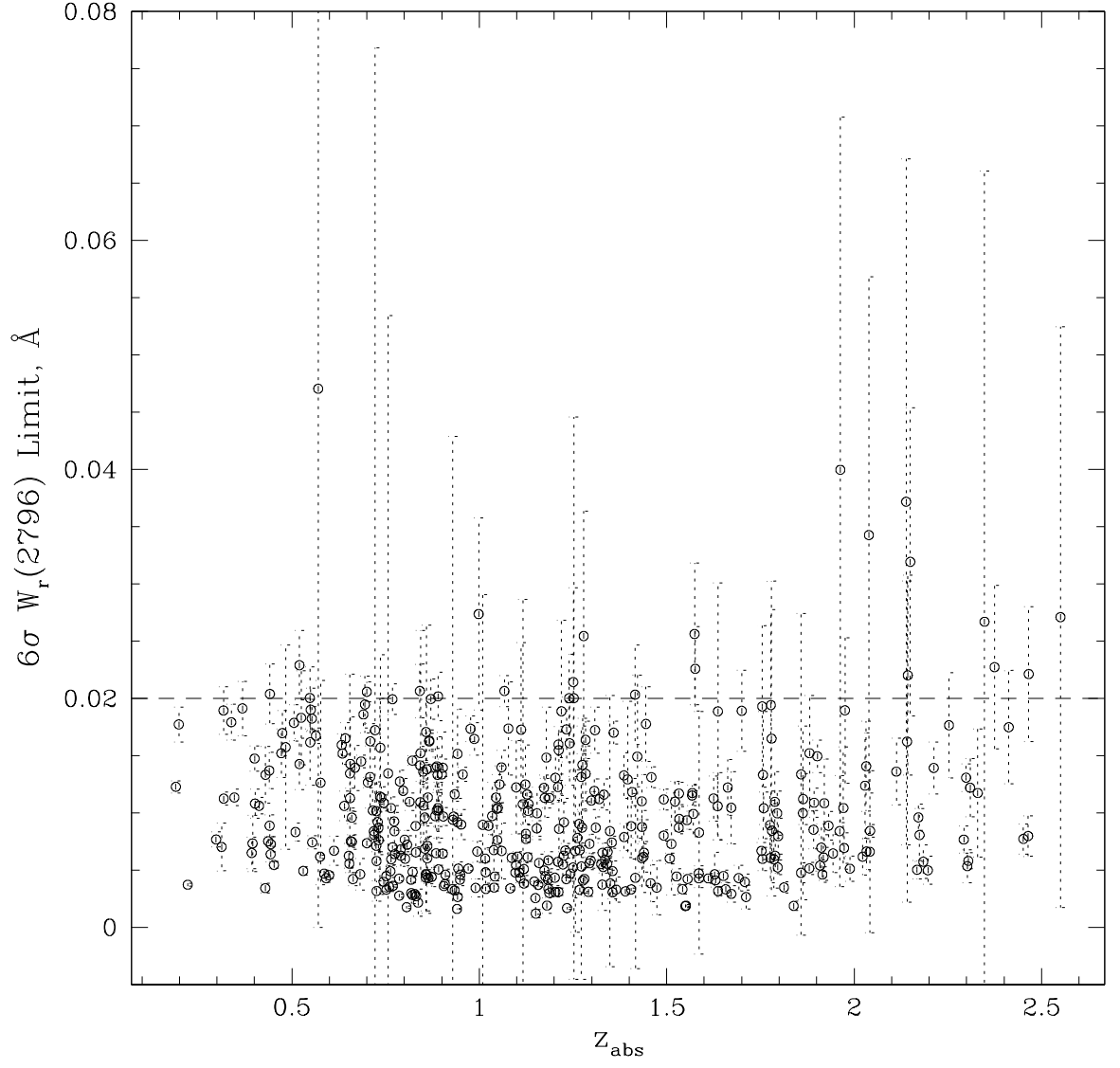


Figure 2.8 The 6σ limiting rest equivalent width, averaged over $\pm 600 \text{ km s}^{-1}$ about the $\text{MgII } \lambda 2796$ feature, as a function of absorption redshift for all the systems included in our sample. The dashed line represents $W_{r,lim}(2796) = 0.02 \text{ \AA}$. The error bars represent the standard deviations.

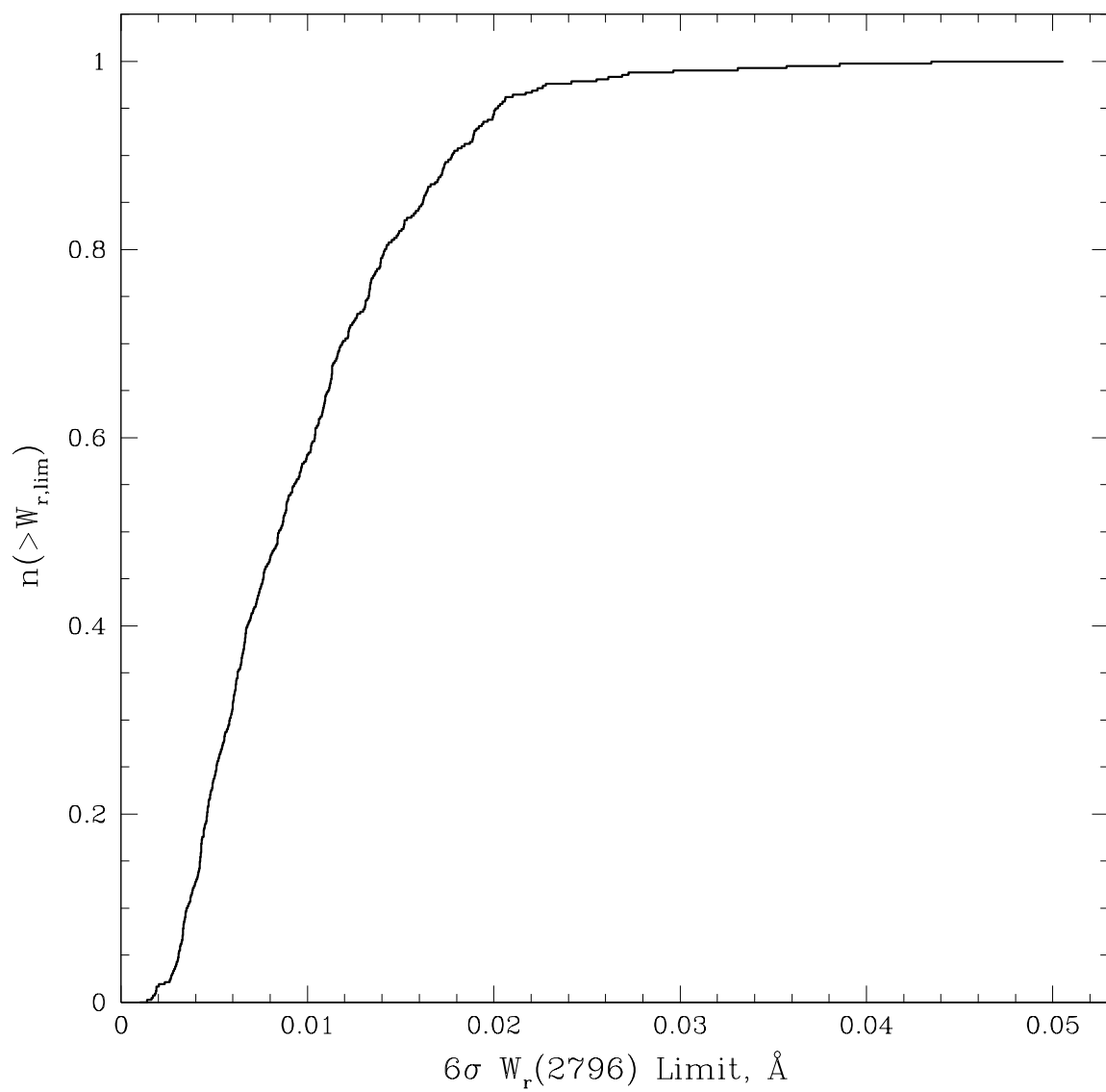


Figure 2.9 The cumulative distribution of 6σ limiting equivalent widths averaged over $\pm 600 \text{ km s}^{-1}$ about the $\text{MgII } \lambda 2796$ feature.

presence of strong MgII absorption had already been ascertained. Given this partial selection bias and the heterogeneous motivations behind the observations of some of these lines of sight, as discussed in § 2.1, it cannot be assumed *a priori* that the strong MgII absorption subset is consistent with an unbiased sample. Some statistically significant reassurance of this would allow us to use our sample to study, for example, the evolutionary aspects of the strong MgII absorption systems (see § 5).

In order to determine whether our strong sample is not inconsistent with an unbiased one, the blind survey of 1331 MgII absorbers of Nestor et al. (2005) was used for comparison. Their study measured MgII $\lambda 2796$ rest equivalent widths in the range $0.3 \leq W_r \leq 5.68$ Å and absorption redshifts $0.336 \leq z_{abs} \leq 2.269$. The maximum likelihood method was used to perform an exponential fit of the form $(N^*/W^*)e^{-W/W^*}$ on the resulting distributions for both the entire sample and for three redshift bins, $0.336 \leq z < 0.871$, $0.871 \leq z < 1.311$, and $1.311 \leq z < 2.269$ (hereafter the low, medium and high redshift samples). The Kolmogorov-Smirnov (K-S) statistical test was employed in order to quantitatively measure the similarity (or lack thereof) between our sample of strong MgII systems and the maximum likelihood exponential fits of Nestor et al. (2005).

Our equivalent width distributions are shown in Figure 2.10. They are plotted for both the entire redshift range and for the low, medium and high redshift samples. We have also performed maximum likelihood best fits on our unbinned equivalent width samples (e.g. Lanzetta et al. (1987)); these models along with those of Nestor et al.

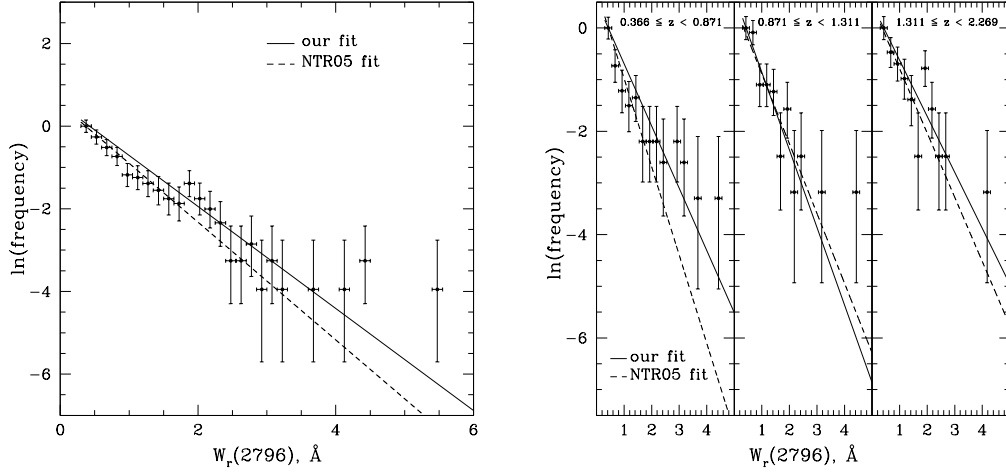


Figure 2.10 At left, the points show the MgII $\lambda 2796$ equivalent width distribution of our sample for $W_r \geq 0.3$ Å. The sloped lines indicate the maximum likelihood exponential fits to our sample and to the sample of Nestor et al. (2005). At right, the same data is divided into the identical redshift bins of the sample of Nestor et al. (2005) and is plotted with the respective fits.

(2005) are shown with the data. The cumulative distributions are shown with the fits and K-S test results in Figure 2.11. The maximum likelihood results are listed in Table 2.2.

Our criterion satisfying the assertion that our sample is not inconsistent with an unbiased sample was that $P(K - S) > 0.0027$, which would mean that it could not be ruled out at the 3σ level that the two populations are consistent with one another. In all four redshift samples this criterion was met; for the full redshift range of Nestor et al. (2005), we obtained $P(K - S) = 0.115$, and for the low, medium and high redshift bins, we obtained $P(K - S) = 0.053$, 0.621 , and 0.322 , respectively. Even the lowest value, corresponding to the low redshift sample, falls well within the criterion, such that the two populations are not inconsistent with each other to even a 2σ level. The

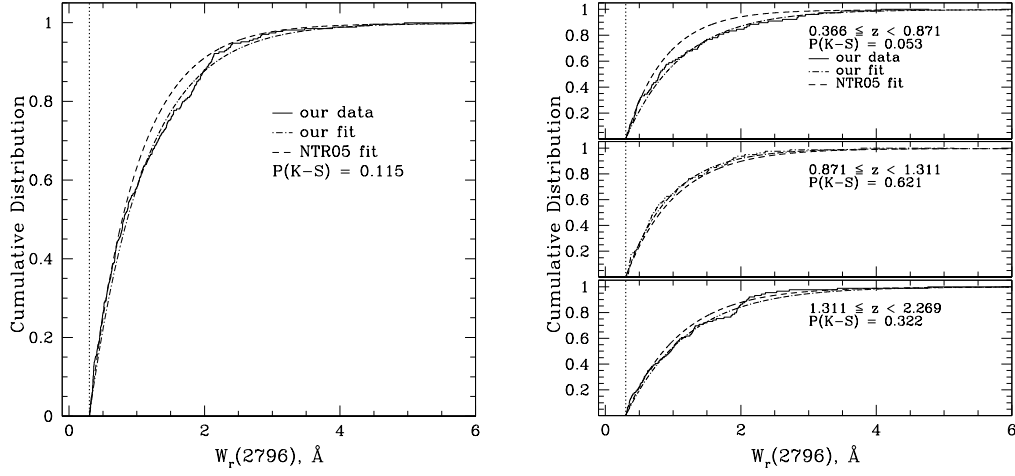


Figure 2.11 At left, the MgII $\lambda 2796$ cumulative equivalent width distribution of our sample for $W_r \geq 0.3 \text{ \AA}$ (the equivalent width cutoff is indicated by the dotted line) and the maximum likelihood exponential fits to our sample and to the sample of Nestor et al. (2005). The K-S test result between the two is also noted. At right, the data is divided into the identical redshift bins of the sample of Nestor et al. (2005) and is plotted with the respective fits.

Table 2.2. Exponential Function Maximum Likelihood Fit Results

Redshift Range	Data	N^*	W^* (\AA)
$0.366 \leq z < 2.269$	this study	1.723 ± 0.178	0.810 ± 0.049
	Nestor et al. (2005)	1.187 ± 0.052	0.702 ± 0.017
$0.366 \leq z < 0.871$	this study	1.680 ± 0.032	0.829 ± 0.093
	Nestor et al. (2005)	1.216 ± 0.124	0.585 ± 0.024
$0.871 \leq z < 1.311$	this study	1.788 ± 0.035	0.667 ± 0.074
	Nestor et al. (2005)	1.171 ± 0.083	0.741 ± 0.032
$1.311 \leq z < 2.269$	this study	1.759 ± 0.307	0.922 ± 0.097
	Nestor et al. (2005)	1.267 ± 0.092	0.804 ± 0.034

exponential function maximum likelihood fit results for our sample and for those of Nestor et al. (2005) are also consistent within 3σ of each other in all redshift bins.

Although our strong MgII absorber sample is not inconsistent with an unbiased sample, Figure 2.10 reveals apparent excesses of absorbers at $W_r \simeq 2\text{ \AA}$ and $\gtrsim 4\text{ \AA}$. These excesses are likely due to some of our quasar lines of sight being chosen for observation because the presence of damped Lyman alpha (DLA) systems was already known.² DLAs are associated with MgII absorbing systems of these equivalent width regimes. The excess at $W_r \gtrsim 4\text{ \AA}$ may also be indicative of galactic winds (see Bond et al. (2001a); Bond et al. (2001b)).

As a result of this analysis, we proceed under the premise that our sample of MgII absorption systems has the characteristics of an unbiased sample, allowing the valid study of their evolution.

2.8 Selected Atomic Transitions and Example MgII Systems

Although SEARCH locates numerous atomic transitions simultaneously when a MgII $\lambda 2796$ candidate is detected, measurements of the absorption features (see § 3) and fitting of their Voigt profile (VP) models (see § 4) were limited to 13 transitions derived from five different elements: MgII $\lambda 2796$ and $\lambda 2803$; MgI $\lambda 2853$; FeII $\lambda 2344$, $\lambda 2374$, $\lambda 2383$, $\lambda 2587$, and $\lambda 2600$; CaII $\lambda 3935$ and $\lambda 3970$; and MnII $\lambda 2577$, $\lambda 2594$, and $\lambda 2606$. The transitions and their relevant atomic data are listed in Table 2.3. Column

²This is primarily due to the HIRES spectra contributed by J. Prochaska, as well as some of the UVES spectra from the VLT archive.

Table 2.3. Analyzed Transitions

Transition	λ_{vac} (Å)	f	$\Gamma \times 10^8$ (sec ⁻¹)
CaII3935	3934.777	0.6346	1.456
CaII3970	3969.591	0.3145	1.414
FeII2344	2344.214	0.1097	2.680
FeII2374	2374.461	0.0282	2.990
FeII2383	2382.765	0.3006	3.100
FeII2587	2586.650	0.0646	2.720
FeII2600	2600.173	0.2239	2.700
MgI2853	2852.964	1.8100	4.950
MgII2796	2796.352	0.6123	2.612
MgII2803	2803.531	0.3054	2.592
MnII2577	2576.877	0.3508	2.741
MnII2594	2594.499	0.2710	2.685
MnII2606	2606.462	0.1927	2.648

(1) lists the transition, (2) the vacuum wavelength, (3) the oscillator strength, which is a measure of the relative absorption strength of different transitions of a given ion, and (4) the natural broadening constant.

Each system’s absorption profiles for all the transitions for which VP components were modeled are shown in “System Profiles and Fits” on the included compact disc; ten example systems are shown in Figures 2.12 - 2.16.

The VP results are discussed in § 4 and are listed in “Voigt Profile Fitting Results”

on the included compact disc; an example of the VP results for a system is listed in Table 4.1. All of the MgII systems in our sample are individually discussed in Appendix A. All systems were fit assuming turbulent Doppler parameters and using a confidence level of 0.97 and a badness of 1.5 (see § 4) unless otherwise noted.

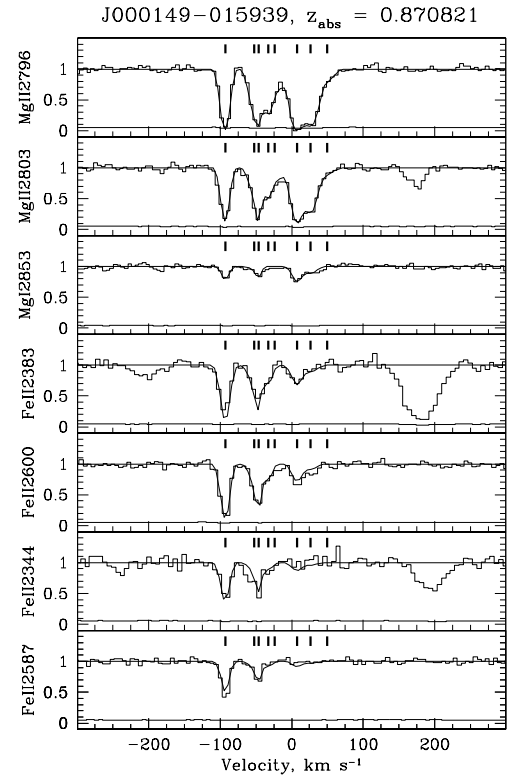
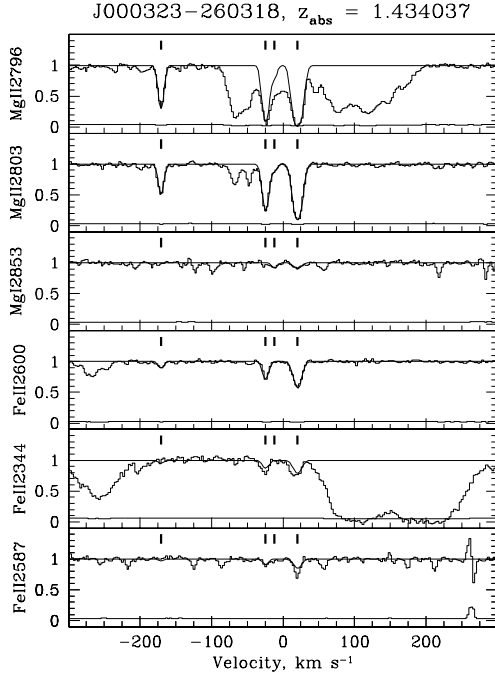


Figure 2.12 System absorption profiles aligned in rest-frame velocity. The Voigt profile models are superimposed; ticks indicate the component centroids.

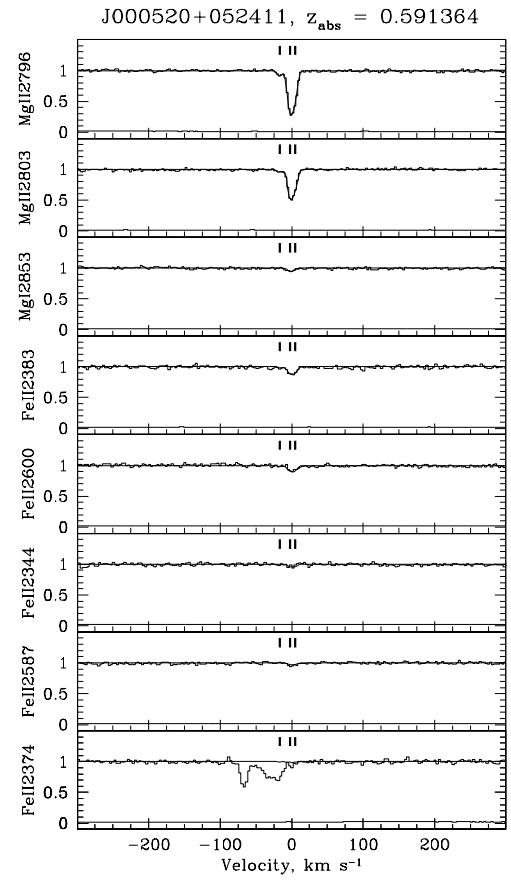
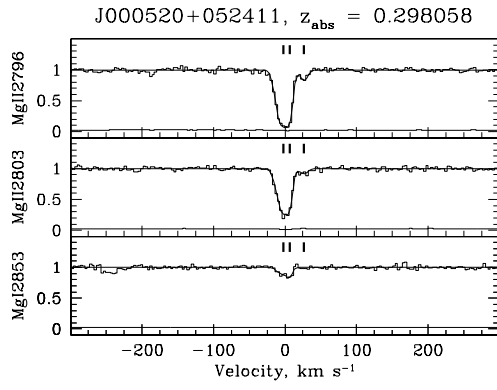


Figure 2.13 Same as Figure 2.12.

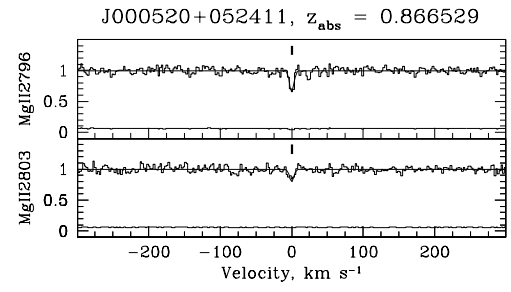
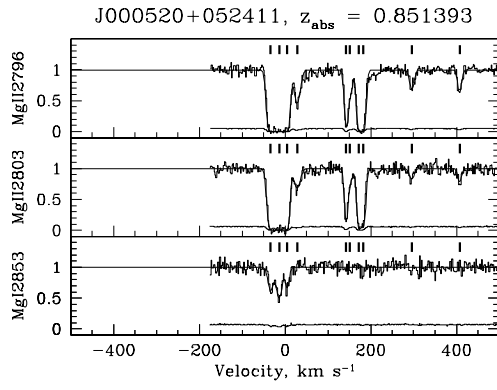


Figure 2.14 Same as Figure 2.12.

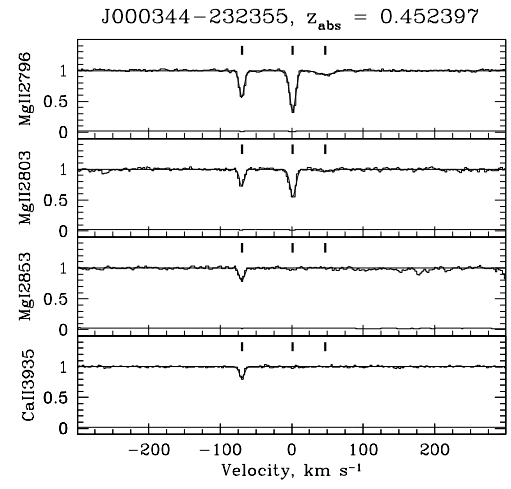
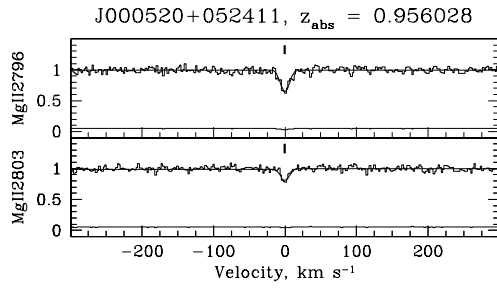


Figure 2.15 Same as Figure 2.12.

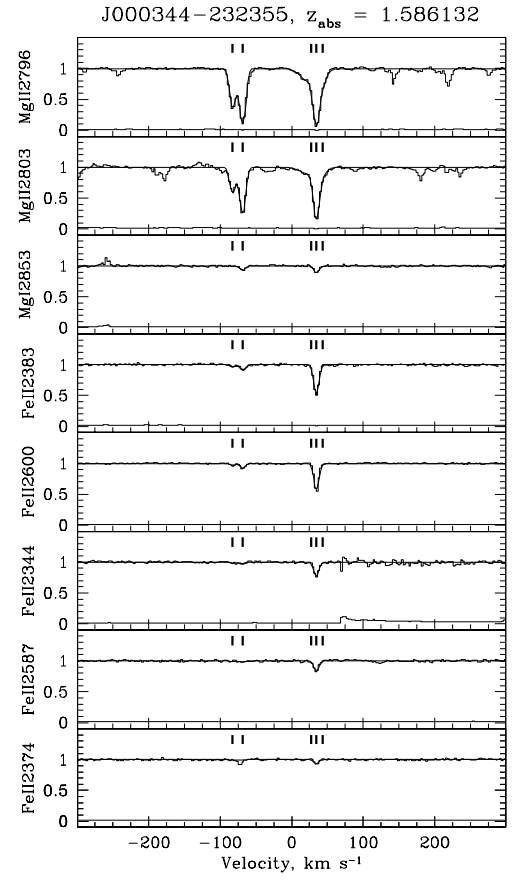
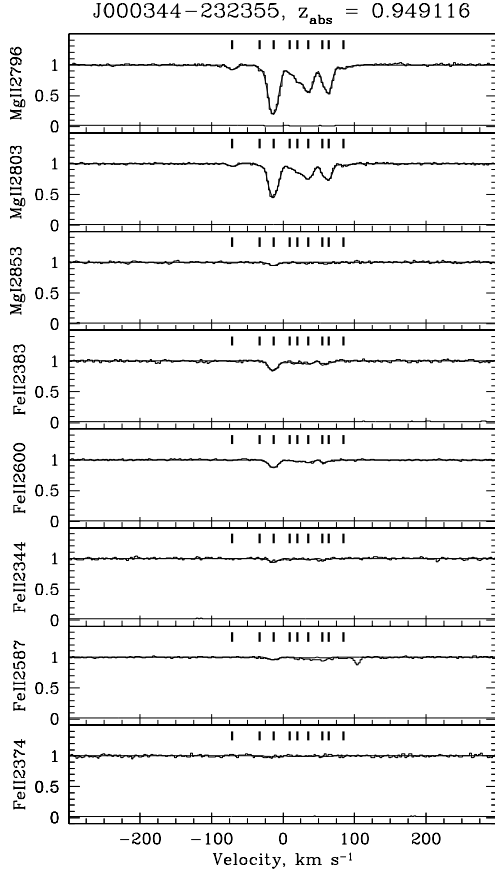


Figure 2.16 Same as Figure 2.12.

3 ANALYSIS OF MGII SYSTEMS

Once the presence of MgII is confirmed directly from the flux decrements, the equivalent width regions, equivalent widths, optical depth-weighted system redshifts, velocity spreads, and upper and lower velocity limits are determined for both the whole system and for the kinematic subsystems using SYSANAL (see Churchill et al. (1999); Churchill & Vogt (2001)). All quantities are calculated for the MgII, MgI, FeII, MnII, and CaII transitions listed in Table 2.3. Kinematic subsystems are regions of detected absorption separated by regions of no detected absorption, but which are close enough together in velocity space that they are considered a single system. We define MgII $\lambda 2796$ features to be part of a single system if they lie within 800 km s^{-1} of each other. Figure 2.6 shows two MgII systems. The largest system spans the region marked by the arrows and consists of five kinematic subsystems; the smaller system lies $\sim 1,000 \text{ km s}^{-1}$ away.

The measured system properties are listed in “System Properties” on the included compact disc; examples are listed in Table 3.1. Column (1) lists the quasar, (2) the system redshift, (3) the rest equivalent width for the MgII $\lambda 2796$ absorption, (4) the apparent optical depth column density, (5) the MgII $\lambda\lambda 2796, 2803$ doublet ratio, and (6) the flux decrement-weighted velocity spread, ω_v . The properties for each kinematic subsystem are listed in “Kinematic Subsystem Properties” on the included compact disc, and examples are listed in Table 3.2. Column (1) lists the quasar, (2) the system

redshift, (3) the subsystem number, (4) the subsystem velocity center, $\langle v \rangle$, (5) the lower subsystem velocity limit, (6) the upper subsystem velocity limit, (7) the subsystem flux decrement-weighted velocity spread, ω_v , (8) the subsystem rest equivalent width for the MgII $\lambda 2796$ line, and (9) the subsystem MgII $\lambda\lambda 2796, 2803$ doublet ratio. These properties are all derived directly from the flux values in each pixel and the methods of determining them are discussed in the following sections; in § 4, properties derived from Voigt profile modeling of the systems are discussed.

Table 3.1. Example System Properties

Quasar	z_{abs}	W_r (Å)	N_{aod} (log cm ⁻²)	DR	ω_v (km s ⁻¹)
J000323 – 260318	1.434037	0.511 ± 0.004	$13.38^{+0.05}_{-0.04}$	1.76 ± 0.03	61.0 ± 1.0
J000149 – 015939	0.870821	0.868 ± 0.013	≥ 13.64	1.25 ± 0.03	45.1 ± 0.7
J000520 + 052411	0.298059	0.244 ± 0.003	$13.08^{+0.08}_{-0.07}$	1.34 ± 0.03	11.6 ± 0.4
J000520 + 052411	0.591365	0.102 ± 0.002	$12.55^{+0.09}_{-0.08}$	1.54 ± 0.04	7.0 ± 0.5
J000520 + 052411	0.866530	0.023 ± 0.003	$11.80^{+0.14}_{-0.10}$	1.64 ± 0.46	2.1 ± 1.5
J000520 + 052411	0.956028	0.054 ± 0.004	$12.18^{+0.08}_{-0.06}$	2.19 ± 0.35	6.3 ± 0.9
J000344 – 232355	0.452398	0.126 ± 0.003	$12.56^{+0.07}_{-0.06}$	1.78 ± 0.08	40.4 ± 1.0
J000344 – 232355	0.949116	0.349 ± 0.003	$13.05^{+0.04}_{-0.04}$	1.71 ± 0.03	36.1 ± 0.5
J000344 – 232355	1.586132	0.324 ± 0.002	$13.12^{+0.05}_{-0.05}$	1.33 ± 0.02	53.8 ± 0.2
J000344 – 232355	1.651460	0.066 ± 0.001	$12.37^{+0.11}_{-0.10}$	1.41 ± 0.04	4.0 ± 0.4
J000344 – 232355	2.184449	0.927 ± 0.006	$13.56^{+0.03}_{-0.03}$	1.61 ± 0.02	142.5 ± 0.4
J000448 – 415728	0.836627	4.422 ± 0.002	≥ 14.65	1.12 ± 0.00	147.5 ± 0.1
J000448 – 415728	1.541852	0.397 ± 0.002	$13.30^{+0.06}_{-0.05}$	1.42 ± 0.01	35.4 ± 0.6
J000448 – 415728	1.988658	0.299 ± 0.002	$13.11^{+0.06}_{-0.06}$	1.41 ± 0.02	24.8 ± 0.3
J000448 – 415728	2.167883	0.358 ± 0.003	$13.15^{+0.05}_{-0.05}$	1.50 ± 0.02	25.4 ± 0.5
J000448 – 415728	2.301942	1.719 ± 0.004	$14.14^{+0.03}_{-0.02}$	1.17 ± 0.00	72.0 ± 0.3
J000448 – 415728	2.464126	0.364 ± 0.003	$13.19^{+0.05}_{-0.05}$	1.40 ± 0.02	16.8 ± 0.2
J001130 + 005550	1.395604	0.330 ± 0.010	$13.10^{+0.06}_{-0.04}$	1.44 ± 0.07	39.6 ± 1.2
J001130 + 005550	1.777929	0.136 ± 0.005	$12.83^{+0.08}_{-0.06}$	1.44 ± 0.09	5.9 ± 0.6
J001210 – 012207	1.202983	0.309 ± 0.005	$13.17^{+0.06}_{-0.05}$	1.30 ± 0.04	38.7 ± 0.6
J001210 – 012207	1.385937	1.087 ± 0.008	$13.79^{+0.03}_{-0.02}$	1.21 ± 0.02	66.7 ± 0.5
J001306 + 000431	1.212007	0.916 ± 0.008	≥ 13.76	1.25 ± 0.02	37.9 ± 0.6
J001602 – 001225	0.635095	0.201 ± 0.008	$12.80^{+0.06}_{-0.05}$	1.34 ± 0.09	100.4 ± 2.4

Table 3.2. Example Kinematic Subsystem Properties

Quasar	z_{abs}	Subsystem	$\langle v \rangle$ (km s ⁻¹)	v^- (km s ⁻¹)	v^+ (km s ⁻¹)	ω_v (km s ⁻¹)	$W_r(2796)$ (Å)	DR
J000323 – 260318	1.434037	1	-170.48 ± 0.38	-184.6	-156.1	4.52 ± 1.20	0.07 ± 0.00	1.45 ± 0.10
		2	-1.45 ± 0.17	-39.6	34.2	21.64 ± 0.12	0.44 ± 0.00	1.82 ± 0.03
J000149 – 015939	0.870821	1	-93.22 ± 0.60	-113.5	-77.4	5.89 ± 1.16	0.15 ± 0.01	1.09 ± 0.07
		2	-4.39 ± 0.71	-72.2	67.0	33.00 ± 0.63	0.72 ± 0.01	1.29 ± 0.03
J000520 + 052411	0.298059	1	0.12 ± 0.33	-32.2	40.5	11.58 ± 0.44	0.24 ± 0.00	1.34 ± 0.03
J000520 + 052411	0.591365	1	-0.39 ± 0.28	-28.0	28.6	7.00 ± 0.47	0.10 ± 0.00	1.54 ± 0.04
J000520 + 052411	0.851393	1	-6.72 ± 0.31	-51.7	60.8	23.70 ± 0.36	0.64 ± 0.00	1.10 ± 0.01
		2	165.65 ± 0.27	124.1	195.3	17.12 ± 0.24	0.36 ± 0.00	1.20 ± 0.02
		3	296.95 ± 0.76	282.6	311.0	5.94 ± 1.49	0.04 ± 0.00	1.74 ± 0.31
		4	407.54 ± 0.71	395.9	420.1	3.09 ± 4.58	0.04 ± 0.00	1.34 ± 0.22
J000520 + 052411	0.866530	1	-0.06 ± 0.85	-8.9	7.2	2.10 ± 1.48	0.02 ± 0.00	1.64 ± 0.46
J000520 + 052411	0.956028	1	0.59 ± 0.81	-16.7	18.4	6.33 ± 0.95	0.05 ± 0.00	2.19 ± 0.35

3.1 Equivalent Width Regions

After a system is identified as described in § 2.4, its equivalent width region must be defined using the equivalent width spectrum and following the formalism of Schneider et al. (1993). The wavelength limits of the feature are determined by first measuring the equivalent width significance in each resolution element. There are three pixels per resolution element in our spectra and the instrumental spread function is assumed to be a Gaussian of width $\Delta\lambda$ (FWHM) given by

$$R = \frac{\lambda}{\Delta\lambda} = 45,000. \quad (3.1)$$

In order to have been identified, the feature must contain a resolution element satisfying the condition

$$\frac{w_j}{\sigma_{w_j}} \geq 5, \quad (3.2)$$

where w_j is the equivalent width of resolution element j and σ_{w_j} is the uncertainty in the equivalent width. From this resolution element the spectrum is then scanned blueward until the significance drops to

$$\frac{w_j}{\sigma_{w_j}} \leq 1; \quad (3.3)$$

this defines the lower wavelength limit of the spectrum. This process is repeated redward to locate the upper wavelength of the feature. An example of an identified system with the equivalent width regions defined for each kinematic subsystem is shown in Figure 3.1. The gray shaded areas indicate the equivalent width regions and the dotted lines indicate the limits of the 1σ significance level.

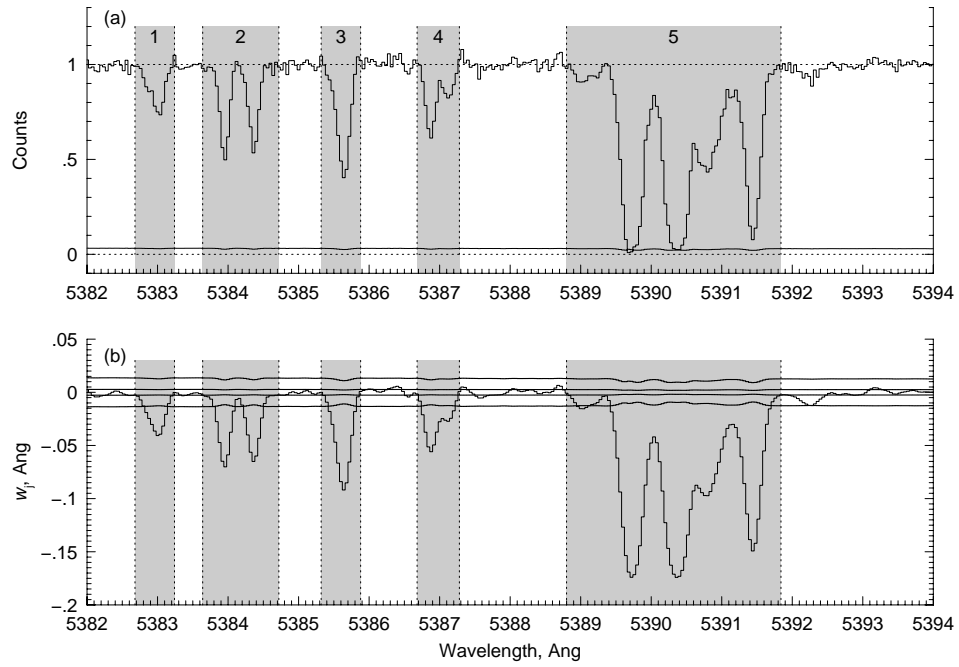


Figure 3.1 (a) The MgII $\lambda 2796$ absorption system shown in Figure 2.6 with its five kinematic subsystems defined. (b) The equivalent width per resolution element. The curves above and below the spectrum provide the $\pm 1 \sigma$ and $\pm 5 \sigma$ uncertainties. Figure provided by Churchill (2012) with permission.

3.2 Equivalent Widths

The equivalent width of a MgII system results from both the column density of its components and its kinematics - i.e., the manner in which the components are distributed in velocity space. The rest frame equivalent width of an absorption line is equal to

$$W_r = \frac{W_{obs}}{1 + z_{abs}}, \quad (3.4)$$

where the definition of the observed equivalent width is

$$W_{obs} = \int_{\lambda_1}^{\lambda_2} \left(1 - \frac{I}{I^c}\right) d\lambda, \quad (3.5)$$

and where λ_1 and λ_2 are the wavelength limits of the feature, I is the flux at wavelength λ , and I^c is the continuum flux at that wavelength. In practice, the observed equivalent width of a system is determined by summing the equivalent width in each pixel over the wavelength range of the feature as defined in § 3.1. For kinematic subsystem k spanning pixels j_k^- to j_k^+ the equivalent width is calculated as

$$W_k = \sum_{j=j_k^-}^{j_k^+} \left(1 - \frac{I_j}{I_j^c}\right) \Delta\lambda_j. \quad (3.6)$$

The quantity $D_j = 1 - \frac{I_j}{I_j^c}$ is the flux decrement in pixel j and $\Delta\lambda_j$ is the wavelength range spanned by pixel j . The variance in W_k is

$$\sigma_{W_k}^2 = \sum_{j=j_k^-}^{j_k^+} \sigma_{D_j}^2 (\Delta\lambda_j)^2, \quad (3.7)$$

where $\sigma_{D_j}^2$ is the variance in the flux decrement and is given by

$$\sigma_{D_j}^2 = \left(\frac{I_j}{I_j^c}\right)^2 \left[\left(\frac{\sigma_{I_j}}{I_j}\right)^2 + \left(\frac{\sigma_{I_j^c}}{I_j^c}\right)^2 \right], \quad (3.8)$$

where σ_{I_j} and $\sigma_{I_j^c}$ are the uncertainties in the counts and continuum of pixel j .

The total system equivalent width then is summed over all subsystems as follows:

$$W = \sum_{k=1}^{N_{\text{sub}}} W_k, \quad (3.9)$$

where N_{sub} is the number of kinematic subsystems. The variance for system equivalent width W is

$$\sigma_W^2 = \sum_{k=1}^{N_{\text{sub}}} \sigma_{W_k}^2. \quad (3.10)$$

3.3 System Redshifts and Velocities

The system redshift is determined using the median wavelength of the flux decrement distribution of the MgII $\lambda 2796$ transition. This wavelength is obtained by solving the implicit equation

$$\int_{\lambda^-}^{\lambda_z} D(\lambda) d\lambda = \int_{\lambda_z}^{\lambda^+} D(\lambda) d\lambda \quad (3.11)$$

for λ_z . $D(\lambda)$ is the flux decrement at λ and λ^- and λ^+ are the lower and upper limits of the MgII $\lambda 2796$ absorption feature. The wavelength λ_z is then the spectral location at which there is an equal amount of integrated flux decrement blueward and redward.

The system redshift is then calculated as

$$z_{\text{abs}} = \frac{\lambda_z}{\lambda_r(2796)} - 1 \quad (3.12)$$

where $\lambda_r(2796)$ is the rest wavelength of the MgII $\lambda 2796$ transition.

Once the system redshift has been determined, it can be used to transform the absorption profiles into velocity space. For a given observed wavelength λ_j of pixel j ,

the corresponding velocity is

$$v_j = c \frac{\lambda_j - \lambda_r(1 + z_{abs})}{\lambda_r(1 + z_{abs})} \quad (3.13)$$

where c is the speed of light and λ_r can refer to the rest wavelength of any of the transitions we are studying within the system. Converting the absorption profiles of all the selected system transitions into velocity space allows us to compare them on a common kinematic scale. In addition, we can now quantify and study kinematic properties as discussed in § 3.4.

3.4 Total Velocity Widths, Mean Velocities, and Velocity Spreads

The total velocity width of a system refers to the highest velocity v^+ of absorption minus the lowest velocity v^- of absorption in the MgII $\lambda 2796$ feature. This quantity represents the total velocity limits that a system spans, irrespective of the amount of absorption in the intervening velocity space. Thus a strong saturated profile spanning $\sim 600 \text{ km s}^{-1}$ might have the same total velocity width as a weak system that has two kinematic subsystems, one at $\sim -300 \text{ km s}^{-1}$ and the other at $\sim +300 \text{ km s}^{-1}$ but with no absorption in between.

We can use the first three velocity moments to calculate the mean velocity $\langle v \rangle$ and the velocity spread ω_v of absorption systems and their subsystems. The definitions of

the first three velocity moments are

$$\begin{aligned}
V^{(0)} &= \int_{v^-}^{v^+} D(v) dv \\
V^{(1)} &= \int_{v^-}^{v^+} v D(v) dv \\
V^{(2)} &= \int_{v^-}^{v^+} (v - \langle v \rangle)^2 D(v) dv,
\end{aligned} \tag{3.14}$$

where $D(v)$ is the flux decrement at velocity v .

The mean velocity or velocity center $\langle v_k \rangle$ of the k th kinematic subsystem is the ratio of the first to the zeroth moment:

$$\langle v_k \rangle = \frac{V_k^{(1)}}{V_k^{(0)}} \tag{3.15}$$

where the zeroth moment is calculated as

$$V_k^{(0)} = \sum_{j=j_k^-}^{j_k^+} D_j \Delta v_j, \tag{3.16}$$

and the first moment is

$$V_k^{(1)} = \sum_{j=j_k^-}^{j_k^+} v_j D_j \Delta v_j, \tag{3.17}$$

where Δv_j is the velocity width and D_j the flux decrement of pixel j .

The kinematic velocity spread, i.e. the dispersion of the flux decrement distribution, is given by

$$\omega_{v,k} = \left(\frac{V_k^{(2)}}{V_k^{(0)}} \right)^{1/2} \tag{3.18}$$

where the second velocity moment is calculated as

$$V_k^{(2)} = \sum_{j=j_k^-}^{j_k^+} (v_j - \langle v_k \rangle)^2 D_j \Delta v_j. \tag{3.19}$$

The variances in the mean velocity and velocity spread are given by

$$\begin{aligned}\sigma_{\langle v_k \rangle}^2 &= \left\{ \frac{\partial[V_k^{(1)}/V_k^{(0)}]}{\partial I_j} \right\}^2 \\ \sigma_{\omega_{v,k}}^2 &= \left\{ \frac{1}{2} [V_k^{(2)}]^{-1} \frac{\partial[V_k^{(2)}/V_k^{(0)}]}{\partial I_j} \right\}^2,\end{aligned}\tag{3.20}$$

where

$$\left\{ \frac{\partial[V_k^{(n)}/V_k^{(0)}]}{\partial I} \right\}^2 = \sum_{j=j_k^-}^{j_k^+} \left\{ \frac{(V_k^{(0)} S_j^{(n)} - V_k^{(1)} S_j^{(0)}) \sigma_{D_j}}{[V_k^{(0)}]^2} \right\}^2,\tag{3.21}$$

and

$$\begin{aligned}S_j^{(0)} &= -\frac{\Delta v_j}{I_j^c} \\ S_j^{(1)} &= v_j S_j^{(0)} \\ S_j^{(2)} &= (v_j - \langle v_k \rangle)^2 S_j^{(0)}.\end{aligned}\tag{3.22}$$

As in the case of the equivalent widths, the total system velocity moments (denoted by dropping the subscript k) are obtained by summing over all subsystems:

$$\begin{aligned}V^{(0)} &= \sum_{k=1}^{N_{\text{sub}}} V_k^{(0)} \\ V^{(1)} &= \sum_{k=1}^{N_{\text{sub}}} V_k^{(1)}\end{aligned}\tag{3.23}$$

and the total system mean velocity is

$$\langle v \rangle = \frac{V^{(1)}}{V^{(0)}}.\tag{3.24}$$

The system second velocity moment is

$$V^{(2)} = \sum_{k=1}^{N_{\text{sub}}} \sum_{j=j_k^-}^{j_k^+} (v_j - \langle v \rangle)^2 D_j \Delta v_j\tag{3.25}$$

and the system velocity spread is

$$\omega_v = \left(\frac{V^{(2)}}{V^{(0)}} \right)^{1/2}. \quad (3.26)$$

The variances in the system mean velocity and velocity spread are

$$\begin{aligned} \sigma_{\langle v \rangle}^2 &= \left\{ \frac{\partial[V^{(1)}/V^{(0)}]}{\partial I_j} \right\}^2 \\ \sigma_{\omega_v}^2 &= \left\{ \frac{1}{2} [V^{(2)}]^{-1} \frac{\partial[V^{(2)}/V^{(0)}]}{\partial I_j} \right\}^2, \end{aligned} \quad (3.27)$$

where

$$\left\{ \frac{\partial[V^{(n)}/V^{(0)}]}{\partial I} \right\}^2 = \sum_{k=1}^{N_{\text{sub}}} \sum_{j=j_k^-}^{j_k^+} \left\{ \frac{(V^{(0)} S_j^{(n)} - V^{(1)} S_j^{(0)}) \sigma_{D_j}}{[V^{(0)}]^2} \right\}^2 \quad (3.28)$$

and

$$\begin{aligned} S_j^{(0)} &= -\frac{\Delta v_j}{I_j^c} \\ S_j^{(1)} &= v_j S_j^{(0)} \\ S_j^{(2)} &= (v_j - \langle v \rangle)^2 S_j^{(0)}. \end{aligned} \quad (3.29)$$

3.5 Results

3.5.1 Equivalent Width Distribution of Mg II Systems

The system Mg II $\lambda 2796$ equivalent width distribution of our sample is shown in Figure 3.2. The weak portion of the distribution was fit using a power law of the form

$$n(W) = CW^{-\delta}, \quad (3.30)$$

where $n(W)$ is the frequency of absorbers of equivalent width W , C is a constant, and δ is the power law slope. In Figure 3.2, systems in the range $0.02 \leq W_r < 0.3 \text{ \AA}$

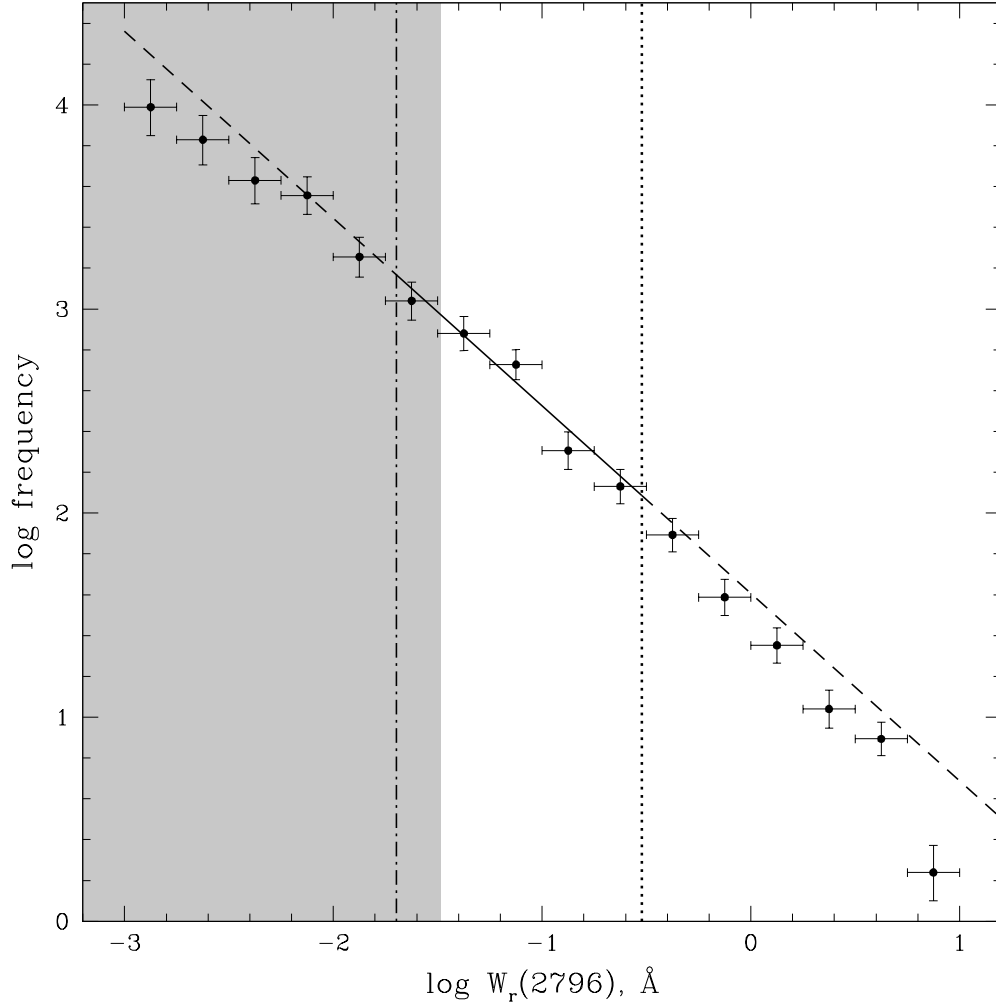


Figure 3.2 The MgII $\lambda 2796$ equivalent width distribution of our sample. The vertical dotted line demarcates the transition from weak to strong absorption, i.e. $W_r = 0.3 \text{ \AA}$, and is the upper boundary of the power law fit. The shaded area represents the equivalent width regime in which our sample falls below 90% completeness, $W_r < 0.0325 \text{ \AA}$ (see § 5.2.2). The vertical dashed-dotted line at $W_r = 0.02 \text{ \AA}$ is the lower boundary of our fit. The sloped line indicates the power law best fit to the weak systems, with slope $\delta = 0.92 \pm 0.02$; the fit was performed only on systems in the range $0.02 \leq W_r < 0.3 \text{ \AA}$ (the solid portion of the line). The line was extended in both directions (dashed) for comparison with higher and lower equivalent widths.

were fit with this parameterization using the maximum likelihood method. The fit was performed on the unbinned data points. The solid sloped line represents our fit result of $\delta = 0.92 \pm 0.02$; the line was extended to both weaker and stronger equivalent widths for comparison. The fit was not performed on systems below 0.02 \AA due to the loss of sensitivity in this regime, which is discussed in § 5.2.2.

Churchill et al. (1999) fit a power law function to their sample of 30 weak systems with $\delta = 1.04 \pm 0.07$, which is consistent with our slope. The authors found no indication of a turnover in the distribution down to $W_r = 0.02 \text{ \AA}$, with which our findings are also in good agreement.

The weak equivalent width distribution of Narayanan et al. (2007), in a study of 112 weak systems, contained evidence for a turnover at $W_r < 0.1 \text{ \AA}$; however, we find no such turnover. Even at very weak equivalent widths where the spectra are not complete and less systems are likely to be recovered, we find our distribution follows the power law best fit of the $0.02 \leq W_r < 0.3 \text{ \AA}$ regime down to $W_r \sim 0.05 \text{ \AA}$. Narayanan et al. (2007) did not perform a fit to their equivalent width distribution.

3.5.2 Kinematic Properties of MgII Systems

System total velocity width and velocity spread distributions are shown in Figure 3.3. The shaded histograms indicate the entire sample; the dotted lines indicate the weak ($W_r(2796) < 0.3 \text{ \AA}$) subsample; and the dashed lines indicate the strong ($W_r(2796) \geq 0.3 \text{ \AA}$) subsample. The two populations exhibit markedly different distri-

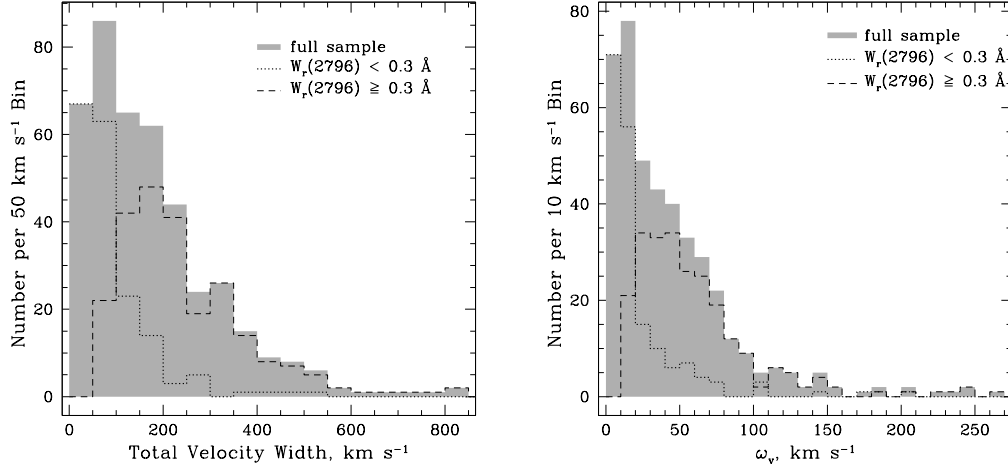


Figure 3.3 At left, the distributions of MgII system total velocity widths for the $\lambda 2796$ transition for $W_r(2796) < 0.3 \text{ \AA}$, $W_r(2796) \geq 0.3 \text{ \AA}$, and the full sample. At right, the velocity spread (ω_v) distributions shown in the same format.

butions, with the weak systems averaging a total velocity width of 88.7 km s^{-1} and the strong systems averaging 247.1 km s^{-1} . Similarly, the weak systems average a velocity spread of 22.9 km s^{-1} and the strong systems 60.0 km s^{-1} . These distributions indicate that differing kinematic extents, not just differing optical depths, contribute to the differences in equivalent widths in the weak and strong MgII absorber populations.

3.5.3 Kinematic Subsystem Properties of Strong MgII Systems

The kinematic properties of MgII absorbing systems can be further studied by quantifying characteristics of individual subsystems. We have divided the kinematic subsystems of the strong population (having total system $W_r(2796) \geq 0.3 \text{ \AA}$) into three classes according to subsystem velocity $\langle v \rangle$, choosing bins of $\langle v \rangle \leq 40 \text{ km s}^{-1}$,

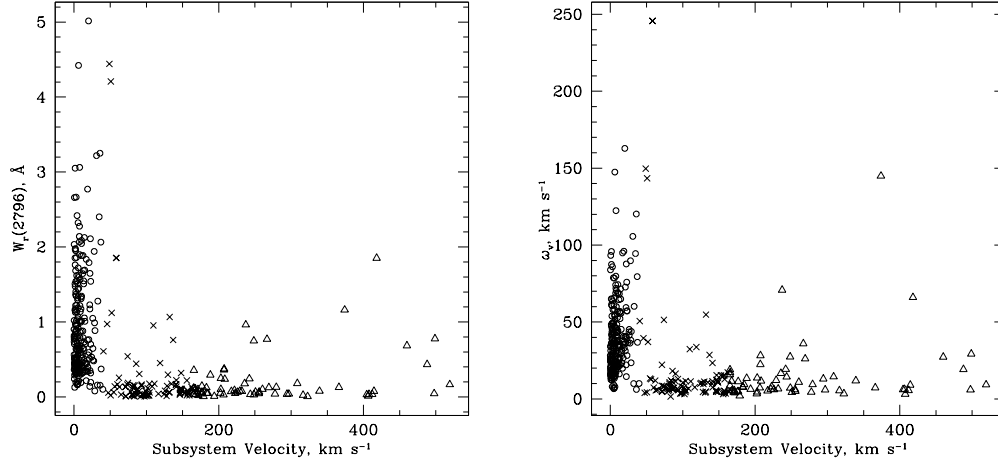


Figure 3.4 At left, subsystem equivalent width versus subsystem velocity for strong systems (total $W_r(2796) \geq 0.3 \text{ \AA}$). At right, subsystem velocity spread ω_v versus subsystem velocity for strong systems. Circles represent subsystem velocities $\langle v \rangle \leq 40 \text{ km s}^{-1}$; x's $40 < \langle v \rangle \leq 165 \text{ km s}^{-1}$; and triangles $\langle v \rangle > 165 \text{ km s}^{-1}$.

$40 < \langle v \rangle \leq 165 \text{ km s}^{-1}$, and $\langle v \rangle > 165 \text{ km s}^{-1}$. This allows comparison with the work of Churchill & Vogt (2001), in which the subsystems of 23 strong MgII systems were analyzed. Figure 3.4 shows the results of our analysis of the 242 strong systems in our sample. The left panel plots subsystem equivalent width versus subsystem velocity and the right panel subsystem velocity spread ω_v versus subsystem velocity; circles, x's and triangles represent the low, intermediate and high velocity bins, respectively.

The low velocity subsystems have an average equivalent width of 0.96 \AA and an average velocity spread of 39.7 km s^{-1} . They represent a class distinct from the intermediate and high velocity subsystems, which have average equivalent widths of 0.29 and 0.20 \AA , respectively, and average velocity spreads of 19.5 and 14.6 km s^{-1} , respectively. These data reflect the fact that low velocity subsystems tend to be the dominant

subsystems in strong MgII absorbers, whereas subsystems having $\langle v \rangle > 40 \text{ km s}^{-1}$ tend to be weak and to have smaller kinematic extents. We can thus characterize strong MgII absorbers generally to consist of a dominant subsystem (though “double” systems do exist) with significantly weaker, kinematically more compact subsystems extending out in one or both directions from the main absorption and spaced tens to hundreds of km s^{-1} away.

Churchill & Vogt (2001) found the same trends between subsystem equivalent width and subsystem velocity and between subsystem velocity spread and subsystem velocity. However, within each velocity bin, their subsystem velocity spreads and subsystem equivalent widths were significantly lower. In the low velocity bin, most of the subsystem equivalent widths ranged from $0.3 \leq W_r(2796) \leq 0.6 \text{ \AA}$ compared to our average of 0.96 \AA , and the velocity spreads were typically between $10 \leq \omega_v \leq 30 \text{ km s}^{-1}$ compared to our average of 39.7 km s^{-1} . Similarly, in the intermediate and high velocity bins, Churchill & Vogt (2001) found subsystem equivalent widths of $W_r \simeq 0.1 \text{ \AA}$ whereas our average for those two bins is 0.25 \AA . They also quote subsystem velocity spreads of typically $< 10 \text{ km s}^{-1}$ to our average of 17.5 km s^{-1} . We believe these differences arise due to the much smaller sample size of Churchill & Vogt (2001) compared to our study; our sample is over a factor of ten larger. As a result, our sample includes the rarest extremely high equivalent width, high velocity spread MgII systems; for example, the highest equivalent width system in the Churchill & Vogt (2001) sample had $W_r(2796) = 1.49 \text{ \AA}$, whereas for our sample it is $W_r(2796) = 6.23 \text{ \AA}$. The number of

systems in our sample exceeding the Churchill & Vogt (2001) equivalent width maximum is 59, or 24% of the systems. We believe our sample is dramatically more robust and its statistics are the more reliable of the two.

3.5.4 Weak MgII Systems versus High Velocity Kinematic Subsystems of Strong MgII Systems

While the high velocity kinematic subsystems of strong MgII are interesting in their own right, we would also like to compare these subsystems to isolated weak MgII absorption. Morphologically these two types of profiles often appear very similar, but we have performed a statistical analysis showing that they are actually two distinct populations.

Kinematic subsystems of strong MgII having $\langle v \rangle > 40 \text{ km s}^{-1}$ and subsystem equivalent widths of $W_r < 0.3 \text{ \AA}$ were culled from the sample for comparison with weak MgII systems (those having total $W_r(2796) < 0.3 \text{ \AA}$). These subsamples comprised 131 kinematic subsystems and 180 weak systems. Figure 3.5 illustrates their cumulative rest equivalent width and velocity spread distributions; both differ dramatically between the two populations. The high velocity kinematic subsystem equivalent width distribution rises faster than that of the weak systems, indicating that their distribution is more skewed toward lower equivalent widths in the $W_r < 0.3 \text{ \AA}$ regime. Even more drastic is the steep rise of the high velocity subsystem velocity spread distribution compared to the distribution of weak systems. The largest velocity spread of the high velocity

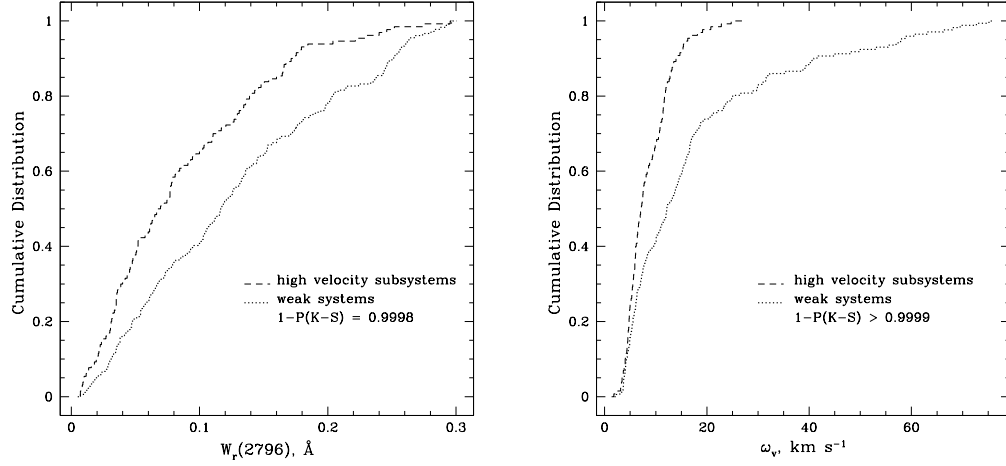


Figure 3.5 At left, the cumulative equivalent width distributions of weak MgII systems and of kinematic subsystems having $\langle v \rangle > 40 \text{ km s}^{-1}$ and $W_r(2796) < 0.3 \text{ \AA}$. At right, the cumulative velocity spread distributions of the same two populations are shown. The confidence levels $1 - P(K - S)$ are shown (see text).

subsystem population is only 26.1 km s^{-1} , while the weak distribution continues to rise to $\omega_v = 75.6 \text{ km s}^{-1}$. The high velocity subsystems exhibit systematically much narrower velocity spreads than the weak systems.

The Kolmogorov-Smirnov (K-S) statistical test was employed in order to quantitatively measure the difference in the distributions of high velocity subsystems compared to weak systems. In the case of the equivalent widths, $P(K - S) = 2 \times 10^{-4}$, meaning it can be ruled out that the two samples were drawn from the same population to a 99.98% confidence level ($1 - P(K - S)$). For the velocity spreads, $P(K - S) = 1 \times 10^{-9}$; the confidence level is greater than 99.99%. These results correspond to significance levels of 3σ and 6σ , respectively. Isolated weak MgII absorption therefore appears to arise from a phenomenon distinct from that of the high velocity kinematic subsystems

of strong MgII absorption.

4 VOIGT PROFILE ANALYSIS

4.1 Introduction to Voigt Profile Fitting

High resolution absorption line spectra can be used to study the kinematic structure of (in our case MgII-selected) intergalactic and galactic halo gas. In order to extract as much information as possible from the MgII systems in our sample, Voigt profile (VP) fitting was used in addition to the kinematic metrics discussed in § 3.

The Voigt profile takes into account two absorption line broadening mechanisms: the natural linewidth, which results from Heisenberg uncertainty, and Doppler broadening, which is a result of the thermal and/or turbulent motions of the gas. The natural linewidth is characterized by a Lorentzian and the Doppler, or thermal, broadening by a Gaussian. Their convolution results in the Voigt profile. Complex absorption systems can be decomposed into individual Voigt profiles, with each model component yielding column density, temperature, and velocity information.

The Voigt function is the real part $u(x, y)$ of the complex probability function

$$w(x) = e^{-x^2} \left[1 + \frac{2i}{\sqrt{\pi}} \int_0^x e^{-t^2} dt \right] = e^{-x^2} \operatorname{erfc}(-iz) = u(x, y) + iv(x, y). \quad (4.1)$$

The Voigt profile is represented by the optical depth as a function of wavelength,

$$\tau(\lambda) = \frac{\sqrt{\pi}e^2}{m_e c^2} \frac{N f \lambda_o^2}{\Delta \lambda_D} u(x, y), \quad (4.2)$$

where e is the electron charge, m_e is the electron mass, c is the speed of light, N is the line of sight integrated column density, f is the atomic oscillator strength, λ_o is

the transition wavelength, and $\Delta\lambda_D$ is the Doppler broadening for an ion of mass m at temperature T :

$$\Delta\lambda_D = \frac{\lambda_o}{c} \sqrt{\frac{2kT}{m}}. \quad (4.3)$$

The quantity x represents the distance from the line center as a function of wavelength:

$$x = \frac{\lambda - \lambda_o}{\Delta\lambda_D}, \quad (4.4)$$

and y the natural width of the transition:

$$y = \frac{\lambda_o^2 \Gamma}{4\pi c} \frac{1}{\Delta\lambda_D}, \quad (4.5)$$

where Γ is the damping constant and represents the inverse of the most probable length of time the electron will remain in the excited level.

The Doppler broadening can also be expressed in terms of the Doppler b parameter:

$$\Delta\lambda_D = \frac{\lambda_o}{c} b. \quad (4.6)$$

Assuming pure thermal broadening, the Doppler b parameter is

$$b = b_{therm} = \sqrt{\frac{2kT}{m}}, \quad (4.7)$$

where k is Boltzmann's constant, T is the temperature of the absorbing gas, and m is the mass of the absorbing species. Under this assumption, the Doppler parameters extracted through Voigt profile analysis are parameterizations of the temperature conditions under which MgII absorption occurs. When a Gaussian turbulent component to the gas motion is assumed, the b parameter becomes:

$$b = \sqrt{b_{therm}^2 + b_{turb}^2}. \quad (4.8)$$

The VP modeling process is explained in the following sections; the results are listed in “Voigt Profile Fitting Results” on the included compact disc, and an example system is listed in Table 4.1. The fits are shown plotted over the data in Figures 3.1 - 3.211. Systems are separated in the table by horizontal lines; the first column numbers the components, and the remaining columns list the column density N and Doppler parameter b for the MgII, FeII, MgI, MnII, and CaII ions. An ion is not listed if it was not available to fit. Column densities listed as being less than or equal to some value represent upper limits (see § 4.3.4). Systems that are present in both our sample and either Churchill (1997) or Churchill et al. (2003) have been refit for uniformity.

Table 4.1. Example Voigt Profile Fitting Results

J000344-232355 $z_{abs} = 0.949116$											
		MgII		FeII		MgI		MnII		CaII	
cloud	v	N	b	N	b	N	b	N	b	N	b
1	-70.84	11.40±0.049	6.24±1.179	≤ 10.45	...	≤ 10.52	...	≤ 10.46	...	≤ 10.36	...
2	-32.98	11.06±0.104	3.13±2.285	≤ 10.35	...	≤ 10.44	...	≤ 10.38	...	≤ 10.30	...
3	-13.40	12.75±0.004	7.90±0.141	12.16±0.015	7.90±0.141	10.80±0.152	7.90±0.141	≤ 10.55	...	≤ 10.45	...
4	9.49	11.53±0.428	4.85±5.246	11.04±0.397	4.85±5.246	≤ 10.54	...	≤ 10.48	...	≤ 10.38	...
5	20.09	11.82±0.290	4.86±2.975	11.22±0.348	4.86±2.975	≤ 10.54	...	≤ 10.47	...	≤ 10.38	...
6	35.04	12.36±0.012	8.94±0.068	11.69±0.050	8.94±0.068	≤ 10.64	...	≤ 10.57	...	≤ 10.48	...
7	55.26	11.71±0.062	1.41±0.263	11.35±0.076	1.41±0.263	≤ 10.44	...	≤ 10.38	...	≤ 10.29	...
8	63.74	12.21±0.022	5.32±0.340	11.33±0.082	5.32±0.340	≤ 10.54	...	≤ 10.47	...	≤ 10.38	...
9	84.73	11.46±0.066	11.16±2.496	≤ 10.56	...	≤ 10.64	...	≤ 10.57	...	≤ 10.48	...

4.2 Fitting Philosophy

The ionization potentials of the five ions included in the fit, MgII, FeII, MgI, MnII, and CaII, are all close to the HI potential of 13.59 eV. Their absorption is therefore all assumed, for the purpose of VP fitting, to arise in the same spatial extent of gas, and to contain the same velocity structure. The MgI and CaII potentials are both below that of HI at 7.65 eV and 11.87 eV, respectively, while those of MgII, FeII, and MnII are all slightly above at 15.04 eV, 16.19 eV, and 15.63 eV, respectively. This spread does mean, however, that the ionization structure of a given parcel of gas might be different for different ions. Inasmuch as this difference affects velocity structure, our assumption of parallel kinematics across ions may not always be completely correct.

Another consideration in VP decomposition is how to fit the Doppler b parameter across ions. For our study, we have chosen to let the user input whether to constrain this parameter as 100% turbulent or 100% thermal. In the former case, the b parameter will be fit such that the result is identical for all ions within a given velocity component; in the latter case, it will vary as the ratio of the square root of the atomic masses. The default condition used was turbulent; departures from this are noted in the descriptions of individual systems in Appendix A. The systems were fit under the thermal condition if a satisfactory fit could not be achieved using the turbulent condition.

The overarching VP fitting philosophy used for this study was to fit the MgII systems using as few components as possible while still achieving a robust fit in which all components were statistically significant. In addition, VP modeling by nature requires

the assumption of isothermal components that occupy distinct points in velocity space.

4.3 Fitting Procedure

Using the graphical interactive program IVPFIT, which is an improved version of PROFIT (Churchill, 1997), an initial model of an absorption system's VP components is created and adjusted to fit the data as closely as possible. The velocity, Doppler parameter, and column density of each component are input by the user.

The least squares fitter MINFIT (Churchill, 1997), using this initial model, iteratively eliminates all statistically insignificant components and adjusts the remaining components until the least squares fit is achieved. This process is outlined in § 4.3.3 and illustrated in Figure 4.1. The velocities, column densities, Doppler parameters, and temperatures are calculated for each VP component. MINFIT utilizes the spectral information from all available transitions to constrain these parameters. The velocity of a given component is constrained to be the same across all transitions. The column density is constrained to be the same across all transitions of a given ion. Finally, the Doppler parameter can be set by the user to either vary thermally across ions or to remain constant across all ions, an improvement (mentioned in § 4.2) over the original code. The other improvements that have been made to the program since the original version are described in § 4.3.1, 4.3.2, and 4.3.4.

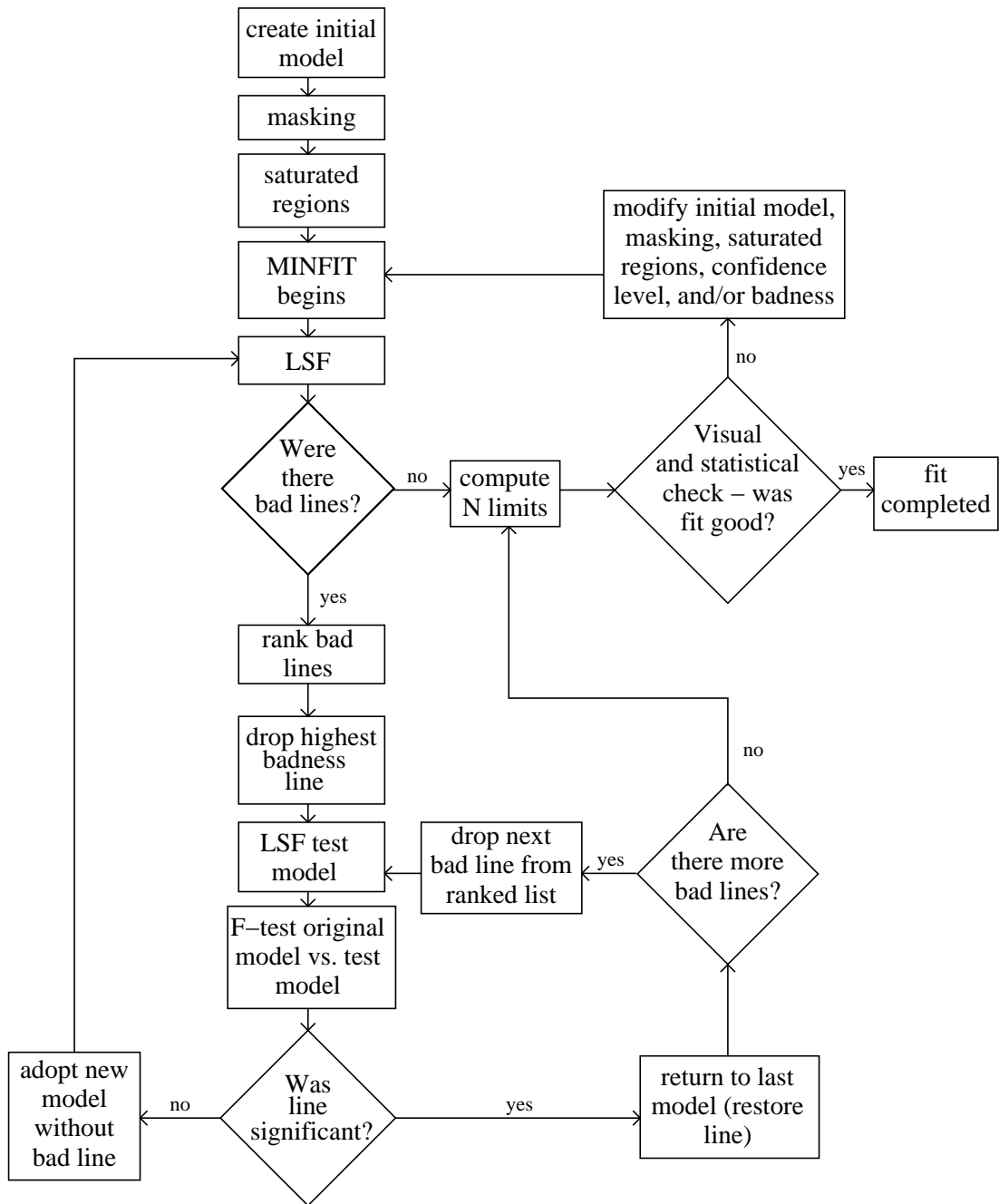


Figure 4.1 The Voigt profile modeling process.

4.3.1 Saturated Regions

Over MgII fitting regions that were saturated but for which the FeII ion retained good column density constraints, a special feature of MINFIT was employed. The user can specify velocity ranges in which the code enforces a $\log N(\text{MgII})$ to $\log N(\text{FeII})$ relationship determined empirically by Churchill et al. (2003):

$$\log N(\text{MgII}) = 1.37 \times \log N(\text{FeII}) - 0.41 \quad (4.9)$$

instead of allowing the column densities of the two ions to be fit independently. This prevents unphysical MgII to FeII column density ratios.

4.3.2 Masking Spectral Regions

In many systems, one or more transitions may be contaminated over portions of the velocity extent by either bad pixels, noisy pixels, or spurious features, all of which have no corroborating absorption in other transitions. In these cases, MINFIT allows the user to interactively mask out regions or individual pixels from the fit. Once this has been done, the code will consider any masked regions of a transition to contain no data and thus to contribute no information to the fit.

4.3.3 χ^2 Minimization and Model Convergence

MINFIT fits three free parameters for each VP component: the column density, the Doppler parameter, and the redshift of the component center. The fitting process and uncertainty calculations are described in detail in Churchill (1997). When there

are multiple kinematic subsystems, the redshift region for each is fit separately. All available transitions within a redshift region are fit simultaneously.

As illustrated in Figure 4.1, MINFIT is started after the initial model is created and any saturated or masked regions have been defined. The program performs the first χ^2 minimization of the first redshift region and then begins the process of determining which components to reject from the model of that region. The badness, or fractional error, of each MgII component is calculated:

$$\text{badness} = \left[\left(\frac{dN}{N} \right)^2 + \left(\frac{db}{b} \right)^2 + \left(\frac{dz}{z} \right)^2 \right]^{1/2}, \quad (4.10)$$

and all components exceeding the user input badness (“bad” components or lines) are ranked. The component with the highest badness is removed from the model and this new “test” model is least squares fit (LSF). Next an F -test is performed comparing the LSFs of the two models; the original model (i.e. containing the bad component) is retained if the resulting confidence level equals or exceeds the user input confidence level. Then the next highest badness component is dropped from the model and the χ^2 minimization process is repeated for this new test model. Otherwise, if the required confidence level was not met, the test model (i.e. with the bad component removed) replaces the original model and the χ^2 minimization process is begun from the beginning (i.e. a new list of bad components, if any, is created). This process is continued until either there are no bad components or any bad components deemed significant to the fit are retained after F -testing.

Once the model has converged for a redshift region, the program moves on to the next region and the LSF process is started again until all regions have been modeled. The code employs a badness of 1.5 and a confidence level of 0.97; on a case-by-case basis, however, these parameters may be altered if it is determined that the final model was unsatisfactory using the default values. These alterations are noted in the descriptions of individual systems in Appendix A.

4.3.4 Column Density Limits

When all regions have been modeled, column density component upper limits are computed. This is done whenever MgII was modeled but the component was deemed not present in another ion, i.e. the data was consistent with the continuum.

4.4 Results

4.4.1 Number of VP Components

The left panel of Figure 4.2 shows the distribution of the number of VP components in each system. The dotted line shows the weak subsample ($W_r(2796) < 0.3 \text{ \AA}$), the dashed line the strong subsample ($W_r(2796) \geq 0.3 \text{ \AA}$), and the shaded area the full sample. The weak systems were modeled with an average of 2.7 components, the strong systems 10.3 components, and the full sample 7.1 components.

Churchill et al. (2003), in modeling simulated complex MgII absorption systems, found that $\sim 30\%$ of VP components were not recovered. If this holds true in our

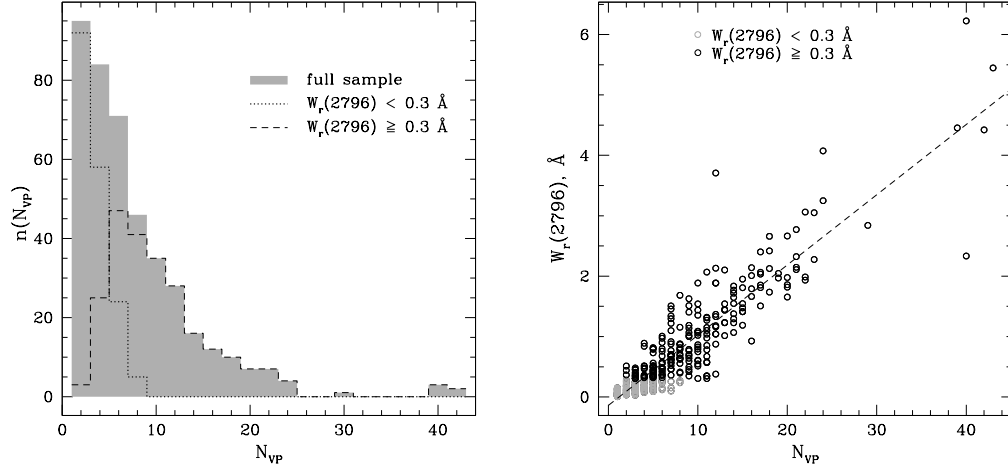


Figure 4.2 At left, the distribution of the number of VP components N_{VP} for $W_r(2796) < 0.3 \text{ \AA}$, $W_r(2796) \geq 0.3 \text{ \AA}$, and the full sample. At right, the system equivalent width versus N_{VP} for weak and strong MgII systems. The dotted line indicates a linear fit to the full sample; the slope is $0.116 \pm 0.003 \text{ \AA cloud}^{-1}$.

sample, it would mean that the actual mean numbers of components are $\sim 43\%$ higher than what was modeled, implying an actual average number of components for the full sample of ~ 10.2 , and for the weak and strong subsamples ~ 3.9 and ~ 14.7 , respectively.

The MgII $\lambda 2796$ system equivalent widths are plotted as a function of the number of VP components in the system in the right panel of Figure 4.2. Gray circles indicate weak systems and black circles indicate strong systems. A linear fit to the full sample resulted in a slope of $0.116 \pm 0.003 \text{ \AA cloud}^{-1}$. The slope found by Churchill (1997) for a sample of 36 MgII systems at the same spectral resolution as this study was $0.076 \pm 0.004 \text{ \AA cloud}^{-1}$. A lower resolution ($\sim 30 \text{ km s}^{-1}$) study by Petitjean & Bergeron (1990) for a sample of 10 MgII systems yielded a steeper slope of $0.35 \text{ \AA cloud}^{-1}$. The W_r -

N_{VP} relationship is strongly affected by the resolution as well as by the signal-to-noise ratio (SN), since higher SN (Churchill, 1997) as well as higher resolution allow more components to be recovered in the VP decomposition.

4.4.2 Column Density Distribution

The column density distribution of MgII VP components can be studied in a manner similar to that of the equivalent widths and modeled using a power law fit. This quantity can sometimes be more revealing because, though more difficult to obtain because of the need to VP fit, it can somewhat account for saturation and therefore the differing sizes of systems that lie on the flat part of the curve of growth.

VP analysis of our full sample of MgII systems yields the component column density distribution shown in Figure 4.3. The 422 MgII systems of our sample yielded 2,989 VP components. The shaded area indicates the region of partial completeness determined by the simulations of Churchill et al. (2003). That study found that the 90% completeness levels for unblended and blended lines were $\log N(\text{MgII}) = 11.6 \text{ cm}^{-2}$ and 12.4 cm^{-2} , respectively, for spectra having a 5σ equivalent width sensitivity of $W_r = 0.02 \text{ \AA}$. “Completeness level” refers to the percentage of simulated components of a given column density recovered during VP analysis. Our distribution peaks in the bin centered at 11.25 cm^{-2} ; however, the turnover at lower column densities is believed to be caused by incompleteness.

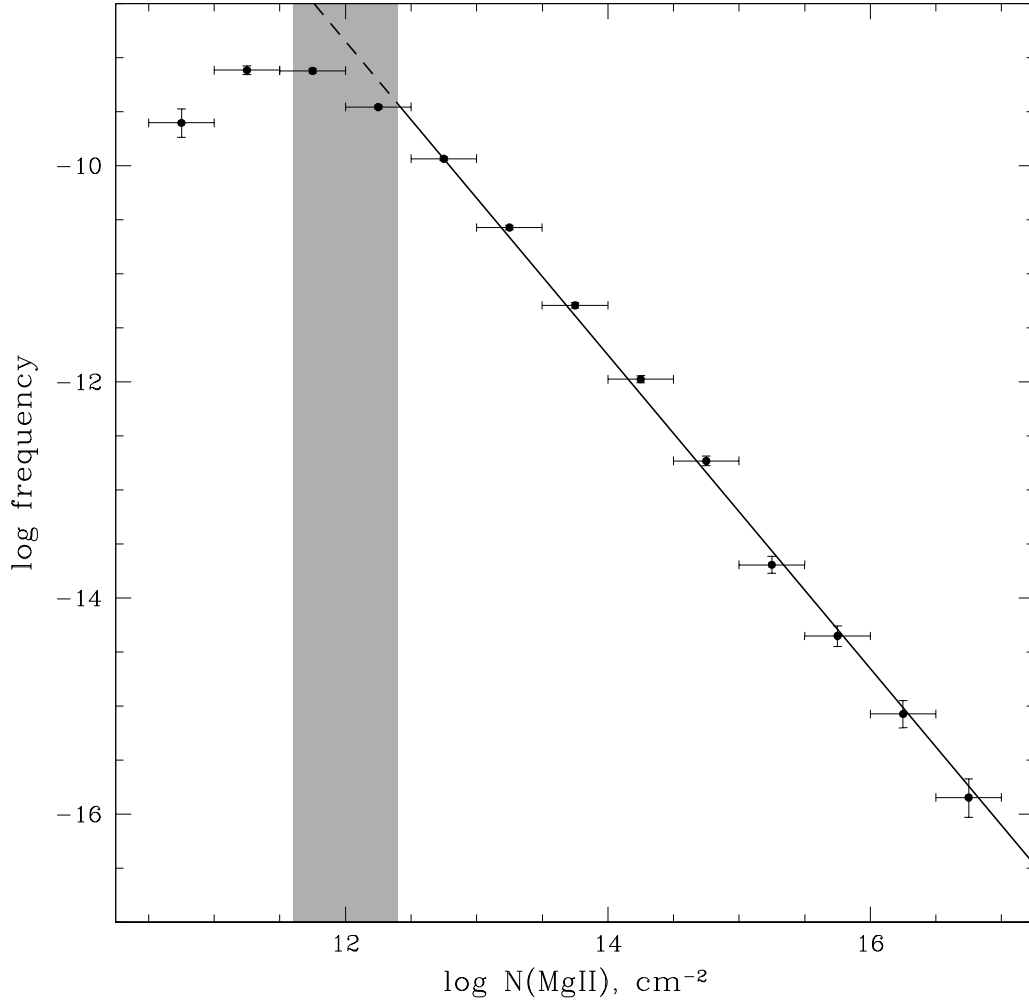


Figure 4.3 The logarithmic VP column density distribution. The shaded area indicates the region of partial completeness (see text). The solid sloped line plots the power law maximum likelihood fit, which was performed on all VP column densities of $\log N(\text{MgII}) > 12.4 \text{ cm}^{-2}$ and which resulted in a slope of $\delta = 1.45 \pm 0.01$. The dashed sloped line shows the fit extended to lower column densities for comparison with the data.

The column density distribution can be fit by a power law, which takes the form

$$f(N) = CN^{-\delta}, \quad (4.11)$$

where $f(N)$ is the number of clouds with column density N per unit column density, C is a normalization constant and δ is the power law slope. The maximum likelihood method was used to obtain the power law fit to the unbinned data. The fit was performed only on column densities above the region of partial completeness ($\log N(\text{MgII}) > 12.4 \text{ cm}^{-2}$) so as not to skew it to an artificially shallower slope. Our result for the power law slope was $\delta = 1.45 \pm 0.01$. In a study of 14 MgII systems containing 33 VP components, Petitjean & Bergeron (1990) obtained a significantly shallower slope of $\delta = 1.0 \pm 0.1$, although their spectral resolution was lower. In a study with comparable resolution to ours, Churchill et al. (2003) obtained $\delta = 1.59 \pm 0.05$ by fitting their sample of 175 VP components in 23 MgII systems. This result agrees closely with our column density distribution fit.

4.4.3 Doppler Parameter Distribution

The MgII Doppler b parameter distribution of VP components is shown in Figure 4.4. The median Doppler parameters and standard deviations are $4.5 \pm 3.5 \text{ km s}^{-1}$, $6.0 \pm 4.5 \text{ km s}^{-1}$, and $5.7 \pm 4.4 \text{ km s}^{-1}$ for the weak, strong, and full samples, respectively. Churchill (1997) found a median Doppler parameter of $\sim 3.5 \text{ km s}^{-1}$ in a study of 48 MgII systems and Churchill et al. (2003) found 5.4 ± 4.3 in a study of 23 MgII systems; in both cases the data were of comparable quality. Petitjean & Bergeron (1990) found

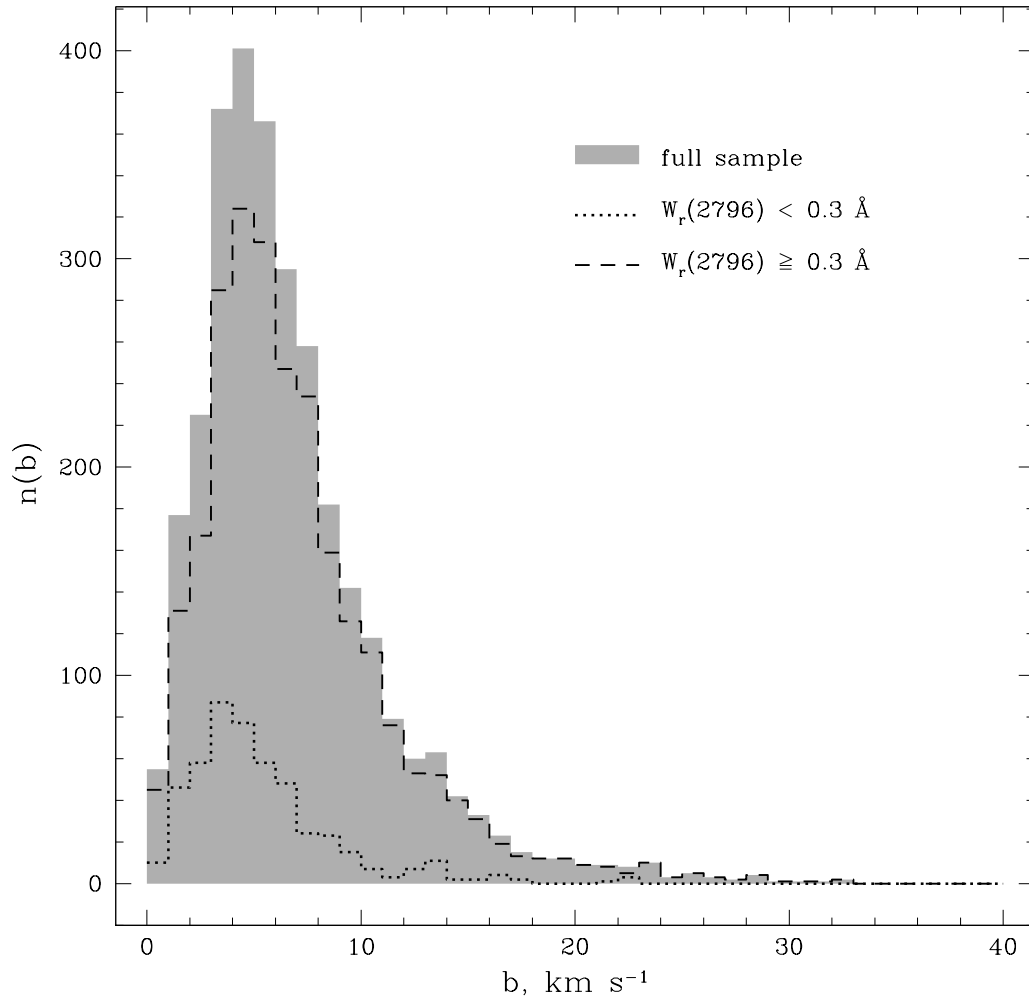


Figure 4.4 The Doppler parameter distribution of VP components for $W_r(2796) < 0.3 \text{ \AA}$, $W_r(2796) \geq 0.3 \text{ \AA}$, and the full sample.

in their study of 14 MgII systems that the b distribution peaked between 10 and 15 km s⁻¹; however, they were limited by an inferior spectral resolution of 30 km s⁻¹ and noted that this significantly distorted the observed distribution. The authors' high Doppler parameter results led them to conclude that a significant turbulent component was broadening the lines, since a purely thermal b would correspond to temperatures too high for MgII to exist.

Based on simulations (Churchill et al., 2003), our observed distribution peak, the bin centered at 4.5 km s⁻¹ for the full sample, is likely $\sim 1\text{--}2$ km s⁻¹ too high relative to the true distribution. In addition, the distribution tail at high b values has been shown in these simulations to be an artifact of component blending. As mentioned in § 4.4.1, $\sim 30\%$ of simulated components are not recovered in the VP decomposition for our spectral quality. As a result, some b parameters in the observed distribution are too broad compared to the true distribution due to compensation for loss of some components, e.g. in saturated profiles where VP component parameters are not well constrained.

If the Doppler broadening is assumed to be purely thermal, then the observed b parameter distribution medians correspond to gas temperatures of $\sim 30,000$ K, $\sim 53,000$ K, and $\sim 47,000$ K for the weak, strong, and full samples, respectively. However, applying the $1\text{--}2$ km s⁻¹ correction to the b parameter would produce, in the case of the full sample, a median temperature of $\sim 20,000 - 32,000$ K; in the weak sample, $\sim 9,000 - 18,000$ K; and in the strong sample, $\sim 23,000 - 37,000$ K. Figure 4.4 reveals

that the high b tail of the distribution is heavily dominated by strong systems, leading to the higher temperature prediction for this subsample; when components having $b > 10$ are excluded, and using the simulation correction to the median, the median temperature of the strong sample becomes $\sim 18,000 - 26,000$ K. Thus, there is no evidence of a significant difference in temperature conditions between the weak and strong MgII system populations. In addition, contrary to the conclusion of Petitjean & Bergeron (1990), we do not believe there is a significant turbulent component to the Doppler parameter.

4.4.4 Cloud-Cloud Velocity Clustering

The velocity two-point correlation function (TPCF) is the probability that any randomly selected pair of VP components within a system will have a particular velocity difference Δv . Our velocity TPCF is shown in Figure 4.5. This probability distribution is commonly fit with Gaussian components that have the functional form

$$f_n = \frac{1}{\sqrt{2\pi}} \frac{a_n}{\sigma_n} e^{-\frac{(\Delta v)^2}{2\sigma_n^2}}, \quad (4.12)$$

where for the n th component a_n is a scaling factor and σ_n is the dispersion. The amplitude of the component is then

$$A_n = \frac{1}{\sqrt{2\pi}} \frac{a_n}{\sigma_n}. \quad (4.13)$$

Petitjean & Bergeron (1990) and Churchill et al. (2003), in their studies of 14 and 23 MgII absorption systems respectively, fit their TPCF distributions of VP components

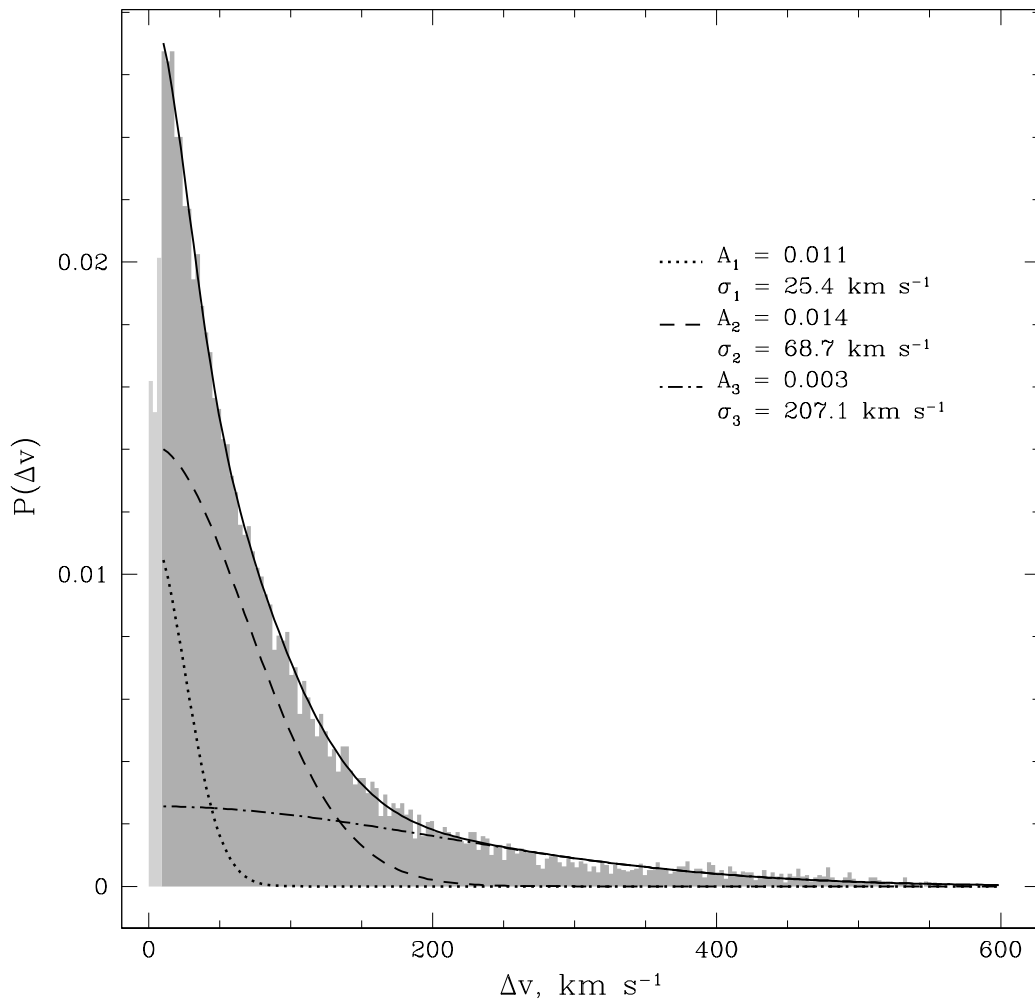


Figure 4.5 The VP component velocity two-point correlation function is shown in gray; velocity separations Δv are plotted in 3 km s^{-1} bins. The dotted, dashed and dot-dashed curves represent components 1, 2 and 3 of the Gaussian fit, respectively; the solid curve is their total. Data for which $\Delta v < 10 \text{ km s}^{-1}$ is shown in lighter gray; this data was not included in the fit. A values represent the Gaussian component amplitudes, and σ values the component dispersions.

using two-component Gaussian models. The dispersion results of Petitjean & Bergeron (1990) were 80 km s^{-1} and 390 km s^{-1} . The authors attributed the narrower of these two components to motions within galaxies, and the broader to the motions of galaxy pairs. However, the Churchill et al. (2003) study, which had superior spectral resolution and drew upon more lines of sight, calculated best fit dispersions of 54 km s^{-1} and 166 km s^{-1} ; the much larger result of the earlier study is believed to be an effect of the lower resolution, which prevented identification of small velocity separations. They suggested that velocity dispersions ranging from face-on vertical dispersion in galaxy disks to edge-on rotational motion might be accounting for the observed TPCF and thus MgII absorption.

We have chosen to fit our TPCF with three Gaussian components; the results are plotted over the data in Figure 4.5. Three components were used because two did not adequately fit the extended tail of our distribution. This fit resulted in velocity dispersions of 25.4 km s^{-1} , 68.7 km s^{-1} , and 207.1 km s^{-1} , with amplitudes of 0.011, 0.014, and 0.003, respectively. Velocity separations of $< 10 \text{ km s}^{-1}$ are shown as lighter gray bins; these data were excluded from the fit because their relative numbers have been artificially lowered due to VP component blending at small Δv .

To assign a specific physical phenomenon to each Gaussian component would seem to be an oversimplification, especially since three components were needed to fit our data. It is, however, a convenient parameterization that aids in characterizing the scale of VP component velocity clustering. For any two components within a MgII

system, the Gaussian fit gives the probability that the pair will have a given velocity separation. Small velocity separations are the most probable and the fit drops steeply up to $\Delta v \sim 150 \text{ km s}^{-1}$; at larger separations the probability decreases more slowly to our maximum separation of $\Delta v = 572.8 \text{ km s}^{-1}$.

5 REDSHIFT EVOLUTION

5.1 Evolution of Strong MgII Systems

In order to study evolution in MgII absorption systems having equivalent widths $W_r(2796) \geq 0.3 \text{ \AA}$, i.e. strong systems, their flux decrements per pixel can be binned by absorption redshift, system equivalent width, and pixel velocity and the resulting cumulative distributions compared. This provides information about the relative system optical depths and the kinematic extents of the absorption and how these have changed through cosmic time.

The flux decrement in each pixel was measured in every equivalent width region (defined in § 3.1) in every MgII system in our sample for the $\lambda 2796$ feature. Pixels having decrements consistent with 1.0, i.e. saturated pixels, were assigned flux decrements of exactly 1.0, since their actual flux decrements vary about one due to noise. Pixels that were masked from the Voigt profile fits (see § 4.3.2) were omitted from the pixel sample.

We chose our absorption redshift binning, as in § 2.7, to match the redshift bins of Nestor et al. (2005). The pixels were binned according to $0.336 \leq z < 0.871$, $0.871 \leq z < 1.311$, and $1.311 \leq z < 2.269$ (hereafter the low, medium and high redshift samples). The pixels were further divided into equivalent width bins of $0.3 \leq W_r(2796) < 0.6 \text{ \AA}$, $0.6 \leq W_r(2796) < 1.0 \text{ \AA}$, $1.0 \leq W_r(2796) < 2.0 \text{ \AA}$, and $W_r(2796) \geq 2.0 \text{ \AA}$; this allows us to determine whether there is differential evolution based on

absorption strength. Finally, the pixels were also binned according to their velocities to examine kinematic evolution with redshift. The method of measuring the relative pixel velocities was discussed in § 3.3.

The cumulative distributions of the resulting flux decrement samples are shown in Figures 5.1 - 5.4. Each panel plots the low, medium and high redshift distributions for a given equivalent width and velocity range.

The Kolmogorov-Smirnov (K-S) statistical test was used to quantitatively compare the three distributions within each panel. In each case the test was performed on the low and medium redshift samples; the medium and high redshift samples; and the low and high redshift samples. This resulted in a $P(K - S)$ statistic, a measure of the equality of two samples, for each pair. The quantity $1 - P(K - S)$ is the confidence level that the two samples are not drawn from the same population; the results are noted in each panel. Ellipses indicate that no data existed for the given redshift, equivalent width and velocity bin. For all panels for which $W_r(2796) \geq 2.0 \text{ \AA}$, we chose not to perform the K-S test between the low and medium redshifts and between the medium and high redshifts because the medium redshift bin contained only four absorption systems. The medium redshift data for these panels is still shown, but this distribution is not believed to be as robust as the others.

For this study we consider two samples to be statistically different if the confidence level resulting from the K-S test exceeds 3σ . For test results of less than 3σ significance, the actual quantity $1 - P(K - S)$ is noted; otherwise the confidence level is noted in

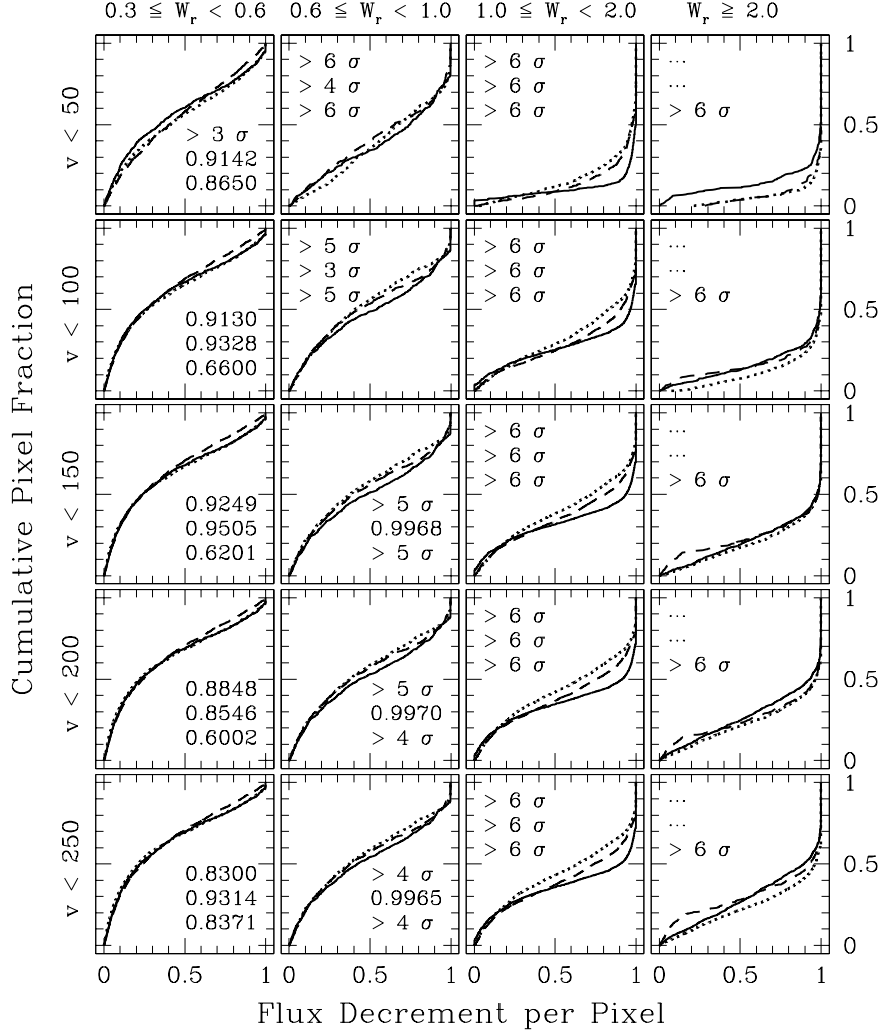


Figure 5.1 The MgII $\lambda 2796$ flux decrement per pixel distribution. The data is binned from left to right across panels by the rest equivalent width of the MgII system in \AA , and from top to bottom by the velocity range of the pixels in km s^{-1} . The solid, dashed and dotted lines trace the low, medium and high absorption redshifts, respectively; these bins are defined as $0.366 \leq z < 0.871$, $0.871 \leq z < 1.311$, and $1.311 \leq z < 2.269$. The confidence levels resulting from $K - S$ testing are shown from top to bottom in each panel for the low to medium redshift, medium to high redshift, and low to high redshift comparisons, respectively.

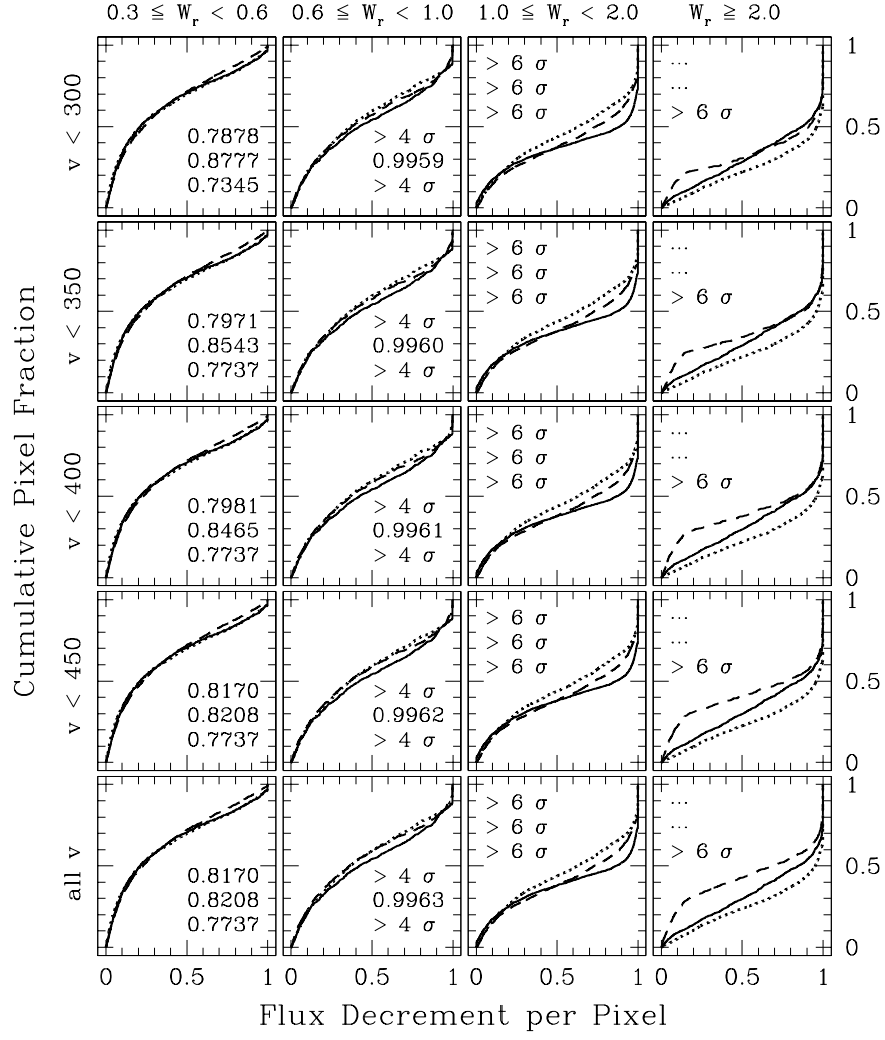


Figure 5.2 Same as in Figure 5.1.

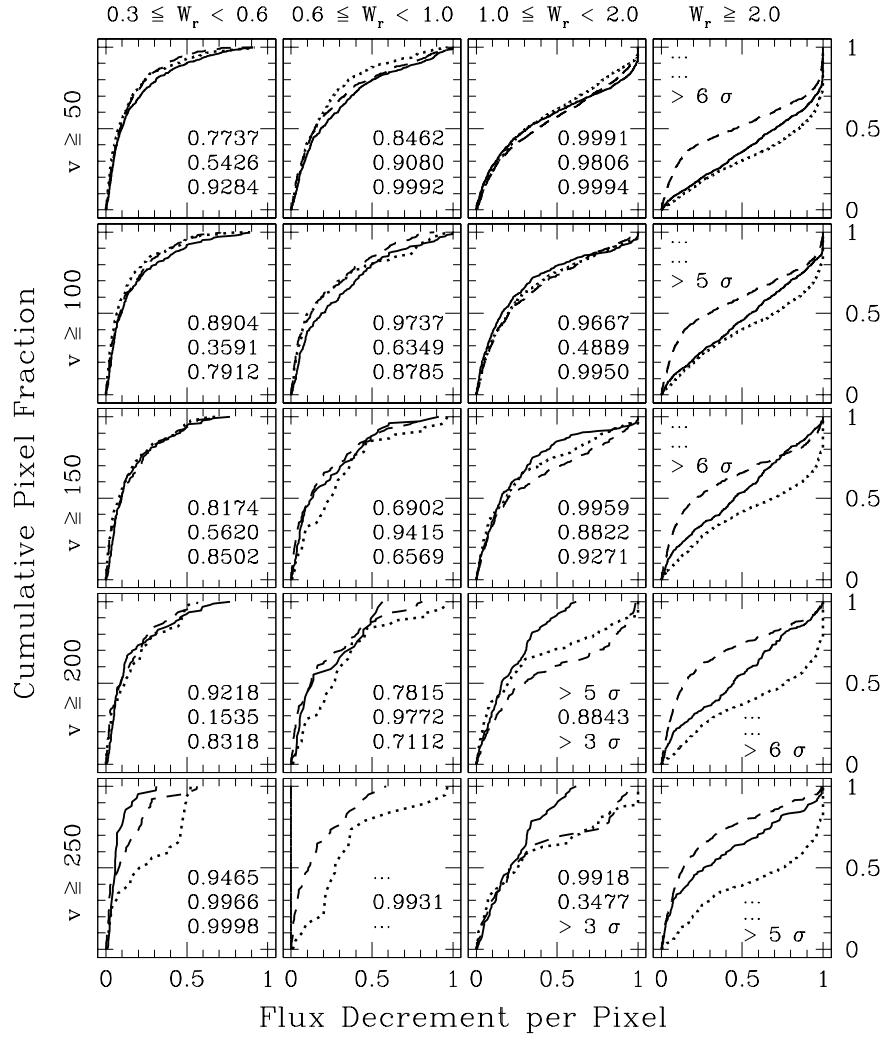


Figure 5.3 Same as in Figure 5.1.

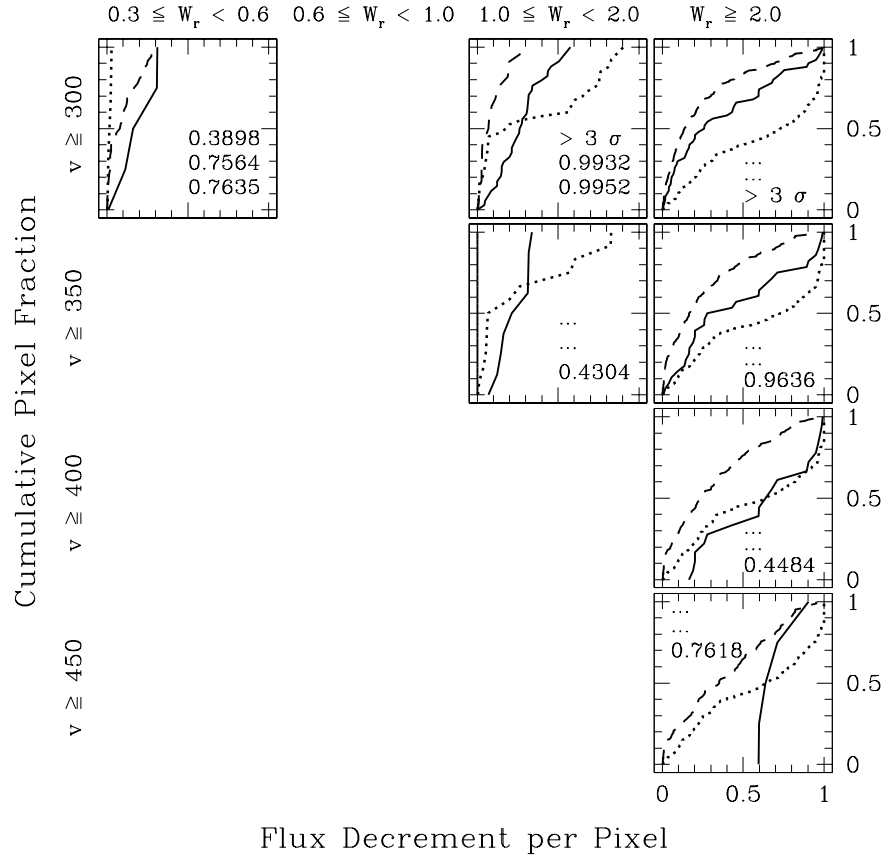


Figure 5.4 Same as in Figure 5.1. Panels containing no data were omitted.

terms of σ significance.

Figures 5.1 and 5.2 show the flux decrement distributions, from top to bottom panels, over increasingly large velocity windows. The top row includes only those pixels for which the velocity is within $\pm 50 \text{ km s}^{-1}$, the next row for which it is within $\pm 100 \text{ km s}^{-1}$, and so on. The distributions are plotted in this manner up to $\pm 450 \text{ km s}^{-1}$, and finally for the entire velocity window. In general these samples change less and less as the velocity window grows because most of the absorbing pixels are concentrated near the profile center. This is especially true of the $0.3 \leq W_r(2796) < 0.6 \text{ \AA}$ sample, the lowest equivalent width bin.

In contrast, Figures 5.3 and 5.4 show the flux decrement distributions, from top to bottom panels, over progressively smaller velocity ranges. Instead of plotting the distributions of pixels in the central portions of the absorption profiles as in the previous two figures, here we have plotted the distributions of pixels having velocities greater than some minimum velocity. The first row of panels includes only pixels for which the velocity is at least 50 km s^{-1} away from the zero point, the next row for which the velocity is at least 100 km s^{-1} away, and so on up to $v \geq 450 \text{ km s}^{-1}$. In this velocity bin only the strongest systems, those having $W_r(2796) \geq 2.0 \text{ \AA}$, contain any absorption and therefore they were the only distributions shown. A number of panels in the $v \geq 300 \text{ km s}^{-1}$ or greater bins contained no absorbing pixels and were omitted. While Figures 5.1 and 5.2 show the distributions of pixels within a given velocity, Figures 5.3 and 5.4 show the distributions of pixels outside of a given velocity. Therefore, especially in the

lower equivalent width bins, distributions may not contain any pixels once the higher velocity cutoffs are reached.

For the $0.3 \leq W_r(2796) < 0.6 \text{ \AA}$ sample, there is for the most part no statistically significant evolution in the flux decrements except in the case of low to medium redshift pixels having $v < 50 \text{ km s}^{-1}$, in which case there is evolution at the 3σ level. The low redshift distribution rises more steeply than the medium, indicating that the low redshift systems tend to have weaker absorption within this velocity range than they do at medium redshift.

The next strongest sample, having equivalent widths of $0.6 \leq W_r(2796) < 1.0 \text{ \AA}$, contains statistically significant flux decrement evolution for all velocity ranges in Figures 5.1 and 5.2, i.e., the inner pixels of the absorption profiles. For $v < 50 \text{ km s}^{-1}$ and $v < 100 \text{ km s}^{-1}$, these systems evolve between low and medium redshifts, between medium and high redshifts, and between low and high redshifts. Over larger velocity windows significant evolution occurs between the low and medium redshifts and between the low and high redshifts. The evolution is such that the medium redshift distribution rises the most steeply in the smallest velocity ($v < 50 \text{ km s}^{-1}$) window, meaning it has the shallowest absorption of the three redshift bins in the profile cores; but in all larger velocity windows, the high redshift distributions rise the most steeply, implying that the absorption in any given pixel tends to be shallower than in the other two redshift bins. In contrast, the low redshift sample in this equivalent width range rises the most slowly. These profiles are as a group the most kinematically concentrated

of the three.

These trends are continued in a more pronounced fashion in the next largest equivalent width range, $1.0 \leq W_r(2796) < 2.0 \text{ \AA}$. As expected, the flux decrement distributions of these stronger absorption systems rise more slowly than those of the weaker systems; this is due to the stronger profiles being more frequently saturated or nearly saturated over larger velocity ranges in all three redshift bins than the weaker profiles. Among the three redshift ranges in this equivalent width sample, evolution is found at the 6σ level for all the inner velocity distributions. As noted for the $0.6 \leq W_r(2796) < 1.0 \text{ \AA}$ sample, the low redshift distributions rise the least rapidly in all of these velocity windows, and the high redshift distributions the most rapidly, indicating that a greater proportion of the absorbing pixels in the former are strongly decremented than in the latter.

It is also in this equivalent width bin that we begin to see significant evolution in the panels of Figures 5.3 and 5.4, i.e., the outer pixels of the absorption profiles. In the range $v \geq 200 \text{ km s}^{-1}$ there is evolution between the low and medium redshift samples and between the low and high redshift samples at the 5σ and 3σ levels, respectively; in the range $v \geq 250 \text{ km s}^{-1}$ there is evolution between the low and high redshift samples at the 3σ level; and in the range $v \geq 300 \text{ km s}^{-1}$ there is evolution between the low and medium redshift samples at the 3σ level. At these high velocities there are fewer absorbing pixels in general; however, what pixels there are show a very different trend than those in the inner velocity distributions. The outer velocity distributions allow

us to isolate and scrutinize absorption trends in the wings of the profiles. Here we see that the low redshift distributions in the higher velocity cutoff panels rise much more steeply than those of the medium and high redshifts, which tells us that in the outer portions of low redshift profiles, absorption in equivalent width regions is on the whole weaker per pixel.

For the strongest MgII absorption bin, i.e. $W_r(2796) \geq 2.0 \text{ \AA}$, we have chosen to compare only the low and high redshift samples due to the small sample size of the medium redshift sample of only four systems. However, between the low and high redshift bins, as in the $1.0 \leq W_r(2796) < 2.0 \text{ \AA}$ sample, there is strong evidence for evolution. In the inner velocity distributions, the high and low redshift distributions differ to a 6σ significance level at all velocity cutoffs. The trend is for the low redshift distribution to rise more rapidly than that of the high redshift; this is due to the tendency of the low redshift profiles to have shallower absorption within a given velocity window than the high redshift profiles.

In these strongest systems there is also statistically significant evolution between the low and high redshift samples in all of the outer velocity distributions up to the $v \geq 300 \text{ km s}^{-1}$ bin; at greater velocity cutoffs there are not enough absorbing pixels to yield significant K-S test results. As in the distributions for the outer velocity bins for the $1.0 \leq W_r(2796) < 2.0 \text{ \AA}$ sample, in the strongest equivalent width regime we also see the low redshift distributions rising more steeply than the high redshift ones due to the pixels in the wings of the low redshift profiles containing, on average, weaker

absorption than those in the high redshift profiles. This effect is believed to result from the tendency of the strong low redshift profiles to exhibit more asymmetry than the strong high redshift profiles, and thus to have more kinematically extended partial flux decrements. This will be discussed further in § 6.

5.2 Evolution of Weak MgII Systems

5.2.1 Calculation of the Redshift Path Sensitivity

The redshift sensitivity function $g(W_r, z)$ (see Lanzetta et al., 1987; Steidel & Sargent, 1992), first introduced in § 2.3.2 and shown in Figure 2.5, is the number of lines of sight along which an absorption feature with rest frame equivalent width of at least W_r and at redshift z could have been detected. The sensitivity function must be taken into account particularly to study the weak systems, since there is a certain equivalent width cutoff at any given point in a spectrum below which the weakest systems are lost in the noise. We have also modified the function to account for the effect of the doublet ratio DR in calculating the redshift path, which is especially important for weak absorbers since their MgII $\lambda 2803$ strengths are often approximately half that of their MgII $\lambda 2796$ strengths (i.e., $DR \simeq 2$). The redshift sensitivity function of the j th rest equivalent width, k th redshift interval, and i th doublet ratio can be written

$$g(W_{r,j}, z_k, DR_i) = \sum_n H(z_k - z_{min,n}) H(z_{max,n} - z_k) H(W_{r,j} - N_\sigma \sigma_{W,k}) H\left(\frac{W_{r,j}}{DR_i} - N'_\sigma \sigma'_{W,k}\right) \quad (5.1)$$

where H is the Heaviside step function; n is the index of the quasar; $z_{min,n}$ is the redshift of either the observed wavelength of the $\text{Ly}\alpha$ emission or the shortest observed wavelength, whichever is larger; $z_{max,n}$ is the redshift of either the wavelength corresponding to $5,000 \text{ km s}^{-1}$ blueward of the MgII emission or the longest observed wavelength, whichever is smaller; N_σ is the significance level of the $\lambda 2796$ detection; $\sigma_{W,k}$ is the rest frame detection limit in the $\lambda 2796$ pixel; N'_σ is the significance level of the $\lambda 2803$ detection; and $\sigma'_{W,k}$ is the rest frame detection limit in the $\lambda 2803$ pixel. H is defined as being equal to 1 when its argument is nonnegative and 0 when its argument is negative. The function $g(W_r, z, DR)$ reveals over which equivalent widths and redshifts the survey is most sensitive.

5.2.2 Cumulative Redshift Path and Survey Completeness

The cumulative redshift path $Z(W_{r,lim}, DR)$ is the total redshift coverage of the survey for some minimum rest frame equivalent width and MgII doublet ratio. It can be expressed as

$$Z(W_{r,lim}, DR) = \int_{z_1}^{z_2} g(W_{r,lim}, z, DR) dz \quad (5.2)$$

where $g(W_{r,lim}, z, DR)$ is the redshift sensitivity function modified from the technique of Lanzetta et al. (1987) (see Churchill et al. (1999)) to include the effect of the $\text{MgII } \lambda\lambda 2796, 2803$ doublet ratio, since this quantity varies from $1 \leq DR \leq 2$ in the weak regime and has a nonnegligible effect on the cumulative redshift path at very small $W_{r,lim}$. The dependence of the cumulative redshift path on $W_{r,lim}$ is useful in

considering the completeness of the survey. This relationship is shown in Figure 5.5 for three different redshift intervals: $0.1 < z < 2.6$, the full redshift range of our survey; $0.4 < z < 2.4$, the range of the Narayanan et al. (2007) survey; and $0.4 < z < 1.4$, the range of the Churchill et al. (1999) survey. These studies represent the largest two previous weak MgII surveys and will serve as our basis for comparison; both used quasar spectra with the same resolution and signal-to-noise ranges. Curves are also plotted for $DR = 1$ and $DR = 2$, the limiting doublet ratio cases. For our full redshift range, the cumulative redshift path reaches $\Delta Z \sim 230.8$; for $0.4 < z < 2.4$, $\Delta Z \sim 213.2$, compared to $\Delta Z \sim 77.3$ for Narayanan et al. (2007); and for $0.4 < z < 1.4$, our survey covers a cumulative redshift path of $\Delta Z \sim 147.9$, compared to $\Delta Z \sim 17.2$ for Churchill et al. (1999). The larger cumulative redshift paths of our survey in each redshift range compared to that of previous works reflect the proportionately larger number of lines of sight in our survey. Churchill et al. (1999) surveyed 26 HIRES quasar spectra and found 30 weak MgII systems, while Narayanan et al. (2007) surveyed 81 UVES quasar spectra and found 112 weak MgII systems.

For $DR = 2$, the more relevant ratio when considering weak systems and the most conservative when calculating the cumulative redshift path, our survey is 76% complete to $W_{r,lim} = 0.02 \text{ \AA}$. This means that a system of rest equivalent width 0.02 \AA could have been detected in 76% of the total spectral coverage. Similarly, our survey completeness levels for the redshift ranges $0.4 < z < 2.4$ and $0.4 < z < 1.4$ are both 78%.

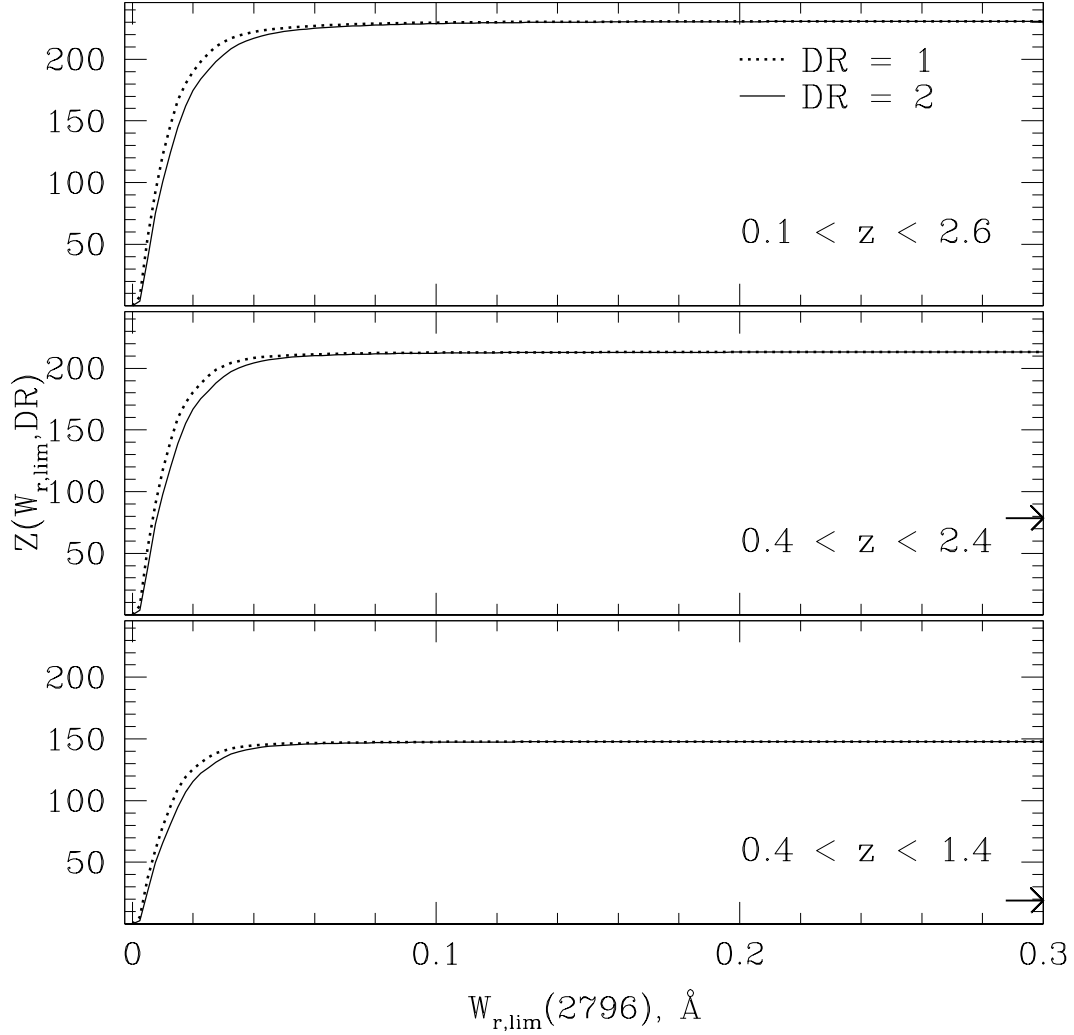


Figure 5.5 The cumulative redshift path as a function of the rest equivalent width limit $W_{r,lim}$. The top panel corresponds to the full redshift range of our survey; the middle panel to the range of Narayanan et al. (2007); and the bottom panel to the range of Churchill et al. (1999). The dotted lines indicate the cumulative redshift path for a MgII doublet ratio of 1, and the solid lines for a doublet ratio of 2. For reference, the cumulative redshift path of the Narayanan et al. (2007) survey at $W_{r,lim} = 0.3 \text{ \AA}$ is indicated in the middle panel with an arrow ($\Delta Z \sim 77.3$). Similarly, $\Delta Z \sim 17.2$ for the Churchill et al. (1999) survey is indicated in the lower panel.

5.2.3 Number of Absorbers per Unit Redshift

Since this survey is unbiased for weak MgII absorption and has the sensitivity to detect systems down to $W_r(2796) < 0.02 \text{ \AA}$, the evolution of these systems with cosmic time can be studied. The redshift number density is the number of absorbers per unit redshift, dN/dz , and is the product of the proper number density of absorbers and the proper geometric absorber cross section. It is a key quantity in determining whether the number of MgII systems is evolving, which in turn can yield clues about galaxy evolution.

The no-evolution expectation (NEE) for the redshift number density can be parameterized as:

$$\left(\frac{dN}{dz}\right)_{NEE} = \frac{c}{H_0} n_0 \sigma_0 \frac{(1+z)^2}{\sqrt{\Omega_m(1+z)^3 + \Omega_\Lambda}} \quad (5.3)$$

where c is the speed of light, H_0 is the Hubble constant, n_0 is the proper number density of absorbers in the current epoch, σ_0 is the proper geometric absorber cross section in the current epoch, and Ω_m and Ω_Λ are cosmological parameters. By assuming a functional form for dN/dz , its behavior with redshift can be studied and compared to the NEE.

In practice, the quantity dN/dz is calculated as the sum of the reciprocal of the cumulative redshift path lengths over all systems in the sample:

$$\frac{dN}{dz} = \sum_i^{N_{sys}} [Z(W_i, DR_i)]^{-1}. \quad (5.4)$$

The path length $Z(W_i, DR_i)$ thus represents the redshift coverage of the survey over

which system i of rest equivalent width W_i and doublet ratio DR_i could have been detected. The variance in dN/dz is

$$\sigma_{dN/dz}^2 = \sum_i^{N_{sys}} [Z(W_i, DR_i)]^{-2}. \quad (5.5)$$

We calculated dN/dz for four redshift bins in order to facilitate comparison with the works of Churchill et al. (1999) and Narayanan et al. (2007); the result is shown in Figure 5.6. The bins are $0.4 \leq z < 0.7$, $0.7 \leq z < 1.0$, $1.0 \leq z < 1.4$, and $1.4 \leq z < 2.4$. The results of the previous works are also plotted. The dashed line represents the NEE, the case in which the product $n(z)\sigma(z)$ is constant throughout cosmic time. This curve was normalized to the average absorption redshift, 1.122, of our weak $0.4 < z < 2.4$ sample and to our overall dN/dz within this redshift range, 0.85. In addition, a concordance model was assumed for the cosmological parameter values, i.e. $\Omega_m = 0.3$ and $\Omega_\Lambda = 0.7$.

Churchill et al. (1999) found dN/dz to be consistent with no evolution over the redshift range $0.4 \leq z \leq 1.4$, with $dN/dz = 1.74 \pm 0.10$ over that range. In contrast, Narayanan et al. (2007) found evidence for evolution, with the number of absorbers per unit redshift peaking at $z = 1.2$ with a value of 1.76 ± 0.08 . This would imply that the absorber number density and/or cross section are evolving with redshift.

We also find dN/dz to be inconsistent with a nonevolving population, though our distribution peaks in the bin centered at $z = 0.85$ with a value of 1.08 ± 0.02 . Our overall distribution is also significantly lower than either of the two previous works.

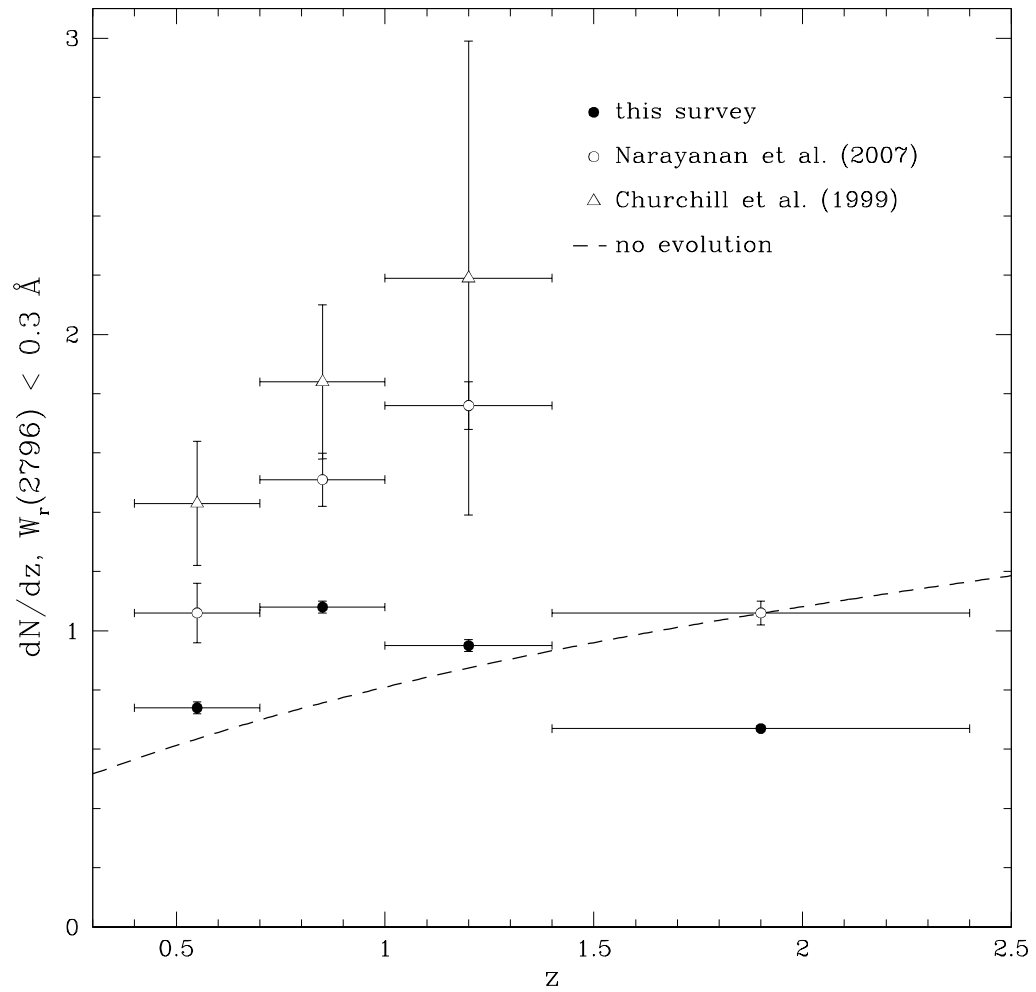


Figure 5.6 The number of weak absorbers per unit redshift over the range $0.4 < z < 2.4$ for this survey, Narayanan et al. (2007), and Churchill et al. (1999). The dashed line represents the no-evolution expectation (see text).

There are several possibilities which could explain why our dN/dz values are lower than the two comparable previous works. The first to consider is the search method by which weak MgII systems are identified in the spectra. However, all three studies used virtually the same search software. Though the software has been updated to improve the ease of use, the same algorithm (see § 2.4) was employed in all three studies.

Another factor which would lower the dN/dz results of this study would be systematically larger redshift path lengths for each weak MgII system. However, our redshift path lengths would, in the example of the first bin in Figure 5.6 centered at $z = 0.55$, have to be decreased by 30% to equal the dN/dz value of Narayanan et al. (2007), and by 48% to equal the dN/dz value of Churchill et al. (1999). This is an extremely large decrease, and since both of these studies also employed the same methodology for calculating the redshift path that was discussed in § 5.2.2, such a significant discrepancy seems implausible.

Since we believe our search algorithm and redshift path lengths are not only robust, but consistent in methodology with the previous two comparable weak MgII studies, we conclude that it is the difference in quasar spectrum selection which results in inconsistent dN/dz results. The Churchill et al. (1999) study, the smallest of the three, used quasar spectra selected because the quasars were the brightest available. The Narayanan et al. (2007) study, the next largest, was also biased in its line of sight selection toward brighter quasars in an effort to increase the signal-to-noise of the survey, although the bias was diluted compared to that of Churchill et al. (1999).

Our study contains the most lines of sight by a factor of three, and comprises the spectra of quasars that were not selected for their brightness. It is possible that quasar brightness is correlated with the incidence of weak MgII absorption. Even though all three surveys cut off their search 5,000 km s⁻¹ blueward of the quasar emission, it is conceivable that extremely high velocity quasar ejecta containing MgII absorbing gas could leave its signature in the spectra. It is possible that such ejecta might be more commonly associated with brighter quasars and thus the previous two surveys could be more contaminated with these types of systems. The overall trend in dN/dz is downward with increasing survey size; future works with surveys unbiased for quasar brightness may be able to confirm our dN/dz results. In addition, future work could include segregating our quasar spectra according to brightness and calculating and comparing the dN/dz results of these subsets.

The weak MgII dN/dz for this study is also plotted in the left panel of Figure 5.7. The four bins of Figure 5.6 are replotted here with white circles. The black circles represent the dN/dz of the same population but in smaller redshift bins, and encompassing the full redshift range of this study of $0.1 < z < 2.6$. The dashed line again represents the NEE, but in this case it has been normalized to the average absorption redshift, 1.098, of our full weak sample and to our overall dN/dz within this redshift range, 0.83. With this binning, dN/dz appears to peak between $1 \lesssim z \lesssim 1.3$ at a value of ~ 1 . At lower redshifts the value hovers around ~ 0.85 , while at higher redshifts there is a sharp dropoff of weak MgII systems per unit redshift. Note that

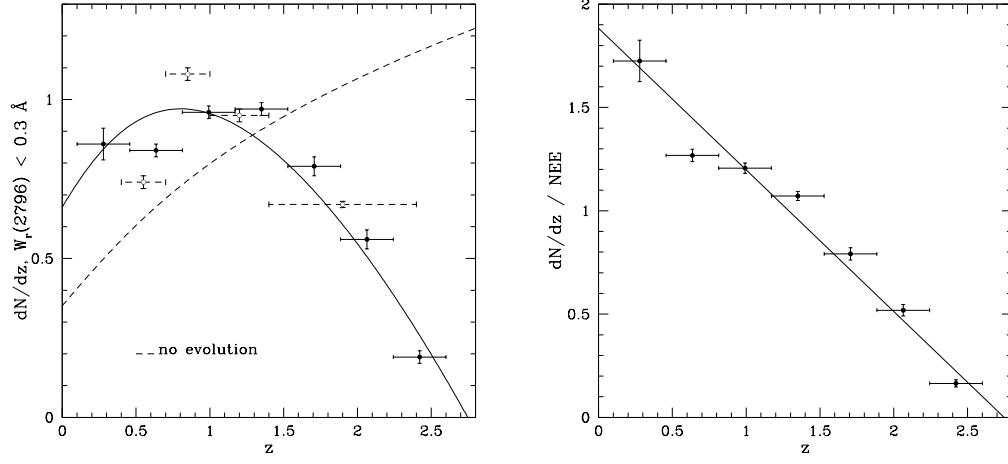


Figure 5.7 At left, the number of weak absorbers per unit redshift for this survey. The white circles represent the four bins of Figure 5.6 over the redshift range $0.4 < z < 2.4$. The black circles represent the same data in smaller bins and encompassing the total survey redshift range of $0.1 < z < 2.6$. The dashed curve is the no-evolution expectation (see text). The solid curve represents the best linear fit to the dN/dz to NEE ratio multiplied by the NEE. This ratio is plotted in the right panel; the solid line is also the linear fit.

this result predicts that there are no weak MgII systems above $z = 2.73$.

The redshift number density can be expressed in a similar manner to Equation 5.3

(the NEE):

$$\frac{dN}{dz} = \frac{c}{H_0} n(z) \sigma(z) \frac{(1+z)^2}{\sqrt{\Omega_m(1+z)^3 + \Omega_\Lambda}}. \quad (5.6)$$

This is the more general case in which n and σ vary as functions of redshift, and thus dN/dz can depart from the no-evolution expectation. The product $n(z)\sigma(z)$ can then be written as

$$n(z)\sigma(z) = n_0\sigma_0 f(z). \quad (5.7)$$

By substituting this into Equation 5.6, dividing it by Equation 5.3, and solving for

$f(z)$, we obtain

$$f(z) = \frac{\frac{dN}{dz}}{NEE} \quad (5.8)$$

The function $f(z)$ represents the dN/dz to NEE ratio, which allows us to study the behavior of dN/dz without the effects of cosmological expansion. The right panel of Figure 5.7 shows our dN/dz values divided by the NEE. The data clearly motivate a linear fit; this was achieved using a function of the form

$$f(z) = 1 - \alpha(z - z^*), \quad (5.9)$$

where α determines the slope and z^* determines the normalization of the function. We performed a linear fit to the data; the result is shown in the right panel of Figure 5.7. The resulting slope was -0.69 ± 0.02 and vertical intercept 1.88 ± 0.03 , corresponding to $\alpha = 0.69 \pm 0.02$ and $z^* = 1.29 \pm 0.05$.

Using this parameterization, the redshift number density can then be expressed as

$$\frac{dN}{dz} = [1 - \alpha(z - z^*)] \frac{c}{H_0} n_0 \sigma_0 \frac{(1+z)^2}{\sqrt{\Omega_m(1+z)^3 + \Omega_\Lambda}}, \quad (5.10)$$

where

$$n(z)\sigma(z) = n_0\sigma_0 [1 - \alpha(z - z^*)]. \quad (5.11)$$

We see that the product $n(z)\sigma(z)$ decreases linearly with redshift at a rate of 0.69 per unit z . Modeling is required to distinguish how the cosmic number density or geometric cross section, or both, evolve (see § 6.2).

6 CONCLUSION

We searched 252 HIRES and UVES quasar spectra and identified 469 MgII $\lambda\lambda 2796, 2803$ doublets in the range $0.1 < z < 2.6$ having $\langle z \rangle = 1.18$, of which 422 were included in the final sample after making the quality cut described in § 2.6.2. The spectra cover a cumulative redshift path of ~ 230.8 and are 76% complete to $W_r = 0.02 \text{ \AA}$ and $\sim 100\%$ complete to $W_r = 0.05 \text{ \AA}$. This constitutes the largest known sample of such high resolution ($R = 45,000$), high signal-to-noise (25 - 80) MgII absorption systems. 180 systems were classified as weak (having $W_r(2796) < 0.3 \text{ \AA}$) and 242 as strong (having $W_r(2796) \geq 0.3 \text{ \AA}$). An analysis was done of each system's absorption and kinematic properties, and Voigt profiles were modeled. Finally, the evolution of MgII systems with redshift was examined.

1. Although some spectra in the survey were selected based on the known presence of strong MgII absorption, our comparative analysis shows that our strong MgII sample is statistically not inconsistent at the 3σ level with the large (1,331 system) unbiased MgII sample of Nestor et al. (2005). This allows us to use our sample to study strong MgII evolution.
2. The distribution of weak MgII equivalent widths in the range $0.02 \leq W_r < 0.3 \text{ \AA}$ was fit with a power law having a slope of $\delta = 0.92 \pm 0.02$. We found no evidence of a turnover in the distribution down to the limit of our survey sensitivity.
3. Our weak MgII systems averaged total velocity widths of 88.7 km s^{-1} and velocity

spreads of 22.9 km s^{-1} . Our strong MgII systems averaged 247.1 km s^{-1} and 60.0 km s^{-1} for those two quantities.

4. The kinematic subsystems of strong MgII systems were segregated by velocity and their characteristics compared among velocity bins. The low velocity subsystems, having $\langle v \rangle \leq 40 \text{ km s}^{-1}$, tend to be the dominant subsystems and to contain the majority of the system absorption; our low velocity subsystem sample has an average equivalent width of 0.96 \AA and an average velocity spread of 39.7 km s^{-1} . The intermediate and high velocity subsystems, which have velocities of $40 < \langle v \rangle \leq 165 \text{ km s}^{-1}$ and $\langle v \rangle > 165 \text{ km s}^{-1}$, average equivalent widths of 0.29 and 0.20 \AA , and average velocity spreads of 19.5 and 14.6 km s^{-1} , respectively, representing relatively minor portions of the absorption in strong MgII systems.
5. Kinematic subsystems having subsystem velocities of $\langle v \rangle > 40 \text{ km s}^{-1}$ were compared to isolated weak MgII systems; superficially these two populations appear similar, but statistically they are very distinct. The kinematic subsystems exhibit systematically lower equivalent widths and systematically narrower velocity spreads than the isolated weak systems, such that it can be ruled out that the two samples were drawn from the same underlying distribution to 3σ and 6σ confidence levels, respectively. This suggests that weak systems are not necessarily associated with strong systems in which the line of sight failed to intersect the bulk of the absorbing gas.

6. The Voigt profile (VP) decomposition yielded a total of 2,989 components, with an average of 2.7 and 10.3 components being recovered for the weak and strong MgII samples, respectively. Simulations of MgII profiles indicate that due to a systematic loss of components in the modeling process, the average actual numbers of components was ~ 3.9 and ~ 14.7 for the weak and strong MgII samples, respectively. A linear fit to the equivalent width as a function of the number of clouds resulted in a slope of $0.116 \pm 0.003 \text{ \AA cloud}^{-1}$.
7. Fitting our VP component column density distribution over the range $12.4 \leq \log N(\text{MgII}) \leq 17.0 \text{ cm}^{-2}$ resulted in a power law slope of $\delta = 1.45 \pm 0.01$.
8. Under the assumption of thermal VP component broadening, our Doppler b parameter results, corrected to account for modeling artifacts, correspond to gas temperatures of $\sim 9,000 - 18,000 \text{ K}$ for the weak MgII sample and $\sim 18,000 - 26,000 \text{ K}$ for the strong sample.
9. Our velocity two-point correlation function (TPCF) was fit with a three-component Gaussian function having dispersions of $\sigma_1 = 25.4 \text{ km s}^{-1}$, $\sigma_2 = 68.7 \text{ km s}^{-1}$ and $\sigma_3 = 207.1 \text{ km s}^{-1}$. The TPCF gives the relative probability of a given velocity separation Δv occurring between two VP components within a MgII system. For our sample, the largest Δv was 572.8 km s^{-1} .
10. By studying the pixel flux decrement distributions of our strong MgII sample, we found significant kinematic evolution among our low, medium, and high redshift

subsamples ($0.366 \leq z < 0.871$, $0.871 \leq z < 1.311$, and $1.311 \leq z < 2.269$, respectively). The most pronounced kinematic evidence for evolution occurs in the strong MgII subset having $W_r \geq 1.0 \text{ \AA}$. The low redshift systems in this equivalent width range have systematically more strongly flux decremented pixels near the profile centers, and systematically shallower absorption in the outer portions of the profiles, than do their high redshift counterparts.

11. We analyzed our weak MgII sample to determine the number of absorbers per unit redshift, dN/dz , and found that it peaks between $1 \lesssim z \lesssim 1.3$ at a value of ~ 1 . The weak MgII dN/dz distribution differs significantly from the no-evolution expectation given by the most current cosmological model. The evolution of the product of the number density of absorbers and their geometric cross section, i.e. its dependence on z , varies linearly with z . The best fit to the data, parameterized as $n(z)\sigma(z) = n_0\sigma_0[1 - \alpha(z - z^*)]$, yielded $\alpha = 0.69 \pm 0.02$ and $z^* = 1.29 \pm 0.05$.

6.1 Strong MgII Systems

We investigated the kinematic changes with redshift in the population of strong MgII systems in § 5.1 and the significant statistical differences among our subsamples were described in detail. The studies of Steidel & Sargent (1992) and Nestor et al. (2005) concluded that the numbers per unit redshift dN/dz of $0.3 \leq W_r < 0.6 \text{ \AA}$ systems are nonevolving. In higher equivalent width regimes, they found that evolution with redshift becomes increasingly significant (for $W_r \gtrsim 1.0 \text{ \AA}$ and $W_r \gtrsim 2.0 \text{ \AA}$ in the

cases of Steidel & Sargent (1992) and Nestor et al. (2005), respectively). Their results regarding the numbers per unit redshift of strong systems indicated that the strongest systems diminish in number toward the present.

However, these studies were limited by their resolution in the types of analyses they could perform. Using our high resolution data, we measured flux decrements and kinematics as has never been done before for such a large sample and found that these, like dN/dz , also evolve in very strong ($W_r \gtrsim 1.0 \text{ \AA}$) MgII. Thus, this study complements, but is fundamentally different from, the previous works, which could not investigate kinematics in any detail due to the nature of the spectra that were used.

We find that systems having $W_r \geq 1.0 \text{ \AA}$ exhibit the most marked changes in pixel flux decrements across our three redshift bins of $0.366 \leq z < 0.871$, $0.871 \leq z < 1.311$, and $1.311 \leq z < 2.269$. In general we find that statistically, the low velocity absorption (near the cores) of our strong MgII profiles is stronger at lower redshifts, i.e. these regions are optically thicker than at high redshifts. In the higher velocity absorption regions, we find that on the whole the opposite is true; absorption per pixel is weaker at lower redshifts than at higher redshifts.

In order to facilitate interpretation of these quantitative results, we can also qualitatively evaluate systems in each equivalent width and redshift bin. We have created composite strong MgII absorption profiles by coadding the spectral windows encompassing each strong system. The result is shown in Figure 6.1. Only absorption within equivalent widths regions was included, and masked pixels (see § 4.3.2) were excluded.

In addition, we chose to coadd the pixel flux values according to their absolute velocity separation from the flux decrement-weighted zero point and then reflect the resulting profiles about $v = 0 \text{ km s}^{-1}$.

From these strong MgII “superprofiles,” we can visually assess and compare the essential characteristics of profiles at different redshifts. For the purposes of this discussion, we will focus on the $1.0 \leq W_r < 2.0 \text{ \AA}$ and $W_r \geq 2.0 \text{ \AA}$ equivalent width bins, where the most pronounced evolution is occurring. Also, the medium redshift $W_r \geq 2.0 \text{ \AA}$ sample contains only four systems; just as we chose not to perform the K-S test between this sample and the other two redshift bins in § 5.1, we would also caution that this composite profile is not as robust as the others due to the small sample size.

In the two strongest equivalent width bins, Figure 6.1 clearly illustrates kinematic evolution of the profiles. In both cases, the low redshift profiles exhibit saturated cores, while the central absorption regions of the high redshift profiles are slightly weaker. At the same time, outside the profile cores, the pixels contain systematically weaker absorption at lower redshift than at higher redshift. Most striking is the complex structure evident in the low redshift sample. The multitude of individually discernible kinematic components exhibited by these two profiles (the low redshift $1.0 \leq W_r < 2.0 \text{ \AA}$ and $W_r \geq 2.0 \text{ \AA}$ cases) is lacking in their high redshift counterparts.

Strong MgII absorption is known to often, though not always, be associated with bright galaxies, and there are many instances of a specific galaxy being associated with a known MgII system (see e.g. Kacprzak et al., 2008). In addition, it has been

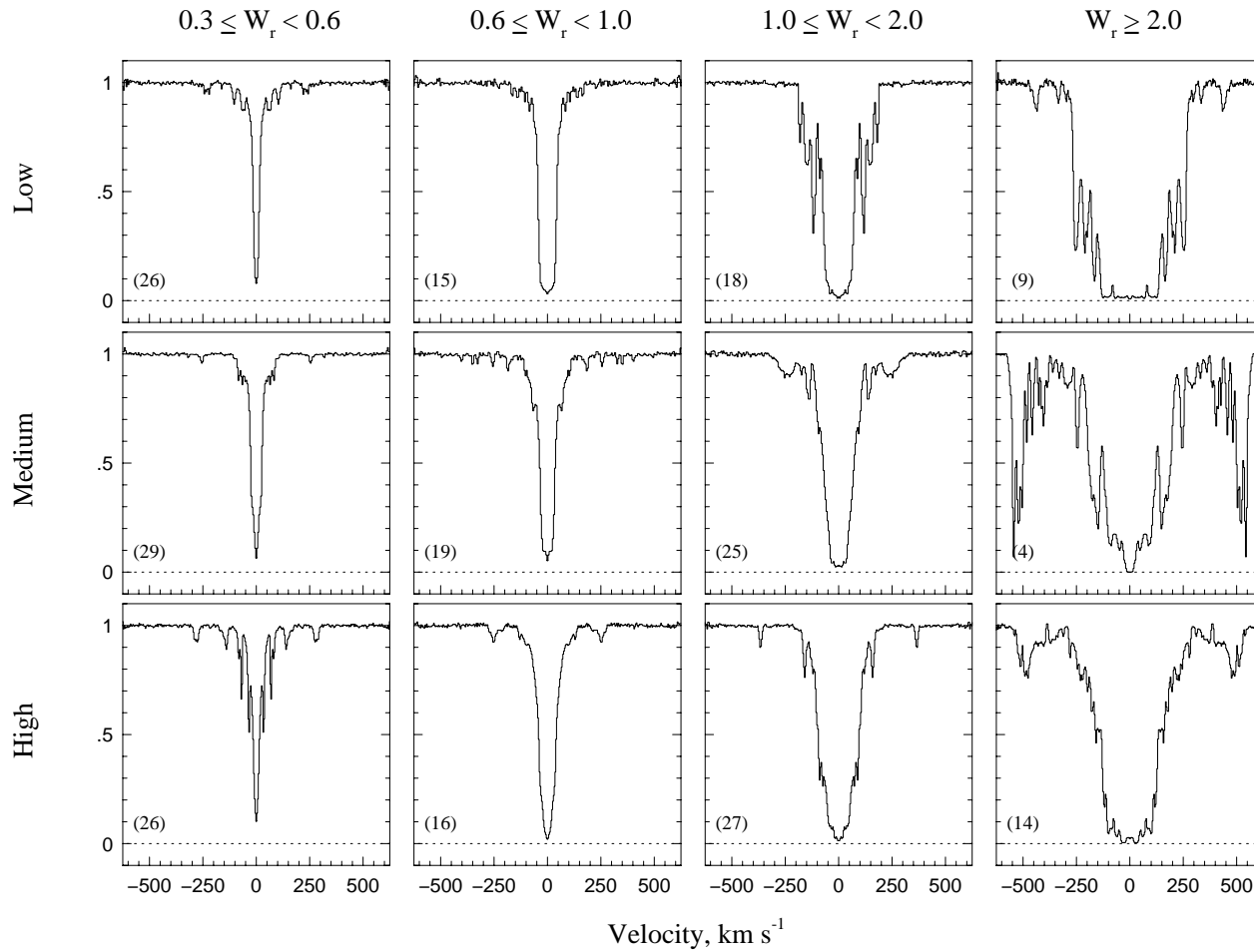


Figure 6.1 Composite strong MgII profiles are shown in increasing equivalent width bins from left to right and in increasing redshift bins from top to bottom. The redshift bins from low to high are $0.366 \leq z < 0.871$, $0.871 \leq z < 1.311$, and $1.311 \leq z < 2.269$. The numbers in the lower left corners of each panel represent the numbers of MgII systems that were used to create the profiles.

suggested that very strong ($W_r \geq 1.8 \text{ \AA}$) MgII absorption often has kinematic structure suggestive of superwinds/superbubbles (Bond et al., 2001a,b). Zibetti et al. (2007), in a statistical study of stacked quasar field images, showed that strong MgII absorption is correlated with significant light excesses within ~ 100 kpc impact parameters that are consistent with blue galaxies.

Earlier dN/dz studies have established definitively that the numbers of very strong MgII systems are diminishing toward the present (for example, Nestor et al. (2005) find that $n(z)\sigma(z)$ of $W_r \geq 2.0 \text{ \AA}$ systems decreases by $\sim 45\%$ from $z = 1.8$ to 0.6). However, it is apparent from our results that those very strong systems that do exist in the low redshift epoch contain more highly saturated profile centers, indicating that these structures are becoming more optically thick over time. This finding supports the suggestion of Steidel & Sargent (1992) that strong MgII is optically thinner at high redshifts, as well as the conclusion by Nestor et al. (2005) that evolution they observe in the dN/dz of the very strong MgII population must be driven by evolution in the kinematic properties of MgII-selected galaxies.

In their study of 33 strong MgII systems of $W_r \geq 0.3 \text{ \AA}$ over the range $0.3 < z < 2.5$, Mshar et al. (2007) reported evidence for evolution in the fraction of absorbing pixels that lie within the total system velocity width (defined in § 3.4) with redshift. They found that higher redshift systems tended to have higher fractions of absorbing pixels than at lower redshift. Our sample, however, does not support this finding. The fraction of absorbing pixels in strong MgII systems versus redshift is shown in the left

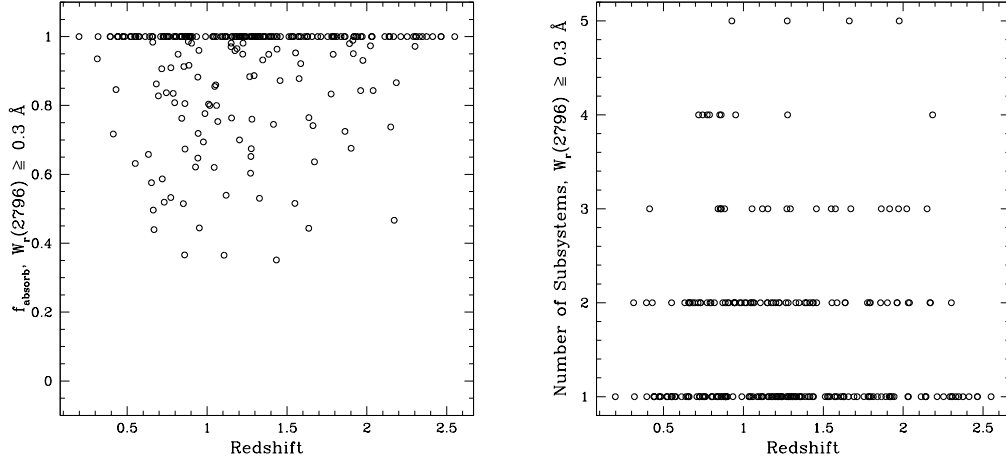


Figure 6.2 At left, the fraction of absorbing pixels in strong MgII systems versus redshift. At right, the number of kinematic subsystems versus redshift.

panel of Figure 6.2. Using our full $W_r \geq 0.3 \text{ \AA}$ sample, we performed the Spearman and Kendall rank correlation tests. It could not be ruled out to greater than 1.27σ and 1.44σ , respectively, that no relationship between these two quantities exists. The tests were repeated on the $1.0 \leq W_r < 2.0 \text{ \AA}$ and $W_r \geq 2.0 \text{ \AA}$ systems with even less significant results.

The authors also stated that the number of kinematic subsystems was significantly correlated with redshift, a claim that our study again does not support. They reported that a lower absorption redshift was correlated with a higher number of subsystems. The number of subsystems for our full strong MgII sample versus redshift is shown in the right panel of Figure 6.2. Similar to the case of the absorbing pixel fraction, the Spearman and Kendall rank correlation tests revealed that it could not be ruled out to greater than 0.48σ and 0.56σ , respectively, that no relationship between these two

quantities exists. Again, the tests were repeated for $1.0 \leq W_r < 2.0 \text{ \AA}$ and $W_r \geq 2.0 \text{ \AA}$, with similar results.

We present these findings to stress that the kinematic evolution of strong MgII is not easily characterized; in agreement with Mshar et al. (2007), we also find that velocity spread does not significantly evolve. In addition, we have investigated the possibility of evolution in total velocity width and VP Doppler b parameter distributions, also without finding significant differences in the populations at different redshifts. It is possible, however, that a much larger study than ours might be able to detect evolution in these quantities.

It seems that the overall kinematic extents of very strong MgII do not evolve, but that their internal velocity structure does. The optically thicker cores of the low redshift absorption profiles in our $W_r \geq 1.0 \text{ \AA}$ subsample may indicate that the physical centers of the absorbing gas are becoming more settled over time. This would cause the flux removal to become more aligned and concentrated in velocity space. On the other hand, the trend we observe at greater velocities of increased kinematic complexity in the low redshift sample may indicate that the gas giving rise to the outer portions of the absorption is condensing into kinematically more distinct clumps.

6.2 Weak MgII Systems

Compelling evidence for evolution in the number of weak MgII absorbers per unit redshift was presented in § 5.2.3. We would like more insight on the nature of weak

MgII-selected objects in the universe. Based on the relative number of weak MgII systems to Lyman limit systems (LLSs) (Churchill et al., 1999), the majority of the former must arise in sub-LLS neutral hydrogen column density environments, i.e., $\log N(\text{HI}) < 17.2 \text{ cm}^{-2}$. Rigby et al. (2002) determined using photoionization modeling that weak MgII absorbers generally have metallicities of > 0.1 times that of the solar value. This finding, combined with the lack of nearby bright (L^*) galaxies known to be associated with these objects, led the authors to conclude that weak MgII tends to arise in metal-enriched gas within small dark matter halos. For weak MgII systems that are also FeII-rich they inferred cloud sizes of $\sim 10 \text{ pc}$, and thus concluded that a sheetlike structure was required to account for the large dN/dz (for systems without detected FeII they were unable to constrain cloud sizes).

At $z > 1$, Rigby et al. (2002) predicted that weak MgII systems would be rarer due to generally lower metallicities and higher ionizing background flux, which this study upholds. They also point out that the luminous objects associated with weak MgII at low redshift, due to these changing conditions, may be different than those selected at high redshift. For $z < 1$, they determined that weak MgII accounts for at least a quarter of $\text{Ly}\alpha$ forest clouds.

In their weak MgII study, Lynch et al. (2006) posited that the peak in dN/dz might be related to the peak in the star formation rate in dwarf galaxies, since these are possible host objects for the observed absorption.

Similar to the conclusion of Rigby et al. (2002), Milutinović et al. (2006) also inferred

that sheets, or possibly filaments, associated with the intergalactic medium, were the most likely host geometries for weak MgII-selected structures, but that dwarf galaxies were also likely to account for a portion of the absorbing population. They based their findings on ionization constraints using several ion species.

6.2.1 Evolution of Absorber Sizes Using Cosmological Structure Growth

We have conducted an analysis by using cosmological structure growth and photoionization models and then applying constraints from our dN/dz and b parameter results to investigate weak MgII cloud sizes and cosmic number densities. We assumed that weak MgII absorption is associated with HI absorption (and thus takes on the same physical extents) in the column density regime $15.5 \leq \log N(\text{HI}) \leq 16.5 \text{ cm}^{-2}$. The HI column density cannot be lower than this unless supersolar metallicity is assumed (Rigby et al., 2002); the upper limit is based upon the assumption that the HI absorbers associated with weak MgII are sub-LLS, which is supported by previous analyses (Churchill et al., 1999, 2000).

In an analysis of the properties of cosmologically distributed HI absorbing clouds, Schaye (2001) derived the radial sizes of absorbers as a function of $N(\text{HI})$:

$$R(z) = 10^2 \text{ kpc} \left(\frac{N(\text{HI})}{10^{14} \text{ cm}^{-2}} \right)^{-1/3} T_4^{0.41} \Gamma_{12}^{-1/3}(z) \left(\frac{f_g}{0.16} \right)^{2/3}, \quad (6.1)$$

where T_4 is the temperature in K divided by 10^4 , $\Gamma_{12}(z)$ is the photoionization rate in $\text{erg s}^{-1} \text{ cm}^{-2} \text{ sr}^{-1} \text{ Hz}^{-1}$ divided by 10^{12} , and f_g is the cosmic fraction of baryonic mass in gas.

The photoionization rate was derived as a function of redshift in an analysis by Haardt & Madau (1996) of the ionizing background radiation:

$$\Gamma_{12}(z) = 1.816 \left(\frac{1+z}{4} \right)^{0.73} e^{-\frac{(z-2.3)^2}{1.9}}. \quad (6.2)$$

The lower left panel of Figure 6.3 shows $\Gamma_{12}(z)$. Substituting Equation 6.2 into Equation 6.1, we obtain

$$R(z) = 82 \text{ kpc} \left(\frac{N(\text{HI})}{10^{14} \text{ cm}^{-2}} \right)^{-1/3} T_4^{0.41} \left(\frac{f_g}{0.16} \right)^{2/3} \left(\frac{1+z}{4} \right)^{-0.243} e^{-\frac{(z-2.3)^2}{5.7}}. \quad (6.3)$$

We then substituted the following values to obtain our final $R(z)$: $N(\text{HI}) = 10^{15} \text{ cm}^{-2}$, $10^{15.5} \text{ cm}^{-2}$, or 10^{16} cm^{-2} , which are within our HI column density constraints; a temperature of $T_4 = 1$, which was our result based on the assumption of thermal b parameters from VP fitting of weak MgII systems; and $f_g \simeq 0.16$. The final function is shown in the upper left panel of Figure 6.3.

The function $R(z)$ is seen to scale downward with increasing column density, which follows from a gravitational collapse model of cloud formation. For a fixed $N(\text{HI})$, $R(z)$ also increases with decreasing z , i.e., decreasing photoionization rate $\Gamma_{12}(z)$.

Next, we used $R(z)$ and the model fit to our dN/dz data from § 5.2.3 to deduce the number density of absorbers as a function of redshift. Recalling the parameterization of the product of the number density of absorbers and the cross section of absorbers that was introduced in § 5.2.3,

$$n(z)\sigma(z) = n_0\sigma_0 [1 - \alpha(z - z^*)], \quad (6.4)$$

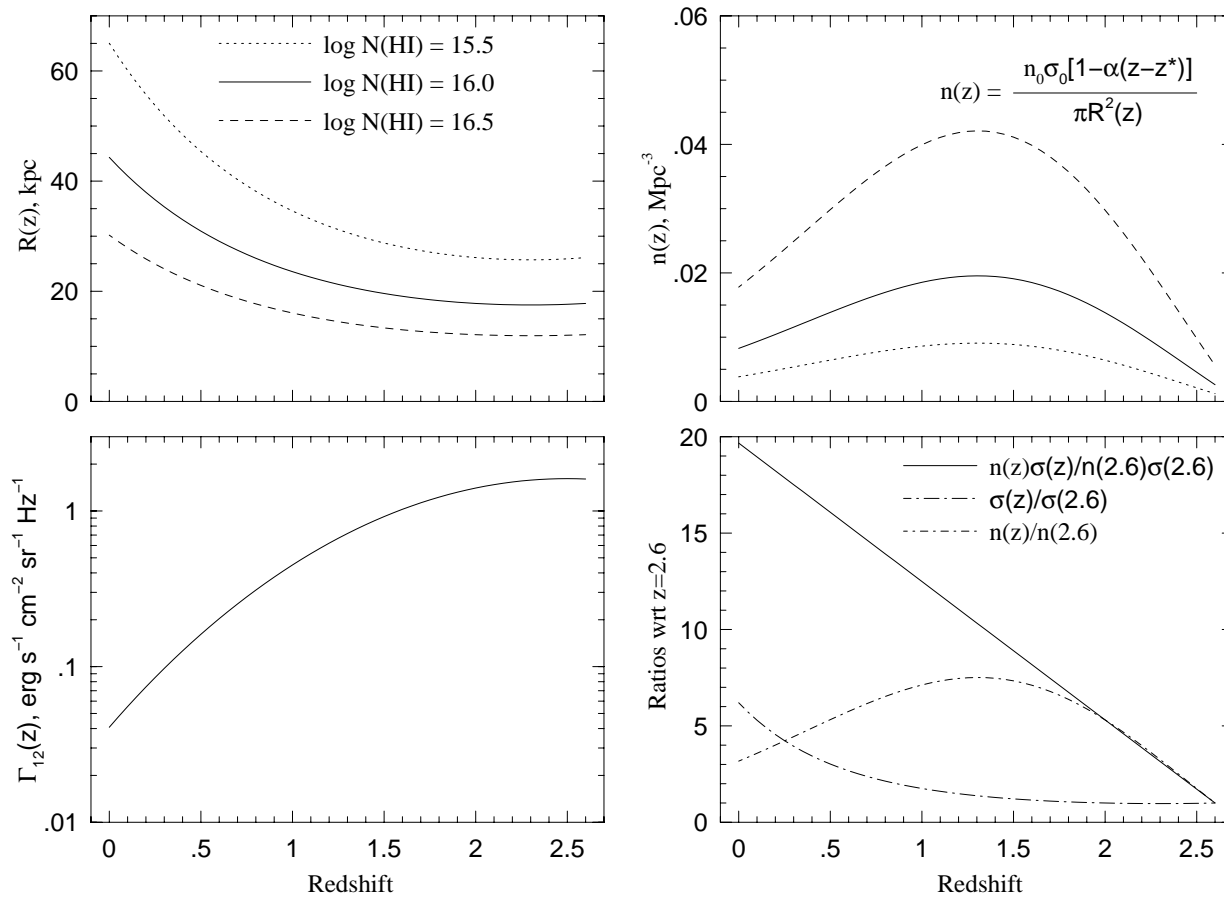


Figure 6.3 The upper left panel shows the derived absorber size $R(z)$ for three different HI column densities. The lower left panel shows the photoionization rate $\Gamma_{12}(z)$. The upper right panel shows the number density of absorbers as a function of z and constrained by the derived $R(z)$ and the weak MgII dN/dz result of this study. The lower right panel shows the number density $n(z)$, the cross section $\sigma(z)$, and their product, all normalized to $z = 2.6$.

solving for $n(z)$, and substituting $\pi R^2(z)$ for $\sigma(z)$, we obtain

$$n(z) = \frac{n_0 \sigma_0 [1 - \alpha(z - z^*)]}{\pi R^2(z)}; \quad (6.5)$$

this function is shown in the upper right panel of Figure 6.3. Finally, $n(z)$, $\sigma(z)$, and their product, all normalized to $z = 2.6$, are shown in the lower right panel of the figure.

We see that the product $n(z)\sigma(z)$ increases by a factor of ~ 20 from $z = 2.6$ to $z = 0$. The relative contributions to this are the increase in the geometric cross section $\sigma(z)$, i.e. cloud size, by a factor of ~ 6 , and in the cosmic number density $n(z)$ by a factor of ~ 3 . This latter quantity, however, actually peaks at $z \simeq 1.3$ before declining again toward the present. Our investigation of weak MgII absorber sizes and number densities using cosmological structure growth, and assuming that weak MgII is associated with the general population of HI absorbers, suggests that $R(z)$ is on the order of tens of kiloparsecs across. This is an order of magnitude less than the sizes of galaxy halos in the regime for which these have been observed ($0 \lesssim z \lesssim 0.9$) (Lanzetta et al., 1995; Chen et al., 2001). Lanzetta et al. (1995) concluded that most luminous galaxies are surrounded by extended gaseous envelopes of $\simeq 160 h^{-1}$ kpc radius, which assuming $h = 0.705$ yields radii of $\simeq 227$ kpc. Similarly, Chen et al. (2001) concluded that L^* galaxies are surrounded by spherical gas halos of radius $\simeq 180 h^{-1}$ kpc, which yields radii of $\simeq 255$ kpc.

In order for the product $n(z)\sigma(z)$ to be consistent with our observed weak MgII

dN/dz , $n(z)$ must then be a few times 10^{-2} Mpc^{-3} , an order of magnitude greater than the number density of L^* galaxies within $z \lesssim 1$ (Faber et al., 2007) as well as for $1 \lesssim z \lesssim 3$ (Reddy & Steidel, 2009; Oesch et al., 2010).

From the analysis of optically thin HI absorbers done by Schaye (2001), it also follows that $n_H \sim 10^{-4} \text{ cm}^{-3}$; however, this environment is realistically too rarefied for MgII to survive. Bergeron et al. (2002) have shown that at such low densities, MgII is destroyed under the prevailing high ionization conditions, and OVI is the dominant metal absorption line.

6.2.2 Evolution of Absorber Sizes Using CLOUDY

The above analysis assumes that the MgII absorbing gas clouds are large and diffuse, occupying the same physical extent as the HI absorbing gas. Using CLOUDY photoionization modeling (Ferland et al., 1998), we investigated another possible scenario along the lines of the study by Rigby et al. (2002). In this scenario, weak MgII selects relatively denser cloudlets and the observed HI absorption arises primarily within the MgII absorption region.

The program CLOUDY requires a number of user inputs. We assumed an ultraviolet background (UVB) model J_ν that varies as a function of z , following the work of Haardt & Madau (1996), which includes the contribution of galaxies. Next, a solar abundance pattern was assumed and a metallicity chosen. The hydrogen number density and stopping condition also had to be supplied; the latter is a quantity that gives

the H I column density of the cloud.

CLOUDY assumes constant density, plane parallel clouds in photoionization equilibrium. For a given cloud, the relationship between the cloud depth, or size, D , and $N(\text{H I})$ is

$$N(\text{H I}) = f_{\text{HI}} n_{\text{H}} D, \quad (6.6)$$

where f_{HI} is the fraction of hydrogen that is neutral and n_{H} is the number density of hydrogen. For optically thin clouds, i.e. $\log N(\text{H I}) < 17.2 \text{ cm}^{-2}$, $N(\text{H I})$ is directly proportional to D because the clouds have no ionization structure and f_{HI} does not change across the cloud depth.

The Mg II column density is given by

$$N(\text{Mg II}) = f_{\text{Mg II}} n_{\text{Mg}} D, \quad (6.7)$$

where $f_{\text{Mg II}}$ is the ionization fraction of Mg II and n_{Mg} is the number density of magnesium, which in general can be expressed as

$$n_{\text{Mg}} = n_{\text{H}} \left(\frac{Z}{Z_{\odot}} \right) \left(\frac{n_{\text{Mg}}}{n_{\text{H}}} \right)_{\odot}, \quad (6.8)$$

where Z is the metallicity of the cloud, Z_{\odot} is the solar metallicity, and $(n_{\text{Mg}}/n_{\text{H}})_{\odot}$ is the solar abundance fraction of Mg to H. Substituting 6.8 into 6.7, we have

$$N(\text{Mg II}) = f_{\text{Mg II}} D n_{\text{H}} \left(\frac{Z}{Z_{\odot}} \right) \left(\frac{n_{\text{Mg}}}{n_{\text{H}}} \right)_{\odot}. \quad (6.9)$$

For this study, we chose $\log N(\text{H I}) = 16.0 \text{ cm}^{-2}$, $Z/Z_{\odot} = 0.1$, and $(n_{\text{Mg}}/n_{\text{H}})_{\odot} = 3.39 \times 10^{-5}$. Although a metallicity of $Z/Z_{\odot} = 0.1$ was used for this model, it has been shown

that the model cloud ionization fractions of metals and hydrogen are insensitive to the choice of model cloud metallicity for $Z/Z_{\odot} < 1$; thus, the results of our model could be applied over the whole range of subsolar metallicity cases (Dittmann & Koeppen, 1995; Bergeron & Stasińska, 1986).

CLOUDY was used to model clouds having number densities of $-2.5 \leq \log n_H \leq -0.5 \text{ cm}^{-3}$, which encompasses the estimates for n_H determined by Bergeron et al. (2002) and Rigby et al. (2002). CLOUDY calculates f_{HI} , f_{MgII} , and D ; using these values and Equation 6.9, we compute $N(\text{MgII})$.

We assumed spherical clouds of size $R(z) = D$. The resulting redshift evolution of the cloud sizes is shown in the upper left panel of Figure 6.4, while the MgII column densities are shown in the lower left panel. The cloud size peaks at $z \sim 2$ and then declines noticeably toward $z = 0$. The behavior of $R(z)$ in the CLOUDY model is governed by the level of ionization, which is determined by $J_{\nu}(z)$, the UVB intensity and shape at redshift z . For a fixed $N(\text{HI})$ and n_H , $R(z)$ depends only on the neutral hydrogen fraction:

$$R(z) \propto \frac{1}{f_{HI}}; \quad (6.10)$$

this fraction is in turn dependent on the strength of the UVB. When $J_{\nu}(z)$ is larger, more hydrogen will be ionized and f_{HI} will be lower, in turn raising $R(z)$.

Using these cloud sizes and our dN/dz results, we calculated the absorber number density $n(z)$ as we did in the cosmological structure growth case (see Equations 6.4 and 6.5). The result is shown in the upper right panel of Figure 6.4.

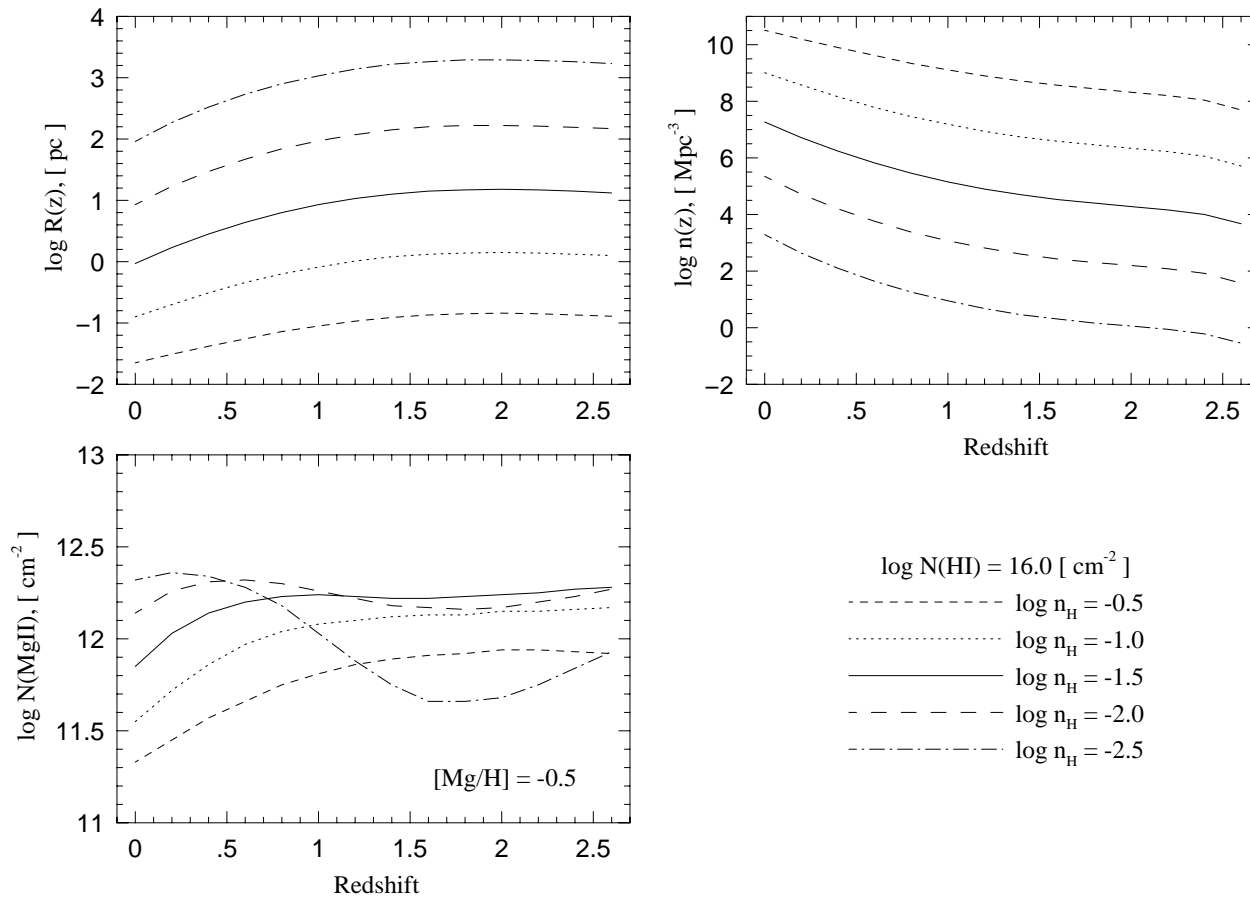


Figure 6.4 The upper left panel shows the CLOUDY absorber size, $\log R(z)$, over the hydrogen number density range $-2.5 \leq \log n_H \leq -0.5 \text{ cm}^{-3}$. The lower left panel shows $\log N(\text{MgII})$ for each n_H value. The upper right panel shows the evolution of the number density of absorbers, $\log n(z)$, for each n_H value.

We assumed a column density of $\log N(\text{HI}) = 16.0 \text{ cm}^{-2}$, but changing this quantity would change $R(z)$ proportionately so that

$$R(z) \propto N(\text{HI}), \quad (6.11)$$

and using our constraint on the absorber number density would yield

$$n(z) \propto \frac{1}{R(z)^2}. \quad (6.12)$$

In addition, the MgII column density scales linearly with that of HI :

$$N(\text{MgII}) \propto N(\text{HI}), \quad (6.13)$$

assuming constant metallicity.

Using CLOUDY photoionization modeling to characterize weak MgII absorption results in cloud sizes on the order of a parsec, which is a factor of $\sim 10^4$ smaller than in the previous analysis presented in § 6.2.1. Our dN/dz constraint puts the cosmic number density of absorbers in this case on the order of $10^6 - 10^9 \text{ Mpc}^{-3}$ over the middle range of hydrogen number density of $-2.0 \leq \log n_H \leq -1.0 \text{ cm}^{-3}$ (Rigby et al. (2002) show that $-1.5 \lesssim \log n_H \lesssim -1.0 \text{ cm}^{-3}$ for weak MgII absorption).

6.2.3 Two Scenarios of MgII -Selected Gas Structure

The striking differences between these two scenarios arise because the Schaye (2001) derivation relies on a gravitational collapse model to describe the formation of HI absorbing clouds. The resulting weak MgII absorbers would be large clouds having an approximately ten-to-one correspondence with bright galaxies.

The CLOUDY model does not involve gravitational collapse; instead, because it assumes plane parallel slabs of gas, it is suggestive of a condensation mechanism into sheet or filament structures characteristic of the intergalactic medium. The model requires small cloud sizes, as well as many, many clouds relative to the number of galaxies. The true nature of weak MgII absorption can almost certainly not be fully explained by either of these models, but they do provide limiting cases in which to couch its discussion.

APPENDIX

Appendix A DISCUSSION OF MGII SYSTEMS

The following sections list each quasar line of sight and describe each MgII $\lambda\lambda 2796, 2803$ doublet system in our sample. Each system's absorption profiles for all the transitions for which VP components were modeled are shown in "System Profiles and Fits" on the included compact disc; ten example systems were shown in Figures 2.12 - 2.16. The VP results were discussed in § 4 and are listed in "Voigt Profile Fitting Results" on the included compact disc; an example of the VP results for a system was listed in Table 4.1.

All systems were fit assuming turbulent Doppler parameters and using a confidence level of 0.97 and a badness of 1.5 (see § 4) unless otherwise noted.

A.1 J000323-260318

A.1.1 $z_{abs} = 1.434037$

This strong system was fit with four VP components, contains two subregions, and spans a total velocity width of 219 km s^{-1} . Most of the MgII $\lambda 2796$ feature was masked due to blending with the CIV $\lambda 1550$ feature at $z_{abs} = 3.390464$. The confidence level in MINFIT had to be reduced to 0.75 in order to retain enough components to achieve a satisfactory fit.

A.2 J000149-015939

A.2.1 $z_{abs} = 0.870821$

This strong system was fit with eight VP components, contains two subregions, and spans a total velocity width of 181 km s^{-1} . The confidence level in MINFIT had to be reduced to 0.03 in order to retain enough components to achieve a satisfactory fit.

A.3 J000520+052411

A.3.1 $z_{abs} = 0.298058$

This weak system was fit with three VP components and spans a total velocity width of 73 km s^{-1} .

A.3.2 $z_{abs} = 0.591364$

This weak system was fit with three VP components and spans a total velocity width of 57 km s^{-1} . The relatively large spurious absorption in the FeII $\lambda 2374$ transition was masked from $\sim -5 \text{ km s}^{-1}$ blueward.

A.3.3 $z_{abs} = 0.851393$

This very strong system was fit with 10 VP components, contains four subregions, and spans a total velocity width of 472 km s^{-1} . Note the well-spaced subregions and their decrease in equivalent width from blue to red. The confidence level in MINFIT

had to be reduced to 0.14 in order to retain enough components to achieve a satisfactory fit.

A.3.4 $z_{abs} = 0.866529$

This weak system was fit with one VP component and spans a total velocity width of 16 km s⁻¹. This absorber has one of the smallest equivalent widths in our sample at 0.023 Å.

A.3.5 $z_{abs} = 0.956028$

This weak system was fit with one VP component and spans a total velocity width of 35 km s⁻¹.

A.4 J000344-232355

A.4.1 $z_{abs} = 0.452397$

This weak system was fit with three VP components, contains two subregions, and spans a total velocity width of 157 km s⁻¹.

A.4.2 $z_{abs} = 0.949116$

This strong system was fit with nine VP components, contains two subregions, and spans a total velocity width of 185 km s⁻¹. Spurious features were masked in the FeII λ2587 transition from 15 to 65 km s⁻¹. The confidence level in MINFIT had to be reduced to 0.63 in order to retain enough components to achieve a satisfactory fit.

A.4.3 $z_{abs} = 1.586132$

This strong system was fit with five VP components, contains two subregions, and spans a total velocity width of 152 km s^{-1} . The confidence level in MINFIT had to be reduced to 0.91 in order to retain enough components to achieve a satisfactory fit.

A.4.4 $z_{abs} = 1.651460$

This weak system was fit with one VP component and spans a total velocity width of 32 km s^{-1} .

A.4.5 $z_{abs} = 2.184448$

This strong system was fit with 16 VP components, contains four subregions, and spans a total velocity width of 428 km s^{-1} . The presence of many atmospheric lines in some of the transitions made fitting this system difficult. Spurious features were masked in the FeII $\lambda 2600$ transition from -150 to -100 km s^{-1} ; in the FeII $\lambda 2587$ transition from -140 to -90 km s^{-1} and from -50 to 0 km s^{-1} ; in the FeII $\lambda 2374$ transition from 120 to 140 km s^{-1} ; in the MnII $\lambda 2594$ transition from -125 to -100 km s^{-1} and from -10 to 10 km s^{-1} ; and in the MnII $\lambda 2606$ transition from -165 to -145 km s^{-1} , 80 to 120 km s^{-1} , and 230 to 290 km s^{-1} . Most of the MgI $\lambda 2853$ transition contained no data, but real absorption was modeled in components 14 and 16.

A.5 J000448-415728

A.5.1 $z_{abs} = 0.836627$

This very strong system spans a total velocity width of 615 km s^{-1} . This is one of the strongest systems in our sample with $W_r = 4.42 \text{ \AA}$. Spurious features were masked in the MnII $\lambda 2577$ absorption at $\sim 175 \text{ km s}^{-1}$ and in an apparent blend in the FeII $\lambda 2587$ line from about 170 to 275 km s^{-1} where MINFIT was not fitting the region well. Although 42 VP components were fit, the parameters for one component were not well constrained. “Voigt Profile Fitting Results” on the included compact disc does not quote errors for this component, and the model should be viewed with caution. The confidence level in MINFIT had to be reduced to 0.03 in order to retain enough components to achieve a satisfactory fit.

A.5.2 $z_{abs} = 1.541851$

This strong system was fit with eight VP components and spans a total velocity width of 180 km s^{-1} . Spurious features were masked in the MgI $\lambda 2853$ transition from -120 to -80 km s^{-1} , -40 to -20 km s^{-1} , and 15 to 30 km s^{-1} . The confidence level in MINFIT had to be reduced to 0.01 in order to retain enough components to achieve a satisfactory fit.

A.5.3 $z_{abs} = 1.988657$

This weak system was fit with five VP components and spans a total velocity width of 113 km s^{-1} . This system has a small area of shallow MgII absorption at $\sim -20 \text{ km s}^{-1}$ that MINFIT was unable to model.

A.5.4 $z_{abs} = 2.167883$

This strong system was fit with five VP components, contains two subregions, and spans a total velocity width of 143 km s^{-1} . Spurious features were masked in the FeII $\lambda 2344$ and $\lambda 2587$ transitions from 80 to 125 km s^{-1} and from -40 to 115 km s^{-1} respectively.

A.5.5 $z_{abs} = 2.301941$

This very strong system was fit with 14 VP components, contains two subregions, and spans a total velocity width of 350 km s^{-1} . An area of absorption in the red wing of the MgII $\lambda 2803$ transition was masked from 170 to 230 km s^{-1} because it does not correspond to absorption in the $\lambda 2796$ transition. A spurious feature was also masked from 125 to 150 km s^{-1} in the MgI $\lambda 2853$ transition. Finally, an area of bad data, possibly a faulty sky subtraction, was masked in the MnII $\lambda 2577$ transition from -80 to -25 km s^{-1} .

A.5.6 $z_{abs} = 2.464126$

This strong system was fit with three VP components and spans a total velocity width of 83 km s^{-1} .

A.6 **J001130+005550**

A.6.1 $z_{abs} = 1.395604$

This strong system was fit with five VP components, contains two subregions, and spans a total velocity width of 140 km s^{-1} . The confidence level in MINFIT had to be reduced to 0.19 in order to retain enough components to achieve a satisfactory fit.

A.6.2 $z_{abs} = 1.777928$

This weak system was fit with one VP component and spans a total velocity width of 35 km s^{-1} .

A.7 **J001210-012207**

A.7.1 $z_{abs} = 1.202983$

This strong system was fit with three VP components, contains two subregions, and spans a total velocity width of 122 km s^{-1} .

A.7.2 $z_{abs} = 1.385936$

This very strong system was fit with 10 VP components, contains two subregions, and spans a total velocity width of 240 km s^{-1} . The two spurious features redward of the FeII $\lambda 2587$ absorption were masked.

A.8 J001306+000431

A.8.1 $z_{abs} = 1.212007$

This strong system was fit with seven VP components and spans a total velocity width of 168 km s^{-1} . In order to better constrain the MgII column densities relative to the FeII, we used the saturated regions option in MINFIT from -25 to 2 km s^{-1} and from 21 to 38 km s^{-1} . Two bad pixels were masked in both the MgII $\lambda 2796$ and the $\lambda 2803$ features at ~ 30 and -10 km s^{-1} , respectively. The confidence level in MINFIT had to be reduced to 0.88 in order to retain enough components to achieve a satisfactory fit.

A.9 J001602-001225

A.9.1 $z_{abs} = 0.635095$

This weak system was fit with four VP components, contains four subregions, and spans a total velocity width of 280 km s^{-1} . The kinematic spread is large relative to the equivalent width. A spurious feature in the vicinity of the FeII $\lambda 2374$ at $\sim 0 \text{ km s}^{-1}$, as well as blending on the red FeII $\lambda 2383$ line, were masked.

A.9.2 $z_{abs} = 0.857465$

This weak system was fit with six VP components, contains two subregions, and spans a total velocity width of 130 km s^{-1} . Spurious features contaminated the MgII $\lambda 2803$ feature but did not interfere with the fit. The confidence level in MINFIT had to be reduced to 0.93 in order to retain enough components to achieve a satisfactory fit.

A.9.3 $z_{abs} = 1.146778$

This weak system was fit with three VP components, contains two subregions, and spans a total velocity width of 92 km s^{-1} . The MnII $\lambda 2577$ transition had to be masked from about -25 to 75 km s^{-1} due to the presence of a spurious absorption feature.

A.9.4 $z_{abs} = 1.971326$

This very strong system contains three subregions and spans a total velocity width of 1097 km s^{-1} . This system has such a broad kinematic range that the MgII $\lambda\lambda 2796, 2803$ doublet is actually self-blended. It has the highest equivalent width of our sample at 6.23 \AA . As a result, the red $\lambda 2796$ wing and the blue $\lambda 2803$ wings overlap and were masked. In addition, the absorption features present in both features at $\sim -250 \text{ km s}^{-1}$ have a clearly inconsistent doublet ratio and were masked. Finally, the portions of the spectrum in both transitions from about -200 to -160 km s^{-1} were masked because they could not be successfully modeled and are likely also blended. Spurious features

were also masked in the FeII $\lambda 2587$ feature from -560 to -470 km s $^{-1}$ and -300 to -230 km s $^{-1}$ (both atmospheric); in the FeII $\lambda 2374$ feature from 470 to 600 km s $^{-1}$; in the MgI $\lambda 2853$ feature from -175 to -290 km s $^{-1}$, and in the MnII $\lambda 2606$ feature at ~ -200 km s $^{-1}$. In the latter transition, several bad pixels were also masked at ~ 300 km s $^{-1}$. Although 40 VP components were fit, the parameters for 39 components were not well constrained. “Voigt Profile Fitting Results” on the included compact disc does not quote errors for these components, and the model should be viewed with caution. The confidence level in MINFIT had to be reduced to 0.74 in order to retain enough components to achieve a satisfactory fit.

A.9.5 $z_{abs} = 2.029186$

This strong system was fit with seven VP components and spans a total velocity width of 180 km s $^{-1}$. An area of spurious absorption had to be masked adjacent to the blue wing of the MgII $\lambda 2796$ feature from -130 to -80 km s $^{-1}$, as well as an atmospheric feature located in the FeII $\lambda 2374$ transition from 0 to 30 km s $^{-1}$. The confidence level in MINFIT had to be reduced to 0.41 in order to retain enough components to achieve a satisfactory fit.

A.10 J002133+004301

A.10.1 $z_{abs} = 0.520353$

This strong system was fit with four VP components and spans a total velocity width of 148 km s^{-1} . The confidence level in MINFIT had to be reduced to 0.81 in order to retain enough components to achieve a satisfactory fit.

A.10.2 $z_{abs} = 0.942041$

This very strong system was fit with 12 VP components, contains two subregions, and spans a total velocity width of 337 km s^{-1} . Since this system is saturated even in portions of the weakest FeII transition present, the $\lambda 2587$, we used the saturated regions option in MINFIT from -77 to 71 km s^{-1} .

A.11 J002151-012833

A.11.1 $z_{abs} = 0.695180$

This strong system was fit with six VP components, contains two subregions, and spans a total velocity width of 230 km s^{-1} . Three bad pixels were masked in the FeII $\lambda 2600$ feature at $\sim -5 \text{ km s}^{-1}$.

A.11.2 $z_{abs} = 1.241235$

This very strong system was fit with seven VP components and spans a total velocity width of 195 km s^{-1} . In order to better constrain the MgII column densities

relative to the FeII, we used the saturated regions option in MINFIT from -56 to 34 km s⁻¹. The confidence level in MINFIT had to be reduced to 0.66 in order to retain enough components to achieve a satisfactory fit.

A.11.3 $z_{abs} = 1.308740$

This weak system contains two subregions and spans a total velocity width of 98 km s⁻¹. Although three VP components were fit, the parameters for one component were not well constrained. “Voigt Profile Fitting Results” on the included compact disc does not quote errors for this component, and the model should be viewed with caution.

A.12 J002208-150539

A.12.1 $z_{abs} = 1.700022$

This weak system was fit with one VP component and spans a total velocity width of 36 km s⁻¹. The absorption to either side of the single MgII $\lambda 2796$ component, as well as the excess absorption in the blue $\lambda 2803$ wing, are believed to be spurious.

A.13 J004428-243417

No MgII systems were found in this spectrum in the redshift range $0.1745 \leq z \leq 0.7772$.

A.14 J004508-291432

No MgII systems were found in this spectrum in the redshift range $0.4729 \leq z \leq 1.4352$.

A.15 J004812-255003

A.15.1 $z_{abs} = 0.690864$

This weak system was fit with two VP components, contains two subregions, and spans a total velocity width of 120 km s^{-1} .

A.16 J004816-254745

No MgII systems were found in this spectrum in the redshift range $0.1745 \leq z \leq 0.4615$.

A.17 J004848-260020

No MgII systems were found in this spectrum in the redshift range $0.1747 \leq z \leq 1.3702$.

A.18 J005024-252234

A.18.1 $z_{abs} = 0.699887$

This weak system was fit with two VP components, contains two subregions, and spans a total velocity width of 88 km s^{-1} . A spurious feature was masked in the FeII

$\lambda 2600$ transition at $\sim \text{km s}^{-1}$.

A.19 J005109-255216

No MgII systems were found in this spectrum in the redshift range $0.4125 \leq z \leq 1.3785$.

A.20 J005127-280433

No MgII systems were found in this spectrum in the redshift range $0.4155 \leq z \leq 1.3783$.

A.21 J005211-251857

A.21.1 $z_{abs} = 0.887325$

This very strong system was fit with 10 VP components and spans a total velocity width of 315 km s^{-1} . This system's absorption is weighted more heavily redward, with weaker components visible to the blue. The confidence level in MINFIT had to be reduced to 0.72 in order to retain enough components to achieve a satisfactory fit.

A.21.2 $z_{abs} = 1.067163$

This strong system was fit with four VP components, contains two subregions, and spans a total velocity width of 180 km s^{-1} . The confidence level in MINFIT had to be reduced to 0.85 in order to retain enough components to achieve a satisfactory fit.

A.22 J005419-254900

No MgII systems were found in this spectrum in the redshift range $0.1747 \leq z \leq 0.5972$.

A.23 J005758-264314

A.23.1 $z_{abs} = 1.267863$

This strong system was fit with five VP components and spans a total velocity width of 118 km s^{-1} . The confidence level in MINFIT had to be reduced to 0.47 in order to retain enough components to achieve a satisfactory fit.

A.23.2 $z_{abs} = 1.533672$

This strong system was fit with five VP components and spans a total velocity width of 126 km s^{-1} . A spurious feature was masked on the red wing of the FeII $\lambda 2600$ transition.

A.24 J005925-411043

No MgII systems were found in this spectrum in the redshift range $0.3259 \leq z \leq 1.4356$.

A.25 J010054+021136

A.25.1 $z_{abs} = 0.346669$

This weak system was fit with one VP component and spans a total velocity width of 29 km s^{-1} .

A.25.2 $z_{abs} = 0.612586$

This very strong system was fit with eight VP components and spans a total velocity width of 234 km s^{-1} . Since this system is saturated in even the weakest of the FeII transitions, we used the saturated regions option in MINFIT from -50 to 6 km s^{-1} .

A.25.3 $z_{abs} = 0.725100$

This weak system was fit with three VP components and spans a total velocity width of 75 km s^{-1} .

A.25.4 $z_{abs} = 0.734779$

This weak system was fit with three VP components and spans a total velocity width of 77 km s^{-1} . The confidence level in MINFIT had to be reduced to 0.12 in order to retain enough components to achieve a satisfactory fit.

A.26 J010311+131617

A.26.1 $z_{abs} = 1.758901$

This weak system was fit with three VP components, contains three subregions, and spans a total velocity width of 388 km s^{-1} .

A.26.2 $z_{abs} = 1.797435$

This very strong system was fit with 13 VP components and spans a total velocity width of 321 km s^{-1} . Spurious features were masked in the MgII $\lambda 2796$ feature at $\sim 70 \text{ km s}^{-1}$; in the FeII $\lambda 2600$ feature from 50 to 80 km s^{-1} ; in the MnII $\lambda 2577$ feature from -95 to -70 km s^{-1} , from -10 to 30 km s^{-1} , and from 125 to 150 km s^{-1} (all atmospheric); in the MnII $\lambda 2594$ feature at $\sim -75 \text{ km s}^{-1}$ and $\sim 95 \text{ km s}^{-1}$; and in the MnII $\lambda 2606$ feature from -70 to -20 km s^{-1} , from 25 to 75 km s^{-1} , and at $\sim 105 \text{ km s}^{-1}$. The confidence level in MINFIT had to be reduced to 0.43 in order to retain enough components to achieve a satisfactory fit.

A.26.3 $z_{abs} = 2.298687$

This weak system was fit with three VP components and spans a total velocity width of 53 km s^{-1} . Blended features were masked on the red wings of both the MgII $\lambda 2796$ and $\lambda 2803$ transitions; these features are not aligned in velocity and are spurious. Also, a large spurious feature was masked in the MnII $\lambda 2594$ transition from about 5 to 100 km s^{-1} .

A.26.4 $z_{abs} = 2.309309$

This strong system was fit with four VP components and spans a total velocity width of 128 km s^{-1} . Since this system is saturated in even the weakest of the FeII transitions, we used the saturated regions option in MINFIT from -30 to -9 km s^{-1} . The three shallow pixels in the MgII $\lambda 2803$ feature at $\sim 25 \text{ km s}^{-1}$ are believed to be noise and to actually be saturated. The confidence level in MINFIT had to be reduced to 0.39 in order to retain enough components to achieve a satisfactory fit.

A.27 **J011143-350300**

A.27.1 $z_{abs} = 0.769642$

This weak system was fit with one VP component and spans a total velocity width of 30 km s^{-1} .

A.27.2 $z_{abs} = 1.182696$

This weak system was fit with five VP components, contains two subregions, and spans a total velocity width of 108 km s^{-1} . The confidence level in MINFIT had to be reduced to 0.41 in order to retain enough components to achieve a satisfactory fit.

A.27.3 $z_{abs} = 1.349591$

This very strong system was fit with 19 VP components and spans a total velocity width of 395 km s^{-1} . The absorption is spread over a structurally rich profile. A region

in the FeII $\lambda 2374$ transition contains no data from -25 to 5 km s^{-1} .

A.28 J012156+144824

No MgII systems were found in this spectrum in the redshift range $0.6801 \leq z \leq 1.4407$.

A.29 J012227-042127

A.29.1 $z_{abs} = 0.338567$

This weak system was fit with one VP component and spans a total velocity width of 54 km s^{-1} .

A.29.2 $z_{abs} = 0.657432$

This strong system was fit with five VP components, contains two subregions, and spans a total velocity width of 158 km s^{-1} .

A.29.3 $z_{abs} = 0.719595$

This strong system was fit with 10 VP components, contains four subregions, and spans a total velocity width of 414 km s^{-1} .

A.30 J012017+213347

A.30.1 $z_{abs} = 0.576397$

This strong system spans a total velocity width of 125 km s^{-1} . This is a highly kinematically concentrated profile; the MgII is saturated throughout, though structure is detected in the weaker transitions. Although six VP components were fit, the parameters for one component were not well constrained. “Voigt Profile Fitting Results” on the included compact disc does not quote errors for this component, and the model should be viewed with caution. The confidence level in MINFIT had to be reduced to 0.11 in order to retain enough components to achieve a satisfactory fit.

A.30.2 $z_{abs} = 0.729076$

This weak system was fit with five VP components, contains three subregions, and spans a total velocity width of 174 km s^{-1} . The spurious feature present in the FeII $\lambda 2600$ transition from about 30 km s^{-1} redward was masked.

A.30.3 $z_{abs} = 1.047970$

This strong system was fit with six VP components, contains two subregions, and spans a total velocity width of 157 km s^{-1} .

A.30.4 $z_{abs} = 1.325293$

This weak system was fit with five VP components, contains three subregions, and spans a total velocity width of 267 km s^{-1} . This system has an interesting profile with four well-spaced, fairly evenly divided components and a fifth smaller one comprising the $W_r = 0029 \text{ Å}$ absorber.

A.31 **J012417-374423**

A.31.1 $z_{abs} = 0.443384$

This strong system was fit with eight VP components and spans a total velocity width of 130 km s^{-1} .

A.31.2 $z_{abs} = 0.822095$

This weak system was fit with seven VP components, contains three subregions, and spans a total velocity width of 463 km s^{-1} .

A.31.3 $z_{abs} = 0.859261$

This strong system was fit with seven VP components, contains three subregions, and spans a total velocity width of 455 km s^{-1} . The system's two nearly equally strong subsystems, $\sim 200 \text{ km s}^{-1}$ apart, are accompanied by a third, weaker subsystem another $\sim 175 \text{ km s}^{-1}$ away. A spurious feature had to be masked on the blue wing of region 2 of the FeII $\lambda 2344$ feature.

A.31.4 $z_{abs} = 0.909587$

This weak system was fit with three VP components, contains two subregions, and spans a total velocity width of 102 km s^{-1} .

A.31.5 $z_{abs} = 1.173634$

This weak system was fit with one VP component and spans a total velocity width of 35 km s^{-1} . This is one of the weakest systems in our sample at $W_r = 0.018 \text{ \AA}$.

A.31.6 $z_{abs} = 1.243344$

This strong system was fit with five VP components and spans a total velocity width of 110 km s^{-1} . Atmospheric features redward of the $\text{MgII } \lambda 2803$ absorption were masked from 60 to 120 km s^{-1} .

A.31.7 $z_{abs} = 1.909192$

This weak system was fit with four VP components, contains three subregions, and spans a total velocity width of 112 km s^{-1} .

A.31.8 $z_{abs} = 1.973356$

This weak system was fit with five VP components, contains two subregions, and spans a total velocity width of 180 km s^{-1} . A possible blend or noise in the data was masked in the $\text{MgII } \lambda 2803$ feature from 10 to 90 km s^{-1} . The confidence level in

MINFIT had to be reduced to 0.95 in order to retain enough components to achieve a satisfactory fit.

A.32 J012642+255901

No MgII systems were found in this spectrum in the redshift range $0.4598 \leq z \leq 1.1797$.

A.33 J012944-403346

No MgII systems were found in this spectrum in the redshift range $0.1740 \leq z \leq 0.4878$.

A.34 J013105-213446

No MgII systems were found in this spectrum in the redshift range $0.2607 \leq z \leq 1.4347$.

A.35 J013405+005109

A.35.1 $z_{abs} = 0.684746$

This weak system was fit with one VP component and spans a total velocity width of 42 km s^{-1} .

A.35.2 $z_{abs} = 0.821387$

This weak system was fit with two VP components and spans a total velocity width of 40 km s^{-1} .

A.35.3 $z_{abs} = 0.842235$

This very strong system was fit with nine VP components and spans a total velocity width of 193 km s^{-1} . In order to better constrain the MgII column densities relative to the FeII, we used the saturated regions option in MINFIT from -46 to 46 km s^{-1} . Two bad pixels were masked in the MgII $\lambda 2796$ absorption at $\sim 45 \text{ km s}^{-1}$. The confidence level in MINFIT had to be reduced to 0.46 in order to retain enough components to achieve a satisfactory fit.

A.35.4 $z_{abs} = 1.272233$

This strong system was fit with seven VP components, contains three subregions, and spans a total velocity width of 300 km s^{-1} . The absorption is split between the first and third subregions, with only a single weak component comprising the second region.

A.36 **J013442-413611**

This spectrum contained no redshift coverage as defined in § 2.4.

A.37 J013857-225447

A.37.1 $z_{abs} = 0.802369$

This strong system was fit with three VP components and spans a total velocity width of 65 km s^{-1} .

A.37.2 $z_{abs} = 0.884865$

This weak system was fit with two VP components and spans a total velocity width of 68 km s^{-1} .

A.37.3 $z_{abs} = 1.184190$

This strong system was fit with nine VP components and spans a total velocity width of 198 km s^{-1} . Though the system contains no distinct subregions, there is nevertheless distinct kinematic structure with the strongest absorption occurring near the blue and red extremes of the profile and weaker absorption about 0 km s^{-1} . The confidence level in MINFIT had to be reduced to 0.95 in order to retain enough components to achieve a satisfactory fit.

A.37.4 $z_{abs} = 1.261748$

This weak system was fit with two VP components and spans a total velocity width of 65 km s^{-1} .

A.37.5 $z_{abs} = 1.294135$

This strong system was fit with nine VP components, contains three subregions, and spans a total velocity width of 263 km s^{-1} . The confidence level in MINFIT had to be reduced to 0.02 in order to retain enough components to achieve a satisfactory fit.

A.37.6 $z_{abs} = 1.353669$

This weak system was fit with three VP components and spans a total velocity width of 70 km s^{-1} .

A.38 **J015234+335032**

A.38.1 $z_{abs} = 0.520292$

This very strong system spans a total velocity width of 377 km s^{-1} . This is a highly kinematically concentrated profile; the MgII is saturated throughout, though structure is detected in the weaker transitions. The b parameter flag in MINFIT was changed from turbulent to thermal to improve the fit. Although 23 VP components were fit, the parameters for five components were not well constrained. “Voigt Profile Fitting Results” on the included compact disc does not quote errors for these components, and the model should be viewed with caution. The confidence level in MINFIT had to be reduced to 0.06 in order to retain enough components to achieve a satisfactory fit.

A.39 J015327-431137

A.39.1 $z_{abs} = 0.663065$

This strong system was fit with nine VP components, contains two subregions, and spans a total velocity width of 345 km s^{-1} . Several pixels were masked on the red wing of region 1 of the MgII $\lambda 2796$ absorption at $\sim 210 \text{ km s}^{-1}$. Large spurious features were masked redward of the FeII $\lambda 2344$, $\lambda 2374$, and $\lambda 2600$ absorption, as well as a region of bad data redward of FeII $\lambda 2587$ between about -400 and -350 km s^{-1} . The confidence level in MINFIT had to be reduced to 0.59 in order to retain enough components to achieve a satisfactory fit.

A.39.2 $z_{abs} = 1.708494$

This weak system was fit with one VP component and spans a total velocity width of 30 km s^{-1} .

A.39.3 $z_{abs} = 2.451566$

This weak system was fit with three VP components and spans a total velocity width of 77 km s^{-1} . This system was contaminated by numerous atmospheric lines; the FeII $\lambda 2600$ transition was masked from -70 to 25 km s^{-1} and the $\lambda 2374$ transition from -75 to 20 km s^{-1} .

A.40 J015734+744244

A.40.1 $z_{abs} = 0.745002$

This strong system was fit with 10 VP components, contains four subregions, and spans a total velocity width of 329 km s^{-1} . There were large spurious absorption features in both the FeII $\lambda 2383$ and the $\lambda 2374$ that were masked. The confidence level in MINFIT had to be reduced to 0.18 in order to retain enough components to achieve a satisfactory fit.

A.41 J015733-004824

A.41.1 $z_{abs} = 0.768336$

This weak system was fit with four VP components, contains three subregions, and spans a total velocity width of 415 km s^{-1} . This system comprises multiple kinematic subsystems though its equivalent width is only 0.15 \AA . The confidence level in MINFIT had to be reduced to 0.76 in order to retain enough components to achieve a satisfactory fit.

A.41.2 $z_{abs} = 1.415684$

This very strong system was fit with 13 VP components, contains two subregions, and spans a total velocity width of 270 km s^{-1} . Since this system is saturated in even the weakest of the FeII transitions, we used the saturated regions option in MINFIT from -15 to 30 km s^{-1} . The b parameter flag in MINFIT was also changed from

turbulent to thermal to improve the fit. The confidence level in MINFIT had to be reduced to 0.17 in order to retain enough components to achieve a satisfactory fit.

A.42 J020346+113445

A.42.1 $z_{abs} = 1.574187$

This very strong system spans a total velocity width of 160 km s^{-1} . An area of noisy data in the MgI $\lambda 2853$ transition was masked from -80 to -10 km s^{-1} . Although seven VP components were fit, the parameters for one component were not well constrained. “Voigt Profile Fitting Results” on the included compact disc does not quote errors for this component, and the model should be viewed with caution. The confidence level in MINFIT had to be reduced to 0.11 in order to retain enough components to achieve a satisfactory fit.

A.43 J020455+364918

A.43.1 $z_{abs} = 0.731671$

This very strong system contains two subregions and spans a total velocity width of 432 km s^{-1} . A large spurious feature was masked in MgI $\lambda 2853$ from -20 km s^{-1} blueward. In addition, a small portion of the red wing of the MgII $\lambda 2796$ absorption in region 1 was masked because it did not correspond to the $\lambda 2803$ profile and is believed to be due to either noise or to a blend. Although 11 VP components were fit, the parameters for one component were not well constrained. “Voigt Profile Fitting

Results” on the included compact disc does not quote errors for this component, and the model should be viewed with caution. The confidence level in MINFIT had to be reduced to 0.71 in order to retain enough components to achieve a satisfactory fit.

A.44 J020930+051730

A.44.1 $z_{abs} = 1.280753$

This very strong system was fit with 18 VP components, contains two subregions, and spans a total velocity width of 468 km s⁻¹. Note the classic saturated MgII double profile; more structure can be seen in the MgI λ 2853 transition, though the areas blueward of region 1 and redward of region 2 were polluted by spurious absorption and had to be masked.

A.44.2 $z_{abs} = 1.532246$

This weak system was fit with one VP component and spans a total velocity width of 27 km s⁻¹.

A.45 J021857+081728

A.45.1 $z_{abs} = 1.459030$

This strong system was fit with four VP components, contains two subregions, and spans a total velocity width of 129 km s⁻¹. The MgII $\lambda\lambda$ 2796, 2803 doublet fell in the atmospheric B-band, requiring extensive masking. The confidence level in MINFIT had

to be reduced to 0.96 in order to retain enough components to achieve a satisfactory fit.

A.46 J023145+132254

No MgII systems were found in this spectrum in the redshift range $0.3333 \leq z \leq 0.7112$.

A.47 J024008-230915

A.47.1 $z_{abs} = 1.184618$

This weak system was fit with five VP components and spans a total velocity width of 111 km s^{-1} .

A.47.2 $z_{abs} = 1.365057$

This very strong system was fit with 17 VP components and spans a total velocity width of 308 km s^{-1} . The confidence level in MINFIT had to be reduced to 0.05 in order to retain enough components to achieve a satisfactory fit.

A.47.3 $z_{abs} = 1.637107$

This strong system was fit with 10 VP components, contains two subregions, and spans a total velocity width of 287 km s^{-1} . Spurious features were masked in the FeII $\lambda 2374$ transition at $\sim -25 \text{ km s}^{-1}$ and from 25 km s^{-1} redward.

A.47.4 $z_{abs} = 1.657430$

This strong system was fit with seven VP components and spans a total velocity width of 207 km s^{-1} . A possible very weak cloud on the red wing of the MgII $\lambda\lambda 2796, 2803$ doublet was included in the initial model at $\sim 75 \text{ km s}^{-1}$, but MINFIT did not retain the component. Spurious features were masked in the FeII $\lambda 2600$ transition from 27 km s^{-1} redward.

A.47.5 $z_{abs} = 1.672358$

This very strong system was fit with 14 VP components, contains three subregions, and spans a total velocity width of 516 km s^{-1} . Spurious features were masked in the FeII $\lambda 2587$ transition from -135 to -55 km s^{-1} and from 300 to 355 km s^{-1} and in the MgI $\lambda 2853$ transition from 180 to 240 km s^{-1} . The confidence level in MINFIT had to be reduced to 0.80 in order to retain enough components to achieve a satisfactory fit.

A.48 **J024401-013402**

No MgII systems were found in this spectrum in the redshift range $1.1967 \leq z \leq 1.7209$.

A.49 **J024854+180250**

No MgII systems were found in this spectrum in the redshift range $1.3571 \leq z \leq 2.0670$.

A.50 J025134+431516

A.50.1 $z_{abs} = 0.655111$

This weak system was fit with four VP components, contains two subregions, and spans a total velocity width of 267 km s^{-1} . The confidence level in MINFIT had to be reduced to 0.77 in order to retain enough components to achieve a satisfactory fit.

A.50.2 $z_{abs} = 0.736163$

This weak system was fit with two VP components and spans a total velocity width of 25 km s^{-1} .

A.51 J025240-553832

A.51.1 $z_{abs} = 1.568340$

This weak system was fit with two VP components and spans a total velocity width of 50 km s^{-1} . This system occurs in a portion of the spectrum crowded with atmospheric lines; however, though spurious features occurred in the vicinity of the MgII $\lambda\lambda 2796, 2803$ doublet absorption, no masking was required.

A.51.2 $z_{abs} = 2.143195$

This strong system was fit with two VP components and spans a total velocity width of 100 km s^{-1} . A blend on the blue wing of the FeII $\lambda 2600$ feature was masked.

A.52 J025518+004847

No MgII systems were found in this spectrum in the redshift range $1.1606 \leq z \leq 1.9167$.

A.53 J025607+011038

A.53.1 $z_{abs} = 0.725487$

This very strong system was fit with 24 VP components and spans a total velocity width of 460 km s^{-1} . The saturation as well as the numerous clouds made this system difficult to fit. There was difficulty especially in fitting the FeII transitions as well as the MgI and MnII. The FeII $\lambda 2374$ feature in particular seems to have been fit in the saturated area with column densities that are too large. In the MgI and MnII transitions, some of the VP components appear too broad. In order to better constrain the MgII column densities relative to the FeII, we used the saturated regions option in MINFIT from -120 to 38 km s^{-1} . The confidence level in MINFIT had to be reduced to 0.54 in order to retain enough components to achieve a satisfactory fit.

A.54 J025634-401300

A.54.1 $z_{abs} = 0.549057$

This very strong system was fit with 17 VP components and spans a total velocity width of 345 km s^{-1} . A large blend was masked in the FeII $\lambda 2600$ feature from about -120 to 25 km s^{-1} , as well as a spurious feature in the MgI $\lambda 2853$ transition from 120

to 175 km s^{-1} . The confidence level in MINFIT had to be reduced to 0.07 in order to retain enough components to achieve a satisfactory fit.

A.54.2 $z_{abs} = 0.888692$

This strong system was fit with eight VP components and spans a total velocity width of 183 km s^{-1} .

A.54.3 $z_{abs} = 1.283867$

This very strong system was fit with nine VP components and spans a total velocity width of 155 km s^{-1} . In order to better constrain the MgII column densities relative to the FeII, we used the saturated regions option in MINFIT from -58 to -26 km s^{-1} and from 25 to 40 km s^{-1} . Also, one bad pixel was masked in the FeII $\lambda 2587$ feature at $\sim -45 \text{ km s}^{-1}$. The confidence level in MINFIT had to be reduced to 0.14 in order to retain enough components to achieve a satisfactory fit.

A.55 **J030211-314030**

No MgII systems were found in this spectrum in the redshift range $0.4651 \leq z \leq 1.3783$.

A.56 **J030449-000813**

No MgII systems were found in this spectrum in the redshift range $0.8650 \leq z \leq 1.3820$.

A.57 J030449-221152

A.57.1 $z_{abs} = 1.009382$

This very strong system was fit with seven VP components, contains two subregions, and spans a total velocity width of 213 km s^{-1} . The MgII $\lambda 2796$ transition contained no data blueward of $\sim -55 \text{ km s}^{-1}$. The confidence level in MINFIT had to be reduced to 0.84 in order to retain enough components to achieve a satisfactory fit.

A.58 J031009-192207

A.58.1 $z_{abs} = 0.889888$

This very strong system was fit with nine VP components and spans a total velocity width of 240 km s^{-1} . A small portion of the FeII $\lambda 2383$ feature was masked from -50 to -30 km s^{-1} because it is disproportionately strong and could not be fit.

A.58.2 $z_{abs} = 1.433701$

This weak system was fit with three VP components and spans a total velocity width of 50 km s^{-1} .

A.58.3 $z_{abs} = 1.636001$

This weak system was fit with five VP components, contains two subregions, and spans a total velocity width of 110 km s^{-1} . The confidence level in MINFIT had to be reduced to 0.45 in order to retain enough components to achieve a satisfactory fit.

A.58.4 $z_{abs} = 1.788440$

This very strong system spans a total velocity width of 313 km s^{-1} . Also, the badness parameter in MINFIT had to be increased to 5.0. One bad pixel in the MgII $\lambda 2796$ absorption was masked at $\sim -130 \text{ km s}^{-1}$. Although 21 VP components were fit, the parameters for one component were not well constrained. “Voigt Profile Fitting Results” on the included compact disc does not quote errors for this component, and the model should be viewed with caution. The confidence level in MINFIT had to be reduced to 0.07 in order to retain enough components to achieve a satisfactory fit.

A.58.5 $z_{abs} = 2.032104$

This strong system was fit with five VP components, contains two subregions, and spans a total velocity width of 120 km s^{-1} . Spurious features were masked in the FeII transitions from 15 to 27 km s^{-1} in $\lambda 2600$, from 7 to 50 km s^{-1} in $\lambda 2587$, and from 20 to 37 km s^{-1} and 50 to 60 km s^{-1} in $\lambda 2374$.

A.59 J033032-270438

A.59.1 $z_{abs} = 0.787945$

This strong system was fit with six VP components, contains four subregions, and spans a total velocity width of 240 km s^{-1} . Two spurious features in the FeII $\lambda 2344$ transition were masked from -180 to -140 km s^{-1} and from 57 to 100 km s^{-1} .

A.59.2 $z_{abs} = 1.122903$

This very strong system was fit with 13 VP components and spans a total velocity width of 243 km s^{-1} . Several bad pixels were masked in the MgII $\lambda 2796$ feature at ~ 25 and $\sim 50 \text{ km s}^{-1}$.

A.59.3 $z_{abs} = 1.298884$

This strong system was fit with eight VP components and spans a total velocity width of 202 km s^{-1} . The confidence level in MINFIT had to be reduced to 0.10 in order to retain enough components to achieve a satisfactory fit.

A.59.4 $z_{abs} = 1.306925$

This strong system was fit with five VP components and spans a total velocity width of 165 km s^{-1} . A small spurious feature was masked in the MnII $\lambda 2606$ transition at $\sim 70 \text{ km s}^{-1}$.

A.60 **J033106-382404**

A.60.1 $z_{abs} = 0.762781$

This strong system was fit with 10 VP components and spans a total velocity width of 215 km s^{-1} . The FeII absorption is noticeably weaker relative to MgII in the seventh component than in the surrounding clouds. The confidence level in MINFIT had to be reduced to 0.35 in order to retain enough components to achieve a satisfactory fit.

A.60.2 $z_{abs} = 0.929587$

This weak system was fit with two VP components and spans a total velocity width of 45 km s^{-1} . A spurious absorption feature was masked in the blue wing of the MgII $\lambda 2796$ line from about -50 to -20 km s^{-1} .

A.60.3 $z_{abs} = 0.970951$

This weak system was fit with two VP components and spans a total velocity width of 53 km s^{-1} .

A.60.4 $z_{abs} = 1.438023$

This strong system was fit with six VP components, contains two subregions, and spans a total velocity width of 202 km s^{-1} . Spurious features were masked in the FeII $\lambda 2587$ transition from -100 to -75 km s^{-1} and from 50 to 100 km s^{-1} . The confidence level in MINFIT had to be reduced to 0.82 in order to retain enough components to achieve a satisfactory fit.

A.61 **J033900-013318**

No MgII systems were found in this spectrum in the redshift range $0.8259 \leq z \leq 1.4200$.

A.62 J034943-381030

A.62.1 $z_{abs} = 1.457112$

This very strong system was fit with 13 VP components, contains three subregions, and spans a total velocity width of 399 km s^{-1} . This system occurs in a very crowded portion of the spectrum and suffers from extensive blending. Spurious features were masked in the MgII $\lambda 2796$ transition from 20 to 75 km s^{-1} ; in the MgII $\lambda 2803$ transition from -180 to -130 km s^{-1} and from 30 to 60 km s^{-1} ; and in the FeII $\lambda 2374$ transition at $\sim 50 \text{ km s}^{-1}$. The confidence level in MINFIT had to be reduced to 0.44 in order to retain enough components to achieve a satisfactory fit.

A.62.2 $z_{abs} = 1.526344$

This strong system was fit with 11 VP components and spans a total velocity width of 192 km s^{-1} .

A.63 J035405-272421

A.63.1 $z_{abs} = 1.405187$

This very strong system was fit with 18 VP components and spans a total velocity width of 388 km s^{-1} . Since this system is saturated in even the weakest of the FeII transitions, we used the saturated regions option in MINFIT from -73 to -47 km s^{-1} and from -15 to 60 km s^{-1} . The confidence level in MINFIT had to be reduced to 0.49 in order to retain enough components to achieve a satisfactory fit.

A.64 J040356-170324

No MgII systems were found in this spectrum in the redshift range $1.2724 \leq z \leq 1.7118$.

A.65 J040718-441013

A.65.1 $z_{abs} = 0.818400$

This very strong system was fit with 16 VP components, contains two subregions, and spans a total velocity width of 290 km s^{-1} . Though the MgII saturates, the MgI profile provides model constraints. The confidence level in MINFIT had to be reduced to 0.81 in order to retain enough components to achieve a satisfactory fit.

A.65.2 $z_{abs} = 1.017638$

This weak system was fit with two VP components and spans a total velocity width of 80 km s^{-1} .

A.65.3 $z_{abs} = 1.912359$

This very strong system was fit with nine VP components and spans a total velocity width of 222 km s^{-1} . The FeII $\lambda 2600$ transition from 25 to 75 km s^{-1} contains no data. Several pixels on the red wing of the MgII $\lambda 2803$ feature were masked because they do not correspond to the $\lambda 2796$ absorption. In order to better constrain the MgII column densities relative to the FeII, we used the saturated regions option in MINFIT from -53

to 74 km s^{-1} . The confidence level in MINFIT had to be reduced to 0.64 in order to retain enough components to achieve a satisfactory fit.

A.65.4 $z_{abs} = 2.412425$

This strong system was fit with three VP components and spans a total velocity width of 75 km s^{-1} . This system occurs in a crowded portion of the spectrum. Spurious features occur on both wings of the MgII $\lambda 2796$ absorption but did not interfere with the fit.

A.65.5 $z_{abs} = 2.550400$

This very strong system spans a total velocity width of 272 km s^{-1} . The MgII $\lambda 2796$ absorption in this system was too corrupted and could not be fit. All quantities quoted for this system refer to the $\lambda 2803$ transition rather than the $\lambda 2796$. Three bad pixels in the $\lambda 2803$ absorption at $\sim -80 \text{ km s}^{-1}$ were masked, as well as the spike in the data immediately blueward of the feature. In addition, blends in the blue wing of the FeII $\lambda 2383$ feature from -155 to -190 km s^{-1} , in the red wing of the FeII $\lambda 2587$ feature from 90 to 140 km s^{-1} , and in the FeII $\lambda 2374$ feature from -170 to -20 km s^{-1} were masked, as well as one bad pixel at $\sim 75 \text{ km s}^{-1}$ in the latter transition. Finally, the b parameter flag in MINFIT was changed from turbulent to thermal to improve the fit. Although 18 VP components were fit, the parameters for 10 components were not well constrained. “Voigt Profile Fitting Results” on the included compact disc does

not quote errors for these components, and the model should be viewed with caution.

A.66 J042214-384452

A.66.1 $z_{abs} = 1.880422$

This weak system was fit with five VP components, contains two subregions, and spans a total velocity width of 177 km s^{-1} .

A.67 J042315-012033

A.67.1 $z_{abs} = 0.633002$

This strong system was fit with seven VP components, contains two subregions, and spans a total velocity width of 297 km s^{-1} . The confidence level in MINFIT had to be reduced to 0.83 in order to retain enough components to achieve a satisfactory fit.

A.68 J042353-261801

A.68.1 $z_{abs} = 1.210044$

This weak system was fit with one VP component and spans a total velocity width of 30 km s^{-1} .

A.69 J042408+020425

A.69.1 $z_{abs} = 0.738949$

This weak system was fit with six VP components, contains three subregions, and spans a total velocity width of 244 km s^{-1} . Several pixels were masked just redward of region 3 in the MgI $\lambda 2853$ feature, from about 150 to 175 km s^{-1} ; the pixels are not believed to be part of the system, but MINFIT was fitting an excessively broad component in order to accommodate them. The confidence level in MINFIT had to be reduced to 0.88 in order to retain enough components to achieve a satisfactory fit.

A.70 J042707-130253

A.70.1 $z_{abs} = 1.034519$

This very strong system was fit with 20 VP components and spans a total velocity width of 267 km s^{-1} . The central portion of the absorption appears to be weaker than at adjacent velocities; this is seen more readily in the MgII $\lambda 2803$ transition than in the $\lambda 2796$. The large region of spurious absorption near the FeII $\lambda 2383$ line was masked from $\sim 100 \text{ km s}^{-1}$ redward. We also used the saturated regions option in MINFIT from -78 to -32 km s^{-1} and from 13 to 66 km s^{-1} .

A.70.2 $z_{abs} = 1.407984$

This weak system was fit with five VP components and spans a total velocity width of 82 km s^{-1} . The confidence level in MINFIT had to be reduced to 0.57 in order to

retain enough components to achieve a satisfactory fit.

A.71 J043037-485523

A.71.1 $z_{abs} = 0.554375$

This strong system was fit with five VP components and spans a total velocity width of 97 km s^{-1} . The double-pronged profile appears to be richer in FeII absorption in the blueward portion. The confidence level in MINFIT had to be reduced to 0.96 in order to retain enough components to achieve a satisfactory fit.

A.71.2 $z_{abs} = 1.119028$

This strong system was fit with six VP components, contains three subregions, and spans a total velocity width of 220 km s^{-1} . Two weak kinematic subsystems are present blueward of the main absorption. Atmospheric features had to be masked redward of the CaII $\lambda 3935$ absorption up to the blue wing, where the telluric lines blended with the feature.

A.71.3 $z_{abs} = 1.355354$

This strong system was fit with six VP components and spans a total velocity width of 132 km s^{-1} . The MgII profile is saturated throughout, but structure is gleaned from the other ions. An atmospheric feature was masked from the fit on the red wing of the CaII $\lambda 3935$ absorption.

A.72 J043038-133546

No MgII systems were found in this spectrum in the redshift range $0.8259 \leq z \leq 1.4432$.

A.73 J044017-433308

A.73.1 $z_{abs} = 1.433457$

This very strong system was fit with nine VP components and spans a total velocity width of 185 km s^{-1} . Two bad pixels were masked in the MgI $\lambda 2853$ transition at $\sim -40 \text{ km s}^{-1}$. In addition, spurious features were masked in the MnII $\lambda 2577$ transition from -220 to -80 km s^{-1} ; in the MnII $\lambda 2594$ transition from -40 to 10 km s^{-1} and from 50 to 75 km s^{-1} ; and in the MnII $\lambda 2606$ transition from -10 to 15 km s^{-1} . The confidence level in MINFIT had to be reduced to 0.45 in order to retain enough components to achieve a satisfactory fit.

A.73.2 $z_{abs} = 1.880918$

This weak system was fit with two VP components, contains two subregions, and spans a total velocity width of 62 km s^{-1} .

A.73.3 $z_{abs} = 2.347761$

This very strong system spans a total velocity width of 203 km s^{-1} . This system occurs in a very crowded portion of the spectrum and suffers from extensive blending.

Spurious features were masked on both wings of the MgII $\lambda 2796$ and $\lambda 2803$ absorption, as well as on the blue wing of the FeII $\lambda 2600$ line and to either side of the MgI $\lambda 2853$ absorption. The model in the latter feature was nevertheless distorted by the multiple lines in the vicinity and should be discounted. Although 10 VP components were fit, the parameters for one component were not well constrained. “Voigt Profile Fitting Results” on the included compact disc does not quote errors for this component, and the model should be viewed with caution. The confidence level in MINFIT had to be reduced to 0.63 in order to retain enough components to achieve a satisfactory fit.

A.74 J044026-163234

No MgII systems were found in this spectrum in the redshift range $0.2890 \leq z \leq 1.3785$.

A.75 J044117-431343

A.75.1 $z_{abs} = 0.440751$

This strong system was fit with four VP components and spans a total velocity width of 80 km s^{-1} .

A.76 J045142-132033

A.76.1 $z_{abs} = 1.266634$

This very strong system was fit with 11 VP components, contains two subregions, and spans a total velocity width of 242 km s^{-1} . Masking was used in the $\text{Mg II } \lambda 2803$ line from about 55 to 120 km s^{-1} due to the presence of a blend between the two absorption regions. Region 2 of the $\text{Fe II } \lambda 2383$ transition was completely masked since the feature there is too strong relative to that of the other Fe II lines and is believed to be spurious. The feature redward of the $\text{Fe II } \lambda 2600$ absorption, between about -120 and -60 km s^{-1} , was also masked. Finally, the spurious features in $\text{Mn II } \lambda 2577$, redward of about 75 km s^{-1} , were masked. The confidence level in MINFIT had to be reduced to 0.13 in order to retain enough components to achieve a satisfactory fit.

A.77 J045218-130503

A.77.1 $z_{abs} = 0.548068$

This strong system was fit with three VP components and spans a total velocity width of 61 km s^{-1} . Spurious features were masked on both wings of the $\text{Mg II } \lambda 2796$ transition. The confidence level in MINFIT had to be reduced to 0.88 in order to retain enough components to achieve a satisfactory fit.

A.77.2 $z_{abs} = 1.174630$

This very strong system was fit with 17 VP components, contains two subregions, and spans a total velocity width of 288 km s^{-1} . The confidence level in MINFIT had to be reduced to 0.37 in order to retain enough components to achieve a satisfactory fit.

A.77.3 $z_{abs} = 1.229493$

This weak system was fit with six VP components, contains three subregions, and spans a total velocity width of 521 km s^{-1} . The confidence level in MINFIT had to be reduced to 0.65 in order to retain enough components to achieve a satisfactory fit.

A.77.4 $z_{abs} = 1.310674$

This strong system was fit with eight VP components and spans a total velocity width of 150 km s^{-1} .

A.78 **J045523-421617**

A.78.1 $z_{abs} = 0.726105$

This very strong system was fit with 12 VP components and spans a total velocity width of 202 km s^{-1} .

A.78.2 $z_{abs} = 0.759820$

This weak system was fit with one VP component and spans a total velocity width of 25 km s^{-1} .

A.78.3 $z_{abs} = 0.908508$

This strong system was fit with 11 VP components, contains two subregions, and spans a total velocity width of 195 km s^{-1} . Though the MgII $\lambda 2796$ absorption is surrounded by spurious features, the fit of the system itself was not affected.

A.78.4 $z_{abs} = 1.039518$

This weak system was fit with five VP components, contains two subregions, and spans a total velocity width of 100 km s^{-1} . Spurious features in the region of the first VP component were masked in FeII $\lambda 2344$ and $\lambda 2374$. These features are not believed to be real FeII absorption due to the lack of corresponding absorption in the $\lambda 2600$ feature, which has the highest oscillator strength of all the FeII transitions present in this system.

A.78.5 $z_{abs} = 1.149873$

This very strong system contains two subregions and spans a total velocity width of 680 km s^{-1} . The saturation as well as the numerous clouds made this system difficult to fit. There was difficulty especially in fitting the FeII transitions as well as the MgI

and MnII. Attempts were made to use the saturated regions option in MINFIT over various velocity ranges and to change the b parameter flag in MINFIT from turbulent to thermal in order to improve the fit, but these changes were not kept in the final model. Spurious features were masked in FeII $\lambda 2383$ from about 320 to 380 km s⁻¹, in FeII $\lambda 2344$ from about 310 to 380 km s⁻¹, and in FeII $\lambda 2374$ from about -250 to -230 km s⁻¹. Although 39 VP components were fit, the parameters for 12 components were not well constrained. “Voigt Profile Fitting Results” on the included compact disc does not quote errors for these components, and the model should be viewed with caution.

A.78.6 $z_{abs} = 1.629987$

This strong system was fit with 11 VP components and spans a total velocity width of 195 km s⁻¹. Spurious absorption was masked in the MnII $\lambda 2606$ transition from -275 to -50 km s⁻¹. The confidence level in MINFIT had to be reduced to 0.02 in order to retain enough components to achieve a satisfactory fit.

A.78.7 $z_{abs} = 1.858376$

This weak system was fit with two VP components, contains two subregions, and spans a total velocity width of 140 km s⁻¹. A data spike was masked in the MgII $\lambda 2796$ transition at ~ 80 km s⁻¹.

A.78.8 $z_{abs} = 2.304567$

This strong system was fit with seven VP components and spans a total velocity width of 145 km s^{-1} .

A.79 **J045608-215909**

A.79.1 $z_{abs} = 0.474417$

This very strong system spans a total velocity width of 189 km s^{-1} . This is a highly kinematically concentrated profile; the MgII is saturated almost across the entire feature, though structure is detected in the weaker transitions. Although nine VP components were fit, the parameters for one component were not well constrained. “Voigt Profile Fitting Results” on the included compact disc does not quote errors for this component, and the model should be viewed with caution. The confidence level in MINFIT had to be reduced to 0.09 in order to retain enough components to achieve a satisfactory fit.

A.79.2 $z_{abs} = 0.483337$

This strong system was fit with six VP components and spans a total velocity width of 104 km s^{-1} . The confidence level in MINFIT had to be reduced to 0.50 in order to retain enough components to achieve a satisfactory fit.

A.80 J045647+040053

A.80.1 $z_{abs} = 0.642827$

This weak system was fit with one VP component and spans a total velocity width of 34 km s⁻¹.

A.80.2 $z_{abs} = 0.859569$

This very strong system spans a total velocity width of 189 km s⁻¹. Since this system is saturated in portions of even the weakest of the FeII transitions, we used the saturated regions option in MINFIT from -86 to 85 km s⁻¹. Although 15 VP components were fit, the parameters for one component were not well constrained. “Voigt Profile Fitting Results” on the included compact disc does not quote errors for this component, and the model should be viewed with caution. The confidence level in MINFIT had to be reduced to 0.66 in order to retain enough components to achieve a satisfactory fit.

A.80.3 $z_{abs} = 0.931502$

This weak system was fit with one VP component and spans a total velocity width of 27 km s⁻¹.

A.80.4 $z_{abs} = 1.153249$

This strong system was fit with seven VP components, contains three subregions, and spans a total velocity width of 217 km s^{-1} . This absorber consists of a strong central core with weak components blueward and redward of the main feature.

A.81 **J050112-015914**

A.81.1 $z_{abs} = 0.890257$

This strong system was fit with six VP components and spans a total velocity width of 133 km s^{-1} . The confidence level in MINFIT had to be reduced to 0.37 in order to retain enough components to achieve a satisfactory fit.

A.81.2 $z_{abs} = 2.039284$

This very strong system contains two subregions and spans a total velocity width of 260 km s^{-1} . Several bad pixels were masked in the FeII $\lambda 2383$ transition at $\sim -30 \text{ km s}^{-1}$ and $\sim 25 \text{ km s}^{-1}$. Although seven VP components were fit, the parameters for one component were not well constrained. “Voigt Profile Fitting Results” on the included compact disc does not quote errors for this component, and the model should be viewed with caution. The confidence level in MINFIT had to be reduced to 0.85 in order to retain enough components to achieve a satisfactory fit.

A.82 J051707-441055

A.82.1 $z_{abs} = 0.222241$

This weak system was fit with five VP components and spans a total velocity width of 142 km s^{-1} .

A.82.2 $z_{abs} = 0.429123$

This weak system was fit with one VP component and spans a total velocity width of 35 km s^{-1} .

A.82.3 $z_{abs} = 0.940626$

This weak system was fit with one VP component and spans a total velocity width of 26 km s^{-1} .

A.82.4 $z_{abs} = 1.150872$

This very strong system was fit with 40 VP components, contains two subregions, and spans a total velocity width of 736 km s^{-1} . This is a double system, captured cleanly except for the complex of spurious features that was masked redward of the MnII $\lambda 2594$ absorption beginning at $\sim 100 \text{ km s}^{-1}$. The confidence level in MINFIT had to be reduced to 0.57 in order to retain enough components to achieve a satisfactory fit.

A.83 J053007-250329

A.83.1 $z_{abs} = 0.944063$

This strong system was fit with four VP components, contains two subregions, and spans a total velocity width of 144 km s^{-1} . A small spurious feature was masked in the CaII $\lambda 3970$ transition at $\sim 120 \text{ km s}^{-1}$.

A.83.2 $z_{abs} = 1.672122$

This weak system was fit with three VP components, contains three subregions, and spans a total velocity width of 148 km s^{-1} .

A.83.3 $z_{abs} = 2.141121$

This very strong system spans a total velocity width of 267 km s^{-1} . Several bad pixels were masked in the MgII $\lambda 2796$ transition at $\sim -120 \text{ km s}^{-1}$. In addition, spurious features were masked on the blue wings of the FeII $\lambda 2383$, $\lambda 2344$, $\lambda 2587$, and $\lambda 2374$ transitions, and on both wings of the FeII $\lambda 2600$ transition. The saturation as well as the numerous clouds made this system difficult to fit. The MnII $\lambda 2577$ feature was fit with some VP components having column densities that are too small. Although 20 VP components were fit, none had well-constrained parameters. “Voigt Profile Fitting Results” on the included compact disc does not quote errors for these components, and the model should be viewed with caution. The confidence level in MINFIT had to be reduced to 0.88 in order to retain enough components to achieve a satisfactory fit.

A.84 J053008-250330

No MgII systems were found in this spectrum in the redshift range $0.6429 \leq z \leq 2.6071$.

A.85 J053056+133154

A.85.1 $z_{abs} = 1.576187$

This very strong system was fit with 12 VP components, contains three subregions, and spans a total velocity width of 427 km s^{-1} . In order to better constrain the MgII column densities relative to the FeII, we used the saturated regions option in MINFIT from -72 to 63 km s^{-1} . The confidence level in MINFIT had to be reduced to 0.44 in order to retain enough components to achieve a satisfactory fit.

A.85.2 $z_{abs} = 1.963172$

This strong system was fit with five VP components, contains two subregions, and spans a total velocity width of 85 km s^{-1} . The confidence level in MINFIT had to be reduced to 0.86 in order to retain enough components to achieve a satisfactory fit.

A.86 J055158-211949

A.86.1 $z_{abs} = 0.439830$

This strong system was fit with two VP components and spans a total velocity width of 72 km s^{-1} .

A.87 J055246-363727

A.87.1 $z_{abs} = 0.505570$

This weak system was fit with three VP components, contains two subregions, and spans a total velocity width of 67 km s^{-1} .

A.87.2 $z_{abs} = 1.225244$

This strong system was fit with five VP components, contains two subregions, and spans a total velocity width of 128 km s^{-1} .

A.87.3 $z_{abs} = 1.492188$

This weak system was fit with two VP components and spans a total velocity width of 60 km s^{-1} .

A.87.4 $z_{abs} = 1.961208$

This very strong system contains two subregions and spans a total velocity width of 830 km s^{-1} . The saturation as well as the numerous clouds made this system difficult to fit. There was difficulty especially in fitting the FeII transitions, which are modeled too weakly around 175 km s^{-1} . Attempts were made to use the saturated regions option in MINFIT over various velocity ranges and to change the b parameter flag in MINFIT from turbulent to thermal in order to improve the fit, but these changes were not kept in the final model. Spurious features were masked in MgII $\lambda 2796$ at ~ 300

km s⁻¹ (a blend on the red wing of region 2); in MgII λ 2803 from -600 to -475 km s⁻¹; in FeII λ 2600 from -575 to -500 km s⁻¹ and -465 to -430 km s⁻¹; in FeII λ 2587 from -575 to -425 km s⁻¹, -340 to -260 km s⁻¹, -140 to -60 km s⁻¹, and 270 to 360 km s⁻¹ (all atmospheric); in MgI λ 2853 at \sim 240 km s⁻¹ (a small data spike); and in region 1 of the MnII λ 2606 feature from -600 to -400 km s⁻¹. Although 43 VP components were fit, the parameters for 37 components were not well constrained. “Voigt Profile Fitting Results” on the included compact disc does not quote errors for these components, and the model should be viewed with caution. The confidence level in MINFIT had to be reduced to 0.14 in order to retain enough components to achieve a satisfactory fit.

A.88 J064204+675836

A.88.1 $z_{abs} = 1.293828$

This strong system was fit with six VP components and spans a total velocity width of 150 km s⁻¹.

A.89 J064326-504112

No MgII systems were found in this spectrum in the redshift range $0.7781 \leq z \leq 2.3854$.

A.90 J064632+445117

No MgII systems were found in this spectrum in the redshift range $0.9163 \leq z \leq 1.4285$.

A.91 J074521+473436

A.91.1 $z_{abs} = 0.857331$

This weak system was fit with three VP components and spans a total velocity width of 66 km s^{-1} .

A.91.2 $z_{abs} = 0.891322$

This weak system was fit with three VP components, contains two subregions, and spans a total velocity width of 156 km s^{-1} . A large spurious feature was masked in the FeII $\lambda 2383$ feature from $\sim -55 \text{ km s}^{-1}$ blueward.

A.91.3 $z_{abs} = 1.611153$

This strong system was fit with five VP components and spans a total velocity width of 99 km s^{-1} . A large spurious feature was masked in the FeII $\lambda 2383$ feature from $\sim -20 \text{ km s}^{-1}$ blueward.

A.92 J075054+425219

No MgII systems were found in this spectrum in the redshift range $0.2594 \leq z \leq 0.7463$.

A.93 J075112+291938

No MgII systems were found in this spectrum in the redshift range $0.3358 \leq z \leq 0.8833$.

A.94 J080117+521034

No MgII systems were found in this spectrum in the redshift range $0.8410 \leq z \leq 1.4153$.

A.95 J081240+320808

A.95.1 $z_{abs} = 1.223076$

This very strong system was fit with 14 VP components, contains two subregions, and spans a total velocity width of 312 km s^{-1} . This double system is characterized by the two strong main absorption components as well as, in this instance, a weaker redward subsystem. The confidence level in MINFIT had to be reduced to 0.69 in order to retain enough components to achieve a satisfactory fit.

A.96 J081331+254503

A.96.1 $z_{abs} = 0.821724$

This weak system was fit with five VP components and spans a total velocity width of 127 km s^{-1} .

A.96.2 $z_{abs} = 0.831524$

This weak system was fit with seven VP components and spans a total velocity width of 140 km s^{-1} .

A.97 J083141+524518

A.97.1 $z_{abs} = 1.180673$

This very strong system was fit with 16 VP components and spans a total velocity width of 244 km s^{-1} . This system contains extensive blending. The MgII $\lambda 2796$ feature had to be masked blueward of $\sim -180 \text{ km s}^{-1}$ and redward of $\sim 110 \text{ km s}^{-1}$, the $\lambda 2803$ line blueward of $\sim -130 \text{ km s}^{-1}$ and redward of $\sim 100 \text{ km s}^{-1}$, and the $\lambda 2803$ line blueward of $\sim -130 \text{ km s}^{-1}$ and redward of $\sim 110 \text{ km s}^{-1}$. Initially only the MgII $\lambda 2796$ was masked, but MINFIT would not function without some $\lambda 2803$ masking. The $\lambda 2803$ profile appears to be blended in any case on the blue wing since the absorption in that portion of the transition is stronger than that of the corresponding $\lambda 2796$ absorption. The confidence level in MINFIT had to be reduced to 0.35 in order to retain enough components to achieve a satisfactory fit.

A.97.2 $z_{abs} = 1.290840$

This weak system was fit with two VP components and spans a total velocity width of 71 km s^{-1} .

A.97.3 $z_{abs} = 1.549929$

This strong system was fit with 12 VP components, contains three subregions, and spans a total velocity width of 533 km s^{-1} . Portions of the MgII $\lambda 2803$ absorption are too strong, likely due to faulty data reduction. Spurious features were masked in the FeII $\lambda 2600$ transition from -80 to -50 km s^{-1} and from -10 to 0 km s^{-1} ; in the FeII $\lambda 2587$ transition from -75 to -30 km s^{-1} ; in the FeII $\lambda 2374$ transition from 230 to 400 km s^{-1} ; and in the MgII $\lambda 2853$ transition from -75 to 25 km s^{-1} . The b parameter flag in MINFIT was also changed from turbulent to thermal to improve the fit. The confidence level in MINFIT had to be reduced to 0.58 in order to retain enough components to achieve a satisfactory fit.

A.97.4 $z_{abs} = 1.812894$

This strong system was fit with seven VP components and spans a total velocity width of 218 km s^{-1} . The MgII $\lambda 2803$ feature was masked from 10 to 50 km s^{-1} . Due to a possible blend or faulty data reduction, the profile is too strong relative to the MgII $\lambda 2796$ line. In addition, spurious features were masked in the FeII $\lambda 2587$ transition from -120 to -20 km s^{-1} and from 15 to 100 km s^{-1} and in the MnII $\lambda 2577$

transition from -70 to 15 km s⁻¹. The confidence level in MINFIT had to be reduced to 0.23 in order to retain enough components to achieve a satisfactory fit.

A.97.5 $z_{abs} = 2.041735$

This weak system was fit with four VP components and spans a total velocity width of 92 km s⁻¹. Three bad pixels were masked in the MgII $\lambda 2796$ feature at ~ 15 km s⁻¹. The model does not ideally fit the first VP component in both the MgII $\lambda 2796$ and the $\lambda 2803$ transitions; the column density appears to have been fit too strongly in the former and too weakly in the latter, possibly due to noise or faulty reduction in the data. The confidence level in MINFIT had to be reduced to 0.17 in order to retain enough components to achieve a satisfactory fit.

A.98 **J083052+241100**

A.98.1 $z_{abs} = 0.524966$

This very strong system spans a total velocity width of 307 km s⁻¹. The b parameter flag in MINFIT was changed from turbulent to thermal to improve the fit. Although 18 VP components were fit, the parameters for four components were not well constrained. “Voigt Profile Fitting Results” on the included compact disc does not quote errors for these components, and the model should be viewed with caution. The confidence level in MINFIT had to be reduced to 0.43 in order to retain enough components to achieve a satisfactory fit.

A.99 J083933+111207

No MgII systems were found in this spectrum in the redshift range $0.6085 \leq z \leq 1.5680$.

A.100 J084424+124546

A.100.1 $z_{abs} = 0.709230$

This weak system was fit with three VP components and spans a total velocity width of 56 km s^{-1} .

A.100.2 $z_{abs} = 1.098401$

This very strong system was fit with 16 VP components and spans a total velocity width of 303 km s^{-1} . Spurious features were masked in the MgII $\lambda 2796$ transition from 120 to 155 km s^{-1} and in the CaII $\lambda 3935$ transition from -110 to -70 km s^{-1} . The confidence level in MINFIT had to be reduced to 0.16 in order to retain enough components to achieve a satisfactory fit.

A.100.3 $z_{abs} = 1.131402$

This weak system was fit with four VP components, contains three subregions, and spans a total velocity width of 290 km s^{-1} . Spurious features were masked in the FeII $\lambda 2374$ at $\sim -230 \text{ km s}^{-1}$ and $\sim -25 \text{ km s}^{-1}$.

A.100.4 $z_{abs} = 1.219175$

This very strong system was fit with 22 VP components and spans a total velocity width of 487 km s^{-1} . A spurious feature was masked in the CaII $\lambda 3935$ transition from -170 to 20 km s^{-1} . The confidence level in MINFIT had to be reduced to 0.62 in order to retain enough components to achieve a satisfactory fit.

A.100.5 $z_{abs} = 1.863904$

This strong system was fit with three VP components and spans a total velocity width of 77 km s^{-1} . One bad pixel was masked in the MgII $\lambda 2796$ transition at $\sim -8 \text{ km s}^{-1}$.

A.100.6 $z_{abs} = 2.374482$

This strong system was fit with five VP components and spans a total velocity width of 126 km s^{-1} . This system occurs in a very crowded portion of the spectrum and suffers from extensive blending. Spurious features were masked in the MgII $\lambda 2796$ transition from -80 to -50 km s^{-1} ; on both wings of the MgII $\lambda 2803$ transition as well as four bad pixels at $\sim 28 \text{ km s}^{-1}$; and in the FeII $\lambda 2587$ transition from 30 km s^{-1} redward.

A.101 J090033+421546

A.101.1 $z_{abs} = 1.355719$

This strong system was fit with 11 VP components and spans a total velocity width of 172 km s^{-1} . The blue wing of the FeII $\lambda 2374$ feature is blended and was masked from about -110 to -10 km s^{-1} . The features just blueward of the MgII lines are spurious. The confidence level in MINFIT had to be reduced to 0.77 in order to retain enough components to achieve a satisfactory fit.

A.102 J091127+055054

A.102.1 $z_{abs} = 0.774684$

This weak system was fit with one VP component and spans a total velocity width of 30 km s^{-1} .

A.102.2 $z_{abs} = 0.994627$

This weak system was fit with one VP component and spans a total velocity width of 40 km s^{-1} .

A.102.3 $z_{abs} = 1.210128$

This weak system was fit with four VP components and spans a total velocity width of 70 km s^{-1} .

A.103 J091613+070224

A.103.1 $z_{abs} = 1.187206$

This weak system was fit with one VP component and spans a total velocity width of 30 km s⁻¹.

A.103.2 $z_{abs} = 1.332451$

This strong system was fit with four VP components and spans a total velocity width of 88 km s⁻¹.

A.104 J092913-021446

A.104.1 $z_{abs} = 1.096330$

This weak system was fit with one VP component and spans a total velocity width of 24 km s⁻¹.

A.104.2 $z_{abs} = 1.106422$

This strong system was fit with 11 VP components, contains two subregions, and spans a total velocity width of 491 km s⁻¹. The spurious features at ~ 90 km s⁻¹ in the MgII $\lambda 2796$ absorption and at ~ -390 km s⁻¹ in the $\lambda 2803$ did not interfere with the fit and were not masked. The confidence level in MINFIT had to be reduced to 0.32 in order to retain enough components to achieve a satisfactory fit.

A.104.3 $z_{abs} = 1.232216$

This weak system was fit with three VP components, contains two subregions, and spans a total velocity width of 93 km s^{-1} .

A.105 **J093337+284532**

No MgII systems were found in this spectrum in the redshift range $0.9221 \leq z \leq 1.5636$.

A.106 **J093748+730158**

No MgII systems were found in this spectrum in the redshift range $0.5337 \leq z \leq 1.3247$.

A.107 **J094253-110426**

A.107.1 $z_{abs} = 1.059675$

This strong system was fit with five VP components and spans a total velocity width of 153 km s^{-1} . Large spurious features were masked in the FeII $\lambda 2383$ transition from $\sim 30 \text{ km s}^{-1}$ redward; in the MnII $\lambda 2594$ transition from $\sim 28 \text{ km s}^{-1}$ redward; and in the MnII $\lambda 2606$ transition at $\sim -40 \text{ km s}^{-1}$ and from $\sim 0 \text{ km s}^{-1}$ redward. The confidence level in MINFIT had to be reduced to 0.96 in order to retain enough components to achieve a satisfactory fit.

A.107.2 $z_{abs} = 1.789114$

This very strong system was fit with 14 VP components, contains two subregions, and spans a total velocity width of 310 km s^{-1} . Spurious features were masked in the FeII $\lambda 2600$ feature from $\sim 70 \text{ km s}^{-1}$ redward and in the FeII $\lambda 2587$ feature at $\sim 175 \text{ km s}^{-1}$. The confidence level in MINFIT had to be reduced to 0.05 in order to retain enough components to achieve a satisfactory fit.

A.107.3 $z_{abs} = 1.918429$

This very strong system was fit with 12 VP components and spans a total velocity width of 305 km s^{-1} . Spurious features were masked on both wings of the MgII $\lambda 2796$ absorption; in the MgII $\lambda 2803$ feature from about -125 to -80 km s^{-1} ; in the FeII $\lambda 2383$ feature at $\sim -125 \text{ km s}^{-1}$ (there is real absorption at that velocity, but due to a blend with an atmospheric line, the component had to be excluded from the fit); in the MgI $\lambda 2853$ feature from about -115 to -70 km s^{-1} ; and in the MnII $\lambda 2594$ feature at $\sim 85 \text{ km s}^{-1}$ (a small data spike). Finally, the b parameter flag in MINFIT was changed from turbulent to thermal to improve the fit. The confidence level in MINFIT had to be reduced to 0.68 in order to retain enough components to achieve a satisfactory fit.

A.107.4 $z_{abs} = 2.174545$

This weak system was fit with one VP component and spans a total velocity width of 31 km s^{-1} .

A.108 J094835+432302

A.108.1 $z_{abs} = 1.232747$

This very strong system was fit with 12 VP components and spans a total velocity width of 174 km s^{-1} . Since this system is saturated in even the weakest of the FeII transitions, we used the saturated regions option in MINFIT from -50 to 50 km s^{-1} . The confidence level in MINFIT had to be reduced to 0.03 in order to retain enough components to achieve a satisfactory fit.

A.109 J095122+263514

No MgII systems were found in this spectrum in the redshift range $0.2843 \leq z \leq 0.8334$.

A.110 J095355-050418

No MgII systems were found in this spectrum in the redshift range $1.3345 \leq z \leq 1.9997$.

A.111 J095500-013006

A.111.1 $z_{abs} = 1.625062$

This strong system was fit with three VP components and spans a total velocity width of 99 km s^{-1} . The confidence level in MINFIT had to be reduced to 0.71 in order to retain enough components to achieve a satisfactory fit.

A.112 J095744+330820

No MgII systems were found in this spectrum in the redshift range $1.3024 \leq z \leq 2.1325$.

A.113 J095852+120245

No MgII systems were found in this spectrum in the redshift range $0.8720 \leq z \leq 1.4421$.

A.114 J100120.8+555354

A.114.1 $z_{abs} = 0.903934$

This weak system was fit with one VP component and spans a total velocity width of 32 km s^{-1} .

A.114.2 $z_{abs} = 1.024809$

This weak system was fit with three VP components and spans a total velocity width of 80 km s^{-1} .

A.114.3 $z_{abs} = 1.124273$

This weak system was fit with three VP components and spans a total velocity width of 44 km s^{-1} . The confidence level in MINFIT had to be reduced to 0.30 in order to retain enough components to achieve a satisfactory fit.

A.115 J100120.9+555349

A.115.1 $z_{abs} = 1.124587$

This weak system was fit with four VP components and spans a total velocity width of 71 km s⁻¹.

A.116 J100129+545438

A.116.1 $z_{abs} = 1.211316$

This weak system was fit with one VP component and spans a total velocity width of 23 km s⁻¹.

A.116.2 $z_{abs} = 1.272383$

This weak system was fit with one VP component and spans a total velocity width of 74 km s⁻¹.

A.117 J101155+294141

A.117.1 $z_{abs} = 1.111735$

This strong system was fit with six VP components and spans a total velocity width of 75 km s⁻¹. The confidence level in MINFIT had to be reduced to 0.17 in order to retain enough components to achieve a satisfactory fit.

A.118 J100930-002619

A.118.1 $z_{abs} = 0.842755$

This strong system was fit with eight VP components and spans a total velocity width of 122 km s^{-1} . The confidence level in MINFIT had to be reduced to 0.25 in order to retain enough components to achieve a satisfactory fit.

A.118.2 $z_{abs} = 0.886487$

This very strong system contains two subregions and spans a total velocity width of 358 km s^{-1} . This system is notable for its weak subsystems, which lie both blueward and redward of the strongest, saturated feature. Although 20 VP components were fit, the parameters for five components were not well constrained. “Voigt Profile Fitting Results” on the included compact disc does not quote errors for these components, and the model should be viewed with caution. The confidence level in MINFIT had to be reduced to 0.27 in order to retain enough components to achieve a satisfactory fit.

A.119 J101447+430031

A.119.1 $z_{abs} = 1.416350$

This very strong system was fit with 19 VP components and spans a total velocity width of 343 km s^{-1} . In order to better constrain the MgII column densities relative to the FeII, we used the saturated regions option in MINFIT from -82 to 68 km s^{-1} . Also, spurious, possibly atmospheric features were masked in FeII $\lambda 2600$ from about

-175 to -155 km s⁻¹ and in Mn II λ 2577 from about -105 to -25 km s⁻¹. The confidence level in MINFIT had to be reduced to 0.84 in order to retain enough components to achieve a satisfactory fit.

A.119.2 $z_{abs} = 2.042606$

This weak system was fit with four VP components, contains two subregions, and spans a total velocity width of 163 km s⁻¹.

A.120 **J101549+002019**

No Mg II systems were found in this spectrum in the redshift range $1.3497 \leq z \leq 2.0598$.

A.121 **J102156+300141**

A.121.1 $z_{abs} = 1.274372$

This strong system was fit with 11 VP components, contains five subregions, and spans a total velocity width of 360 km s⁻¹. Two bad pixels were masked in the Mg II λ 2803 transition at ~ 24 km s⁻¹, as well as spurious absorption in Fe II λ 2344 from about -30 to -80 km s⁻¹ and from about 80 to 195 km s⁻¹. The confidence level in MINFIT had to be reduced to 0.27 in order to retain enough components to achieve a satisfactory fit.

A.122 J102837-010027

A.122.1 $z_{abs} = 0.708803$

This very strong system was fit with seven VP components and spans a total velocity width of 165 km s^{-1} . Since this system is saturated in even the weakest of the FeII transitions, we used the saturated regions option in MINFIT from -49 to 49 km s^{-1} . The red wing of the FeII $\lambda 2344$ transition was masked from about 50 to 60 km s^{-1} because that portion of the feature does not correspond to the other FeII profiles.

A.123 J103623-034320

No MgII systems were found in this spectrum in the redshift range $1.3950 \leq z \leq 2.0707$.

A.124 J104117+061016

A.124.1 $z_{abs} = 0.441452$

This strong system was fit with seven VP components and spans a total velocity width of 167 km s^{-1} .

A.124.2 $z_{abs} = 0.655331$

This weak system was fit with four VP components, contains three subregions, and spans a total velocity width of 202 km s^{-1} . This absorber contains three kinematic

regions ranging from 0.013 to 0.078 Å in equivalent width. The confidence level in MINFIT had to be reduced to 0.96 in order to retain enough components to achieve a satisfactory fit.

A.125 J104733+052454

A.125.1 $z_{abs} = 0.198417$

This strong system was fit with five VP components and spans a total velocity width of 95 km s⁻¹.

A.125.2 $z_{abs} = 0.318212$

This weak system was fit with one VP component and spans a total velocity width of 38 km s⁻¹.

A.125.3 $z_{abs} = 0.801159$

This strong system was fit with five VP components and spans a total velocity width of 100 km s⁻¹.

A.126 J104800+052209

No MgII systems were found in this spectrum in the redshift range $0.0888 \leq z \leq 1.1940$.

A.127 J105440-002048

A.127.1 $z_{abs} = 0.830173$

This very strong system spans a total velocity width of 188 km s^{-1} . This is a highly kinematically concentrated profile; the MgII is saturated throughout, though structure is detected in the weaker transitions. Although 12 VP components were fit, the parameters for one component were not well constrained. “Voigt Profile Fitting Results” on the included compact disc does not quote errors for this component, and the model should be viewed with caution. The confidence level in MINFIT had to be reduced to 0.05 in order to retain enough components to achieve a satisfactory fit.

A.127.2 $z_{abs} = 0.941984$

This weak system was fit with four VP components and spans a total velocity width of 80 km s^{-1} . Four pixels were masked at $\sim 30 \text{ km s}^{-1}$ in the MgI $\lambda 2853$ feature. They are believed to be noise in the data but were causing MINFIT to attempt to model that portion of the spectrum. The spurious features blueward of the FeII $\lambda 2600$ line did not interfere with the fit and were not masked. The confidence level in MINFIT had to be reduced to 0.96 in order to retain enough components to achieve a satisfactory fit.

A.127.3 $z_{abs} = 0.951693$

This strong system was fit with 10 VP components, contains four subregions, and spans a total velocity width of 582 km s^{-1} . Note the kinematically complex structure,

including the very weak high velocity subsystem at $\sim -500 \text{ km s}^{-1}$.

A.128 J105756+455552

A.128.1 $z_{abs} = 1.386417$

This very strong system was fit with 11 VP components and spans a total velocity width of 234 km s^{-1} . Blending on the red wings of both the MgII $\lambda 2796$ and $\lambda 2803$ lines was masked. The excluded absorption is believed to be spurious because the doublet ratio in that velocity range (above $\sim 125 \text{ km s}^{-1}$) is inconsistent with the MgII $\lambda\lambda 2796, 2803$ doublet ratio range of $1 \leq DR \leq 2$. The confidence level in MINFIT had to be reduced to 0.13 in order to retain enough components to achieve a satisfactory fit.

A.128.2 $z_{abs} = 1.522192$

This weak system was fit with three VP components, contains two subregions, and spans a total velocity width of 82 km s^{-1} . Spurious absorption was masked on the red wing of the MgII $\lambda 2803$ feature from 58 to 75 km s^{-1} and in the FeII $\lambda 2600$ transition from 20 to 100 km s^{-1} .

A.128.3 $z_{abs} = 1.567824$

This weak system was fit with six VP components, contains two subregions, and spans a total velocity width of 115 km s^{-1} . The confidence level in MINFIT had to be

reduced to 0.36 in order to retain enough components to achieve a satisfactory fit.

A.129 J110325-264515

A.129.1 $z_{abs} = 1.186892$

This strong system was fit with nine VP components, contains two subregions, and spans a total velocity width of 212 km s^{-1} . There is a relative deficiency of FeII to MgII in the redward components as compared to the $\sim 0 \text{ km s}^{-1}$ central absorption feature.

A.129.2 $z_{abs} = 1.202831$

This strong system was fit with nine VP components and spans a total velocity width of 203 km s^{-1} . Atmospheric features were masked both blueward and redward of the MgI $\lambda 2853$ absorption.

A.129.3 $z_{abs} = 1.211354$

This weak system was fit with one VP component and spans a total velocity width of 30 km s^{-1} .

A.129.4 $z_{abs} = 1.267694$

This weak system was fit with two VP components and spans a total velocity width of 55 km s^{-1} . A small spurious feature had to be masked near the region of the CaII $\lambda 3935$ feature at $\sim -15 \text{ km s}^{-1}$. A column density was calculated for the second

of the two VP components in CaII (see “Voigt Profile Fitting Results” on the included compact disc). The atmospheric lines near the CaII $\lambda 3970$ feature did not interfere with the fit.

A.129.5 $z_{abs} = 1.551516$

This weak system was fit with two VP components and spans a total velocity width of 37 km s^{-1} .

A.129.6 $z_{abs} = 1.838688$

This very strong system was fit with 12 VP components and spans a total velocity width of 247 km s^{-1} .

A.130 **J1111038+483116**

A.130.1 $z_{abs} = 0.807537$

This strong system was fit with five VP components and spans a total velocity width of 116 km s^{-1} . The confidence level in MINFIT had to be reduced to 0.96 in order to retain enough components to achieve a satisfactory fit.

A.130.2 $z_{abs} = 0.861875$

This very strong system was fit with nine VP components, contains three subregions, and spans a total velocity width of 336 km s^{-1} . The third region in MgII $\lambda 2803$

was completely masked due to either a blend or faulty continuum fit, which made the absorption in that feature too strong relative to the MgII $\lambda 2796$.

A.130.3 $z_{abs} = 1.015805$

This weak system was fit with two VP components, contains two subregions, and spans a total velocity width of 115 km s⁻¹.

A.131 **J111113-080402**

A.131.1 $z_{abs} = 1.901669$

This strong system was fit with four VP components, contains two subregions, and spans a total velocity width of 146 km s⁻¹.

A.131.2 $z_{abs} = 1.975442$

This very strong system was fit with 22 VP components, contains five subregions, and spans a total velocity width of 548 km s⁻¹. Several bad pixels were masked in the MgII $\lambda 2803$ feature at ~ 120 and 180 km s⁻¹, as well as spurious features in the FeII $\lambda 2383$ transition from -230 to -80 km s⁻¹ and in the FeII $\lambda 2587$ at ~ -150 km s⁻¹ and ~ 80 km s⁻¹. The latter transition contains no data from -275 km s⁻¹ blueward. The confidence level in MINFIT had to be reduced to 0.08 in order to retain enough components to achieve a satisfactory fit.

A.132 J111350-153333

A.132.1 $z_{abs} = 1.038732$

This very strong system was fit with 13 VP components and spans a total velocity width of 245 km s^{-1} . Three bad pixels were masked in the MgII $\lambda 2796$ absorption at $\sim 55 \text{ km s}^{-1}$, as well as a small spurious feature in the MnII $\lambda 2606$ transition at $\sim -130 \text{ km s}^{-1}$. The confidence level in MINFIT had to be reduced to 0.23 in order to retain enough components to achieve a satisfactory fit.

A.132.2 $z_{abs} = 1.256076$

This weak system was fit with two VP components and spans a total velocity width of 50 km s^{-1} .

A.133 J222006-280323

A.133.1 $z_{abs} = 0.599508$

This weak system was fit with two VP components and spans a total velocity width of 54 km s^{-1} .

A.133.2 $z_{abs} = 0.786511$

This weak system was fit with five VP components and spans a total velocity width of 102 km s^{-1} . The complex of absorption redward of the MgII $\lambda 2796$ line is spurious, but did not need to be masked.

A.133.3 $z_{abs} = 0.942415$

This strong system was fit with 11 VP components, contains two subregions, and spans a total velocity width of 420 km s⁻¹.

A.133.4 $z_{abs} = 1.082795$

This weak system was fit with four VP components and spans a total velocity width of 61 km s⁻¹. The feature just blueward of the MgII $\lambda 2796$ feature is not believed to be part of the system. An atmospheric feature on the blue wing of the CaII $\lambda 3935$ absorption was masked from about -50 to -10 km s⁻¹.

A.133.5 $z_{abs} = 1.555851$

This weak system was fit with six VP components, contains two subregions, and spans a total velocity width of 119 km s⁻¹. The weak features present in both MgII $\lambda\lambda 2796, 2803$ doublet transitions at ~ -80 km s⁻¹ are not aligned in velocity and are not believed to be part of the system. In addition, a spurious feature in the MgI $\lambda 2853$ transition at ~ 30 km s⁻¹ was masked.

A.133.6 $z_{abs} = 1.627859$

This strong system was fit with eight VP components and spans a total velocity width of 133 km s⁻¹. The confidence level in MINFIT had to be reduced to 0.92 in order to retain enough components to achieve a satisfactory fit.

A.133.7 $z_{abs} = 1.692150$

This very strong system spans a total velocity width of 362 km s^{-1} . Numerous atmospheric features were masked in the MgI $\lambda 2853$ transition as well as in all three of the MnII transitions. Although 14 VP components were fit, none had well-constrained parameters. “Voigt Profile Fitting Results” on the included compact disc does not quote errors for these components, and the model should be viewed with caution.

A.134 **J111654-221652**

No MgII systems were found in this spectrum in the redshift range $0.4268 \leq z \leq 1.3788$.

A.135 **J112442-170517****A.135.1** $z_{abs} = 0.682269$

This very strong system was fit with 15 VP components, contains two subregions, and spans a total velocity width of 325 km s^{-1} . This system is unusual in that it consists of a saturated central profile with weaker absorption occurring both redward and blueward of the core. Blending in the redward portion of the FeII $\lambda 2344$ feature was masked from $\sim 70 \text{ km s}^{-1}$ onward. The b parameter flag in MINFIT was changed from turbulent to thermal to improve the fit. The confidence level in MINFIT had to be reduced to 0.12 in order to retain enough components to achieve a satisfactory fit.

A.135.2 $z_{abs} = 0.806213$

This weak system was fit with eight VP components, contains two subregions, and spans a total velocity width of 193 km s^{-1} . Absorption is concentrated at the red and blue extremes of the profile. Very weak absorption was detected in CaII in clouds 6 and 8. Atmospheric lines were masked about -25 to 25 km s^{-1} and 75 to 125 km s^{-1} of the CaII $\lambda 3970$ line.

A.135.3 $z_{abs} = 1.234142$

This weak system was fit with three VP components and spans a total velocity width of 102 km s^{-1} .

A.136 **J113007-144927**

A.136.1 $z_{abs} = 0.190569$

This weak system was fit with one VP component and spans a total velocity width of 83 km s^{-1} .

A.136.2 $z_{abs} = 0.312709$

This very strong system was fit with 14 VP components, contains two subregions, and spans a total velocity width of 307 km s^{-1} . Since this system is saturated in even the weakest of the FeII transitions, we used the saturated regions option in MINFIT from -94 to 88 km s^{-1} . The b parameter flag in MINFIT was also changed from

turbulent to thermal to improve the fit. The region blueward of the FeII $\lambda 2383$ feature, from about -210 to -130 km s⁻¹, is believed to be either bad data or a faulty continuum fit, and was masked.

A.137 J113508+222716

A.137.1 $z_{abs} = 0.718958$

This weak system was fit with three VP components and spans a total velocity width of 50 km s⁻¹. The spurious feature blended with the red wing of the MgII $\lambda 2796$ absorption was masked from about 30 to 70 km s⁻¹.

A.138 J114254+265457

A.138.1 $z_{abs} = 1.711805$

This very strong system spans a total velocity width of 335 km s⁻¹. The MgII $\lambda 2803$ feature in this system was severely blended and could not be fit. Small features on the blue and red wings of the MgII $\lambda 2796$ feature were masked blueward of -150 km s⁻¹ and redward of 170 km s⁻¹. These features were conservatively not considered part of the system since the next strongest available transition, the FeII $\lambda 2600$, did not contain corresponding absorption at these velocities. Two small blends in the FeII $\lambda 2587$ feature at ~ -70 km s⁻¹ and ~ 175 km s⁻¹ were also masked. Finally, spurious features in the MnII $\lambda 2577$ transition were masked from -40 to 62 km s⁻¹ and from 80 to 115 km s⁻¹. The b parameter flag in MINFIT was changed from turbulent to

thermal to improve the fit. Although 23 VP components were fit, the parameters for five components were not well constrained. “Voigt Profile Fitting Results” on the included compact disc does not quote errors for these components, and the model should be viewed with caution. The confidence level in MINFIT had to be reduced to 0.45 in order to retain enough components to achieve a satisfactory fit.

A.138.2 $z_{abs} = 2.196632$

This weak system was fit with three VP components and spans a total velocity width of 92 km s⁻¹.

A.139 **J114308+345220**

No MgII systems were found in this spectrum in the redshift range $0.8030 \leq z \leq 1.4149$.

A.140 **J115129+382552**

A.140.1 $z_{abs} = 0.553363$

This strong system was fit with eight VP components and spans a total velocity width of 202 km s⁻¹. Although $W_r = 0.64$ Å, the absorption occurs over a relatively broad kinematic range.

A.141 J115944+011206

A.141.1 $z_{abs} = 0.790815$

This weak system was fit with one VP component and spans a total velocity width of 38 km s^{-1} .

A.141.2 $z_{abs} = 1.098251$

This weak system was fit with one VP component and spans a total velocity width of 40 km s^{-1} .

A.141.3 $z_{abs} = 1.330499$

This weak system was fit with two VP components and spans a total velocity width of 40 km s^{-1} .

A.141.4 $z_{abs} = 1.943649$

This very strong system spans a total velocity width of 222 km s^{-1} . The shallow pixels in the MgII $\lambda 2803$ feature at $\sim 36 \text{ km s}^{-1}$ are not real and were masked; they are believed to be due to a faulty sky subtraction. The saturation as well as the numerous clouds made this system difficult to fit. Attempts were made to use the saturated regions option in MINFIT over various velocity ranges and to change the b parameter flag in MINFIT from turbulent to thermal in order to improve the fit, but these changes were not kept in the final model. The MgI $\lambda 2853$ feature in particular was modeled in

some VP components with column densities that are too small. Spurious features were masked on both wings of the FeII $\lambda 2600$ and $\lambda 2344$ transitions; in a data spike in the MgI $\lambda 2853$ transition at $\sim 90 \text{ km s}^{-1}$; and in the MnII $\lambda 2577$ transition from 60 to 85 km s^{-1} . Although 15 VP components were fit, the parameters for 14 components were not well constrained. “Voigt Profile Fitting Results” on the included compact disc does not quote errors for these components, and the model should be viewed with caution. The confidence level in MINFIT had to be reduced to 0.19 in order to retain enough components to achieve a satisfactory fit.

A.142 J120523-074232

A.142.1 $z_{abs} = 1.754690$

This very strong system spans a total velocity width of 296 km s^{-1} . The saturation made this system difficult to fit. Attempts were made to use the saturated regions option in MINFIT over various velocity ranges and to change the b parameter flag in MINFIT from turbulent to thermal in order to improve the fit, but these changes were not kept in the final model. Spurious features were masked in MnII $\lambda 2577$ from 52 to 65 km s^{-1} and in MnII $\lambda 2594$ from 76 to 215 km s^{-1} . Although 11 VP components were fit, the parameters for one component were not well constrained. “Voigt Profile Fitting Results” on the included compact disc does not quote errors for this component, and the model should be viewed with caution. The confidence level in MINFIT had to be reduced to 0.15 in order to retain enough components to achieve a satisfactory fit.

A.143 J120550+020131

A.143.1 $z_{abs} = 1.252126$

This weak system was fit with two VP components and spans a total velocity width of 63 km s^{-1} . Possibly due to errors in the data reduction, the model fit of the MgII $\lambda 2796$ of this system did not align well with the other transitions, though an attempt was made to correct it. The feature is fit well in the MgII $\lambda 2803$ and FeII lines, however. Three bad pixels were masked just redward of the $\lambda 2803$ line.

A.144 J120858+454036

A.144.1 $z_{abs} = 0.927592$

This strong system was fit with 12 VP components, contains five subregions, and spans a total velocity width of 521 km s^{-1} .

A.144.2 $z_{abs} = 0.934277$

This weak system was fit with one VP component and spans a total velocity width of 42 km s^{-1} .

A.145 J121135+090223

No MgII systems were found in this spectrum in the redshift range $0.8681 \leq z \leq 1.3205$.

A.146 J121140+103002

A.146.1 $z_{abs} = 0.392923$

This very strong system was fit with 12 VP components, contains two subregions, and spans a total velocity width of 365 km s^{-1} . A small spurious feature on the red wing of region 2 of this large absorbing complex was masked in MgII λ 2796 from about 120 to 140 km s^{-1} . The confidence level in MINFIT had to be reduced to 0.57 in order to retain enough components to achieve a satisfactory fit.

A.146.2 $z_{abs} = 1.049608$

This weak system was fit with one VP component and spans a total velocity width of 42 km s^{-1} .

A.147 J121303+171423

A.147.1 $z_{abs} = 0.841454$

This strong system was fit with eight VP components, contains three subregions, and spans a total velocity width of 304 km s^{-1} . A large spurious feature was masked in the FeII λ 2344 transition from -300 to -65 km s^{-1} .

A.147.2 $z_{abs} = 1.891680$

This very strong system was fit with six VP components and spans a total velocity width of 160 km s^{-1} . Two bad pixels were masked in the MgII λ 2803 transition at \sim

27 km s⁻¹. In addition, atmospheric features were masked on both wings of the FeII λ 2383 transition.

A.147.3 $z_{abs} = 1.931468$

This strong system was fit with three VP components and spans a total velocity width of 99 km s⁻¹. Spurious features were masked on both wings of the MgII λ 2796 transition.

A.148 **J121509+330955**

No MgII systems were found in this spectrum in the redshift range $0.1760 \leq z \leq 0.5874$.

A.149 **J121549-003434**

A.149.1 $z_{abs} = 1.127698$

This weak system was fit with one VP component and spans a total velocity width of 28 km s⁻¹.

A.149.2 $z_{abs} = 1.320047$

This very strong system was fit with 21 VP components and spans a total velocity width of 368 km s⁻¹. This is a fairly evenly split double system. In order to better constrain the MgII column densities relative to the FeII, we used the saturated regions option in MINFIT from -136 to -33 km s⁻¹ and from -9 to 104 km s⁻¹. The confidence

level in MINFIT had to be reduced to 0.88 in order to retain enough components to achieve a satisfactory fit.

A.149.3 $z_{abs} = 1.554148$

This very strong system was fit with 22 VP components, contains two subregions, and spans a total velocity width of 423 km s^{-1} . A large spurious feature was masked in the Mn II $\lambda 2594$ transition from -350 to -215 km s^{-1} . The confidence level in MINFIT had to be reduced to 0.57 in order to retain enough components to achieve a satisfactory fit.

A.150 **J121732+330539**

No Mg II systems were found in this spectrum in the redshift range $0.5694 \leq z \leq 1.2561$.

A.151 **J121930+494051**

No Mg II systems were found in this spectrum in the redshift range $0.6076 \leq z \leq 0.6593$.

A.152 **J122310-181642**

No Mg II systems were found in this spectrum in the redshift range $0.3738 \leq z \leq 1.3797$.

A.153 J122527+223513

A.153.1 $z_{abs} = 0.668056$

This strong system was fit with six VP components, contains two subregions, and spans a total velocity width of 296 km s⁻¹.

A.154 J122607+173648

No MgII systems were found in this spectrum in the redshift range $0.7033 \leq z \leq 2.6073$.

A.155 J122824+312838

A.155.1 $z_{abs} = 0.530457$

This weak system was fit with two VP components, contains two subregions, and spans a total velocity width of 64 km s⁻¹.

A.155.2 $z_{abs} = 1.794827$

This very strong system was fit with 16 VP components, contains two subregions, and spans a total velocity width of 333 km s⁻¹. Small blends in the MgII $\lambda 2796$ feature were masked from 150 to 160 km s⁻¹ and from 180 to 195 km s⁻¹. The confidence level in MINFIT had to be reduced to 0.14 in order to retain enough components to achieve a satisfactory fit.

A.156 J122607+173650

A.156.1 $z_{abs} = 1.421516$

This weak system was fit with one VP component and spans a total velocity width of 28 km s⁻¹.

A.156.2 $z_{abs} = 1.492086$

This weak system was fit with one VP component and spans a total velocity width of 46 km s⁻¹.

A.156.3 $z_{abs} = 2.465802$

This very strong system spans a total velocity width of 206 km s⁻¹. The saturation as well as the numerous clouds made this system difficult to fit. Since this system is saturated in even the weakest of the FeII transitions, we used the saturated regions option in MINFIT from -52 to -28 km s⁻¹ and from 7 to 46 km s⁻¹. Spurious features were masked on the blue wing of the MgII $\lambda 2796$ feature from -110 to -80 km s⁻¹; on both wings of the FeII $\lambda 2600$ transition; and on the red wings of the FeII $\lambda 2587$ and $\lambda 2374$ transitions. Although 10 VP components were fit, none had well-constrained parameters. “Voigt Profile Fitting Results” on the included compact disc does not quote errors for these components, and the model should be viewed with caution. The confidence level in MINFIT had to be reduced to 0.12 in order to retain enough components to achieve a satisfactory fit.

A.157 J123200-022404

A.157.1 $z_{abs} = 0.395139$

This very strong system was fit with 17 VP components and spans a total velocity width of 325 km s^{-1} . Note the asymmetric kinematic profile with the absorption progressively weakening towards the red. Since this system saturates in even the weakest of the FeII transitions, we used the saturated regions option in MINFIT from -75 to 25 km s^{-1} . Also, the blue wing of FeII $\lambda 2383$ contains a blend or possibly bad data, and was masked from about -100 to -75 km s^{-1} . The confidence level in MINFIT had to be reduced to 0.53 in order to retain enough components to achieve a satisfactory fit.

A.157.2 $z_{abs} = 0.700375$

This weak system was fit with one VP component and spans a total velocity width of 22 km s^{-1} . This is one of the smallest equivalent width MgII absorbers in our sample at $W_r = 0.014$.

A.157.3 $z_{abs} = 0.756903$

This strong system was fit with three VP components and spans a total velocity width of 100 km s^{-1} . A small region near the red MgII $\lambda 2796$ wing was masked because the apparent absorption there did not correspond to the $\lambda 2803$ profile, and is possibly due to noise, a spurious feature, or a faulty continuum fit.

A.157.4 $z_{abs} = 0.768850$

This weak system was fit with one VP component and spans a total velocity width of 30 km s⁻¹.

A.157.5 $z_{abs} = 0.830851$

This weak system was fit with four VP components, contains three subregions, and spans a total velocity width of 188 km s⁻¹.

A.158 J123437+075843

A.158.1 $z_{abs} = 0.765120$

This weak system was fit with three VP components and spans a total velocity width of 92 km s⁻¹.

A.158.2 $z_{abs} = 0.861292$

This very strong system contains four subregions and spans a total velocity width of 465 km s⁻¹. Note the unusual multitude of weak components at high velocities in either direction relative to the central, saturated absorption. A weak spurious absorption feature at ~ 175 km s⁻¹ in the MgII $\lambda 2796$ feature was masked. Also masked were a weak spurious feature on the red wing of the central absorption of the FeII $\lambda 2383$ transition at ~ 80 km s⁻¹ and a spurious line polluting the MnII $\lambda 2577$ feature from -10 to 75 km s⁻¹. Although 14 VP components were fit, the parameters for one component

were not well constrained. “Voigt Profile Fitting Results” on the included compact disc does not quote errors for this component, and the model should be viewed with caution.

A.159 J124410+172104

A.159.1 $z_{abs} = 0.550481$

This strong system was fit with four VP components, contains two subregions, and spans a total velocity width of 207 km s⁻¹.

A.160 J124604-073046

No MgII systems were found in this spectrum in the redshift range $0.0887 \leq z \leq 1.2483$.

A.161 J124714+312640

A.161.1 $z_{abs} = 0.850493$

This weak system was fit with three VP components and spans a total velocity width of 76 km s⁻¹.

A.162 J124524-000938

A.162.1 $z_{abs} = 1.275301$

This weak system was fit with one VP component and spans a total velocity width of 27 km s^{-1} .

A.163 J124913-055918

A.163.1 $z_{abs} = 0.639908$

This strong system was fit with three VP components and spans a total velocity width of 89 km s^{-1} . A small area near the red wing of the FeII $\lambda 2587$ feature was masked from -44 to -24 km s^{-1} ; the area appears to consist of noise in those pixels, but was adversely affecting the fit.

A.163.2 $z_{abs} = 0.902603$

This weak system was fit with three VP components and spans a total velocity width of 61 km s^{-1} .

A.163.3 $z_{abs} = 1.201507$

This strong system was fit with 10 VP components and spans a total velocity width of 183 km s^{-1} . The confidence level in MINFIT had to be reduced to 0.34 in order to retain enough components to achieve a satisfactory fit.

A.164 J124924-023339

A.164.1 $z_{abs} = 0.436843$

This weak system was fit with two VP components and spans a total velocity width of 58 km s⁻¹.

A.164.2 $z_{abs} = 0.725983$

This strong system was fit with two VP components and spans a total velocity width of 122 km s⁻¹.

A.164.3 $z_{abs} = 1.341271$

This weak system was fit with four VP components and spans a total velocity width of 100 km s⁻¹.

A.164.4 $z_{abs} = 1.775414$

This weak system was fit with three VP components and spans a total velocity width of 65 km s⁻¹. A large blend on the blue wing of the MgII λ 2803 feature was masked blueward of ~ -20 km s⁻¹ and is the MgII λ 2796 feature in the $z_{abs} = 1.780539$ system.

A.164.5 $z_{abs} = 1.780539$

This very strong system spans a total velocity width of 360 km s^{-1} . The blend on the red wing of the MgII $\lambda 2796$ absorption was masked redward of $\sim 200 \text{ km s}^{-1}$ and is the MgII $\lambda 2803$ feature in the $z_{abs} = 1.775414$ system. Spurious features were also masked in the FeII transitions in $\lambda 2600$ from 200 to 230 km s^{-1} and in $\lambda 2587$ from -150 to -110 km s^{-1} , 80 to 105 km s^{-1} , 125 to 180 km s^{-1} , and 195 to 205 km s^{-1} . A small spurious feature was masked in MgI $\lambda 2853$ at $\sim 120 \text{ km s}^{-1}$. Finally, numerous atmospheric lines were masked in all three MnII transitions. Although 17 VP components were fit, the parameters for one component were not well constrained. “Voigt Profile Fitting Results” on the included compact disc does not quote errors for this component, and the model should be viewed with caution.

A.164.6 $z_{abs} = 1.892961$

This weak system was fit with three VP components, contains two subregions, and spans a total velocity width of 195 km s^{-1} .

A.165 **J125048+395140****A.165.1** $z_{abs} = 0.772956$

This strong system was fit with seven VP components, contains two subregions, and spans a total velocity width of 293 km s^{-1} .

A.165.2 $z_{abs} = 0.854562$

This weak system contains two subregions and spans a total velocity width of 277 km s⁻¹. Although eight VP components were fit, the parameters for one component were not well constrained. “Voigt Profile Fitting Results” on the included compact disc does not quote errors for this component, and the model should be viewed with caution. The confidence level in MINFIT had to be reduced to 0.07 in order to retain enough components to achieve a satisfactory fit.

A.166 **J125659+042734**

A.166.1 $z_{abs} = 0.934231$

This strong system was fit with three VP components and spans a total velocity width of 89 km s⁻¹. The blueward of the two “prongs” of the system seems to be noticeably more deficient in FeII relative to the MgII.

A.167 **J131011+460124**

No MgII systems were found in this spectrum in the redshift range $0.3625 \leq z \leq 0.8283$.

A.168 J131956+272808

A.168.1 $z_{abs} = 0.660049$

This strong system was fit with six VP components, contains two subregions, and spans a total velocity width of 158 km s^{-1} . The confidence level in MINFIT had to be reduced to 0.84 in order to retain enough components to achieve a satisfactory fit.

A.169 J132323-002155

A.169.1 $z_{abs} = 0.564142$

This weak system was fit with one VP component and spans a total velocity width of 35 km s^{-1} .

A.169.2 $z_{abs} = 0.716096$

This very strong system was fit with 21 VP components, contains two subregions, and spans a total velocity width of 345 km s^{-1} . Since this system is saturated in even the weakest of the FeII transitions, we used the saturated regions option in MINFIT from -76 to 85 km s^{-1} . The b parameter flag in MINFIT was also changed from turbulent to thermal to improve the fit. The saturation as well as the numerous clouds made this system difficult to model. In particular, some of the VP components in the FeII $\lambda 2374$ feature were fit with column densities that appear too high. In addition, one bad pixel in the FeII $\lambda 2587$ transition was masked at $\sim -80 \text{ km s}^{-1}$ as well as a small feature at $\sim 175 \text{ km s}^{-1}$ which could be either spurious absorption or noise.

The confidence level in MINFIT had to be reduced to 0.14 in order to retain enough components to achieve a satisfactory fit.

A.170 J133141+410158

A.170.1 $z_{abs} = 0.998359$

This weak system was fit with one VP component and spans a total velocity width of 47 km s⁻¹.

A.171 J133335+164903

A.171.1 $z_{abs} = 0.744641$

This very strong system was fit with 14 VP components and spans a total velocity width of 366 km s⁻¹. Atmospheric features were masked in the CaII λ 3935 feature from ~ 170 km s⁻¹ redward and in the CaII λ 3970 feature from -50 to 20 km s⁻¹ and from 175 to 250 km s⁻¹.

A.171.2 $z_{abs} = 1.328180$

This very strong system was fit with 11 VP components, contains two subregions, and spans a total velocity width of 561 km s⁻¹. Spurious features were masked on the blue wing of region 2 of the MgII λ 2796 feature and on the red wing of region 2 of the MgII λ 2803 feature. The confidence level in MINFIT had to be reduced to 0.82 in order to retain enough components to achieve a satisfactory fit.

A.171.3 $z_{abs} = 1.776598$

This very strong system was fit with 11 VP components, contains two subregions, and spans a total velocity width of 366 km s^{-1} . In order to better constrain the MgII column densities relative to the FeII, we used the saturated regions option in MINFIT from -32 to -12 km s^{-1} . Also, spurious features were masked in the FeII $\lambda 2600$ transition at $\sim -70 \text{ km s}^{-1}$; in the FeII $\lambda 2344$ transition from $\sim 50 \text{ km s}^{-1}$ redward; in the FeII $\lambda 2587$ transition at $\sim -195 \text{ km s}^{-1}$ and $\sim 180 \text{ km s}^{-1}$; in the MnII $\lambda 2594$ transition at $\sim -200 \text{ km s}^{-1}$, $\sim -50 \text{ km s}^{-1}$, and from $\sim 50 \text{ km s}^{-1}$ redward; and in the MnII $\lambda 2606$ transition at $\sim -40 \text{ km s}^{-1}$ and $\sim 25 \text{ km s}^{-1}$.

A.171.4 $z_{abs} = 1.786300$

This strong system was fit with eight VP components and spans a total velocity width of 204 km s^{-1} . Spurious features were masked in the FeII $\lambda 2600$ transition at $\sim 85 \text{ km s}^{-1}$; in the FeII $\lambda 2344$ transition from $\sim -60 \text{ km s}^{-1}$ redward; in the FeII $\lambda 2587$ transition at $\sim -60 \text{ km s}^{-1}$ and $\sim 20 \text{ km s}^{-1}$; in the MgI $\lambda 2853$ transition at $\sim 60 \text{ km s}^{-1}$; in the MnII $\lambda 2577$ transition at $\sim -50 \text{ km s}^{-1}$ and from $\sim 20 \text{ km s}^{-1}$ redward; and in the MnII $\lambda 2594$ transition from about -25 to -5 km s^{-1} .

A.172 J134002+110630

A.172.1 $z_{abs} = 1.636630$

This strong system was fit with seven VP components, contains two subregions, and spans a total velocity width of 333 km s⁻¹.

A.172.2 $z_{abs} = 2.138662$

This strong system was fit with five VP components and spans a total velocity width of 136 km s⁻¹. Several bad pixels were masked in the MgII $\lambda 2796$ feature at ~ 40 km s⁻¹. The confidence level in MINFIT had to be reduced to 0.24 in order to retain enough components to achieve a satisfactory fit.

A.172.3 $z_{abs} = 2.149819$

This strong system was fit with 10 VP components, contains three subregions, and spans a total velocity width of 210 km s⁻¹. A spurious feature was masked on the red wing of region 2 of the FeII $\lambda 2600$ feature at ~ 22 km s⁻¹ as well as on the blue wing of region 2 of the FeII $\lambda 2344$ feature at ~ -27 km s⁻¹. The confidence level in MINFIT had to be reduced to 0.08 in order to retain enough components to achieve a satisfactory fit.

A.173 J134427-103541

A.173.1 $z_{abs} = 0.752226$

This weak system was fit with one VP component and spans a total velocity width of 30 km s^{-1} . It is one of the lowest equivalent width systems at 0.01 \AA .

A.173.2 $z_{abs} = 0.786156$

This weak system was fit with one VP component and spans a total velocity width of 22 km s^{-1} . It is, like the absorber at $z_{abs} = 0.752226$, also one of the weakest systems in our sample at 0.008 \AA .

A.173.3 $z_{abs} = 0.872827$

This strong system was fit with seven VP components and spans a total velocity width of 117 km s^{-1} . The large spurious absorption features located redward of the FeII $\lambda 2600$ line from $\sim 30 \text{ km s}^{-1}$ on were masked. The confidence level in MINFIT had to be reduced to 0.05 in order to retain enough components to achieve a satisfactory fit.

A.173.4 $z_{abs} = 1.276747$

This very strong system was fit with 13 VP components, contains four subregions, and spans a total velocity width of 428 km s^{-1} . Note the classic pattern of weak subsystems grouped in velocity space to one side of the main absorbing region. The

spurious features redward of the FeII $\lambda 2383$ and $\lambda 2344$ lines, both located at ~ 325 km s $^{-1}$, were masked. The b parameter flag in MINFIT was changed from turbulent to thermal to improve the fit.

A.173.5 $z_{abs} = 1.915412$

This strong system was fit with 11 VP components, contains three subregions, and spans a total velocity width of 250 km s $^{-1}$. This system was contaminated by numerous atmospheric lines; the MgII $\lambda 2803$ transition was masked from -120 to -40 km s $^{-1}$ and the FeII $\lambda 2374$ transition from -130 to -60 km s $^{-1}$.

A.174 **J134916-033715**

No MgII systems were found in this spectrum in the redshift range $1.1693 \leq z \leq 1.9844$.

A.175 **J135038-251216**

A.175.1 $z_{abs} = 0.575543$

This weak system was fit with one VP component and spans a total velocity width of 29 km s $^{-1}$.

A.175.2 $z_{abs} = 1.439264$

This strong system was fit with nine VP components and spans a total velocity width of 181 km s $^{-1}$. Spurious features were masked in the MgI $\lambda 2853$ transition from

-30 to -15 km s⁻¹ and from 90 to 130 km s⁻¹.

A.175.3 $z_{abs} = 1.508140$

This weak system was fit with three VP components and spans a total velocity width of 72 km s⁻¹. A small blend was masked in the FeII $\lambda 2600$ feature at ~ 10 km s⁻¹.

A.175.4 $z_{abs} = 1.752902$

This weak system was fit with one VP component and spans a total velocity width of 46 km s⁻¹.

A.176 **J135646-110128**

A.176.1 $z_{abs} = 0.764777$

This weak system was fit with two VP components and spans a total velocity width of 57 km s⁻¹.

A.176.2 $z_{abs} = 2.212410$

This strong system was fit with 10 VP components and spans a total velocity width of 195 km s⁻¹. The large spurious feature redward of the MnII $\lambda 2594$ absorption was masked. Also, a small area of absorption just blueward of the MgII $\lambda 2803$ feature, from about -175 to -150 km s⁻¹, was masked; it does not correspond to the $\lambda 2796$ absorption

and is spurious. The confidence level in MINFIT had to be reduced to 0.45 in order to retain enough components to achieve a satisfactory fit.

A.177 J135704+191906

No MgII systems were found in this spectrum in the redshift range $0.3468 \leq z \leq 0.6906$.

A.178 J140039+112022

A.178.1 $z_{abs} = 1.077748$

This weak system was fit with two VP components, contains two subregions, and spans a total velocity width of 70 km s^{-1} .

A.179 B1422+231A

No MgII systems were found in this spectrum in the redshift range $1.0085 \leq z \leq 1.6190$.

A.180 B1422+231B

No MgII systems were found in this spectrum in the redshift range $1.0085 \leq z \leq 1.6129$.

A.181 B1422+231C

No MgII systems were found in this spectrum in the redshift range $1.0085 \leq z \leq 1.6188$.

A.182 J142326+325220

A.182.1 $z_{abs} = 0.843247$

This weak system was fit with one VP component and spans a total velocity width of 26 km s^{-1} .

A.182.2 $z_{abs} = 0.902870$

This very strong system was fit with 12 VP components, contains two subregions, and spans a total velocity width of 232 km s^{-1} . The confidence level in MINFIT had to be reduced to 0.34 in order to retain enough components to achieve a satisfactory fit.

A.182.3 $z_{abs} = 1.172607$

This strong system was fit with five VP components and spans a total velocity width of 111 km s^{-1} .

A.183 J142656+602551

A.183.1 $z_{abs} = 1.586326$

This strong system was fit with seven VP components and spans a total velocity width of 114 km s^{-1} . A blend was masked on the red wing of the FeII $\lambda 2344$ feature.

A.184 J142756-420619

No MgII systems were found in this spectrum in the redshift range $0.1737 \leq z \leq 1.4804$.

A.185 J142906+011705

This spectrum contained no redshift coverage as defined in § 2.4.

A.186 J143229-010614B

No MgII systems were found in this spectrum in the redshift range $0.3414 \leq z \leq 2.0347$.

A.187 J143229-010616A

A.187.1 $z_{abs} = 0.400768$

This weak system was fit with two VP components and spans a total velocity width of 47 km s^{-1} . The confidence level in MINFIT had to be reduced to 0.90 in order to retain enough components to achieve a satisfactory fit.

A.187.2 $z_{abs} = 1.512464$

This very strong system was fit with 21 VP components and spans a total velocity width of 295 km s^{-1} . The confidence level in MINFIT had to be reduced to 0.73 in order to retain enough components to achieve a satisfactory fit.

A.187.3 $z_{abs} = 1.662854$

This very strong system was fit with 13 VP components, contains five subregions, and spans a total velocity width of 510 km s^{-1} . Three bad pixels in the MgII $\lambda 2803$ feature were masked at $\sim 80 \text{ km s}^{-1}$, as well as numerous B-band features in the FeII $\lambda 2587$ transition. The confidence level in MINFIT had to be reduced to 0.50 in order to retain enough components to achieve a satisfactory fit.

A.188 **J143649-161341**

This spectrum contained no redshift coverage as defined in § 2.4.

A.189 **J143912+295447**

A.189.1 $z_{abs} = 1.225850$

This strong system was fit with five VP components and spans a total velocity width of 152 km s^{-1} . The confidence level in MINFIT had to be reduced to 0.73 in order to retain enough components to achieve a satisfactory fit.

A.190 J144453+291905

No MgII systems were found in this spectrum in the redshift range $0.5955 \leq z \leq 1.1998$.

A.191 J144331+272436

No MgII systems were found in this spectrum in the redshift range $1.3563 \leq z \leq 2.2837$.

A.192 J144653+011356

A.192.1 $z_{abs} = 0.444005$

This weak system was fit with four VP components, contains two subregions, and spans a total velocity width of 200 km s^{-1} .

A.192.2 $z_{abs} = 0.509678$

This weak system was fit with four VP components and spans a total velocity width of 98 km s^{-1} .

A.192.3 $z_{abs} = 0.660216$

This strong system was fit with four VP components and spans a total velocity width of 82 km s^{-1} .

A.192.4 $z_{abs} = 1.102006$

This weak system was fit with three VP components and spans a total velocity width of 75 km s^{-1} .

A.192.5 $z_{abs} = 1.129140$

This weak system was fit with five VP components, contains two subregions, and spans a total velocity width of 183 km s^{-1} . Several pixels were masked just redward of region 2 in the MgII $\lambda 2796$ feature; the pixels are not believed to be part of the system, but MINFIT was fitting an excessively broad component in order to accommodate them.

A.192.6 $z_{abs} = 1.159458$

This strong system was fit with eight VP components and spans a total velocity width of 183 km s^{-1} .

A.193 J145102-232930

A.193.1 $z_{abs} = 1.473211$

This weak system was fit with four VP components, contains two subregions, and spans a total velocity width of 115 km s^{-1} . Spurious features were masked in the MgII $\lambda 2796$ transition at $\sim -60 \text{ km s}^{-1}$ and in the FeII $\lambda 2383$ transition from -100 to -30 km s^{-1} .

A.193.2 $z_{abs} = 1.585465$

This weak system was fit with one VP component and spans a total velocity width of 28 km s^{-1} .

A.194 **J145418+121053**

No MgII systems were found in this spectrum in the redshift range $0.8459 \leq z \leq 2.3624$.

A.195 **J151352+085555**

A.195.1 $z_{abs} = 1.179037$

This weak system was fit with two VP components and spans a total velocity width of 75 km s^{-1} .

A.196 **J154420+591227**

No MgII systems were found in this spectrum in the redshift range $0.3205 \leq z \leq 0.7772$.

A.197 **J155152+191104**

No MgII systems were found in this spectrum in the redshift range $0.6650 \leq z \leq 1.1757$.

A.198 J155103+090850

No MgII systems were found in this spectrum in the redshift range $0.6307 \leq z \leq 1.0709$.

A.199 J160455+381214

No MgII systems were found in this spectrum in the redshift range $0.5259 \leq z \leq 0.6595$.

A.200 J162439+234512**A.200.1** $z_{abs} = 0.317597$

This strong system was fit with six VP components and spans a total velocity width of 150 km s^{-1} . The confidence level in MINFIT had to be reduced to 0.84 in order to retain enough components to achieve a satisfactory fit.

A.200.2 $z_{abs} = 0.368111$

This weak system was fit with three VP components and spans a total velocity width of 52 km s^{-1} . It is possible that there is a very weak additional component at $\sim 85 \text{ km s}^{-1}$, but due to the spurious feature in that region of the MgII $\lambda 2796$ and the lack of a detection there in other ions, the potential feature could not be recovered. The confidence level in MINFIT had to be reduced to 0.90 in order to retain enough components to achieve a satisfactory fit.

A.200.3 $z_{abs} = 0.471930$

This strong system was fit with seven VP components and spans a total velocity width of 125 km s^{-1} . The large blend polluting the FeII $\lambda 2383$ absorption from 35 km s^{-1} redward was masked. The confidence level in MINFIT had to be reduced to 0.23 in order to retain enough components to achieve a satisfactory fit.

A.200.4 $z_{abs} = 0.656105$

This very strong system spans a total velocity width of 200 km s^{-1} . Several bad pixels were masked in the FeII $\lambda 2374$ feature at $\sim 25 \text{ km s}^{-1}$. Although 15 VP components were fit, the parameters for seven components were not well constrained. “Voigt Profile Fitting Results” on the included compact disc does not quote errors for these components, and the model should be viewed with caution. The confidence level in MINFIT had to be reduced to 0.22 in order to retain enough components to achieve a satisfactory fit.

A.200.5 $z_{abs} = 0.702901$

This weak system was fit with one VP component and spans a total velocity width of 20 km s^{-1} .

A.200.6 $z_{abs} = 0.797078$

This strong system was fit with six VP components, contains two subregions, and spans a total velocity width of 245 km s^{-1} . This profile consists of several kinematically distinct features. The large spurious feature redward of the FeII $\lambda 2383$ absorption feature was masked.

A.200.7 $z_{abs} = 0.891275$

This very strong system spans a total velocity width of 205 km s^{-1} . This is a highly kinematically concentrated profile; the MgII is saturated across most of the profile, though more structure can be seen in the weaker transitions. Although 14 VP components were fit, the parameters for one component were not well constrained. “Voigt Profile Fitting Results” on the included compact disc does not quote errors for this component, and the model should be viewed with caution. The confidence level in MINFIT had to be reduced to 0.43 in order to retain enough components to achieve a satisfactory fit.

A.201 **J162645+642654****A.201.1** $z_{abs} = 0.585946$

This weak system was fit with three VP components and spans a total velocity width of 87 km s^{-1} .

A.202 J163145+115602

A.202.1 $z_{abs} = 0.900256$

This very strong system was fit with nine VP components and spans a total velocity width of 190 km s^{-1} . The confidence level in MINFIT had to be reduced to 0.36 in order to retain enough components to achieve a satisfactory fit.

A.203 J163429+703133

A.203.1 $z_{abs} = 0.653417$

This weak system was fit with two VP components and spans a total velocity width of 39 km s^{-1} .

A.203.2 $z_{abs} = 0.818166$

This weak system was fit with one VP component and spans a total velocity width of 27 km s^{-1} .

A.203.3 $z_{abs} = 0.905563$

This weak system was fit with one VP component and spans a total velocity width of 34 km s^{-1} .

A.203.4 $z_{abs} = 0.990248$

This strong system was fit with six VP components and spans a total velocity width of 110 km s^{-1} .

A.203.5 $z_{abs} = 1.041435$

This weak system was fit with five VP components, contains two subregions, and spans a total velocity width of 181 km s^{-1} .

A.204 **J164656+551446**

No MgII systems were found in this spectrum in the redshift range $1.1898 \leq z \leq 1.9050$.

A.205 **J170100+641209**

A.205.1 $z_{abs} = 0.722179$

This weak system was fit with four VP components and spans a total velocity width of 80 km s^{-1} . The C IV $\lambda 1550$ feature just blueward of the MgI $\lambda 2853$ feature was masked, along with a small spurious feature adjacent to the red MgII $\lambda 2796$ wing.

A.205.2 $z_{abs} = 0.864598$

This weak system was fit with seven VP components, contains three subregions, and spans a total velocity width of 184 km s^{-1} .

A.205.3 $z_{abs} = 1.157277$

This weak system was fit with four VP components and spans a total velocity width of 85 km s^{-1} . The confidence level in MINFIT had to be reduced to 0.16 in order to retain enough components to achieve a satisfactory fit.

A.206 **J173302-130449**

No MgII systems were found in this spectrum in the redshift range $0.1743 \leq z \leq 0.8706$.

A.207 **J174358-035004**

No MgII systems were found in this spectrum in the redshift range $0.1743 \leq z \leq 1.0201$.

A.208 **J175746+753916**

A.208.1 $z_{abs} = 1.348499$

This strong system was fit with three VP components, contains two subregions, and spans a total velocity width of 116 km s^{-1} . A spurious absorption region was masked in the FeII $\lambda 2587$ transition from about -100 to -45 km s^{-1} .

A.209 J182402+104424**A.209.1** $z_{abs} = 0.570319$

This strong system spans a total velocity width of 101 km s^{-1} . A blend in the MgII $\lambda 2796$ absorption from about -100 to -45 km s^{-1} was masked. Although eight VP components were fit, the parameters for one component were not well constrained. “Voigt Profile Fitting Results” on the included compact disc does not quote errors for this component, and the model should be viewed with caution.

A.209.2 $z_{abs} = 1.250752$

This weak system was fit with two VP components, contains two subregions, and spans a total velocity width of 76 km s^{-1} .

A.210 J185230+401907

No MgII systems were found in this spectrum in the redshift range $0.3612 \leq z \leq 1.7897$.

A.211 J194025-690756

No MgII systems were found in this spectrum in the redshift range $0.8059 \leq z \leq 1.4358$.

A.212 J194454+770552

A.212.1 $z_{abs} = 1.119022$

This weak system was fit with three VP components and spans a total velocity width of 75 km s⁻¹.

A.213 J200324-325144

A.213.1 $z_{abs} = 1.176407$

This weak system was fit with five VP components and spans a total velocity width of 100 km s⁻¹. The feature blueward of the MgII λ 2796 absorption at ~ 75 km s⁻¹ is spurious.

A.213.2 $z_{abs} = 1.249861$

This weak system was fit with one VP component and spans a total velocity width of 27 km s⁻¹.

A.213.3 $z_{abs} = 2.032931$

This strong system was fit with five VP components and spans a total velocity width of 123 km s⁻¹. The red wing of the FeII λ 2344, as well as both wings of the λ 2374 line, were masked. The component of the λ 2587 line at ~ 0 km s⁻¹ is blended and was also masked.

A.213.4 $z_{abs} = 2.292483$

This strong system was fit with three VP components and spans a total velocity width of 87 km s^{-1} .

A.214 **J204719-163905**

A.214.1 $z_{abs} = 1.328615$

This strong system was fit with six VP components and spans a total velocity width of 110 km s^{-1} .

A.214.2 $z_{abs} = 1.342527$

This weak system was fit with two VP components and spans a total velocity width of 62 km s^{-1} .

A.215 **J213135-120704**

A.215.1 $z_{abs} = 0.429811$

This strong system contains two subregions and spans a total velocity width of 171 km s^{-1} . Although five VP components were fit, the parameters for one component were not well constrained. “Voigt Profile Fitting Results” on the included compact disc does not quote errors for this component, and the model should be viewed with caution. The confidence level in MINFIT had to be reduced to 0.82 in order to retain enough components to achieve a satisfactory fit.

A.216 J212912-153841**A.216.1** $z_{abs} = 2.022555$

This strong system was fit with nine VP components, contains three subregions, and spans a total velocity width of 185 km s^{-1} . Spurious features near the red FeII $\lambda 2383$ wing were masked from 25 to 70 km s^{-1} . The confidence level in MINFIT had to be reduced to 0.94 in order to retain enough components to achieve a satisfactory fit.

A.217 J213302-464026

No MgII systems were found in this spectrum in the redshift range $0.4042 \leq z \leq 1.3792$.

A.218 J213314-464030**A.218.1** $z_{abs} = 0.858062$

This weak system was fit with two VP components and spans a total velocity width of 62 km s^{-1} .

A.218.2 $z_{abs} = 0.866594$

This weak system was fit with three VP components and spans a total velocity width of 73 km s^{-1} . The confidence level in MINFIT had to be reduced to 0.45 in order to retain enough components to achieve a satisfactory fit.

A.218.3 $z_{abs} = 0.976707$

This strong system was fit with five VP components, contains two subregions, and spans a total velocity width of 210 km s⁻¹.

A.218.4 $z_{abs} = 1.239735$

This strong system was fit with five VP components and spans a total velocity width of 120 km s⁻¹. Three bad pixels were masked in the MgII λ 2803 feature at ~ 50 km s⁻¹. The data in this transition about the last VP component is noisy, but the fit appears better in the λ 2796 feature.

A.219 J214225-442018

A.219.1 $z_{abs} = 0.882526$

This very strong system was fit with 15 VP components, contains three subregions, and spans a total velocity width of 348 km s⁻¹. The confidence level in MINFIT had to be reduced to 0.75 in order to retain enough components to achieve a satisfactory fit.

A.219.2 $z_{abs} = 0.986668$

This strong system was fit with seven VP components, contains two subregions, and spans a total velocity width of 210 km s⁻¹. A large spurious region of absorption was masked from ~ 10 km s⁻¹ blueward in the FeII λ 2587 transition.

A.219.3 $z_{abs} = 1.054139$

This very strong system was fit with 15 VP components, contains three subregions, and spans a total velocity width of 407 km s^{-1} . The kinematically complex absorption suffered from strong spurious blending in the FeII $\lambda 2383$, $\lambda 2344$, and $\lambda 2374$ transitions; both redward and blueward of the system was masked for these features. The confidence level in MINFIT had to be reduced to 0.57 in order to retain enough components to achieve a satisfactory fit.

A.219.4 $z_{abs} = 1.153996$

This strong system was fit with eight VP components and spans a total velocity width of 147 km s^{-1} . A complex of spurious features blueward of the FeII $\lambda 2587$ line was masked. The confidence level in MINFIT had to be reduced to 0.76 in order to retain enough components to achieve a satisfactory fit.

A.219.5 $z_{abs} = 1.571067$

This very strong system was fit with 10 VP components and spans a total velocity width of 153 km s^{-1} . Since this system is saturated in even the weakest of the FeII transitions, we used the saturated regions option in MINFIT from -19 to 40 km s^{-1} .

A.219.6 $z_{abs} = 1.756896$

This weak system was fit with three VP components and spans a total velocity width of 72 km s^{-1} . A bad pixel was masked from the MgII $\lambda 2796$ line at $\sim 25 \text{ km s}^{-1}$. There is a small region thought to possibly be very weak absorption between about 25 and 40 km s^{-1} ; however, MINFIT rejected this portion as not significant. The confidence level in MINFIT had to be reduced to 0.38 in order to retain enough components to achieve a satisfactory fit.

A.219.7 $z_{abs} = 2.112678$

This very strong system was fit with 11 VP components and spans a total velocity width of 230 km s^{-1} . Since this system is saturated in even the weakest of the FeII transitions, we used the saturated regions option in MINFIT from -47 to 34 km s^{-1} . Also, the two spurious absorption features redward of the FeII $\lambda 2587$ profile were masked. The confidence level in MINFIT had to be reduced to 0.17 in order to retain enough components to achieve a satisfactory fit.

A.219.8 $z_{abs} = 2.253089$

This very strong system was fit with 12 VP components and spans a total velocity width of 232 km s^{-1} . Note that the first component in MgII $\lambda 2796$ seems to be fit with too high a column density; we believe this is due to a blend in the MgII $\lambda 2803$ component that made the feature too strong relative to the $\lambda 2796$. The confidence level

in MINFIT had to be reduced to 0.73 in order to retain enough components to achieve a satisfactory fit.

A.220 J214805+065738

A.220.1 $z_{abs} = 0.790866$

This strong system was fit with 10 VP components, contains two subregions, and spans a total velocity width of 251 km s⁻¹.

A.221 J215501-092224

This spectrum contained no redshift coverage as defined in § 2.4.

A.222 J220734-403655

A.222.1 $z_{abs} = 1.335290$

This weak system was fit with two VP components, contains two subregions, and spans a total velocity width of 103 km s⁻¹. This is a nearly symmetrical system, with just 0.045 Å of equivalent width split between the two features, though the redward component is somewhat narrower.

A.223 J220852-194359

A.223.1 $z_{abs} = 0.751922$

This strong system was fit with four VP components and spans a total velocity width of 164 km s^{-1} . Spurious features were masked on both wings of the FeII $\lambda 2344$ transition; on the blue wing of the FeII $\lambda 2587$ transition; and in the MnII $\lambda 2606$ transition at $\sim 70 \text{ km s}^{-1}$. The confidence level in MINFIT had to be reduced to 0.02 in order to retain enough components to achieve a satisfactory fit.

A.223.2 $z_{abs} = 0.948362$

This weak system was fit with three VP components, contains two subregions, and spans a total velocity width of 134 km s^{-1} . A small spurious feature was masked in the FeII $\lambda 2344$ transition from -110 to -50 km s^{-1} .

A.223.3 $z_{abs} = 1.017049$

This very strong system was fit with 10 VP components, contains two subregions, and spans a total velocity width of 286 km s^{-1} . The confidence level in MINFIT had to be reduced to 0.14 in order to retain enough components to achieve a satisfactory fit.

A.223.4 $z_{abs} = 1.297040$

This weak system was fit with three VP components and spans a total velocity width of 47 km s^{-1} .

A.223.5 $z_{abs} = 1.532744$

This weak system was fit with one VP component and spans a total velocity width of 21 km s^{-1} . This is one of the smallest equivalent width systems in our sample at $W_r = 0.014 \text{ \AA}$.

A.223.6 $z_{abs} = 1.920499$

This very strong system was fit with 15 VP components and spans a total velocity width of 231 km s^{-1} . In order to better constrain the MgII column densities relative to the FeII, we used the saturated regions option in MINFIT from -58 to 60 km s^{-1} . Also, atmospheric A-band features were masked on the red wing of the FeII $\lambda 2600$ transition. The confidence level in MINFIT had to be reduced to 0.84 in order to retain enough components to achieve a satisfactory fit.

A.224 **J221653-445156**

This spectrum contained no redshift coverage as defined in § 2.4.

A.225 J222826-400957**A.225.1** $z_{abs} = 1.278561$

This very strong system was fit with eight VP components and spans a total velocity width of 170 km s^{-1} .

A.226 J223409+000002**A.226.1** $z_{abs} = 0.855069$

This strong system was fit with eight VP components, contains three subregions, and spans a total velocity width of 169 km s^{-1} . Spurious features were masked in the FeII $\lambda 2587$ transition from 110 to 230 km s^{-1} ; in the MnII $\lambda 2577$ transition from -400 to 0 km s^{-1} and from 75 to 185 km s^{-1} ; in the MnII $\lambda 2594$ transition from -10 km s^{-1} blueward; and in the MnII $\lambda 2606$ transition from 30 km s^{-1} blueward.

A.226.2 $z_{abs} = 1.086635$

This strong system was fit with five VP components and spans a total velocity width of 95 km s^{-1} .

A.226.3 $z_{abs} = 1.212785$

This strong system was fit with seven VP components and spans a total velocity width of 131 km s^{-1} . A spurious feature was masked in the MnII $\lambda 2577$ transition from -50 to -5 km s^{-1} . The confidence level in MINFIT had to be reduced to 0.59 in order

to retain enough components to achieve a satisfactory fit.

A.227 J223235+024755

A.227.1 $z_{abs} = 1.059191$

This very strong system was fit with seven VP components, contains two subregions, and spans a total velocity width of 323 km s⁻¹.

A.227.2 $z_{abs} = 1.358435$

This weak system was fit with two VP components and spans a total velocity width of 57 km s⁻¹. The confidence level in MINFIT had to be reduced to 0.31 in order to retain enough components to achieve a satisfactory fit.

A.227.3 $z_{abs} = 1.779723$

This weak system was fit with one VP component and spans a total velocity width of 38 km s⁻¹.

A.227.4 $z_{abs} = 1.858585$

This strong system contains two subregions and spans a total velocity width of 159 km s⁻¹. The MgII λ 2796 transition contains no data from 40 to 74 km s⁻¹; as a result, MINFIT would not model the component there, though it is visible in the MgII λ 2803 and stronger FeII transitions. The MgII λ 2803 transition was masked from ~ -30 km s⁻¹ due to a large blend. Spurious features were also masked in the FeII

$\lambda 2600$ transition from -45 km s^{-1} blueward and in the $\text{MgI } \lambda 2853$ transition from -50 to -30 km s^{-1} and from 25 to 55 km s^{-1} . Although nine VP components were fit, the parameters for one component were not well constrained. “Voigt Profile Fitting Results” on the included compact disc does not quote errors for this component, and the model should be viewed with caution. The confidence level in MINFIT had to be reduced to 0.12 in order to retain enough components to achieve a satisfactory fit.

A.227.5 $z_{abs} = 1.863297$

This very strong system contains three subregions and spans a total velocity width of 807 km s^{-1} . This system has such a broad kinematic range that the $\text{MgII } \lambda\lambda 2796, 2803$ doublet is actually self-blended. The equivalent width is 4.07 \AA . As a result, the red $\lambda 2796$ wing and the blue $\lambda 2803$ wings overlap and were masked. The saturation as well as the numerous clouds made this system difficult to fit. Attempts were made to use the saturated regions option in MINFIT over various velocity ranges and to change the b parameter flag in MINFIT from turbulent to thermal in order to improve the fit, but these changes were not kept in the final model. In addition, the following masks were applied: the data spike in the $\text{MgII } \lambda 2796$ feature at $\sim -440 \text{ km s}^{-1}$; a small region of bad data in the $\text{MgII } \lambda 2803$ feature at $\sim -425 \text{ km s}^{-1}$; the blue wing of region 1 of the $\text{FeII } \lambda 2600$ feature blueward of -530 km s^{-1} ; two bad pixels in the $\text{FeII } \lambda 2587$ feature at $\sim -125 \text{ km s}^{-1}$; small spurious absorption features in the $\text{MgI } \lambda 2853$ feature at ~ -535 , ~ -460 , and $\sim -95 \text{ km s}^{-1}$; several bad pixels in the $\text{MnII } \lambda 2577$ transition

at $\sim -290 \text{ km s}^{-1}$; and a large spurious absorption feature in the $\text{Mn II } \lambda 2606$ transition from -475 km s^{-1} blueward. The system contains a small absorption component between VP components 6 and 7 at $\sim -430 \text{ km s}^{-1}$ that is real and visible in the $\text{Fe II } \lambda 2383$ and $\lambda 2600$ transitions; however, due to the data quality at that velocity in the $\text{Mg II } \lambda \lambda 2796, 2803$ doublet, the component could not be modeled. Although 24 VP components were fit, the parameters for three components were not well constrained. “Voigt Profile Fitting Results” on the included compact disc does not quote errors for these components, and the model should be viewed with caution. The confidence level in MINFIT had to be reduced to 0.05 in order to retain enough components to achieve a satisfactory fit.

A.228 J223619+132620

No Mg II systems were found in this spectrum in the redshift range $0.8685 \leq z \leq 1.6120$.

A.229 J223953-055219

No Mg II systems were found in this spectrum in the redshift range $1.4163 \leq z \leq 2.1475$.

A.230 J224708-601545

A.230.1 $z_{abs} = 0.828079$

This weak system was fit with six VP components, contains three subregions, and spans a total velocity width of 187 km s^{-1} . Strong spurious features were masked blueward of the FeII $\lambda 2383$ line as well as in the $\lambda 2600$ line from $\sim -10 \text{ km s}^{-1}$ blueward.

A.230.2 $z_{abs} = 1.389900$

This weak system was fit with six VP components, contains three subregions, and spans a total velocity width of 238 km s^{-1} . Spurious features were masked in FeII in the $\lambda 2383$ feature from $\sim -5 \text{ km s}^{-1}$ blueward and in the $\lambda 2374$ feature from about -80 to 100 km s^{-1} .

A.230.3 $z_{abs} = 1.755705$

This weak system was fit with two VP components and spans a total velocity width of 40 km s^{-1} .

A.230.4 $z_{abs} = 2.329761$

This very strong system spans a total velocity width of 360 km s^{-1} . This MgII system occurs in a very crowded portion of the spectrum. Several pixels were masked redward of the MgII $\lambda 2796$ absorption, as well as on both wings of the MgII $\lambda 2803$ line. The b parameter flag in MINFIT was changed from turbulent to thermal to improve

the fit. Although 20 VP components were fit, the parameters for four components were not well constrained. “Voigt Profile Fitting Results” on the included compact disc does not quote errors for these components, and the model should be viewed with caution. The confidence level in MINFIT had to be reduced to 0.94 in order to retain enough components to achieve a satisfactory fit.

A.231 J230001-341319

A.231.1 $z_{abs} = 0.882589$

This strong system was fit with seven VP components and spans a total velocity width of 142 km s^{-1} . In order to better constrain the MgII column densities relative to the FeII, we used the saturated regions option in MINFIT from -13 to 16 km s^{-1} .

A.231.2 $z_{abs} = 1.283661$

This strong system was fit with six VP components and spans a total velocity width of 142 km s^{-1} . Though the system contains no distinct subregions, there is nevertheless distinct kinematic structure with the strongest absorption occurring near the blue and red extremes of the profile and weaker absorption about -30 km s^{-1} . The confidence level in MINFIT had to be reduced to 0.87 in order to retain enough components to achieve a satisfactory fit.

A.232 J230445+031146

No MgII systems were found in this spectrum in the redshift range $0.1988 \leq z \leq 1.0181$.

A.233 J231646-404120

A.233.1 $z_{abs} = 1.044634$

This strong system was fit with four VP components, contains two subregions, and spans a total velocity width of 195 km s^{-1} .

A.234 J232059-295521

No MgII systems were found in this spectrum in the redshift range $0.4420 \leq z \leq 2.2623$.

A.235 J232121-294350

No MgII systems were found in this spectrum in the redshift range $0.3842 \leq z \leq 2.1315$.

A.236 J232820+002238

A.236.1 $z_{abs} = 0.401901$

This weak system was fit with four VP components and spans a total velocity width of 68 km s^{-1} . The confidence level in MINFIT had to be reduced to 0.93 in

order to retain enough components to achieve a satisfactory fit.

A.236.2 $z_{abs} = 0.412753$

This strong system was fit with six VP components, contains three subregions, and spans a total velocity width of 245 km s^{-1} . The confidence level in MINFIT had to be reduced to 0.91 in order to retain enough components to achieve a satisfactory fit.

A.236.3 $z_{abs} = 0.651926$

This very strong system spans a total velocity width of 250 km s^{-1} . The MgII $\lambda 2796$ absorption in this system was too corrupted and could not be fit. All quantities quoted for this system refer to the $\lambda 2803$ transition rather than the $\lambda 2796$. There was difficulty fitting the MgI $\lambda 2853$ feature; some of the VP components appear too broad. Finally, The b parameter flag in MINFIT was changed from turbulent to thermal to improve the fit. Although 17 VP components were fit, the parameters for six components were not well constrained. “Voigt Profile Fitting Results” on the included compact disc does not quote errors for these components, and the model should be viewed with caution.

A.237 **J234023-005326**

No MgII systems were found in this spectrum in the redshift range $0.3988 \leq z \leq 1.2545$.

A.238 2343+125**A.238.1** $z_{abs} = 0.731219$

This very strong system contains two subregions and spans a total velocity width of 295 km s^{-1} . The large spurious features in the FeII $\lambda 2600$ transition from 94 to 160 km s^{-1} and in the $\lambda 2587$ transition from -140 to -68 km s^{-1} were masked. Although 20 VP components were fit, the parameters for three components were not well constrained. “Voigt Profile Fitting Results” on the included compact disc does not quote errors for these components, and the model should be viewed with caution. The confidence level in MINFIT had to be reduced to 0.76 in order to retain enough components to achieve a satisfactory fit.

A.238.2 $z_{abs} = 2.171346$

This strong system was fit with six VP components, contains two subregions, and spans a total velocity width of 283 km s^{-1} . Spurious features were masked in the FeII $\lambda 2600$ transition from -50 to -30 km s^{-1} and in the FeII $\lambda 2587$ transition from -80 to -15 km s^{-1} .

A.239 2344+125**A.239.1** $z_{abs} = 1.046488$

This strong system spans a total velocity width of 138 km s^{-1} . The spurious complex in the MnII $\lambda 2594$ feature from -6 km s^{-1} blueward was masked. Although 11

VP components were fit, the parameters for four components were not well constrained. “Voigt Profile Fitting Results” on the included compact disc does not quote errors for these components, and the model should be viewed with caution. The confidence level in MINFIT had to be reduced to 0.39 in order to retain enough components to achieve a satisfactory fit.

A.239.2 $z_{abs} = 1.116097$

This strong system was fit with nine VP components and spans a total velocity width of 152 km s^{-1} . A spurious feature adjacent to the FeII $\lambda 2344$ absorption feature was masked from -57 to -20 km s^{-1} . The confidence level in MINFIT had to be reduced to 0.15 in order to retain enough components to achieve a satisfactory fit.

A.240 **J234451+343349**

No MgII systems were found in this spectrum in the redshift range $0.7029 \leq z \leq 2.8524$.

A.241 **J234625+124743**

No MgII systems were found in this spectrum in the redshift range $0.5555 \leq z \leq 1.3786$.

A.242 J234819+005721A**A.242.1** $z_{abs} = 1.130321$

This weak system was fit with five VP components, contains two subregions, and spans a total velocity width of 92 km s^{-1} . The confidence level in MINFIT had to be reduced to 0.17 in order to retain enough components to achieve a satisfactory fit.

A.243 J234825+002040

No MgII systems were found in this spectrum in the redshift range $0.5868 \leq z \leq 1.3783$.

A.244 2348-147

No MgII systems were found in this spectrum in the redshift range $0.8110 \leq z \leq 1.6799$.

A.245 J235034-432559**A.245.1** $z_{abs} = 1.109631$

This weak system was fit with one VP component and spans a total velocity width of 42 km s^{-1} . The extremely weak region just redward of the MgII lines was deemed conservatively to not actually be part of the absorption.

A.245.2 $z_{abs} = 1.405362$

This weak system was fit with two VP components and spans a total velocity width of 37 km s^{-1} .

A.245.3 $z_{abs} = 1.796237$

This weak system was fit with two VP components and spans a total velocity width of 50 km s^{-1} . A spurious feature was masked in the MnII $\lambda 2577$ transition from 5 to 25 km s^{-1} .

A.246 J235057-005209

A.246.1 $z_{abs} = 0.773680$

This very strong system was fit with 29 VP components, contains four subregions, and spans a total velocity width of 761 km s^{-1} . The FeII $\lambda 2383$ transition contains no data from -560 to -440 km s^{-1} . Spurious features were masked in the MgII $\lambda 2796$ transition from -470 km s^{-1} blueward and in the FeII $\lambda 2374$ transition at $\sim -100 \text{ km s}^{-1}$, $\sim 30 \text{ km s}^{-1}$, and $\sim 175 \text{ km s}^{-1}$. The confidence level in MINFIT had to be reduced to 0.23 in order to retain enough components to achieve a satisfactory fit.

A.246.2 $z_{abs} = 0.814061$

This weak system was fit with one VP component and spans a total velocity width of 37 km s^{-1} . This is one of the smallest equivalent width systems in our sample at

$$W_r = 0.017 \text{ \AA}.$$

$$\mathbf{A.246.3} \quad z_{abs} = 0.862944$$

This very strong system was fit with 10 VP components and spans a total velocity width of 216 km s^{-1} . A spurious feature was masked in the FeII $\lambda 2587$ transition from -175 to -25 km s^{-1} . The confidence level in MINFIT had to be reduced to 0.86 in order to retain enough components to achieve a satisfactory fit.

$$\mathbf{A.246.4} \quad z_{abs} = 1.444764$$

This weak system was fit with one VP component and spans a total velocity width of 35 km s^{-1} .

REFERENCES

- Barlow, T. 2005, MAKEE software package, www2.keck.hawaii.edu/inst/hires/data_reduction.html
- Bennett, C. L., Bay, M., Halpern, M., Hinshaw, G., Jackson, C., Jarosik, N., Kogut, A., Limon, M., Meyer, S. S., Page, L., Spergel, D. N., Tucker, G. S., Wilkinson, D. T., Wollack, E., Wright, E. L. 2003, ApJ, 583, 1
- Bergeron, J., Aracil, B., Petitjean, P., & Pichon, C. 2002, A&A, 419, 811
- Bergeron, J., & Stasińska, G. 1986, A&A, 169, 1
- Bond, N. A., Churchill, C. W., Charlton, J. C., & Vogt, S. S. 2001, ApJ, 557, 761
- Bond, N. A., Churchill, C. W., Charlton, J. C., & Vogt, S. S. 2001, ApJ, 562, 641
- Chen, H., Lanzetta, K. M., Webb, J. K., Barcons, X. 2001, ApJ, 559, 654
- Churchill, C. W. 1997, Ph.D. thesis, University of California, Santa Cruz
- Churchill, C. W., Mellon, R. R., Charlton, J. C., Jannuzi, B. T., Kirhakos, S., Steidel, C. C., Schneider, D. P. 2000, ApJS, 130, 91
- Churchill, C. W., Rigby, J. R., Charlton, J. C., & Vogt, S. S. 1999, ApJS, 120, 51
- Churchill, C. W., & Vogt, S. S. 2001, ApJ, 112, 679
- Churchill, C. W., Vogt, S. S., & Charlton, J. C. 2003, ApJ, 125, 98
- Churchill, C. W. 2012, *Cosmological Absorption Line Spectroscopy*. New York, NY: Cambridge University Press.
- Dekker, H., D’Odorico, S., Kaufer, A., Delabre, B., & Kotzlowski, H. 2000, SPIE, 4008, 534
- Dittmann, O. J., & Koeppen, J. 1995, A&A, 297, 671
- Faber, S. M. et al. 2007, ApJ, 665, 265
- Ferland, G. J., Korista, K. T., Verner, D. A., Ferguson, J. W., Kingdon, J. B., & Verner, E. M. 1998, PASP, 110, 761
- Haardt, F., & Madau, P. 1996, ApJ, 461, 20
- Kacprzak, G. G., Churchill, C. W., Steidel, C. C., & Murphy, M. T. 2008, AJ, 135, 922
- Lanzetta, K. M., Bowen, D. V., Tytler, D., & Webb, J. K. 1995, ApJ, 442, 538

- Lanzetta, K. M., Turnshek, D. A., & Wolfe, A. M. 1987, *ApJ*, 332, 739
- Lynch, R. S., & Charlton, J. C. 2007, *ApJ*, 666, 64
- Lynch, R. R., Charlton, J. C., and Kim, T. S. 2006, *ApJ*, 640, 81
- Milutinović, N., Rigby, J. R., Masiero, J. R., Lynch, R. R., Palma, C., Charlton, J. C. 2006, *ApJ*, 641, 190
- Mshar, A. C., Charlton, J. C., Lynch, R. S., Churchill, C. W., Kim, T. 2007, *ApJ*, 669, 135
- Murphy, M. T. 2008, UVES_popler software package, astronomy.swin.edu.au/~mmurphy/UVES_popler
- Narayanan, A., Misawa, T., Charlton, J. C., & Kim, T. 2007, *ApJ*, 660, 1093
- Nestor, D. B., Turnshek, D. A., & Rao, S. M. 2005, *ApJ*, 628, 637
- Oesch, P. A., Bouwens, R. J., Carollo, C. M., Illingworth, G. D., Magee, D., Trenti, M., Stiavelli, M., Franx, M., Labbé, I., & van Dokkum, P. G. 2010, *ApJ*, 725, 150
- Patnaik, A. R., Browne, I. W. A., Walsh, D., Chaffee, F. H., & Foltz, C. B., 1992, *MNRAS*, 259, 1
- Petitjean, P., & Bergeron, J. 1990, *A&A*, 231, 309
- Pettini, M., Lipman, K., & Hunstead, R. W. 1995, *ApJ*, 451, 100
- Prochaska, J. X., Wolfe, A. M., Howk, J. C., Gawiser, E., Burles, S. M., & Cooke, J. 2007, *ApJS*, 171, 29
- Prochter, G. E., & Prochaska, J. X. 2006, *ApJ*, 639, 766
- Reddy, N.A., & Steidel, C. C. 2009, *ApJ*, 692, 778
- Rigby, J. R., Charlton, J. C., & Churchill, C. W. 2002, *ApJ*, 565, 743
- Sargent, W. L. W., Steidel, C. C., & Boksenberg, A. 1988, *ApJ*, 334, 22
- Savage, B. D., & Sembach, K. R. 1991, *ApJ*, 379, 245
- Schaye, J. 2001, *ApJ*, 559, 507
- Schneider, D. P. et al. 1993, *ApJS*, 87, 45
- Schneider, D. P. et al. 2007, *AJ*, 134, 102

- Steidel, C. C., Dickinson, M., & Persson, S. E. 1994, *ApJ*, 437, 75
- Steidel, C. C. 1995, in *ESO Astrophysics Symp., QSO Absorption Lines*, ed. G. Meylan, (Berlin: Springer-Verlag), 139
- Steidel, C. C., Kollmeier, J. A., Shapley, A. E., Churchill, C. W., Dickinson, M., & Pettini, M. 2002, *ApJ*, 570, 526
- Steidel, C. C., & Sargent, W. L. W. 1992, *ApJS*, 80, 1
- Tytler, D., Boksenberg, A., Sargent, W. L. W., Young, P. J., & Kunth, D. 1987, *ApJS*, 64, 667
- Veron-Cetty, M. P., & Veron, P. 2001, *A&A*, 374, 92
- Weymann, R. J., Morris, S. L., Foltz, C. B., & Hewett, P. C. 1991, *ApJ*, 373, 23
- Zibetti, S., Ménard, B., Nestor, D. B., Quider, A. M., Rao, S. M., Turnshek, D. A. 2007, *ApJ*, 658, 161